

Ministry of Education and Science of the Russian Federation
Saint Petersburg National Research University of Information
Technologies, Mechanics, and Optics

NANOSYSTEMS:
PHYSICS, CHEMISTRY, MATHEMATICS

2013, volume 4(3)

Наносистемы: физика, химия, математика

2013, том 4, № 3



NANOSYSTEMS:

PHYSICS, CHEMISTRY, MATHEMATICS

ADVISORY BOARD MEMBERS

Chairman: V.N. Vasiliev (*St. Petersburg, Russia*),
V.M. Ievlev (*Voronezh*), P.S. Kop'ev (*St. Petersburg, Russia*),
V.N. Parmon (*Novosibirsk*), A.I. Rusanov (*St. Petersburg, Russia*).

EDITORIAL BOARD

Editor-in-Chief: N.F. Morozov (*St. Petersburg, Russia*)
Deputy Editor-in-Chief: I.Yu. Popov (*St. Petersburg, Russia*)

Section Co-Editors:

Physics – V.M. Uzdin (*St. Petersburg, Russia*),
Chemistry, material science – V.V. Gusarov (*St. Petersburg, Russia*),
Mechanics – A.K. Belyaev (*St. Petersburg, Russia*),
Mathematics – I.Yu. Popov (*St. Petersburg, Russia*).

Editorial Board Members:

V.M. Adamyan (*Odessa, Ukraine*); O.V. Al'myasheva (*St. Petersburg, Russia*); S. Bechta (*Stockholm, Sweden*); V.G. Bepalov (*St. Petersburg, Russia*); A. Chatterjee (*Hyderabad, India*); S.A. Chivilikhin (*St. Petersburg, Russia*); A.V. Chizhov (*Dubna, Russia*); P.P. Fedorov (*Moscow, Russia*); E.A. Gudilin (*Moscow, Russia*); D.A. Indeitsev (*St. Petersburg, Russia*); A.L. Ivanovskii (*Ekaterinburg, Russia*); H. Jónsson (*Reykjavik, Iceland*); A.A. Kiselev (*Madison, USA*); Yu.S. Kivshar (*Canberra, Australia*); S.A. Kozlov (*St. Petersburg, Russia*); Yu.B. Kudasov (*Sarov, Russia*); S.E. Kul'kova (*Tomsk, Russia*); P.A. Kurasov (*Stockholm, Sweden*); A.V. Lukashin (*Moscow, Russia*); V.A. Margulis (*Saransk, Russia*); I.V. Melikhov (*Moscow, Russia*); G.P. Miroshnichenko (*St. Petersburg, Russia*); H. Neidhardt (*Berlin, Germany*); K. Pankrashkin (*Orsay, France*); B.S. Pavlov (*Auckland, New Zealand*); A.V. Ragulya (*Kiev, Ukraine*); V. Rajendran (*Tamil Nadu, India*); V.P. Romanov (*St. Petersburg, Russia*); V.Ya. Rudyak (*Novosibirsk, Russia*); V.M. Talanov (*Novocherkassk, Russia*); A.Ya. Vul' (*St. Petersburg, Russia*).

Editors:

I.V. Blinova; A.I. Popov; M.A. Skryabin; A.I. Trifanov; E.S. Trifanova (*St. Petersburg, Russia*),
R. Simoneaux (*Philadelphia, Pennsylvania, USA*).

Address: University ITMO, Kronverkskiy pr., 49, St. Petersburg 197101, Russia.

Phone: +7(812)232-67-65, **Journal site:** <http://nanojournal.ifmo.ru/>,

E-mail: popov1955@gmail.com

AIM AND SCOPE

The scope of the journal includes all areas of nano-sciences. Papers devoted to basic problems of physics, chemistry, material science and mathematics inspired by nanosystems investigations are welcomed. Both theoretical and experimental works concerning the properties and behavior of nanosystems, problems of its creation and application, mathematical methods of nanosystem studies are considered.

The journal publishes scientific reviews (up to 30 journal pages), research papers (up to 15 pages) and letters (up to 5 pages). All manuscripts are peer-reviewed. Authors are informed about the referee opinion and the Editorial decision.

Content

From the Editorial Board 305

MATHEMATICS

Yu.N. Belyayev

Method of symmetric polynomials in the computations of scattering matrix 306

PHYSICS

V.A. Batischev, V.V. Zaikin, E.V. Horoshunova

Heat transport in Marangoni layer with nanoparticles 313

I.V. Blinova

Model of non-axisymmetric flow in nanotube 320

V.V. Karpunin, V.A. Margulis

Absorption of electromagnetic radiation in the quantum well placed in a magnetic field 324

A.V. Pak, M.B. Belonenko, O.Y. Tuzalina

Ultrashort optical pulse propagation in a double layer of graphene boron nitride with accounting the material dispersion 329

V.E. Zalizniak

Interatomic interaction in fcc metals 336

CHEMISTRY AND MATERIAL SCIENCE

V.A. Keskinov, N.A. Charykov, M.V. Keskinova, Yu.V. Murashkin, A.A. Blokhin, K.N. Semenov

Pre-chromatography crude separation of light fullerenes by poly-termical (re)crystallization method 344

E.A. Tugova, V.V. Gusarov

Structure peculiarities of nanocrystalline solid solutions in $GdAlO_3 - GdFeO_3$ system 352

Papers, presented at MAM-12

N. Aloysius Sabu, K.P. Priyanka, Smitha Thankachan, Anu Tresa Sunny, E.M. Mohammed, O. P. Jaseentha, Thomas Varghese

Dielectric studies of nanocrystalline Manganese Tungstate 357

C.C. Chauhan, R.B. Jotania, K.R. Jotania Structural properties of cobalt substituted barium hexaferrite nanoparticles prepared by a thermal treatment method	363
C. Deepa, A. Nishara Begum, S. Aravindan Preparation and antimicrobial observations of zinc doped nanohydroxyapatite	370
Ayman Karar; Chee Leong Tan; Kamal Alameh; Yong Tak Lee Dielectric Waveguide Optimization for the Enhancement of TE-Polarization Transmission of Plasmonics-Based MSM-PD	378
Nazme Moushummy, Kamal Alameh, V. Rajendran, Yong Tak Lee Silver-Nanoparticle-Based Etch Mask Control for Subwavelength Structure Development	387
Partha P. Pal, J. Manam Effect of Li⁺ co-doping on the luminescence properties of ZnO:Tb³⁺ nanophosphors	395
S. Sivasathya, D. JohnThiruvadigal The effects of defects on electron transport in metallic single wall carbon nanotubes	405
R.R. Vaishaka, A.C. Hegde Electrofabrication of nanostructured multilayer coatings for better corrosion protection	409
Valentina Tiporlini, Hoang N. Nguyen, Kamal Alameh Noise Cancellation in Unshielded Magnetocardiography based on Least-Mean-Squared Algorithm and Genetic Algorithm	417
M. Vijay Kumar, S. Krishna Prasad Composites of single walled carbon nanotubes and liquid crystals as switchable conductors	425
Sheena Xavier, Smitha Thankachan, Binu P. Jacob, E. M. Mohammed Effect of Sintering Temperature on the Structural and Magnetic Properties of Cobalt Ferrite Nanoparticles	430
Information for authors	438

FROM THE EDITORIAL BOARD

In this issue we continue to publish works presented at 6th International Symposium on Macro- and Supramolecular Architectures and Materials; Special Theme: Nano Systems and Applications (MAM-12).

Scope of the Conference

As novel materials will play a key role in science and technology in the 21st century, the objectives of this symposium series are in providing an interdisciplinary forum for scientists engaged in the full spectrum of research, development, application, and to discuss the current status and recent developments of these materials with a focus on the chemistry and practical approaches. In addition, the meeting will provide an opportunity to overview the field by covering a wide range of topics. Themes have selected to accommodate a wide range of interests to facilitate interdisciplinary interaction in both academic fields and industrial science and technology.

MAM is a series of conferences which is organized by Prof. Dr. K.E. Geckeler. MAM-12 is 6th conference in this series which was held at Coimbatore, India during 21-25 November 2012. Chairman of MAM-12 is Dr. V. Rajendran, Director, R&D and Centre for Nanoscience and Technology K.S.R. College of Technology, India.

Steering committee

Chairs:

K.E. Geckeler (Gwangju, South Korea)

V. Rajendran (Coimbatore, India)

Members:

Kahwa (Kingston, West Indies); **H. Nishide** (Tokyo, Japan); **H. Ritter** (Dusseldorf, Germany); **B. Rivas** (Concepcion, Chile); **E. Rosenberg** (Missoula, USA).

METHOD OF SYMMETRIC POLYNOMIALS IN THE COMPUTATIONS OF SCATTERING MATRIX

Yu. N. Belyayev

Syktyvkar State University, Oktyabrskii pr. 55, Syktyvkar-167001, Russia
ybelyayev@mail.ru

PACS 02.10.Yn, 02.30.Hq, 11.55.-m

The method for calculating any analytic matrix function by means of symmetric polynomials is presented. The method of symmetric polynomials (MSP) is applied to the calculation of the fundamental matrix of a differential equations system. The scaling method is developed for computation of the scattering matrix. An analytical estimate of the scaling parameter, allowing the calculation of the matrix exponential with the required reliability and accuracy is obtained. This parameter depends on the matrix order n , the value of the matrix elements and layer thickness.

Keywords: layered media, matrix, exponential, symmetric polynomials, roundoff error, truncation error, scaling.

1. Introduction

The dynamical theory of electron diffraction in crystals is based on the equations of Howie-Whelan [1]. An analogous approach to X-ray diffraction is based on Takagi-Taupin equations [2]. Calculation of multiple-wave diffraction in the crystalline layer thickness z on these equations leads to the Cauchy problem

$$\frac{d\Psi(z)}{dz} = A\Psi(z), \quad \Psi(0) = \Psi_0, \quad (1)$$

where $\Psi(z)$ — column matrix whose components are wave functions $\psi_i(z)$, $i = 1, 2, \dots, n$; $A \equiv \|a_{ij}\|$ — matrix of order n ; column matrix Ψ_0 consists of n known ψ_{i0} .

The fundamental matrix S of the differential equations system (1) converts the wave field $\Psi(0)$ in the field $\Psi(z)$ at a depth z : $\Psi(z) = S\Psi_0$. In the theory of diffraction S is known as the scattering matrix.

If the crystal is perfect, the scattering matrix is defined as follows:

$$S = \exp(Az) \equiv I + Az + \frac{(Az)^2}{2!} + \frac{(Az)^3}{3!} + \dots, \quad (2)$$

where I — unit matrix. If the coefficients a_{ij} of differential equations (1) are functions of z , then one way to solve the problem (1) is the partition of the interval $[0, z]$ on N subdomains: $[0 = z_0, z_1]$, $[z_1, z_2]$, \dots , $[z_{N-1}, z_N = z]$. The number N should be large enough so that $A \simeq A_l = \text{const}_l$ for any $z \in [z_{l-1}, z_l]$, $l = 1, 2, \dots, N$, and the scattering matrix can be approximated by the product: $S = \prod_{l=N}^1 \exp(A_l(z_l - z_{l-1}))$.

Calculations of $\exp(Az)$ with the aid of the Lagrange-Sylvester [3], Becker [4], Newton [5] formulas or matrix decomposition methods [6] requires the prior determination of the matrix A eigenvalues λ_j , $j = 1, 2, \dots, n$. Another approach to the calculation of the matrix exponential is based on the use of symmetric polynomials [7]. This method is applied in the present work to calculate the scattering matrix.

2. Method of symmetric polynomials (MSP)

According to the Cayley-Hamilton theorem, any matrix $A \equiv \|a_{ij}\|$ of order n satisfies its characteristic equation $\lambda^n - \sigma_1\lambda^{n-1} + \sigma_2\lambda^{n-2} - \dots (-1)^n\sigma_n = 0$, i.e.

$$A^n - p_1A^{n-1} - p_2A^{n-2} - \dots - p_nI = 0. \tag{3}$$

Here we use the notations

$$p_j = (-1)^{j-1}\sigma_j, \quad j = 1, \dots, n, \tag{4}$$

$I \equiv A^0$, and $\sigma_i, i = 1, 2, \dots, n$, — sums of principal minors of i -th order $\det A$:

$$\sigma_1 = a_{11} + a_{22} + \dots + a_{nn}, \quad \sigma_2 = \sum_{j>i} \begin{vmatrix} a_{ii} & a_{ij} \\ a_{ji} & a_{jj} \end{vmatrix}, \quad \dots, \quad \sigma_n = \det A. \tag{5}$$

Conversely, as is known, σ_j are the elementary symmetric polynomials in the eigenvalues λ_j of matrix A : $\sigma_1 = \lambda_1 + \lambda_2 + \dots + \lambda_n, \sigma_2 = \sum_{l \neq j} \lambda_l \lambda_j, \dots, \sigma_n = \lambda_1 \lambda_2 \dots \lambda_n$. Therefore, any function of the elementary symmetric polynomials σ_i is also symmetric in the eigenvalues λ_j of the matrix A .

Definition 1. Functions $\mathcal{B}_g(n) \equiv \mathcal{B}_g(p_1, \dots, p_n)$ that satisfy the recurrence relations

$$\mathcal{B}_g(n) = \begin{cases} 0, & \text{if } g = 0, 1, \dots, n - 2, \\ 1, & \text{if } g = n - 1, \\ p_1\mathcal{B}_{g-1}(n) + p_2\mathcal{B}_{g-1}(n) + \dots + p_n\mathcal{B}_{g-n}(n), \end{cases} \tag{6}$$

are called *symmetric polynomials of n -th order*.

2.1. Representation of matrix functions by means of symmetric polynomials

As a result of equality (3) any integer power $j > 0$ matrix A can be expressed as a linear combination of the first n powers A^0, A, \dots, A^{n-1} :

$$A^j = \sum_{l=0}^{n-1} C_{jl}A^l, \tag{7}$$

where C_{jl} are functions of p_i .

Theorem 1. *If the matrix A is nonsingular, then the coordinates C_{jl} of the matrix A^j in the basis A^0, A, \dots, A^{n-1} are represented by the formulas:*

$$\left. \begin{aligned} C_{j0} &= \mathcal{B}_{j+n-1}(n) - p_1\mathcal{B}_{j+n-2}(n) - \dots - p_{n-1}\mathcal{B}_j(n), \\ C_{j1} &= \mathcal{B}_{j+n-2}(n) - p_1\mathcal{B}_{j+n-3}(n) - \dots - p_{n-2}\mathcal{B}_j(n), \\ &\vdots \\ C_{j(n-2)} &= \mathcal{B}_{j+1}(n) - p_1\mathcal{B}_j(n), \\ C_{j(n-1)} &= \mathcal{B}_j(n), \end{aligned} \right\} \tag{8}$$

where j is any integer, and $\mathcal{B}_j(n)$ — symmetric polynomials of n -th order matrix A .

If $\det A = 0$, then (8) determine the coefficients C_{jl} for $j \geq 0$.

Relations (8) is easily verified for $j = 0, 1, \dots, n - 1$ and for other values of j formulas (8) can be proved by induction.

Corollary 1.1.

$$C_{jl} = \sum_{g=0}^l p_{n-l+g}\mathcal{B}_{j-1-g}(n), \quad l = 0, \dots, n - 1, \quad \text{where } \begin{cases} j \text{ is any integer,} & \text{if } \det A \neq 0, \\ j \geq n, & \text{if } \det A = 0. \end{cases} \tag{9}$$

Formulas (8) and (9) are equivalent in the sense that their right-hand sides are equal to each other due to the recurrence relations (6).

Corollary 1.2. *Let $f(\zeta)$ be an entire function of complex variable ζ , then the function $f(A)$ of n -th order matrix A has the following representation*

$$f(A) = \sum_{l=0}^{n-1} A^l \left[\alpha_l + \sum_{g=0}^l p_{n-l+g} \sum_{j=n}^{\infty} \alpha_j \mathcal{B}_{j-1-g}(n) \right], \tag{10}$$

where symmetric polynomials $\mathcal{B}_{j-1-g}(n)$ of n -th order matrix A are defined by (6) and α_l — coefficients of the power series: $f(\zeta) = \sum_{j=0}^{\infty} \alpha_j \zeta^j$.

Proof. If $f(\zeta)$ is an analytic function on the whole complex plane, then the expansion $f(\zeta) = \sum_{j=0}^{\infty} \alpha_j \zeta^j$ remains valid when replacing the complex variable ζ on a square matrix A : $f(A) = \sum_{j=0}^{\infty} \alpha_j A^j$. We substitute in the last equality the expression of the matrix A^j according to formulas (7) and (9). Equality (10) - is the result of this substitution. □

Corollary 1.3. *For any n -th order matrix A and scalar z*

$$\exp(Az) = \sum_{l=0}^{n-1} (Az)^l \frac{1}{l!} \left[1 + l! \sum_{g=0}^l p_{n-l+g} \sum_{j=n}^{\infty} \frac{1}{j!} \mathcal{B}_{j-1-g}(n) \right], \tag{11}$$

where $p_g, g = 1, \dots, n$, and $\mathcal{B}_j(n)$ are symmetric polynomials of matrix Az .

2.2. Estimation of symmetric polynomials modulus

The elementary symmetric polynomial σ_j is the sum of the principal minors of j -th order determinant of the matrix A . The number of such minors is C_n^j . One minor of j -th order contains $j!$ terms, each of which is a product of the j matrix elements a_{ij} . We denote by $\max |a_{gl}|$ the greatest value of the modulus of the matrix elements a_{gl} . Therefore, using the definition (4), we obtain the following relations

$$|p_j| \leq p_{jM} = \frac{n!}{(n-j)!} (\max |a_{gl}|)^j, \quad j = 1, 2, \dots, n. \tag{12}$$

Theorem 2.

$$|\mathcal{B}_j(n)| < \frac{n}{2n-1} x^{j-n+1}, \tag{13}$$

where

$$x = (2n-1) \max |a_{gl}|. \tag{14}$$

Proof. Using (12) and definition (6), we obtain

$$\begin{aligned} |\mathcal{B}_j(n)| &= \left| \sum_{l=1}^n p_l \mathcal{B}_{j-l}(n) \right| \leq p_{1M} |\mathcal{B}_{j-1}(n)| + p_{2M} |\mathcal{B}_{j-2}(n)| + \dots + p_{nM} |\mathcal{B}_{j-n}(n)| \leq \\ &\leq p_{1M} (p_{1M} |\mathcal{B}_{j-2}(n)| + p_{2M} |\mathcal{B}_{j-3}(n)| + \dots + p_{nM} |\mathcal{B}_{j-n-1}(n)|) + \\ &\quad + p_{2M} |\mathcal{B}_{j-2}(n)| + \dots + p_{(n-1)M} |\mathcal{B}_{j-n+1}(n)| + p_{nM} |\mathcal{B}_{j-n}(n)| = \\ &= \frac{p_{1M}^2 + p_{2M}}{p_{1M}} \sum_{l=1}^n c_l |\mathcal{B}_{j-1-l}(n)|. \end{aligned} \tag{15}$$

Here

$$c_l = \frac{p_{lM}}{p_{1M}^2 + p_{2M}} \left(p_{1M}^2 + \frac{p_{1M}p_{(l+1)M}}{p_{lM}} \right), \quad l = 0, 1, \dots, n-1; \quad c_n = p_{nM} \frac{p_{1M}^2}{p_{1M}^2 + p_{2M}}.$$

Applying (12) we find: $\frac{p_{1M}^2 + p_{2M}}{p_{1M}} = \frac{2n-1}{n} p_{1M}$ and $\frac{p_{1M}p_{(l+1)M}}{p_{lM}} < p_{2M}$. Consequently, $c_l < p_{lM}$, $l = 0, \dots, n$. These relations allow us to rewrite the formula (15) as follows

$$|\mathcal{B}_j(n)| \leq \sum_{l=1}^n p_{lM} |\mathcal{B}_{j-l}(n)| < x \sum_{l=1}^n p_{lM} |\mathcal{B}_{j-l-1}(n)|. \tag{16}$$

where x is defined by (14). The last inequality in (16) is recursive. Continuation of this inequality gives: $|\mathcal{B}_j(n)| < x^{j-n} \sum_{l=1}^n p_{lM} |\mathcal{B}_{n-l}(n)| = p_{1M} x^{j-n}$, which is equivalent to (13). □

Remark. For matrix Az , where z some scalar, the inequality (13) remains valid, but the parameter x is defined in this case by the expression

$$x = (2n-1) \max |a_{gl}z|. \tag{17}$$

Corollary 2.1.

$$\begin{aligned} \left| \sum_{j=N}^{\infty} \frac{1}{j!} C_{jl} \right| &< \frac{x^{-l}n}{(2n-1)^{n-l+1}} \sum_{g=0}^l \frac{n!}{(l-g)!(2n-1)^g} \sum_{j=N}^{\infty} \frac{x^j}{j!} < \\ &< \frac{x^{N-l}n(N+1)}{(2n-1)^{n-l+1}N!(N+1-x)} \sum_{g=0}^l \frac{n!}{(l-g)!(2n-1)^g}, \quad \text{if } x < N+1. \end{aligned} \tag{18}$$

3. Computation of the matrix exponential

According to relations (11) and (9)

$$\exp(Az) \simeq \mathcal{E}(J) \equiv \|e_{ik}(J)\| = \sum_{l=0}^{n-1} (Az)^l \left[\frac{1}{l!} + \mathcal{E}_l(J) \right], \tag{19}$$

where $J \geq n$ and

$$\mathcal{E}_l(J) = \sum_{j=n}^J \frac{1}{j!} C_{jl} = \sum_{g=0}^l p_{n-l+g} \sum_{j=n}^J \frac{1}{j!} \mathcal{B}_{j-1-g}(n). \tag{20}$$

The approximation in (19) is replaced by the exact equality if J goes to infinity.

The calculation of the matrix exponential by formulas (19)-(20) can be performed using the following algorithm.

1. First, the consecutive computations $1/(2!), \dots, 1/(J!)$ are done.
2. Powers of the matrix Az are computed from the second to n -th inclusive, and traces of these matrices

$$s_g = \text{tr}(Az)^g, \quad g = 1, \dots, n$$

are calculated.

3. Sequential calculation of the coefficient p_g , defined by (4) can be performed by Newton's formula [3]:

$$gp_g = s_g - p_1s_{g-1} - \dots - p_{g-1}s_g, \quad g = 1, \dots, n.$$

In particular, $p_1 = s_1$, $p_2 = (s_2 - p_1s_1)/2$, $p_3 = (s_3 - p_1s_2 - p_2s_1)/3, \dots$

4. After that, the symmetric polynomials $\mathcal{B}_l(n)$ for $l = n, n + 1, \dots, J - 1$ are calculated by recurrence formulas (6).
5. The calculation of the sums $\Sigma_g \equiv \sum_{j=n}^J \mathcal{B}_{j-1-g}(n)/(j!)$ for $g = 0, 1, \dots, n - 1$.
6. Substitution of the values which were found in the previous steps in the formula (19) and calculation

$$\begin{aligned} \exp(Az) = I[1 + p_n \Sigma_0] + (Az)[1 + (p_{n-1} \Sigma_0 + p_n \Sigma_1)] + \dots + \\ + (Az)^{n-1} \left[\frac{1}{(n-1)!} + (p_1 \Sigma_0 + p_2 \Sigma_1 + \dots + p_n \Sigma_{n-1}) \right]. \end{aligned}$$

3.1. Estimation of roundoff errors

Multiplication of numbers generates roundoff errors. Therefore, the accuracy of the scattering matrix computations can be estimated by the number of multiplications which are used in the calculations. The six steps listed above require for their implementation the following number of multiplications, respectively: $N_{1_1} = J - 1$, $N_{1_2} = n^3(n - 1)$, $N_{1_3} = (n - 1)(n + 2)/2$, $N_{1_4} = n(J - n)$, $N_{1_5} = nJ - n(3n - 1)/2$, $N_{1_6} = n^3 + n(n + 1)/2$. On the whole $N_1 = (2n + 1)J + n^4 - n^2 - 2 - 3n(n - 1)/2$.

For comparison, calculations according formula (2)

$$\exp(Az) = I + (Az) + (Az) \frac{(Az)}{2} + (Az) \frac{(Az)}{2} \frac{(Az)}{3} + \dots + (Az) \frac{(Az)}{2} \frac{(Az)}{3} \dots \frac{(Az)}{J}$$

require $N_2 = (n^3 + n^2)(J - 1)$ multiplications.

It is easy to verify that $N_1 < N_2$ if $J > n$. For these values of J , the computation $\exp(Az)$ by the MSP generates a smaller roundoff error than calculations by formula (2). Asymptotics of the ratio of N_2 to N_1 is characterized by

$$\lim_{J \rightarrow \infty} \frac{N_2}{N_1} = \frac{n^3 + n^2}{2n + 1} > \frac{n^2}{2}.$$

3.2. Truncation error

Let us consider error caused by truncation of series

$$\sum_{j=n}^{\infty} \frac{1}{j!} \mathcal{B}_{j-1-g}(n) \approx \sum_{j=n}^{n+N} \frac{1}{j!} \mathcal{B}_{j-1-g}(n),$$

and substitution of exact formula (11) for (19).

Definition 2. *The relative truncation error of the matrix exponential is*

$$\epsilon(J) = \max \left| \frac{e_{ik}(\infty) - e_{ik}(J)}{e_{ik}(\infty)} \right|. \tag{21}$$

Obviously

$$|e_{ik}(\infty) - e_{ik}(J)| < \left| \sum_{l=0}^{n-1} \frac{(a_{ik}z)^l}{l!} \right| \max \left| l! \sum_{j=J+1}^{\infty} \frac{1}{j!} C_{jl} \right|, \tag{22}$$

and

$$|e_{ik}(\infty)| = \left| \sum_{l=0}^{n-1} \frac{(a_{ik}z)^l}{l!} \right| |1 + T| > \left| \sum_{l=0}^{n-1} \frac{(a_{ik}z)^l}{l!} \right| (1 - |T|), \tag{23}$$

where

$$|T| = \left| \left(\sum_{l=0}^{n-1} \frac{(a_{ik}z)^l}{l!} l! \mathcal{C}_l(\infty) \right) / \left(\sum_{l=0}^{n-1} \frac{(a_{ik}z)^l}{l!} \right) \right| \leq \max \left| l! \sum_{j=n}^{\infty} \frac{1}{j!} C_{jl} \right|. \tag{24}$$

For $x < 1$ from (18) and (24) it follows

$$|T| < \frac{x^{n-l} n(n+1)(n-1)!}{(2n-1)^{n-l+1} n!(n+1-x)} \sum_{g=0}^{n-1} \frac{n!}{(n-1-g)!(2n-1)^g} < \frac{1}{2}.$$

From this relation and (23) we find

$$|e_{ik}(\infty)| > \left| \sum_{l=0}^{n-1} \frac{(a_{ik}z)^l}{l!} \right| \frac{1}{2} > \frac{xn(n+1)(n-1)!}{(2n-1)^2 n!(n+1-x)} \Sigma, \tag{25}$$

and from (22) and (18) —

$$|e_{ik}(\infty) - e_{ik}(N+n)| < \frac{n!(N+n+2)x^{N+2}}{(2n-1)^2(N+n+1)!(N+n+2-x)} \Sigma. \tag{26}$$

Here $\Sigma = \left| \sum_{l=0}^{n-1} \frac{(a_{ik}z)^l}{l!} \right| \sum_{g=0}^{n-1} \frac{n!}{(n-1-g)!(2n-1)^g}.$

Finally, substitution of expressions (25) and (26) in the definition (21) gives the proof of the following theorem.

Theorem 3. *If $\max |a_{gl}z| < 1/(2n-1)$, the relative truncation error $\epsilon(N+n)$ of the matrix exponential $\exp(Az)$ satisfies the inequality*

$$\epsilon(N+n) < \frac{n!(N+n+2)x^{N+1}}{(N+n+1)!(N+n+1)},$$

where x is defined by (17).

3.3. Scaling exponent

Using the fundamental property of the exponential function $\exp A = [\exp(A/m)]^m$, we represent the scattering matrix as follows: $S = X^m$, where

$$X \simeq \sum_{l=0}^{n-1} \left(\frac{Az}{m} \right)^l \frac{1}{l!} \left[1 + l! \sum_{g=0}^l p_{n-l+g} \sum_{j=n}^{n+N} \frac{1}{j!} \mathcal{B}_{j-l-g}(n) \right], \tag{27}$$

m - integer; $p_i = (-1)^{i-1} \sigma_i$; $\sigma_i, i = 1, 2, \dots, n$, and $\mathcal{B}_l(n)$ are elementary symmetric polynomials and symmetric polynomials of n -th order of matrix (Az/m) , respectively.

Corollary 3.1. *The relative truncation error of the matrix X calculation according to the formula (27) $\epsilon < \frac{n!(N+n+2)\xi^{N+1}}{(N+n+1)!(N+n+1)}$, provided that $\xi = (2n-1) \frac{\max |a_{jl}z|}{m} < 1$.*

Example. Let the scaling factor m for matrix Az of order $n = 4$ is the smallest integer satisfying the condition $m \geq 10(2n-1) \max |a_{jl}z|$. In this case $\xi < 0.1$, and the calculation by formula (27) with the value $N = 2$ gives the matrix X with a relative truncation error less than 10^{-5} .

When $m > n + 1$, the most efficient way of calculating the matrix X^m , as shown in [7], is to use the theorem (8):

$$X^m = \sum_{l=0}^{n-1} X^l \sum_{g=0}^l (-1)^{n-l+g-1} \sigma_{n-l+g} \mathcal{B}_{m-1-g}(n),$$

where σ_j and $\mathcal{B}_l(n)$ are symmetric polynomials of matrix X .

4. Conclusion

Among the dozens of techniques that were used to calculate the matrix exponential, the method of symmetric polynomials (MSP) has significant advantages. One of the most important of them - is carrying out calculations using analytical estimates. Another is that these estimates do not depend on the eigenvalues of the matrix. Accuracy of the scattering matrix $S = \exp(Az)$ calculation by the method of scaling is determined by the truncation errors in the calculation of matrix X and roundoff errors in the computation of the matrix X^m . MSP allows one to control the first error and minimize the latter.

References

- [1] Cowley J. M. *Diffraction Physics*. North-Holland Pub. Co., Amsterdam, 410 pp. (1975).
- [2] Pinsker Z. G. *Dynamical scattering of X-rays in perfect crystals*. Springer-Verlag, Heidelberg, 511 pp. (1978).
- [3] Gantmacher F. R. *The Theory of Matrices*. Nauka, Moscow, 552 pp. (1988).
- [4] Angot A. *Compléments de mathématiques à l'usage des ingénieurs de l'électrotechnique et des télécommunications*. Masson, Paris, 868 pp. (1982).
- [5] MacDuffee C. C. *The Theory of Matrices*. Chelsea, New York, 128 pp. (1956).
- [6] Faddeev D. K., Faddeeva V. N. *Computational methods of linear algebra*. Nauka, Moscow, 656 pp. (1963).
- [7] Belyayev Yu. N. Calculations of transfer matrix by means of symmetric polynomials. Proceedings of the International Conference "Days on Diffraction 2012", St.Petersburg, Russia May 28 – June 1, 2012. P. 36–41.

HEAT TRANSPORT IN MARANGONI LAYERS WITH NANOPARTICLES

V. A. Batischev, V. V. Zaikin, E. V. Horoshunova

344090, Milchakova, 8a. Department of Theoretical and Computer Hydrodynamics,
Southern Federal University, Rostov-on-Don, Russia

batischev-v@mail.ru

PACS 47.55.Nb, 47.55.Pf

This study investigates the influence of nanoparticle concentration on the Marangoni effect in the boundary layer near the free boundary of an incompressible fluid with small kinematic viscosity and thermal conductivity. The study was conducted on the basis of a single-phase model derived from the Navier-Stokes equations by replacing thermal parameters for their effective values. Two cases of stationary axisymmetric fluid flow are considered. In the first case, the fluid is cooled on the free surface near the symmetry axis, and in the second case, the fluid is heated. In the first case, a rotation of the fluid in a thin boundary layer appears near the free boundary, while there is no rotation outside the layer. In both cases, as the concentration of nanoparticles increases, the heat flux and the fluid velocity at the free boundary decrease.

Keywords: nanoparticles, a free boundary, the Marangoni effect, the boundary layer, thermal conductivity.

1. Introduction

The idea of the heat transport by fluid with micron-sized particles was proposed by Maxwell in the late nineteenth century [1]. However, at that time, the method failed to develop. The model of heat transport by a fluid containing metal nanoparticles was offered by Choi S. and Estman J. in 1995 [2]. It was thought that the thermal conductivities of some metals are hundreds of times greater than the thermal conductivities of some liquids. In an initial paper, several calculations were made for heat transport in the convective motion of a fluid with nanoparticles in areas with solid boundaries [2]. It was shown that the heat flux can be changed by tens of percent, depending on the concentration and type of nanoparticles. The calculations were based on single-phase and two-phase models. These studies indicated that the quantitative differences in these models were small, so, in this paper, a simple single-phase model was used. Recently, a number of reviews and articles on the convection of fluid with nanoparticles have been published [3–5]. The experimental results on the problem [5] confirmed the theoretical calculations. The heat transport in Marangoni layers in the plane case was previously studied [6]. In this article, the axisymmetric case was studied using constant thermal parameters. The flow of fluid at a given longitudinal temperature gradient on the free surface was calculated. Two cases were considered; when the temperature of the free boundary either increased or decreased with distance from the axis of symmetry. In the first case, a rotation of the fluid in the boundary layer appears near the free boundary with an absence of rotation outside this layer. In both cases, the heat flux on the free boundary decreased with increasing nanoparticle concentration and may be reduced by tens of percent, depending on the concentration of the nanoparticles and their composition.

2. The Equations of the Model

This study investigates the stationary axisymmetric flow of a viscous heat-conducting incompressible fluid in a layer of infinite thickness, limited to the top by the free boundary Γ . Along Γ , a temperature gradient is given which is positive in the first case and negative in the second. For small values of the kinematic viscosity and thermal diffusivity near the free boundary, there occurs a thin boundary Marangoni layer, outside of which, the fluid flow is slow and in the first approximation is described by the equations of an inviscid fluid. The study explores cases when metallic nanoparticles such as copper, silver, alumina and titanium oxide are placed in the base fluid, water. In these calculations, the single-phase model of nanofluids is used. It is assumed that the base fluid and the nanoparticles are in thermodynamic equilibrium, with no slide occurring between the fluid and the nanoparticles. The nanoparticles are spherical in shape and of uniform size. The equations of motion in the case of single-phase fluid issue from the Navier-Stokes equations by replacing the physical parameters on their effective values:

$$\begin{aligned}(\mathbf{v}, \nabla) \mathbf{v} &= -\rho_{nf}^{-1} \nabla p + \mu_{nf} \rho_{nf}^{-1} \nabla^2 \mathbf{v}, \\ (\mathbf{v}, \nabla) T &= \chi_{nf} \nabla^2 T, \quad \operatorname{div} \mathbf{v} = 0,\end{aligned}$$

where $\mathbf{v} = (v_r, v_\theta, v_z)$ is the velocity vector, p is the pressure, T is the temperature. (r, θ, z) are cylindrical coordinates. Parameters ρ_{nf} , μ_{nf} , χ_{nf} are the effective values of density, dynamic factor of viscosity, thermal diffusivity of fluid with nanoparticles. The fluid motion is axially symmetric, i.e. velocity vector, pressure and temperature are independent of the circumferential coordinate θ . It is assumed that the surface tension is linearly dependent on the temperature $\sigma = \sigma_0 - |\sigma_T| (T - T_*)$, where σ_0 , $|\sigma_T|$, T_* are constant. Deformability of the free boundary is to be neglected. On the free surface Γ , there are satisfied dynamic conditions for shear stresses, the kinematic condition and the temperature is set [6]:

$$\begin{aligned}2\mu_{nf} (\Pi \mathbf{n} - (\mathbf{n} \Pi \mathbf{n}) \mathbf{n}) &= \nabla_\Gamma \sigma, \\ \mathbf{v} \mathbf{n} &= 0, \quad T = T_\Gamma(r, z), \quad (r, z) \in \Gamma,\end{aligned}$$

where Π is the strain rate tensor, \mathbf{n} is the normal vector to the free boundary Γ . ∇_Γ is the gradient along Γ , T_Γ is the set temperature of the free boundary. Along Γ , a temperature gradient satisfies the condition $\nabla_\Gamma T_\Gamma \neq 0$ at $r \leq L$ and $T_\Gamma = \text{const}$ at $r > L$. We turn to the dimensionless variables in equations of motion and boundary conditions, having selected as a scale of length, velocity, pressure and temperature the following parameters L , U , σ_0/L , $A_T L$. Where $U = (|\sigma_T|^2 A_T^2 L \rho_f^{-2} \nu_f^{-1})^{1/3}$ and A_T are the scale of the temperature gradient along the surface Γ . Parameters ρ_f , ν_f indicate the density and viscosity kinematic factor of the base fluid. With large temperature gradients along the free surface and small diffusion coefficients, the boundary layer that arises near Γ is characterized by a large value for the velocity gradient across the boundary layer. We introduce a small parameter of the formula $\varepsilon = (\rho_f \nu_f^2 |\sigma_T|^{-1} L^{-2} A_T^{-1})^{1/3}$ and note that the order of the thickness of the boundary layer is εL .

The effective values of the physical parameters for a fluid with nanoparticles ρ_{nf} , μ_{nf} , χ_{nf} , k_{nf} are expressed by the parameters of the base fluid ρ_f , μ_f , χ_f , k_f and the parameters of metal particles – density ρ_S and coefficient of thermal conductivity k_S of the known formulas [7, 8]:

$$\begin{aligned}\rho_{nf} &= (1 - \varphi) \rho_f + \varphi \rho_S, \quad \mu_{nf} = \mu_f (1 - \varphi)^{-5/2}, \\ \chi_{nf} &= k_{nf} / (\rho c_p)_{nf}, \quad (\rho c_p)_{nf} = (1 - \varphi) (\rho c_p)_f + \varphi (\rho c_p)_s,\end{aligned}$$

where φ is the volume concentration of nanoparticles in the mixture. The coefficient k_{nf} is determined by the formula [9]:

$$k_{nf} = k_f \frac{k_S + 2k_f - 2\varphi(k_f - k_S)}{k_S + 2k_f + \varphi(k_f - k_S)},$$

where k_{nf} , k_f denote the thermal conductivity coefficients of nanofluids and base fluid. The thermal parameters are considered constant. The dynamic viscosity of nanofluids is shown in [7], published by Brinkman H.C. in 1952.

3. Asymptotic Method

The solution to the problem is built through the boundary layer method. The top of the cylindrical coordinate system is put on a free surface whose equation is in the form $z = 0$. Furthermore, in the boundary layer D_Γ we introduce a stretching transformation, $z = \varepsilon s$. Note that $s \leq 0$ is in the field D_Γ . Asymptotic expansion of the velocity and temperature components are built in the form of series in powers of a small parameter ε with $\varepsilon \rightarrow 0$ [10]:

$$\begin{aligned} v_r &= h_{r0} + \varepsilon(h_{r1} + v_{r1}) + \dots, & v_z &= \varepsilon(h_{z1} + v_{z1}) + \dots \\ v_\theta &= h_{\theta0} + \varepsilon(h_{\theta1} + v_{\theta1}) + \dots, & T &= \theta_0 + \varepsilon\theta_1 + \dots \end{aligned}$$

Similar series are built for the pressure as well. Note that the functions h_{r0} , h_{z1} , $h_{\theta0}$ are defined in the field of the boundary layer D_Γ ; as they depend on the coordinates s , r and disappear outside of D_Γ . Functions v_{r1} , v_{z1} are defined outside the boundary layer; depending on the cylindrical coordinates z , r and satisfying the Euler equations that describe the first approximation for an ideal fluid outside D_Γ . Asymptotic expansions are substituted in the Navier-Stokes equations, heat-conductivity equation, the boundary conditions, here we pass to the variables s , r in D_Γ , and the sum of the coefficients of the same powers of the parameter ε equate to zero. As a result, the leading asymptotic term satisfies the equations:

$$\begin{aligned} h_{r0} \frac{\partial h_{r0}}{\partial r} + H_{z1} \frac{\partial h_{r0}}{\partial s} - \frac{h_{\theta0}^2}{r} &= A \frac{\partial^2 h_{r0}}{\partial s^2}, \\ \frac{\partial h_{r0}}{\partial r} + \frac{h_{r0}}{r} + \frac{\partial H_{z1}}{\partial s} &= 0, \\ h_{r0} \frac{\partial h_{\theta0}}{\partial r} + H_{z1} \frac{\partial h_{\theta0}}{\partial s} + \frac{h_{r0} h_{\theta0}}{r} &= A \frac{\partial^2 h_{\theta0}}{\partial s^2}, \\ h_{r0} \frac{\partial \theta_0}{\partial r} + H_{z1} \frac{\partial \theta_0}{\partial s} &= \frac{B}{Pr} \frac{\partial^2 \theta_0}{\partial s^2}. \end{aligned} \tag{1}$$

Here, we introduce the designation: $H_{z1} = h_{z1} + v_{z1}|_\Gamma$.

For this system of equations, we give the boundary conditions:

$$\begin{aligned} \frac{1}{(1-\varphi)^{5/2}} \frac{\partial h_{r0}}{\partial s} &= -\frac{\partial T_\Gamma}{\partial r}, & H_{z1} &= 0, & \frac{\partial h_{\theta0}}{\partial s} &= 0, & \theta_0 &= T_\Gamma (s=0), \\ h_{r0} \rightarrow 0, & h_{\theta0} \rightarrow 0, & \theta_0 &\rightarrow T_\infty & (s \rightarrow -\infty). \end{aligned} \tag{2}$$

It should be noted that $T_\infty = const$ is the constant temperature at infinity. $Pr = \nu_f/\chi_f$ is the Prandtl number for water. The coefficients A and B in the equations of the boundary layer are expressed via the parameters of nanoparticles and the base fluid by the following formulas:

$$A = D(1-\varphi)^{-5/2}, \quad D = (1-\varphi + \varphi\rho_f/\rho_S)^{-1},$$

$$B = D \frac{k_S/k_f + 2 - 2\varphi(1 - k_S/k_f)}{k_S/k_f + 2 + \varphi(1 - k_S/k_f)}.$$

We consider the case when the temperature at the free surface is defined by the power law $T_\Gamma = T_\infty + \tau r^{n+1}/(n+1)$, ($n \neq -1$). Here, the parameter τ takes only two values $\tau = \pm 1$. In the first case, for $\tau = 1$, the temperature is the lowest value on the free surface of Γ at $r = 0$ on the symmetry axis and the fluid temperature increases with distance from the axis. In the second case, at $\tau = -1$, the temperature reaches its highest value on the axis of symmetry on Γ and the fluid cools with distance from the axis. Here the self-similar solution of the problem (1), (2) is determined. We introduce the stream function $\psi(s, r)$ by the formulas: $h_{r0} = \partial\psi/\partial s$, $H_{z1} = -r^{-1}\partial(r\psi)/\partial r$. The solution of the problem is performed as:

$$\psi = -r^{(n+2)/3}f(\xi), \quad \theta_0 = T_\infty + \tau r^{n+1}\theta_c(\xi)/(n+1), \quad h_{\theta 0} = r^{(2n+1)/3}G(\xi), \quad (3)$$

where $\xi = -sr^{(n-1)/3}$ (the minus sign is chosen for the realization of the inequality $\xi \geq 0$, as here $s \leq 0$). The functions $f(\xi)$, $\theta_c(\xi)$, $G(\xi)$ are determined by the boundary value problem:

$$\begin{aligned} 3Af''' &= (2n+1)f'^2 - (n+5)ff'' - 3G^2, \\ 3AG'' &= (2n+4)Gf' - (n+5)fG', \\ BPr^{-1}\theta_c'' &= (n+1)\theta_c f' - (n+5)f\theta_c'/3, \\ f(0) &= 0, \quad f''(0) = \tau(1-\varphi)^{5/2}, \quad \theta_c(0) = 1, \quad G'(0) = 0, \\ f'(\infty) &= 0, \quad G(\infty) = 0, \quad \theta_c(\infty) = 0. \end{aligned} \quad (4)$$

The heat flux on the free boundary is determined after solving the problem (4)

$$q_\Gamma = -k_{nf}\partial T/\partial z = \varepsilon^{-1}k_{nf}r^{(4n+2)/3}\tau\theta_c'(0)/(n+1), \quad (z=0)$$

and local Nusselts number $Nu = -\varepsilon^{-1}k_{nf}k_f^{-1}r^{(n+2)/3}\theta_c'(0)$.

We note the particular case when $n = 4$. The system (4) admits an exact solution at $\tau = -1$, depending on the variable by exponential law $f(\xi) = a(1 - \exp(-\gamma\xi))$, $G \equiv 0$. Here we have $\gamma = \sqrt[3]{3/A}(1-\varphi)^{5/6}$, $a = A\gamma/3$. The temperature distribution is calculated numerically.

4. The Results of the Calculations

The boundary value problem (4) was solved numerically by the shooting method. We note that the problem (4) was divided into two boundary value problems: at first we count the function $f(\xi)$, $G(\xi)$ and then we determine the function $\theta_c(\xi)$. When nanoparticles were absent in liquid for $\varphi = 0$, $A = B = 1$ and at $\tau = -1$, the solution of the problem without rotation of a thin layer was found in paper [10] for different values of the parameter n . In this paper, the solution was constructed when $\varphi \neq 0$ for the four types of nanoparticles – copper (Cu), silver (Ag), titanium oxide (TiO₂) and alumina (Al₂O₃). Concentration of the nanoparticles corresponding to the parameter φ was varied from zero to 0.2. The numerical values of thermodynamic parameters k , μ , ρ , c_p were given in paper [6]. The calculations were made at $n = 0$. It was shown that cooling at the point of $r = 0$ on the free boundary for $\tau = 1$, the rotation of the liquid appears in a thin boundary layer near the free surface. Additionally, there is no rotation outside this layer. The presence of nanoparticles in the liquid slows down the rotation of the layer, correspondingly, the higher the nanoparticle concentration, the larger the degree of inhibition. Liquid can rotate both clockwise and counterclockwise. The boundary value problem (4) for each fixed set of initial parameters admits two symmetric solutions: f ,

$\pm G, \theta_c$. At $n = 0, \tau = 1, \varphi = 0$ for system (4), we give numerical values $f'(0) = -0.5793, G(0) = \pm 0.9934, \theta'_c(0) = 1.1039$. In the case when $\tau = -1$ the rotational effect is absent. Here, $f'(0) = 1.0563, \theta'_c(0) = -3.3629, G = 0$ at $\varphi = 0$.

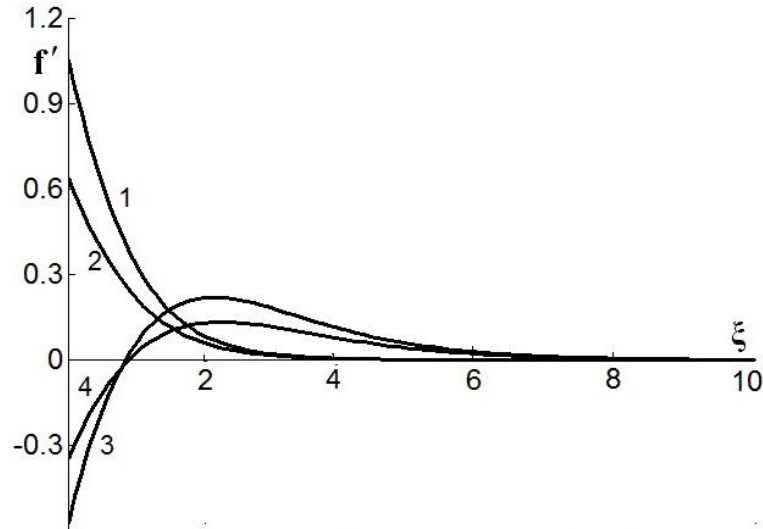


FIG. 1. The dependence of the amplitude of the radial velocity component on the transverse coordinate. Curves 1 and 2 correspond to the fluid flow without rotation, curves 3 and 4 – to the flow with rotation.

Figure 1 shows graphs of the radial velocity components' amplitude $f'(\xi)$ depending on a function of the transverse coordinate ξ in the boundary layer at various concentrations φ of copper nanoparticles. The flow without rotation corresponds to curves 1 and 2. The absence of nanoparticles in the layer ($\varphi = 0$) corresponds to curve 1, and value $\varphi = 0.2$ corresponds to curve 2. The radial component of the velocity decreased monotonically with distance from the free boundary. The presence of nanoparticles slowed down the flow of a liquid, with the braking effect appearing most prominently at the free surface. Curves 3 and 4 correspond to the values $\varphi = 0$ and $\varphi = 0.2$ for the flow of liquid with rotation. Without rotation, the velocity of the liquid decreased monotonically with the increased ξ and was positive, in this case, the rotational speed is not monotonic and a zone of countercurrent appears by the free surface (where $v_r < 0$).

Calculations showed that the circumferential velocity component h_{θ_0} decreased monotonically with distance from the free surface. When the concentration of nanoparticles increased, fluid flow inhibition occurred and the rotational effect weakened.

The graph of the function $\theta_c(\xi)$, which influences the temperature distribution in the boundary layer, in accordance with (3), is shown on Fig. 2. Curves 1 and 2 correspond to the flow of liquid with rotation, and curves 3 and 4 correspond to the flow of liquid without rotation. Curves 1 and 4 represent a nanoparticle concentration of 0 ($\varphi = 0$), while curves 2 and 3 correspond to a concentration of $\varphi = 0.2$. The temperature of the liquid with rotationless flow was defined by the function $\theta_0(r, \xi)$ in (3) and increased monotonically in the direction of the free surface inside the boundary layer with $r > 0$ and remained constant equal to T_∞ on the rotation axis $r = 0$. With higher nanoparticle concentrations, the temperature decreased monotonically in fixed section within the layer $\xi = const$. With a rotating boundary layer ($\tau = 1$), the temperature distribution inside the layer was not monotonous and differed from the one without rotation. A thin sublayer appeared inside the boundary layer D_Γ near the free boundary Γ , where the temperature increased with distance from Γ , and then fell outside this sublayer to a value of T_∞ on leaving D_Γ . Depending on the parameter φ , the temperature

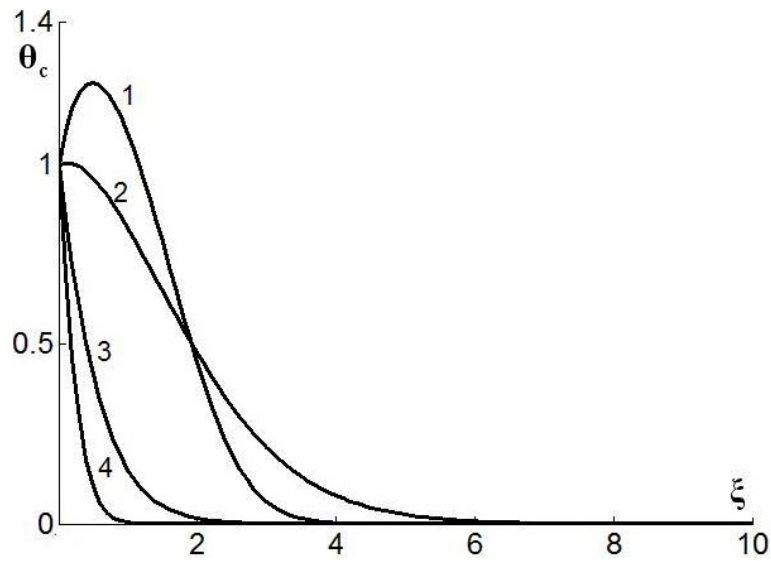


FIG. 2. The dependence of the function θ_c on the transverse coordinate in the boundary layer. Curves 1 and 2 correspond to the fluid flow with rotation, curves 3 and 4 – to the flow without rotation.

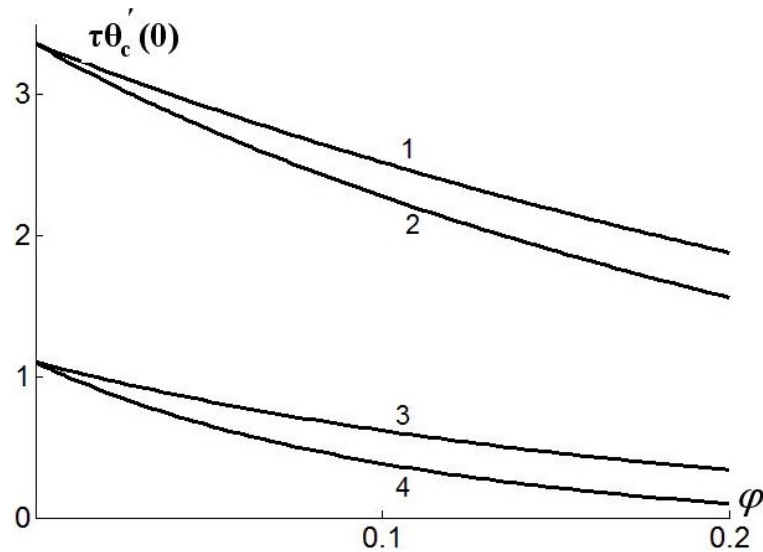


FIG. 3. The dependence of the amplitude of the heat flow on the volume concentration of nanoparticles on the free boundary. Curves 1 and 2 correspond to the fluid flow without rotation, curves 3 and 4 – to the flow with rotation.

distribution inside the layer was not monotonic at fixed transverse coordinate ξ . The value ξ_* exists for each value of the parameter φ . The temperature of the liquid decreased at $0 < \xi < \xi_*$ with an increase of the concentration parameter, φ . The temperature of the liquid increased at $\xi > \xi_*$.

Figure 3 shows graphs of the amplitude of the heat flux $\tau\theta'_c(0)$ on the free surface depending on the nanoparticle concentration φ of titanium oxide (curves 1 and 3) and copper (curves 2 and 4). The flow of liquid without rotation corresponds to curves 1 and 2, while curves 3 and 4 were calculated for a rotating layer. In all cases, increased nanoparticle concentrations reduced the amount of heat flux monotonically. Moreover, the heat flux reduction was dependent upon the nanoparticle composition.

5. Conclusion

The influence of nanoparticle concentration on heat transfer in a thin Marangoni boundary layer near a free, nondeformable boundary with given uneven temperature distribution along this boundary was researched in this paper. It was shown that depending on the temperature gradient's direction along the boundary, there might be a flow either with or without rotation. During the rotation of the liquid, a countercurrent zone appears near the free surface. It was shown that in both cases, with higher nanoparticle concentrations, the heat flux on the free surface decreased monotonically on the order of several tens of percent, depending on the concentration and composition of the nanoparticles. The liquid velocity inside the Marangoni layer decreased with higher nanoparticle concentrations. The rotational effect was weakened with the presence of nanoparticles in the liquid.

Acknowledgment

This work was supported by the RFBR grant No. 12-01-00582-a.

References

- [1] J.C. Maxwell. *A Treatise on Electricity and Magnetism*. Clarendon Press, 2nd ed., 435 p. (1881).
- [2] S.U.S. Choi. Enhancing thermal conductivity of fluids with nanoparticles. *The Proceedings of the 1995 ASME International Mechanical Engineering Congress and Exposition*, San Francisco, USA, ASME, FED 231/MD 66, P. 99–105 (1995).
- [3] V. Bianco, F. Chiacchio, O. Manca, S. Nardini. Numerical investigation of nanofluids forced convection in circular tubes. *Applied Thermal Engineering*, **29** (17–18), P. 3632–3642 (2009).
- [4] S. Kakac, A. Pramuanjaroenkij. Review of convective heat transfer enhancement with nanofluids. *International Journal of Heat and Mass Transfer*, **52**, P. 3187–3196 (2009).
- [5] W. Daungthongsuk, S. Wongwises. A critical review of convective heat transfer of nanofluids. *Renew. Sustain. Energy Rev.*, **11**, P. 797–817 (2007).
- [6] N.M. Arifin, R. Nazar, I. Pop. Marangoni-driven boundary layer flow in nanofluids. *Proceedings of the 2010 international conference on theoretical and applied mechanics, 2010 and 2010 international conference on Fluid mechanics and heat & mass transfer*, P. 32–35 (2010).
- [7] H.C. Brinkman. The viscosity of concentrated suspensions and solutions. *J. Chem. Phys.*, **20**, P. 571–581 (1952).
- [8] K. Khanafer, K. Vafai, M. Lightstone. Buoyancy-driven heat transfer enhancement in a two-dimensional enclosure utilizing nanofluids. *Int. J. Heat Mass Transfer*, **46**, P. 3639–3653 (2003).
- [9] R.K. Shukla, V.K. Dhir. Numerical study of the effective thermal conductivity of nanofluids. *Proceedings of ASME Heat Transfer Conference*, San Francisco, California, July, 17–22, P. 1–9 (2005).
- [10] V.A. Batschev. Asymptotics of unevenly heated free surface of capillary liquid at large Marangoni numbers. *Applied Mathematics and Mechanics*, **53** (3), P. 425–432 (1989).

MODEL OF NON-AXISYMMETRIC FLOW IN NANOTUBE

I. V. Blinova

Saint Petersburg National Research University of Information Technologies, Mechanics
and Optics, 49 Kronverkskiy, Saint Petersburg, 197101, Russia

irin-a@yandex.ru

PACS 62.10.+s

The asymmetric Stokes flow in a circular cylinder due to a rotlet is considered. This is a model for nanotube flow induced by a small rotating particle. The 3D Stokes and continuity equations are reduced to boundary problems for two scalar functions. Analytical solutions in terms of the Fourier transform is obtained.

Keywords: Stokes flow, rotlet.

1. Introduction

The Stokes flow description is a classical problem of fluid mechanics, having a long history. In recent years, it attracted new interest due to appearance of a new field, related with the development of nanotechnology. The flow through nanostructures is known to have many interesting unusual peculiarities [1]. Particularly, one observes a phenomenon analogous to superfluidity [2], dependence of the viscosity on the nanotube diameter [3] and other effects. The theory of nanoflow is not well-developed. There are only a few works suggesting theoretical explanation of these phenomena (see, e.g., [4], [5], [6]). It has been shown that hydrodynamic equations should be modified for nanoflows [7], but the Stokes approximation is appropriate due to the smallness of the Reynolds number [8].

In the present paper, we use the Stokes model for nanotube flow. Namely, we study the creeping flow inside the nanotube induced by a rotlet. From a physical point of view, a molecule rotating due to external magnetic field in the nanotube can play the role of the rotlet. A rotlet is the point source of vorticity, i.e. it is the solution of the Stokes equation with point singularity (see, e.g., [9], [10]). Correct mathematical description of such type of singular solutions was given in the framework of the theory of self-adjoint extensions of symmetric operators [11], [12], [13]. The advantage of the approach is that it allows one to obtain analytical solutions in many interesting cases. In the present paper we consider asymmetric Stokes flow in a cylinder caused by a rotlet having the axis orthogonal to the cylinder axis. Earlier the asymmetric Stokes flow was describe only for the domain between two parallel planes [14].

2. Problem formulation

Consider a cylinder of radius R_0 having OZ as the axis. We deal with the Stokes flow inside the cylinder caused by a rotlet at the origin having OX as the axis. Let \mathbf{v} be the flow velocity, p be the pressure. Then the Stokes and continuity equations takes place:

$$\Delta \mathbf{v} = \nabla p, \quad \nabla \cdot \mathbf{v} = 0. \quad (1)$$

We assume that the flow is induced by a rotlet, hence, we seek the solution in the form:

$$\mathbf{v} = \mathbf{v}_0 + \mathbf{v}_1, \quad v_0 = \frac{\mathbf{i} \times \mathbf{r}}{|\mathbf{r}|},$$

\mathbf{r} is radius-vector of a point, \mathbf{i} is the unit vector, parallel to the OX axis.

We will use the cylindrical coordinates (ρ, φ, z) . There is an interesting technique suggested in [15] which allows one to reduce the system (1) of the Stokes and continuity equation to two equations for two scalar functions ψ, χ . Namely, the solution of (1) can be represented in the form:

$$\begin{aligned} \mathbf{v} &= \text{rot}(\text{rot}(\frac{\psi}{\rho} \mathbf{k} \cos \varphi) + \frac{\chi}{\rho} \mathbf{k} \sin \varphi), \\ p &= \frac{1}{\rho} \frac{\partial}{\partial z} (L_{-1} \psi) \cos \varphi, \end{aligned}$$

where ψ, χ are scalar functions of two variables (ρ, z) satisfying the equations:

$$\begin{aligned} L_{-1}^2 \psi &= 0, \quad L_{-1} \chi = 0, \\ L_{-1} &= \frac{\partial^2}{\partial z^2} + \frac{\partial^2}{\partial \rho^2} - \frac{1}{\rho} \frac{\partial}{\partial \rho}. \end{aligned}$$

The velocity components is related with these functions by the following manner:

$$v_z = -\frac{\partial}{\partial \rho} \left(\frac{1}{\rho} \frac{\partial \psi}{\partial \rho} \right) \cos \varphi, \tag{2}$$

$$v_\rho = \left(\frac{\partial}{\partial \rho} \left(\frac{1}{\rho} \frac{\partial \psi}{\partial z} \right) + \frac{\chi}{\rho^2} \right) \cos \varphi, \tag{3}$$

$$v_\varphi = -\left(\frac{1}{\rho^2} \frac{\partial \psi}{\partial z} + \frac{\partial}{\partial \rho} \left(\frac{\chi}{\rho} \right) \right) \sin \varphi. \tag{4}$$

The no-slip boundary condition (zero velocity at the boundary) is as follows:

$$\begin{aligned} \left. \left(\frac{\partial}{\partial \rho} \left(\frac{1}{\rho} \frac{\partial \psi}{\partial \rho} \right) \right) \right|_{\rho=R_0} &= 0, \\ \left. \left(\frac{\partial}{\partial \rho} \left(\rho \frac{\partial}{\partial \rho} \left(\frac{1}{\rho} \frac{\partial \psi}{\partial z} \right) \right) - \frac{1}{\rho^2} \frac{\partial \psi}{\partial z} \right) \right|_{\rho=R_0} &= 0, \\ \left. \left(\frac{\partial}{\partial \rho} \left(\rho \frac{\partial}{\partial \rho} \left(\frac{\chi}{\rho} \right) \right) - \frac{\chi}{\rho^2} \right) \right|_{\rho=R_0} &= 0. \end{aligned}$$

Moreover, $\mathbf{v} \rightarrow 0$ if $z \rightarrow \infty$.

3. Problem solution

Note that the functions ψ, χ corresponding to the rotlet in free space are as follows

$$\psi_0 = -\sqrt{z^2 + \rho^2}, \quad \chi_0 = -\frac{z}{\sqrt{z^2 + \rho^2}}.$$

We seek the solution in the form $\psi = \psi_0 + \psi_1, \chi = \chi_0 + \chi_1$. At first, let us consider the problem for χ_1 :

$$\frac{\partial^2 \chi_1}{\partial z^2} + \frac{\partial^2 \chi_1}{\partial \rho^2} - \frac{1}{\rho} \frac{\partial \chi_1}{\partial \rho} = 0,$$

$$\left(\frac{\partial}{\partial \rho}(\rho \frac{\partial}{\partial \rho}(\frac{\chi_1}{\rho})) - \frac{\chi_1}{\rho^2}\right)\Big|_{\rho=R_0} = - \left(\frac{\partial}{\partial \rho}(\rho \frac{\partial}{\partial \rho}(\frac{\chi_0}{\rho})) - \frac{\chi_0}{\rho^2}\right)\Big|_{\rho=R_0} .$$

Making the Fourier transform F in respect to z , one gets

$$-k^2 X + X''_{\rho\rho} - \frac{1}{\rho} X'_\rho = 0,$$

$$\left(\frac{\partial}{\partial \rho}(\rho \frac{\partial}{\partial \rho}(\frac{X}{\rho})) - \frac{X}{\rho^2}\right)\Big|_{\rho=R_0} = - \left(\frac{\partial}{\partial \rho}(\rho \frac{\partial}{\partial \rho}(\frac{X_0}{\rho})) - \frac{X_0}{\rho^2}\right)\Big|_{\rho=R_0} .$$

Here $X(k, \rho) = F(\chi_1(z, \rho))$, $X_0(k, \rho) = F(\chi_0(z, \rho))$. Note that X, X_0 should be considered as distributions. One can solve the problem and find X and, correspondingly, χ :

$$\chi = \chi_0 + \chi_1, \tag{5}$$

$$\chi_1 = F^{-1}(X) = \frac{1}{\sqrt{2\pi}} \int_{-\infty}^{\infty} A J_1(ik\rho) e^{ikz} dk,$$

$$A = - \frac{\left(\frac{\partial}{\partial \rho}(\rho \frac{\partial}{\partial \rho}(\frac{X_0}{\rho})) - \frac{X_0}{\rho^2}\right)\Big|_{\rho=R_0}}{\left(\frac{\partial}{\partial \rho}(\rho \frac{\partial}{\partial \rho}(\frac{J_1(ik\rho)}{\rho})) - \frac{J_1(ik\rho)}{\rho^2}\right)\Big|_{\rho=R_0}},$$

where J_1 is the Bessel function.

Consider the problem for ψ . Making the Fourier transform in respect to z , one obtains the equation

$$\left(-k^2 + \frac{\partial^2}{\partial \rho^2} - \frac{1}{\rho}\right)^2 \Psi = 0,$$

where $\Psi(k, \rho) = F(\psi(z, \rho))$. To construct the solution to the boundary problem, we need two linearly independent solutions having no singularity at zero. One of them is, evidently, $J_1(ik\rho)$. The second solution is sought in the form $f(\rho)J_1(ik\rho)$. Routine procedure gives us the expression for $f(\rho)$:

$$f(\rho) = \int_0^\rho \frac{\rho_1 d\rho_1}{J_1(ik\rho_1)} \left(\int_0^{\rho_1} \frac{J_1^2(ik\rho_2)}{\rho_2} d\rho_2 \right).$$

The solution is linear combination of these two functions with coefficients determined by the boundary conditions. As a result, one has:

$$\psi = \psi_0 + \psi_1, \tag{6}$$

$$\psi_1 = F^{-1}(\Psi_1) = \frac{1}{\sqrt{2\pi}} \int_{-\infty}^{\infty} \Psi_1(k, \rho) e^{ikz} dk,$$

$$\Psi_1(k, \rho) = \frac{b_1 a_{22} - b_2 a_{12}}{a_{11} a_{22} - a_{21} a_{12}} J_1(ik\rho) + \frac{b_2 a_{11} - b_1 a_{21}}{a_{11} a_{22} - a_{21} a_{12}} f(\rho) J_1(ik\rho),$$

$$a_{11} = \left(\frac{\partial}{\partial \rho}(\frac{1}{\rho} \frac{\partial J_1(ik\rho)}{\partial \rho})\right)\Big|_{\rho=R_0}, \quad a_{12} = \left(\frac{\partial}{\partial \rho}(\frac{1}{\rho} \frac{\partial (f(\rho) J_1(ik\rho))}{\partial \rho})\right)\Big|_{\rho=R_0},$$

$$a_{21} = \left(\frac{\partial}{\partial \rho}(\rho \frac{\partial}{\partial \rho}(\frac{J_1(ik\rho)}{\rho})) - \frac{J_1(ik\rho)}{\rho^2}\right)\Big|_{\rho=R_0},$$

$$a_{22} = \left(\frac{\partial}{\partial \rho}(\rho \frac{\partial}{\partial \rho}(\frac{f(\rho) J_1(ik\rho)}{\rho})) - \frac{f(\rho) J_1(ik\rho)}{\rho^2}\right)\Big|_{\rho=R_0},$$

$$b_1 = - \left(\frac{\partial}{\partial \rho} \left(\frac{1}{\rho} \frac{\partial \Psi_0(\rho)}{\partial \rho} \right) \right) \Big|_{\rho=R_0},$$

$$b_2 = - \left(\frac{\partial}{\partial \rho} \left(\rho \frac{\partial}{\partial \rho} \left(\frac{\Psi_0(\rho)}{\rho} \right) \right) + \frac{\Psi_0(\rho)}{\rho^2} \right) \Big|_{\rho=R_0}.$$

Inserting of expressions (5), (6) for χ and ψ into (2), allows one to obtain the velocity and the pressure fields.

Acknowledgements

The work was supported by FTP "Scientific and Educational Human Resources for Innovation-Driven Russia" (contract 16.740.11.0030), grant 11-08-00267 of RFBR, FTP "Researches and Development in the Priority Directions Developments of a Scientific and Technological Complex of Russia 2007-2013" (state contract 07.514.11.4146) and grants of the President of Russia (state contract 14.124.13.2045-MK and grant MK-1493.2013.1).

References

- [1] Li D. Encyclopedia of Microfluidics and Nanofluidics. Springer, New York (2008).
- [2] Rivera J. L., Starr F. W. Rapid transport of water via carbon nanotube. *J. Phys. Chem. C*, **114**, P. 3737–3742 (2010).
- [3] Kang W., Landman U. Universality crossover of the pinch-off shape profiles of collapsing liquid nanobridges. *Phys. Rev. Lett.*, **98**, P. 064504/1-4 (2007).
- [4] Chivilikhin S. A., Popov I. Yu., Gusarov V. V., Svitnikov A. I. Model of fluid flow in a nano-channel. *Russian J. Math. Phys.*, **15**, P. 410–412 (2007).
- [5] Maslov V. P. Superfluidity of classical liquid in a nanotube for even and odd numbers of neutrons in a molecule. *Theor. Math. Phys.*, **153**, P. 1677–1696 (2007).
- [6] Belonenko M. B., Chivilikhin S. A., Gusarov V. V., Popov I. Yu., Rodygina O. A. Soliton-induced flow in carbon nanotube. *Europhys. Lett.* **101**, P. 66001/1-3 (2013).
- [7] Popov I. Yu. Statistical derivation of modified hydrodynamic equations for nanotube flows. *Physica Scripta*, **83**, P. 045601/1-3 (2011).
- [8] Chivilikhin S. A., Gusarov V. V., Popov I. Yu. Flows in nanostructures: hybrid classical-quantum models. *Nanosystems: Phys. Chem. Math.*, **3**(1), P. 7–26 (2012).
- [9] Pozrikidis C. Computation of periodic Green's functions of Stokes flow. *J. Eng. Math.* **38**, P. 79–96 (1996).
- [10] Blake J. R., Chwang A. T. Fundamental singularities of viscous flow. Part I: The image systems in the vicinity of a stationary no-slip boundary. *J. Eng. Math.* **8**(1), P. 23–29 (1974).
- [11] Popov I. Yu. Operator extension theory and eddies in creeping flow. *Phys. Scripta*. **47**, P. 682–686 (1993).
- [12] Popov I. Yu. Stokeslet and the operator extension theory. *Rev. Matem. Univ. Compl. Madrid*. **9**, P. 235–258 (1996).
- [13] Gugel Yu. V., Popov I. Yu., Popova S. L. Hydrotron: creep and slip. *Fluid Dyn. Res.* **18**, P. 199–210 (1996).
- [14] Hackborn W. W. Asymmetric Stokes flow between parallel planes due to a rotlat. *J. Fluid Mech.* **218**, P. 531–546 (1990).
- [15] Ranger K. B. *Intl. J. Multiphase Flow.*, **4**, P. 263 (1978).

ABSORPTION OF ELECTROMAGNETIC RADIATION IN THE QUANTUM WELL PLACED IN A MAGNETIC FIELD

V. V. Karpunin^{1,2}, V. A. Margulis²

¹ Mordovian State Pedagogical Institute, Saransk, Russia

² Mordovian State University, Saransk, Russia

karpuninvv@mail.ru, theorphysics@mrsu.ru

PACS 71.70.Ej,73.21.Fg,78.67.De,85.75.-d

The absorption of electromagnetic radiation by electrons of the quantum well is investigated. These calculations take into account the spin-orbit interaction (SOI) in the Rashba model. Analytical expression of the absorption coefficient is obtained. Resonant frequencies and positions of the resonance peaks were found.

Keywords: quantum well, spin-orbit interaction, the absorption coefficient.

1. Introduction

Optical properties of low-dimensional systems is a major branch of nanostructure-based physics. The interest in the study of the absorption coefficient of electromagnetic radiation in nanostructures has increased greatly in recent years. The emerging field of spintronics has generated interest in the effects of the spin-orbit interaction (SOI) in low-dimensional semiconductor heterostructures.

The absorption of electromagnetic radiation in semiconductors while taking into account the SOI have been investigated previously [1]. The spin-orbit interaction of 2D electrons were investigated previously [2,3], where the value of the coupling constant α , and the expression for the magnetic susceptibility were found.

Splitting of the cyclotron resonance for two-dimensional electrons in InAs quantum wells was observed [4]. This effect can be explained by the use of the SOI in the Rashba model.

The electron transport and the cyclotron resonance in a one-sided, selectively doped HgTe/CdHgTe (013) heterostructure with a 15-nm quantum well with an inverted band structure have been investigated [5]. Modulation of the Shubnikov-de Haas oscillations was observed, and the spin splitting in a zero magnetic field was found to be about 30 meV. A large $\Delta m_c/m_c \simeq 0.12$ splitting of the cyclotron resonance line was discovered and shown to be due to both the spin splitting and the strong nonparabolicity of the dispersion relation in the conduction band.

The Rashba effect in the ring was previously considered [6]. The behavior of the energy spectrum was analyzed in detail. The energy spectrum depended on the width of the ring and the Rashba parameter of the spin-orbit interaction.

Inelastic light scattering by a two-dimensional system of electrons in a conduction band with Rashba spin-orbit coupling was studied theoretically for the resonance case where the frequencies of the incident and scattered light were close to the effective distance between the conduction band and spin-split band in a III-V semiconductor [7].

2. Absorption coefficient

In this paper we studied the absorption coefficient of electromagnetic radiation in the quantum well with (SOI). The Hamiltonian has the form [3]

$$H = \frac{1}{2m^*}(p_x + \frac{e}{c}By)^2 + \frac{p_y^2}{2m^*} + \frac{p_z^2}{2m^*} + \alpha \mathbf{v} \left[\boldsymbol{\sigma} \times \frac{\mathbf{p} - \frac{e}{c}\mathbf{A}}{\hbar} \right],$$

the vector potential of magnetic field \mathbf{A} is $\mathbf{A} = (-By, 0, 0)$.

The electron energy spectrum of the problem has the form [3]

$$E_s^\pm = \hbar\omega_c[s \pm \sqrt{(1/2 - g\beta/2)^2 + \gamma^2 s}] + \varepsilon_0, s \geq 1$$

$$E_0 = \hbar\omega_c(1/2 - g\beta/2) + \varepsilon_0, s = 0,$$

where $\beta = m^*/2m_0, \gamma^2 = \alpha^2/A\hbar\omega_c, A = \hbar^2/2m^*, \varepsilon_0$ — is the lower level of the electron energy in the well, α — coupling constant, m^* — effective electron mass, m_0 — free electron mass, $\omega_c = eB/m^*c$ — cyclotron frequency, g — g factor of electrons.

The electronic transitions with the change s , but without changing the sign (plus-plus, or minus-minus transitions) correspond to the cyclotron resonance [3]. Also introduced was the concept of the combined resonance responsible for transitions with a change of sign and the change s [3].

The wave functions has the form: [1]

$$\begin{pmatrix} f_1 \\ f_2 \end{pmatrix} = \begin{pmatrix} \sum_{s=0}^{\infty} a_s \psi_s \\ \sum_{s=0}^{\infty} b_s \psi_s \end{pmatrix},$$

where ψ_s — oscillator functions, a_s, b_s — coefficient of expansion f_1 and f_2 respectively.

$$a_{s-1}^{(s)} = \pm i \sqrt{\frac{\sqrt{(\frac{1}{2} - \beta)^2 + \gamma^2 s} \mp (\frac{1}{2} - \beta)}{2\sqrt{(\frac{1}{2} - \beta)^2 + \gamma^2 s}}},$$

$$b_s^{(s)} = \sqrt{\frac{\sqrt{(\frac{1}{2} - \beta)^2 + \gamma^2 s} \pm (\frac{1}{2} - \beta)}{2\sqrt{(\frac{1}{2} - \beta)^2 + \gamma^2 s}}}.$$

The remaining coefficients $a_t^{(s)}$ and $b_t^{(s)}$ equal to zero [1].

Then the transition matrix elements due to electromagnetic radiation has the form

$$\begin{aligned} \langle (f_1 f_2) | H_R | \begin{pmatrix} f_1 \\ f_2 \end{pmatrix} \rangle &= \langle (f_1 f_2) \left(\begin{array}{c} \sum_{s'=1}^{\infty} a_{s'} H_R \psi_{s'} \\ \sum_{s'=1}^{\infty} b_{s'} H_R \psi_{s'} \end{array} \right) \rangle = \frac{ie\hbar}{m^* l_0} \sqrt{\frac{2\pi\hbar N_f}{\epsilon\omega}} \\ &\times \left(\sum_{s=0}^{\infty} \sum_{s'=1}^{\infty} a_s^* a_{s'} \left(\sqrt{\frac{s+1}{2}} \delta_{s,s'-1} - \sqrt{\frac{s}{2}} \delta_{s,s'+1} \right) + b_s^* b_{s'} \left(\sqrt{\frac{s+1}{2}} \delta_{s,s'-1} - \sqrt{\frac{s}{2}} \delta_{s,s'+1} \right) \right), \end{aligned} \quad (1)$$

l_0 — is a magnetic length, $\delta_{s,s'}$ — Kronecker delta symbol, N_f — number of photons, H_R — operator of the electron-photon interaction.

We consider the case of a non-degenerate electron gas. Expression for the absorption due to these transitions are given by

$$\Gamma(\omega) = \frac{2\pi\sqrt{\epsilon(\omega)}n}{c\hbar N_f} \left[1 - \exp\left(-\frac{\hbar\omega}{T}\right) \right] \times \sum_{\alpha} \sum_{\beta} f_0(E_{\alpha}) |\langle (f_1 f_2) | H_R | \begin{pmatrix} f_1 \\ f_2 \end{pmatrix} \rangle|^2 \delta(E_{\alpha} - E_{\beta} + \hbar\omega), \quad (2)$$

where α, β — quantum numbers of the electron to initial and final states, f_0 — is the electronic-Boltzmann distribution function, $\epsilon(\omega)$ — real part of the dielectric constant, ω — frequency of the photon, $(1 - \exp(-\hbar\omega/T))$ — takes into account the stimulated emission of photons, $\delta(x)$ — Dirac delta function, n — the concentration of electrons. Under the condition $\hbar\omega \gg T$ this term will be neglected. This expression (2) is similar to that used in [8].

We obtain the following expression for the absorption coefficient using (1) and (2):

$$\Gamma(\omega) = \frac{2\pi\sqrt{\epsilon}n}{c\hbar N_f} \frac{e^2\hbar^2}{m^{*2}l_0^2} \frac{2\pi\hbar N_f}{\epsilon\omega} \sum_{s=0}^{\infty} \sum_{s'=1}^{\infty} \left(\frac{s+1}{2} \delta_{s,s'-1} - \frac{s}{2} \delta_{s,s'+1} \right) \times (a_s a_{s'} a_s^* a_{s'}^* + b_s a_{s'} a_s^* b_{s'}^* + a_s b_s^* a_{s'}^* b_{s'} + b_s b_s^* b_{s'}^* b_{s'}^*) f_0(E_s^{\pm}) \delta(E_s^{\pm} - E_{s'}^{\pm} + \hbar\omega). \quad (3)$$

It is clear that the least s' is equal to one. It is the lowest level on which an electron can be found after the absorption of a photon.

After calculating the sum from s we obtain:

$$\Gamma(\omega) = \frac{2\pi\sqrt{\epsilon}n}{c\hbar N_f} \frac{e^2\hbar^2}{m^{*2}l_0^2} \frac{2\pi\hbar N_f}{\epsilon\omega} \sum_{s'=1}^{\infty} \frac{s'}{2} (a_{s'-1} a_{s'} a_{s'-1}^* a_{s'}^* + b_{s'-1} a_{s'} a_{s'-1}^* b_{s'}^* + a_{s'-1} b_{s'-1}^* a_{s'}^* b_{s'} + b_{s'-1} b_{s'}^* b_{s'-1}^* b_{s'}^*) f_0(E_{s'-1}^{\pm}) \delta(E_{s'-1}^{\pm} - E_{s'}^{\pm} + \hbar\omega) - \frac{2\pi\sqrt{\epsilon}n}{c\hbar N_f} \frac{e^2\hbar^2}{m^{*2}l_0^2} \frac{2\pi\hbar N_f}{\epsilon\omega} \sum_{s'=1}^{\infty} \frac{s'+1}{2} (a_{s'+1} a_{s'} a_{s'+1}^* a_{s'}^* + b_{s'+1} a_{s'} a_{s'+1}^* b_{s'}^* + a_{s'+1} b_{s'+1}^* a_{s'}^* b_{s'} + b_{s'+1} b_{s'}^* b_{s'+1}^* b_{s'}^*) f_0(E_{s'+1}^{\pm}) \delta(E_{s'+1}^{\pm} - E_{s'}^{\pm} + \hbar\omega). \quad (4)$$

We take into account the broadening of delta peaks using the Lorentz formula [8]. The following expression of the absorption coefficient is given by:

$$\frac{\Gamma(\omega)}{\Gamma_0} = \sum_{s'=1}^{\infty} \frac{\omega_c}{\omega} \frac{s'}{2} (a_{s'-1} a_{s'} a_{s'-1}^* a_{s'}^* + b_{s'-1} a_{s'} a_{s'-1}^* b_{s'}^* + a_{s'-1} b_{s'-1}^* a_{s'}^* b_{s'} + b_{s'-1} b_{s'}^* b_{s'-1}^* b_{s'}^*) \times f_0(E_{s'-1}^{\pm}) \frac{1}{1 + \tau^2((E_{s'-1}^{\pm} - E_{s'}^{\pm})\hbar^{-1} + \omega)^2} - \sum_{s'=1}^{\infty} \frac{\omega_c}{\omega} \frac{s'+1}{2} (a_{s'+1} a_{s'} a_{s'+1}^* a_{s'}^* + b_{s'+1} a_{s'} a_{s'+1}^* b_{s'}^* + a_{s'+1} b_{s'+1}^* a_{s'}^* b_{s'} + b_{s'+1} b_{s'}^* b_{s'+1}^* b_{s'}^*) \times f_0(E_{s'+1}^{\pm}) \frac{1}{1 + \tau^2((E_{s'+1}^{\pm} - E_{s'}^{\pm})\hbar^{-1} + \omega)^2}, \quad (5)$$

where we introduced

$$\Gamma_0 = \frac{4\pi}{c\sqrt{\epsilon}} \frac{e^2\tau}{m^*} n,$$

τ — phenomenological relaxation time.

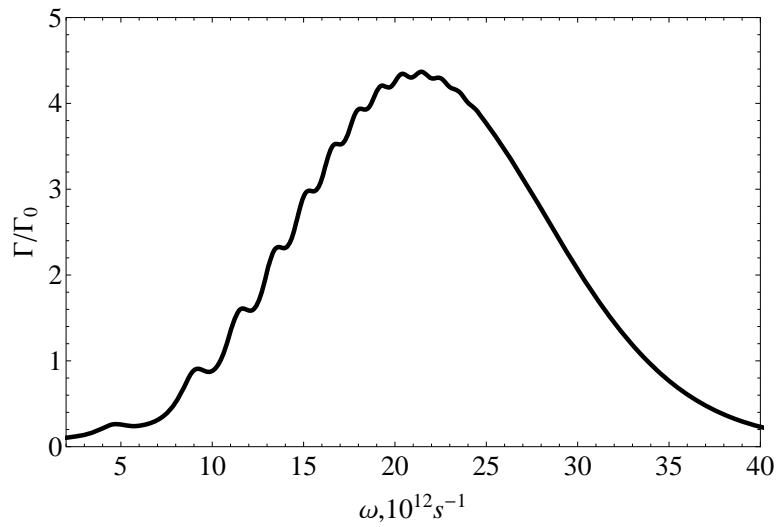


FIG. 1. The dependence of the absorption of electromagnetic radiation on the radiation frequency. $\gamma^2 = 11$, $\beta = 0.25$, $T = 100\text{K}$

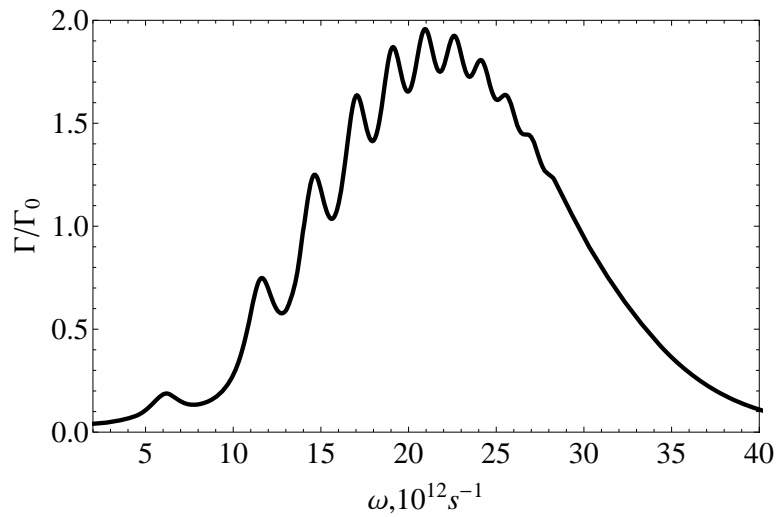


FIG. 2. The dependence of the absorption of electromagnetic radiation on the radiation frequency. $\gamma^2 = 7$, $\beta = 0.25$, $T = 100\text{K}$

The graph of the absorption coefficient as a function of electromagnetic radiation frequency is presented in fig. 1,2. The right wing of graph is almost smooth, however, the left wing contains a series of peaks due to the electronic transitions between discrete levels. The smooth form of the right wing at high-frequencies is stipulated by the distribution function $f_0(E_{s'+1}^\pm)$.

The resonance curve in the absence of the SOI is shown in fig. 3.

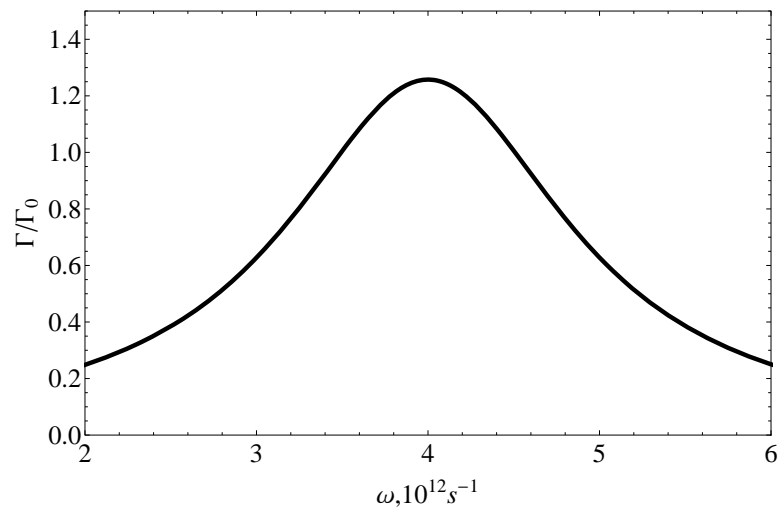


FIG. 3. The dependence of the absorption of electromagnetic radiation on the radiation frequency. $\gamma^2 = 0$, $\beta = 0.25$, $T = 100\text{K}$

Acknowledgements

This work was supported by Russian Ministry of Education and Science within task “Optical and transport properties of semiconductor nanostructures and superlattices” (project No 2.2676.2011) and by Russian Foundation for Basic Research (grant No 11-02-00699).

The work was financially supported by Russian Ministry of Education and Science by the project 2.2.1.2. Research and development of educational laboratory “Basics of nanotechnology, and scanning probe microscopy”.

References

- [1] Rashba E. I. Properties of semiconductors with a loop of extrema. *Physics of the Solid State*, **2**, P. 1224–1238 (1960).
- [2] Bychkov Yu. A., Rashba E. I. Oscillatory effects and the magnetic susceptibility of carriers in inversion layers. *J. Phys. C: Solid State Phys.*, **17**, P. 6039–6045 (1984).
- [3] Bychkov Yu. A., Rashba E. I. Properties of a two-dimensional electron gas with lifted spectral degeneracy. *JETP Letters*, **39**, P. 78–81 (1984).
- [4] Vasilyev Yu. B., Suchalkin S. D., Ivanov S. V., Meltzer B. J., Kop'ev P. S. Effect of the spin-orbit interaction on the cyclotron resonance of two-dimensional electrons. *JETP Letters*, **79**, P. 545–549 (2004).
- [5] Spirin K. E., Ikonnikov A. V., Lastovkin A. A., Gavrilenko V. I., Dvoretzki S. A., Mikhailov N. N. Spin splitting in HgTe/CdHgTe (013) quantum well heterostructures. *JETP Letters*, **92**, P. 63–66 (2010).
- [6] Tsurikov D. E., Zubkov A. V., Yafyasov A. M. Rashba effect in the ring: the structure of the energy spectrum. *Bulletin of the University of St. Petersburg*, ser. 4, P. 51–55 (2010).
- [7] Vitlina R. Z., Magarill L. I., Chaplik A. V. Inelastic light scattering by a two-dimensional electron system with Rashba spin-orbit coupling. *JETP Letters*, **95**, P. 253–258 (2012).
- [8] Galkin N. G., Margulis V. A., Shorokhov A. V. Intraband absorption of electromagnetic radiation by quantum nanostructures with parabolic confinement potential. *Physics of the Solid State*, **43**, P. 530–538 (2001).

ULTRASHORT OPTICAL PULSE PROPAGATION IN A DOUBLE LAYER OF GRAPHENE BORON NITRIDE WITH ACCOUNTING THE MATERIAL DISPERSION

A. V. Pak¹, M. B. Belonenko², O. Y. Tuzalina³

¹ Volgograd State University, 400062, Volgograd, Russia

² Laboratory of Nanotechnologies, Volgograd Institute of Business, 400048, Volgograd, Russia

³ Volgograd State Agricultural University, 400002, Volgograd, Russia
pak.anastasia@gmail.com

PACS 78.20.-e, 78.67 Wj

The propagation of ultra-short optical pulses in a thin film created by graphene grown on a boron nitride base will be considered, taking into account the environment's dispersion characteristics, electron conduction in such a system described by the framework of an effective long-wave Hamiltonian for low-temperature media. The electromagnetic field is taken as classical Maxwell's. We reveal the dependence of the electric field on the maximum amplitude of ultra-short optical pulses, as well as on empirical dispersion constants.

Keywords: graphene, propagation of ultra-short optical pulses, boron nitride base.

1. Introduction

Recently, laminated structures based on graphene have attracted the interest of many researchers. Graphene, which grown on the boron nitride base is one of these structures.

Both boron nitride and graphene have hexagonal crystal lattices, that allows the construction of hybrid materials on their basis. This structure is interesting because a boron nitride is an insulator, and graphene is a conductor. It is possible to obtain substances with different band gaps by combining them together in the various ways. Many other authors are interested in both the theoretical and experimental investigations of these structures. [2–11].

The dynamics of ultra-short optical pulses propagating in a double-layer graphene-boron nitride structure were investigated in the hopes that dispersion qualities in non-magnetic environments would be revealed.

2. Principal equations

We considered a graphene layer on a boron nitride base. The Hamiltonian we chose in a long-wave approximation, in basis ϕ_{g1} , ϕ_{g2} , ϕ_{nb1} , ϕ_{nb2} , where the wave functions are conformed to an electron, localized on one graphene sub-lattice, on another graphene sub-lattice, on one boron nitride sub-lattice and on another boron nitride sub-lattice accordingly, depicted in matrix view as:

$$H(k) = \begin{pmatrix} 0 & k^* & 0 & t \\ k & 0 & 0 & 0 \\ 0 & 0 & \Delta & f^* \\ t & 0 & f & -\Delta \end{pmatrix} \quad (1)$$

Here, t — is an electron jumping integral between graphene and boron nitride layers; Δ — is a forbidden zone quantity for boron nitride; $k = v_{fg}(k_x + ik_y)$, \mathbf{v}_{fg} — is the Fermi velocity for graphene; k_x, k_y — are the electron pulse components; $\mathbf{f} = \mathbf{v}_{fng}(\mathbf{k}_x + i\mathbf{k}_y)$; $\mathbf{v}_{fng} - \mathbf{v}_{fg}$ — are the Fermi velocity for the boron nitride.

The Hamiltonian (1) we can rewrite, using a block matrix structure [13]:

$$H(k) = \begin{pmatrix} 0 & k^* & 0 & t \\ k & 0 & 0 & 0 \\ 0 & 0 & \Delta & f^* \\ t & 0 & f & -\Delta \end{pmatrix} \equiv \begin{pmatrix} H_{11} & H_{12} \\ H_{21} & H_{22} \end{pmatrix}.$$

For cases when the forbidden zone quantity in the boron nitride is large as compared to the electron's energy, the long-wave approximation can be considered, allowing one to write the effective Hamiltonian by analogy with bigraphene [13]:

$$H^{eff} \equiv H_{11} - H_{12}H_{22}^{-1}H_{21} = -\frac{1}{t} \begin{pmatrix} \Delta & -\frac{1}{t}f^*k^* \\ -\frac{1}{t}fk & -\frac{1}{t^2}|k|^2\Delta \end{pmatrix}. \quad (2)$$

The operated approximation practically is a supplementary limitation on the ultimate electrons pulse, which we can consider within the bounds of a long-wave approximation and match to originally usable a long-wave approximation for electronic graphene sub-system. The Hamiltonian (2) can be easily diagonalized. It gives us the electron spectrum:

$$\varepsilon(k_x, k_y) = \frac{1}{2} \left(\Delta (1 - v_{fg}^2 (k_x^2 + k_y^2)) + \sqrt{\Delta^2 (1 - v_{fg}^2 (k_x^2 + k_y^2))^2 + \frac{4v_{fg}^2 v_{fng}^2}{t^2} (k_x^2 + k_y^2)^2} \right), \quad (3)$$

where v_{fg}, v_{fng} — are the Fermi velocities of electrons in graphene and boron nitride, respectively.

According to quantum mechanics laws, in the presence of an external electric field \mathbf{E} , which directed along the x axis, the gauge can be chosen for the field in the following form: $\vec{E} = -\partial\vec{A}/c\partial t$, where c is the speed of light in a vacuum, we need to change the momentum to a generalized momentum $p \rightarrow p - eA/c$, where e is the electron charge. In this case, the effective Hamiltonian (2) can be written as follows:

$$H = \sum_{p\sigma} \varepsilon \left(p - \frac{e}{c}A(t) \right) a_{p\sigma}^+ a_{p\sigma},$$

where $a_{p\sigma}^+, a_{p\sigma}$ — are the creation and annihilation operators of the electron with quasimomentum p and spin σ .

We can write the Maxwell equations without accounting for material dispersion as follows [8]:

$$\frac{\partial^2 \mathbf{E}}{\partial x^2} - \frac{1}{c^2} \frac{\partial^2 \mathbf{E}}{\partial t^2} + \frac{4\pi}{c} \frac{\partial \mathbf{j}}{\partial t} = 0. \quad (4)$$

Here, we neglect the laser-beam diffraction in the directions perpendicular to the beam-propagation axes.

Here, \vec{E} is an electric field of the light wave, t is a time, C is the speed of light in a vacuum.

We modified equation (4) to describe pulse propagation with wide spectrum in a linear medium. The linear refraction index dependence for an isotropic environment n on

light frequency ω in the environment's transparency range can be accurately described by the expression [9]

$$n^2(\omega) = N_0^2 + 2cN_0a\omega^2 + 2cN_0a_1\omega^4 + \dots - 2cN_0b\omega^{-2} - 2cN_0b_1\omega^{-4}, \quad (5)$$

where $N_0, a, a_1, \dots, b, b_1, \dots$ — are empirical constants of environment dispersion. The dispersion relation (5) gives birth to the wave equation:

$$\frac{\partial^2 \mathbf{E}}{\partial x^2} - \frac{N_0^2}{c^2} \frac{\partial^2 \mathbf{E}}{\partial t^2} = -\frac{2N_0}{c} a \frac{\partial^4 \mathbf{E}}{\partial t^4} + \frac{2N_0}{c} a_1 \frac{\partial^6 \mathbf{E}}{\partial t^6} - \dots + \frac{2N_0}{c} b \mathbf{E} - \frac{2N_0}{c} b_1 \int_{-\infty}^t dt' \int_{-\infty}^{t'} \mathbf{E} dt'' + \dots \quad (6)$$

Equation (5) describes the pulse propagation along the x axis in a forward and a reverse direction.

When comparing equations (4) and (6), taking into account the gauge described above, and limiting oneself by the fourth derivative, one can say that the equation (6); takes the following form:

$$\frac{\partial^2 A}{\partial x^2} + \frac{2N_0}{c} a \frac{\partial^4 A}{\partial t^4} - \frac{2N_0}{c} b A + \frac{4\pi}{c} j - \frac{N_0^2}{c^2} \frac{\partial^2 A}{\partial t^2} = 0. \quad (7)$$

Vector potential \mathbf{A} has the following form: $\mathbf{A} = (0, 0, A(x, t))$.

Written in the standard expression for the current density:

$$j_0 = e \sum_{ps} v_s \left(p - \frac{e}{c} A(t) \right) \langle a_{ps}^+ a_{ps} \rangle, \quad (8)$$

where $v_s(p) = \frac{\partial \varepsilon_s(p)}{\partial p}$, and the brackets denote averaging with a non-equilibrium density matrix $\rho(t)$: $\langle B \rangle = Sp(B(0)\rho(t))$.

Further, we considered the low-temperature case, where only a small area of the pulse space near the Fermi level gives a nonzero contribution to the sum (or integral) of (8).

According to this, we can rewrite the standard expression for the current density as follows:

$$j = e \int_{-\Delta}^{\Delta} \int_{-\Delta}^{\Delta} dp_x dp_y v_y \left(p - \frac{e}{c} A(x, t) \right). \quad (9)$$

The range of pulses integration in (9) can be defined from a view of the equality for the particle: $\int_{-\Delta}^{\Delta} \int_{-\Delta}^{\Delta} dp_x dp_y = \int_{-\Delta}^{\Delta} \int_{-\Delta}^{\Delta} dp_x dp_y \langle a_{p_x, p_y}^+ a_{p_x, p_y} \rangle$.

3. Numerical simulation results

We solve Eq. (7) numerically using a direct finite-difference cross-like scheme [15]. Stride by time and coordinate are determine by standard conditions of stability, even so, strides of finite-difference scheme are halved serially, until the solution didn't change in 8^{th} sign.

The initial condition is chosen in a view of an ultra-short optical pulse, which was composed of one field oscillation that, accordingly, can be given with using of vector potential \mathbf{A} :

$$A(x, t) = Q \exp(-(x - vt)^2/\gamma) \\ \gamma = (1 - v^2)^{1/2}, \quad (10)$$

where Q — is the amplitude, and v — is the initial ultra-short optical pulse velocity on the sample input.

This initial condition corresponds to the fact, that we deal with the ultra-short optical pulse which is composed of one electric field oscillation.

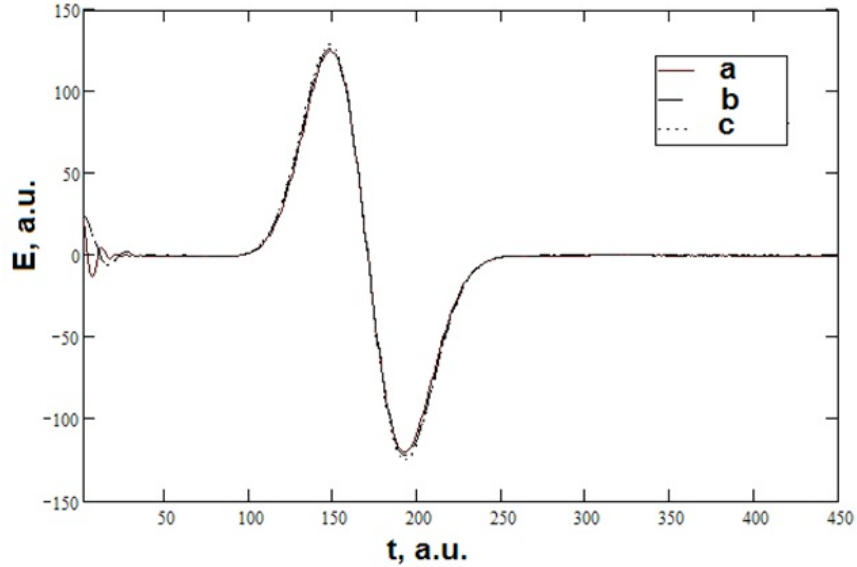


Fig. 1. Dependence of the electric-field on time. On the X-axis is time (unit is $1 \cdot 10^{-16}$ s), on the Y-axis is electric-field (unit is 10^8 V/m). $a=0.01, b=0.01$; $a=0.1, b=0.3$; $a=0.1, b=0.5$

Values of energy characteristics are shown in Δ units. The evolution of the propagating electric field in the sample is presented in Fig. 1.

Such behavior of the optical pulse follows from the dispersion effects, which can be obtained from the linearized equation (7). These effects lead to pulse spreading. It should also be noted that nonlinearity results in pulse shrinking. The impact of these two effects leads to both the origin pulse shape deformation and its propagation in an invariable form.

The most sharply nonlinear influence is tied with the pulse form's dependence on the initial amplitude, that is presented in Fig. 2.

Especially sharp effects are related with the nonlinear influence on the pulse front, leading to pulse widening. This can be explained by the lack of balance between the dispersion and the nonlinearity in our system Fig. 3.

Also notice that the ultra-short optical pulse evolution depend upon, in general, the pulse velocity on the sample input, as shown in Fig. 4.

4. Conclusion

It follows from the obtained results that stable ultra-short optical pulses can undergo propagation in graphene, grown on a hexagonal boron nitride base.

If the initial pulse amplitude increases, then a wave front becomes wider, and also originates a second pulse with smaller intensity. This effect can be useful for the development of hybrid devices based on the light interaction effect with graphene electrons.

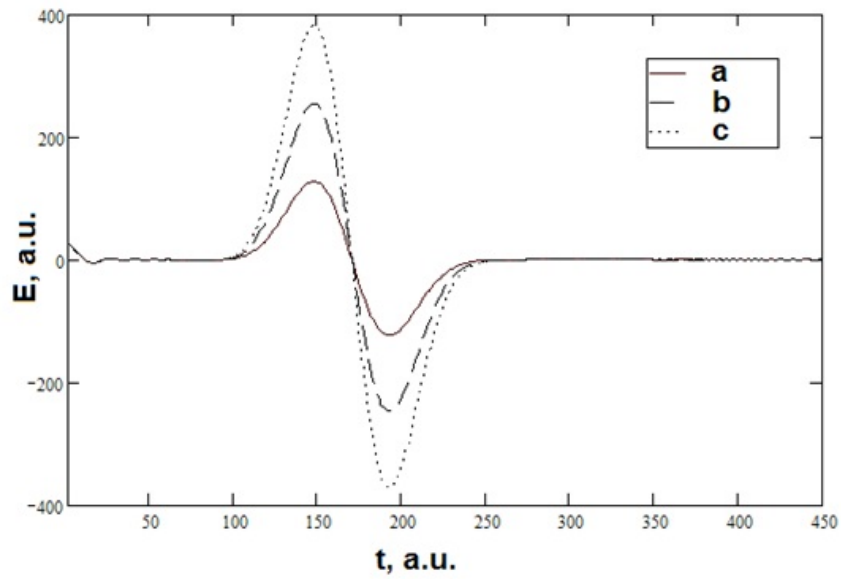


Fig. 2. Dependence of the pulse form on time for different cases of pulse amplitude value: On the X-axis is time (unit is $1 \cdot 10^{-16}$ s). On the Y-axis is electric-field (unit is 10^7 V/m). a) $Q=2$; b) $Q=4$; c) $Q=6$

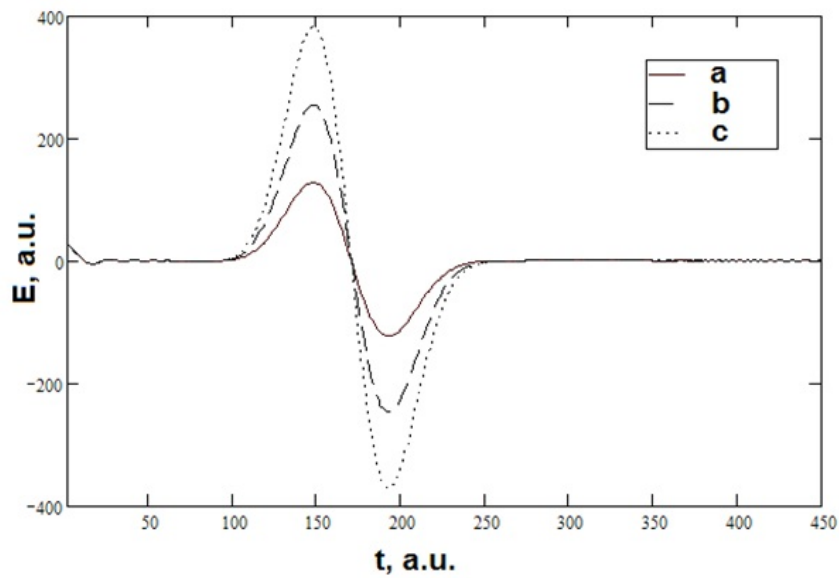


Fig. 3. Dependence of the pulse form on time for different cases of pulse amplitude value: On the X-axis is time (unit is $1 \cdot 10^{-16}$ s) while the Y-axis is electric-field (unit is 10^7 V/m). a) $Q=2$; b) $Q=4$; c) $Q=6$

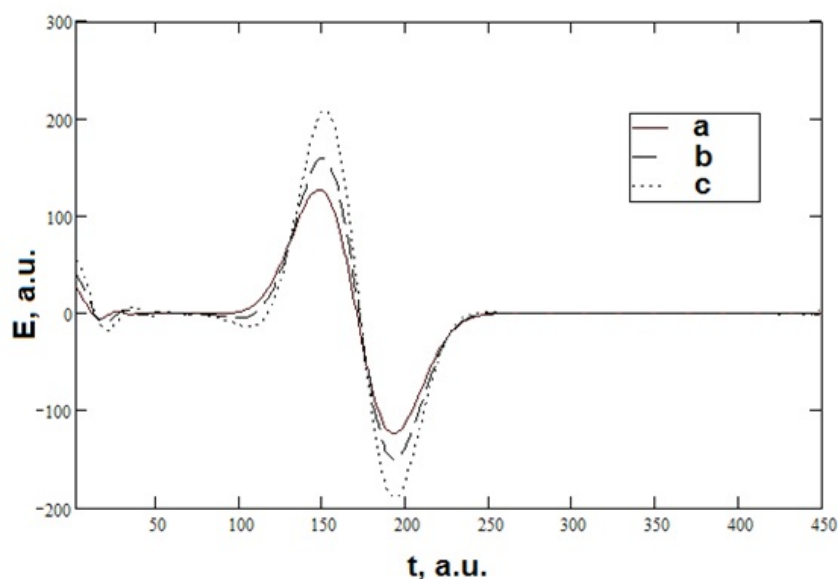


Fig. 4. Dependence of the electric-field on time. On the X-axis is time (unit is $1 \cdot 10^{-16}$ s), on the Y-axis is electric-field (unit is 10^8 V/m). For curve (b) traveled by pulse distance is half as much again as for (a), for curve (c) — twice as much again as for curve (a): $a=0.1$, $b=0.4$

Acknowledgements

This work was supported by the Russian Foundation for Basic Research under Project No. 11-02-97054, 12-02-31654.

References

- [1] Ci L., Song L., Jin C., Jariwala D., Wu D., Li Y.J., Srivastava A., Wang Z.F., Storr K., Balicas L., Liu F., and Ajayan P.M. Atomic layers of hybridized boron nitride and graphene domains. *Nature Materials*, **9**, P. 430–435 (2010). doi:10.1038/nmat2711.
- [2] Giovannetti G., Khomyakov P.A., Brocks G., Kelly P.J., and Van den Brink J., Substrate-induced band gap in graphene on hexagonal boron nitride: *Ab initio* density functional calculations. *Physics Review*, **B 76**, P. 073103 (2007).
- [3] Greber T. *Graphene and boron nitride single layers*. In: Sattler K., editor. The Handbook of Nanophysics. Taylor and Francis Books, Inc, Oxfordshire (2010).
- [4] Partoens B., Peeters F. M. From graphene to graphite: electronic structure around the K point. *Physical Review*, **B 74**, P. 075404-11 (2006).
- [5] Avetisyan A. A., Partoens B., and Peeters F. M. Stacking order dependent electric field tuning of the band gap in graphene multilayers. *Physical Review*, **B 79**, P. 035421 (2009).
- [6] Avetisyan A. A., Partoens B., and Peeters F. M. Electric field control of the band gap and Fermi energy in graphene multilayers by top end back gates. *Phys. Rev.*, **B 80**, P. 195401 (2009).
- [7] Wakabayashi K., Takane Y., Sigrist M. Perfectly conducting channel and universality crossover in disordered graphene nanoribbons. *Physical Review Letters*, **99**, P. 036601 (2007).
- [8] Blase X., Rubio A., Louie S.G., and Cohen M.L. Stability and band-gap constancy of boron-nitride nanotubes. *Europhys Letters*, **28**(6), P. 355–340 (1994).
- [9] Hernández E., Goze C., Bernier P., and Rubio A. Elastic properties of C and $B_xC_yN_z$ composite nanotubes. *Physical Review Letters*, **80**(20), P. 4502–4505 (1998).
- [10] Chen Y., Zou J., Campbell S.J., and Le Caer G. Boron nitride nanotubes: Pronounced resistance to oxidation. *Applied Physics Letters*, **84**, P. 2430–2432 (2004).
- [11] Suryavanshi A. P., Yu M., Wen J., Tang C., and Bando Y. Elastic modulus and resonance behavior of boron nitride nanotubes. *Applied Physics Letters*, **84**, P. 2527–2529 (2004).

- [12] Breshenan M.S., Hollander M.J., Wetherington M. and al. Integration of hexagonal boron nitride with quasi-freestanding epitaxial graphene: toward wafer-scale, high-performance devices. *ACS Nano*, **6**(6), P. 5234-5241 (2012). DOI: 10.1021/nn300996t.
- [13] Xue J., Sanchez-Yamagishi J., Bulmash D., Jacquod Ph., Deshpande A., Watanabe K., Taniguchi T., Jarillo-Herrero P., LeRoy B.J. Scanning tunneling microscopy and spectroscopy of ultra-flat graphene on hexagonal boron nitride. *Nature Materials*, **10**, P. 282–285 (2011).
- [14] Cortijo A., Guinea F., Vozmediano M.A.H., Geometrical and topological aspects of graphene and related materials. arXiv: 1112.2054v1 (2011).
- [15] Landau L. D., Lifshitz E. M. *Theoretical physics*, T. II. Field theory, Science, Moscow, 512 p. (1988).
- [16] Bakhvalov N.S. *Calculus of approximations (analysis, algebra, ordinary differential equations)*. Science, Moscow, 632 p. (1975).

INTERATOMIC INTERACTION IN FCC METALS

V. E. Zalizniak

Siberian Federal University, 79 Svobodny Prospect, Krasnoyarsk 660041, Russia
 vzalizniak@sfu-kras.ru

PACS 34.20.Cf, 61.50.Ah

The parameters of interatomic potential for 10 fcc metals are presented in this paper. The potential is based on the embedded atom method [6]. Parameters are determined empirically by fitting to the equilibrium lattice constant, cohesion energy, vacancy formation energy, bulk modulus and three elastic constants. The proposed potentials are suitable for atomistic computer simulations of practical applications in areas of material science and engineering.

Keywords: interatomic potential, embedded atom method.

Notation

a	– equilibrium lattice constant,
E_c, E_{vf}	– cohesion energy per atom and unrelaxed vacancy formation energy,
B	– bulk modulus,
c_{11}, c_{12}, c_{44}	– crystal elastic constants,
$c_{11}^{(a)}, c_{12}^{(a)}, c_{44}^{(a)}, B^{(a)}$	– calculated values of elastic constants.

1. Introduction

Computer simulations have become an increasingly powerful tool for studying material properties. While first principle quantum methods generally give the most accurate results, they can rarely be applied to complex systems, which require a large number of atoms or longer calculations. However, empirical potentials have proven to be efficient for investigating the structure and properties of materials in many fields, though these results are less accurate than first principle quantum calculations. The embedded-atom method (EAM) is widely used to represent the interaction between metal atoms. A general description of the method was done by Daw and Baskes [1, 2]. In the framework of EAM, the total energy of a system can be written as

$$E_{tot} = \sum_{n=1}^N E_n, \quad E_n = F(\rho_n) + \frac{1}{2} \sum_{\substack{m=1 \\ m \neq n}}^N \varphi(r_{nm}), \quad \rho_n = \sum_{\substack{m=1 \\ m \neq n}}^N \rho(r_{nm}),$$

where E_{tot} – total energy of the system of N atoms, E_n – the internal energy associated with atom n , ρ_n – the electron density at atom n due to all other atoms, $\rho(r_{nm})$ – the contribution to the electron density at atom n due to atom m at the distance r_{nm} from atom n , $F(\rho_n)$ – the embedding energy of the atom into the electron density ρ_n , $\varphi(r_{nm})$ – the two body central potential between atoms n and m separated by r_{nm} . Interpretation and functional form of $\varphi(r)$, $\rho(r)$, and $F(\rho)$ depend on a particular method.

The popularity of the EAM model results from its quantum mechanical justification, as well as its mathematical simplicity, which makes this model conducive to large-scale computer modeling.

In recent years, a number of EAM potential models for fcc metals have been proposed. For example, Sheng *et al.* [3] have developed EAM potentials for fourteen fcc metals. The potentials were developed by fitting the potential-energy surface of each element derived from high-precision first-principles calculations. The three determining functions were expressed with quintic spline functions for each element. Typically, 15 equidistant spline knots were used for both the density and the pair functions, and 6 spline knots were used for the embedding function. This results in a great quantity of fitting parameters. Hijazi and Park [4] have proposed potential for seven fcc metals: Ag, Al, Au, Cu, Ni, Pd and Pt. They have used the following potential functions:

$$\begin{aligned}\rho(r) &= \rho_0 \exp(-\alpha(r - r_e)), \\ \varphi(r) &= -\varphi_0 \left(1 + \gamma \left(\frac{r}{r_e} - 1\right)\right) \exp\left(-\beta \left(\frac{r}{r_e} - 1\right)\right), \\ F(\rho) &= F(\rho_e) \left(1 - a \cdot \ln\left(\frac{\rho}{\rho_e}\right)\right) \left(\frac{\rho}{\rho_e}\right)^a,\end{aligned}$$

where r_e is the equilibrium nearest distance. This potential has six adjustable parameters, α , β , γ , a and ρ_e . Dai *et al.* [5] have proposed an extended Finnis-Sinclair potential for six fcc metals: Ag, Au, Cu, Ni, Pd and Pt. The following potential functions have been employed

$$\begin{aligned}\rho(r) &= \begin{cases} (r - r_1)^2 + a^2 (r - r_1)^4, & r \leq r_1 \\ 0, & r > r_1 \end{cases}, \\ \varphi(r) &= \begin{cases} (r - r_2)^2 (c_0 + c_1 r + c_2 r^2 + c_3 r^3 + c_4 r^4), & r \leq r_2 \\ 0, & r > r_2 \end{cases}, \\ F(\rho) &= F_0 \sqrt{\rho},\end{aligned}$$

where r_1 and r_2 are cut-off parameters assumed to lie between the second and third neighbor atoms. By this means, one needs to fit nine parameters.

The above mentioned potential models do not provide an equally accurate description of basic properties for all fcc metals to which those potentials have been applied to. The purpose of this paper is to present potential parameters for a consistent and practicable EAM model [6], which can be applied to widely used fcc metals.

2. Embedded atom potential

Zalizniak and Zolotov [6] have assumed that the atomic electron density has the following functional form:

$$\rho(r) = \rho_0(1 + \beta r)^2 \exp(-\alpha r), \quad (1)$$

where α and β are parameters of the atomic electron density distribution. Pair potential follows from the electrostatic interaction of two atoms that have positively charged nuclei and the electron densities defined by expression (1). The resulting expression is rather cumbersome and it can be written in a concise form as follows [6]:

$$\varphi(r) = \varepsilon \cdot \exp(-\alpha r) \sum_{n=-1}^6 a_n (\alpha r)^n, \quad (2)$$

where parameters a_n depend on α and β . The embedding function $F(\rho)$ is taken in the polynomial form

$$F(\rho) = \sum_{n=0}^4 c_n \left(\frac{\rho}{\rho_e} - 1 \right)^n, \quad (3)$$

where ρ_e — equilibrium electron density.

3. Results of potential fitting

In order to define the potential of interaction between the same metal atoms one need to fit only two parameters: α and β . The experimental data used in the fitting procedure consist of the equilibrium lattice constant, the cohesive energy, the vacancy formation energy, the bulk modulus and three elastic constants, given in Table 1.

Table 1. Pure metal properties used in fitting

	a , Å	E_c , eV	E_{vf} , eV	B , eV/Å ³	c_{11} , eV/Å ³	c_{12} , eV/Å ³	c_{44} , eV/Å ³
Al	4.05 [7]	3.34 [7]	0.64 [8]	0.474 [12]	0.666 [12]	0.377 [12]	0.177 [12]
Ca	5.58 [7]	1.84 [7]	0.70 [9]	0.133 [13]	0.173 [13]	0.114 [13]	0.102 [13]
Ni	3.52 [7]	4.44 [7]	1.79 [10]	1.161 [12]	1.548 [12]	0.967 [12]	0.775 [12]
Cu	3.61 [7]	3.49 [7]	1.28 [10]	0.863 [14]	1.042 [14]	0.754 [14]	0.466 [14]
Pd	3.89 [7]	3.89 [7]	1.85 [11]	1.205 [12]	1.417 [12]	1.099 [12]	0.447 [12]
Ag	4.09 [7]	2.95 [7]	1.10 [10]	0.632 [12]	0.763 [12]	0.566 [12]	0.283 [12]
Ir	3.84 [7]	6.94 [7]	1.97 [8]	2.216 [15]	3.683 [15]	1.554 [15]	1.635 [15]
Pt	3.92 [7]	5.84 [7]	1.35 [10]	1.765 [12]	2.164 [12]	1.565 [12]	0.478 [12]
Au	4.08 [7]	3.81 [7]	0.90 [10]	1.083 [12]	1.204 [12]	1.022 [12]	0.259 [12]
Pb	4.95 [7]	2.03 [7]	0.58 [10]	0.279 [12]	0.310 [12]	0.264 [12]	0.094 [12]

Table 2. Parameters of the atomic electron density distribution (1)

	α , 1/Å	β , 1/Å	ρ_0 , e/Å ³
Al	1.8008	-2.5380	0.1844
Ca	1.0958	-6.0630	0.0031
Ni	1.5900	14.6900	0.0041
Cu	1.6300	-28.0390	0.0014
Pd	1.5239	-18.3850	0.0039
Ag	1.5568	-5.0950	0.0642
Ir	2.6116	-1.4845	37.2065
Pt	2.2320	-1.7440	9.4854
Au	2.0585	-1.7950	5.6041
Pb	1.2000	-13.2940	0.0040

As the fitting procedure [6] suggests, the equilibrium lattice constant, cohesive energy, vacancy formation energy and bulk modulus are reproduced exactly. The fitting procedure is performed using a cutoff distance of $2a$, so that long-range interactions are included.

The results of fitting for ten fcc metals are presented below. Table 2 lists the parameters of the atomic electron density distribution. Parameters of pair potential are

Table 3. Parameters of pair potential (2)

	Al	Ca	Ni	Cu	Pd
ε , eV	4.4736	4.2963	9.1686	7.2840	10.3465
a_{-1}	1	1	1	1	1
a_0	0.7236	0.6932	0.6747	0.6854	0.6867
a_1	0.8981	0.5757	0.4606	0.5229	0.5331
a_2	5.6170E-02	2.2931E-02	1.0457E-02	1.7243E-02	1.8342E-02
a_3	-1.4951E-02	-1.3498E-02	-1.2742E-02	-1.3173E-02	-1.3238E-02
a_4	-1.9584E-03	-1.6589E-03	-1.5067E-03	-1.5930E-03	-1.6062E-03
a_5	-1.9226E-04	-1.4436E-04	-1.2237E-04	-1.3462E-04	-1.3654E-04
a_6	-1.3088E-05	-7.4251E-06	-5.5519E-06	-6.5523E-06	-6.7185E-06

Table 4. Parameters of pair potential (2)

	Ag	Ir	Pt	Au	Pb
ε , eV	7.2321	28.0893	10.4249	6.4193	2.6628
a_{-1}	1	1	1	1	1
a_0	0.7010	0.6979	0.7351	0.7360	0.6874
a_1	0.6366	2.4252	1.5272	1.3442	0.5361
a_2	2.9404E-02	0.19029	0.1149	9.8534E-02	1.8674E-02
a_3	-1.3835E-02	-1.8071E-02	-1.6559E-02	-1.6179E-02	-1.3258E-02
a_4	-1.7277E-03	-2.4684E-03	-2.2677E-03	-2.2009E-03	-1.6101E-03
a_5	-1.5489E-04	-2.2692E-04	-2.3969E-04	-2.3129E-04	-1.3711E-04
a_6	-8.4546E-06	-4.3189E-05	-2.5063E-05	-2.1497E-05	-6.7690E-06

Table 5. Parameters of embedding function (3)

	Al	Ca	Ni	Cu	Pd
ρ_e , e/A ³	0.6726	0.4105	2.3029	2.2059	2.7952
c_0 , eV	-3.3376	-1.8389	-4.4357	-3.4868	-3.8874
c_1 , eV	-0.5328	-0.6987	-1.7850	-1.2768	-1.7893
c_2 , eV	1.0845	0.0032	0.0098	0.0006	0.8255
c_3 , eV	-0.6668	0.1761	0.5071	0.2571	1.8814
c_4 , eV	1.0536	1.3131	3.1479	2.4665	3.1539

Table 6. Parameters of embedding function (3)

	Ag	Ir	Pt	Au	Pb
ρ_e , e/A ³	2.4369	3.8042	4.0881	3.7648	2.4181
c_0 , eV	-2.9485	-6.9379	-5.8390	-3.8094	-2.029765
c_1 , eV	-1.0896	-1.9624	-0.9382	-0.6167	-0.4593
c_2 , eV	0.1118	0.0404	3.4135	2.4495	1.7075
c_3 , eV	0.4725	-1.8474	-0.0709	0.3350	0.6488
c_4 , eV	2.2196	3.0877	1.4164	1.0778	0.5118

Table 7. Calculated and experimental properties of pure metals, the proposed potential (1)–(3). The first lines present the experimental values of the three elastic constants (they are used in fitting procedure) and the commonly accepted values of vacancy formation energies. The second lines present the values predicted by the potential

	c_{11} , eV/Å ³	c_{12} , eV/Å ³	c_{44} , eV/Å ³	B , eV/Å ³	E_{vf} , eV	d , %
Al	0.666 0.666	0.377 0.377	0.177 0.176	0.474 0.474	0.62-0.66 [8] 0.64	0.14
Ca	0.173 0.177	0.114 0.111	0.102 0.066	0.133 0.133	0.7 [9] 0.70	10
Ni	1.548 1.583	0.967 0.950	0.775 0.586	1.161 1.161	1.6, 1.79 [16, 10] 1.79	7.1
Cu	1.042 1.130	0.754 0.729	0.466 0.422	0.863 0.863	1.28, 1.3 [10, 17] 1.28	5.3
Pd	1.417 1.422	1.099 1.096	0.447 0.478	1.205 1.205	1.7, 1.85 [10, 11] 1.85	1.9
Ag	0.763 0.762	0.566 0.567	0.283 0.281	0.632 0.632	1.1 [10, 17] 1.1	0.25
Ir	3.683 3.823	1.554 1.412	1.635 1.484	2.216 2.216	1.79, 2.27*[10, 18] 1.97	5.5
Pt	2.164 2.165	1.565 1.565	0.478 0.479	1.765 1.765	1.35, 1.5 [10, 17] 1.35	0.05
Au	1.204 1.217	1.022 1.016	0.259 0.257	1.083 1.083	0.89, 0.93 [11, 10] 0.9	0.6
Pb	0.310 0.304	0.264 0.266	0.094 0.060	0.279 0.279	0.58 [10] 0.58	9

* — result of *ab initio* calculations

listed in Tables 3 and 4, while coefficients of the embedding function $F(\rho)$ are given in Tables 5 and 6.

The calculated properties of pure metals from the proposed potential were compared with the experimental values, to which they were fitted in Table 7. The first lines contain the experimental values, while the second lines contain the values predicted by the potential. The last column presents the average discrepancy

$$d = \frac{1}{4} \left(\frac{|c_{11}^{(a)} - c_{11}|}{c_{11}} + \frac{|c_{12}^{(a)} - c_{12}|}{c_{12}} + \frac{|c_{44}^{(a)} - c_{44}|}{c_{44}} + \frac{|B^{(a)} - B|}{B} \right)$$

computed for every metal. For softer materials, such as Ca, Pb and Ni, the average discrepancies between the calculated and experimental results were found to be relatively large, but for other metals, the match between experiment and the proposed EAM model was good.

For comparative purposes, pure metal properties derived for ten fcc metals using the optimized EAM potential [3] and analytic EAM potential [4] are shown in Tables 8 and 9. The equilibrium lattice constant and the cohesive energy were reproduced exactly by all potentials. Generally, the proposed potential and the optimized EAM potential [3]

Table 8. Calculated and experimental properties of pure metals, optimized EAM potential [3]. The first lines present the experimental values of the three elastic constants (they are used in fitting procedure) and the commonly accepted values of vacancy formation energies. The second lines present the values predicted by the potential

	c_{11} , GPa	c_{12} , GPa	c_{44} , GPa	B , GPa	E_{vf} , eV	d , %
Al	114	61.9	31.6	76	0.62-0.66 [8]	1
	113	61.6	32	77	0.67	
Ca	28	18.2	16.3	14.1–19.3	0.7 [9]	7.8
	28	18	17	21	0.95	
Ni	261	151	132	180	1.6, 1.79 [16, 10]	2.5
	263	154	127	186	1.12	
Cu	176	125	82	140	1.28, 1.3 [10, 17]	1.4
	175	124	79	141	0.99	
Pd	234	176	71.2	180	1.7, 1.85 [10, 11]	5.7
	235	180	82	188	1.44	
Ag	132	97	51	100	1.1 [10, 17]	0.7
	131	97	51	98	1.17	
Ir	582	241	262	320	1.79, 2.27*[10, 18]	4.3
	578	241	243	350	1.67	
Pt	347	251	77	228–275	1.35, 1.5 [10, 17]	3
	347	253	78	282	1.50	
Au	193	163	42	180.3	0.89, 0.93 [11, 10]	2.9
	197	165	45	178	0.98	
Pb	49.4	42.1	14.9	46	0.58 [10]	1.5
	50.1	42	15.2	45	0.45	

* — result of *ab initio* calculations

provide similar descriptions of the elastic properties for ten fcc metals (see Tables 7 and 8). The values of vacancy formation energy estimated by the EAM potential [3] were not in satisfactory agreement with the data measured for most metals. Analytic EAM potential [4] provided a better description of elastic properties for Cu and Ni in comparison with the proposed potential, but for the other metals, the proposed potential gave a better fit to the experimental data (see Tables 7 and 9).

4. Conclusion

This paper presents parameters of a new EAM potential model to describe pure fcc metals. The potential model has a simple function form with two adjustable parameters and is easy to use in computer simulations. The potential parameters were determined by fitting the pure metal bulk properties: equilibrium lattice constant, cohesive energy, bulk modulus, three elastic constants and vacancy formation energy. The fitting procedure was applied to ten fcc metals: Al, Ca, Ni, Cu, Pd, Ag, Ir, Pt, Au, and Pb. The equilibrium lattice constant, cohesive energy, bulk modulus and vacancy formation energy were reproduced exactly. The agreement between the calculated elastic constants and the

Table 9. Calculated and experimental properties of pure metals, analytic EAM potential [4]. The first lines present the experimental values of the three elastic constants (they are used in fitting procedure) and the commonly accepted values of vacancy formation energies. The second lines present the values predicted by the potential

	c_{11} , GPa	c_{12} , GPa	c_{44} , GPa	B , GPa	E_{vf} , eV	d , %
Al	114 98	61.9 69.9	31.6 44.7	79 79	0.62-0.66 [8] 0.866	17.1
Ni	246.5 232.4	147.3 154.8	124.7 127.6	180.4 180.2	1.6, 1.79 [16, 10] 1.7	3.3
Cu	170 167	122.5 124.3	75.8 77.3	138 138	1.28, 1.3 [10, 17] 1.3	1.1
Pd	234.1 225.5	176 180	71.2 77.7	195 195	1.7, 1.85 [10, 11] 1.54	3.8
Ag	124 122	93.4 94.2	46.1 47.5	104 103	1.1 [10, 17] 1.1	1.4
Pt	347 324	251 262	76.5 95.4	283 283	1.35, 1.5 [10, 17] 1.6	8.9
Au	186 184	157 157	42 43	167 167	0.89, 0.93 [11, 10] 0.9	0.9

experimental data was good. The proposed EAM potentials are believed to find applications in diverse areas of materials science and engineering.

References

- [1] Daw M.S. and Baskes M.I. Semiempirical, quantum mechanical calculation of hydrogen embrittlement in metals. *Phys. Rev. Letters*, **50**(17), P. 1285–1288 (1983).
- [2] Daw M.S. and Baskes M.I. Embedded-atom method: Derivation and application to impurities, surfaces, and other defects in metals. *Phys. Rev. B*, **29**, P. 6443–6453 (1983).
- [3] Sheng H.W., Kramer M.J., Cadien A., Fujita T., and Chen M.W. Highly optimized embedded-atom-method potentials for fourteen fcc metals. *Phys. Rev. B*, **83**(13), P. 134118(20 p.) (2011).
- [4] Hijazi I.A and Park Y.H. Consistent analytic embedded atom potential for face-centered cubic metals and alloys. *J. Mater. Sci. Technol.*, **25**(6), P. 835–846 (2009).
- [5] Dai X.D., Kong Y., Li L.H. and Lin B.X. Extended Finnis-Sinclair potential for b and f metals and alloys. *J. Phys.: Condensed Matter*, **18**, P. 4527–4542 (2006).
- [6] Zalizniak V.E. and Zolotov O.A. Universal interatomic potential for pure metals. *Nanosystems: Physics, Chemistry, Mathematics*, **3**(1), P. 76–86 (2012).
- [7] Kittel C. *Introduction to solid state physics*. Wiley, New York, 996pp.
- [8] de Boer F.R., Boom R., Mattens W.C.M., Miedema A.R., Niessen A.K. *Cohesion in metals* V.1. North Holland, Amsterdam, (1988).
- [9] Ziesche P., Perdew J.P. and Fiolhais C. Spherical voids in the stabilized jellium model: Rigorous theorems and Padé representation of the void-formation energy. *Phys. Rev. B*, **49**(12), P. 7916–7928 (1994).
- [10] Schultz H. and Ehrhart P., *In Atomic defects in metals*, Landolt-Bornstein New series, Group III Springer-Verlag, Berlin, (1991).
- [11] Schaefer H.E. Investigation of thermal equilibrium vacancies in metals by positron annihilation. *Phys. Status Solidi A*, **102**(1), P. 47–65 (1987).

- [12] Ledbetter H. and Kim S. *Monocrystal elastic constants and derived properties of the cubic and the hexagonal elements*: in Handbook of elastic properties of solids, liquids, and gases, Vol. 2. Academic Press (2001).
- [13] Sisoda P. and Verma M.P. Shear moduli of polycrystalline cubic elements. *J. Phys. Chem. Solids*, **50**, P. 223–224 (1989).
- [14] Ogi H., Ledbetter H., Kim S., and Hirao M. Contactless mode-selective resonance ultrasound spectroscopy: electromagnetic acoustic resonance. *J. Acoust. Soc. Am.*, **106**, P. 660–665 (1999).
- [15] Simmons R.O. and Wang H. *Single Crystal Elastic Constants and Calculated Aggregate Properties: A Handbook*. MIT Press, Cambridge MA (1977).
- [16] Wycisk W. and Feller-Kniepmeier M. Quenching experiments in high purity Ni. *J. Nucl. Mater.*, **69/70**, P. 616–619 (1978).
- [17] Balluffi R. W. Vacancy defect mobilities and binding energies obtained from annealing studies. *J. Nucl. Mater.*, **69/70**, P. 240–263 (1978).
- [18] Korzhavyi P.A., Abrikosov I.A., Johansson B., Ruban A.V. and Skriver H.L.. First-principles calculations of the vacancy formation energy in transition and noble metals. *Phys. Rev. B.*, **59**(18), P. 11693–11703 (1999).

PRE-CHROMATOGRAPHY CRUDE SEPARATION OF LIGHT FULLERENES BY POLY-TERMICAL (RE)CRYSTALLIZATION METHOD

V. A. Keskinov^{3,1}, N. A. Charykov^{1,3}, M. V. Keskinova¹, Yu. V. Murashkin^{3,1},
A. A. Blokhin^{3,1}, K. N. Semenov^{2,1}

ILIP Ltd. (Innovations of Leningrad Universities and Enterprises),
Saint Petersburg, Russia

Saint Petersburg State University, Saint Petersburg, Russia

Saint-Petersburg State Technological Institute (Technological University),
Saint Petersburg, Russia

keskinov@mail.ru

PACS 61.48.+c

The pre-chromatography method of crude separation of light fullerenes (C_{60} and C_{70}) is based on multistage processes of (re)crystallization — the solution of fullerenes solid solutions in liquid solvent (o-xylene) or in liquid o-xylene solutions at high temperature (85 °C) and crystallization of solid solutions from saturated liquid solutions at low temperature (–20 °C). As a result, for example, the initial standard fullerene extract may be efficiently divided into two different solid solutions — the first, considerably enriched in C_{60} fullerene and the second, considerably enriched by the C_{70} fullerene. In this separation process, the concentrate enriched by C_{60} , is also enriched in C_{84} . In that process, 98.6 mass % of C_{60} was contained in the C_{60} -enriched concentrate (from the sum content of C_{60} in the initial extract), simultaneously, 65.9 mass % of C_{70} contained in the C_{70} -enriched concentrate (from the sum content of C_{70} in the initial extract).

Keywords: light fullerenes, heavy fullerenes, o-xylene, separation, solution, (re)crystallization, temperature, counter-current, pre-chromatography, high efficiency.

1. Introduction

The most important current technological process of fullerenes production of consists of 3 consequent stages: synthesis of fullerene soot, extraction of fullerenes from the soot and separation of the extract into individual fullerenes [1–3]. Fullerene soot is usually provided by the sublimation of carbon electrodes in an inert atmosphere. Extraction of fullerenes from this soot usually is accomplished with the use of aromatic solvents. The fullerenes extract, which consists of light fullerenes (C_{60} and C_{70}) and heavy (high) fullerenes (C_{76} , C_{78} and C_{84} etc) may be separated into individual fullerenes with discrete molecular masses by different methods. For separation and production of individual fullerenes, the following methods are used: chromatography [4], crystallization [5], combined method, which can include additional stages, such as thermal vacuum sublimation [6–8]. Only light fullerenes (C_{60} and C_{70}) may be provided using these methods. Heavy fullerenes are distributed in some different products or by-products [6] or stay in activated carbon, used as the absorbent in separation processes for light fullerenes [7, 8].

In this work, we were interested in processes for the (re)crystallization of fullerene extracts with the aim of separating the initial extract into two concentrates (all light and heavy fullerenes in such process will be naturally distributed between these concentrates).

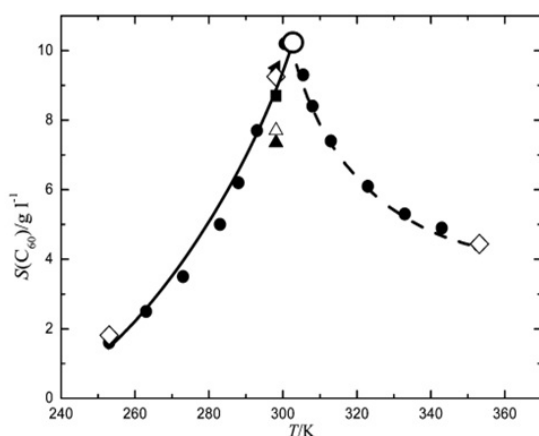


Fig. 1. Solubility of the C₆₀ fullerene in o-xylene (S) against temperature (T)

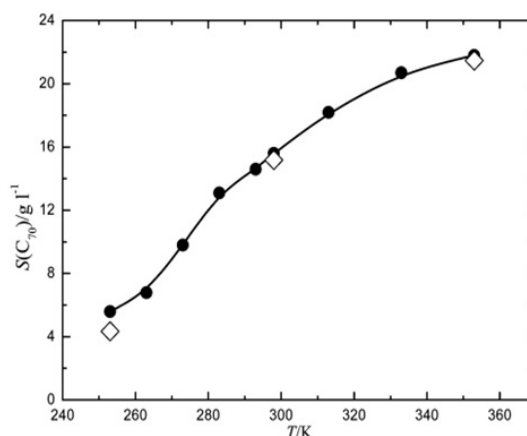


Fig. 2. Solubility of the C₇₀ fullerene in o-xylene (S) against temperature (T)

In the final processes of chromatographic separation and purification of concentrates, the latter may be provided with an efficiency considerably higher than in the initial processes of extract separation and purification [9]. In different patents and papers, the processes which were realized during the interaction of the fullerene extract (or fullerene mixture) with aromatic solvents, for example o-xylene, are named differently and the titles of the stages depend on the conditions and goals of the experiments: crystallization [5], fractional concentrating at 80 to 85 °C [6–8], fractional crystallization at –20 to –24 °C [8], (re)crystallization [10, 11] and polythermal (re)crystallization [11]. Phase processes, realized in such cases are the following:

- solution of fullerene solid solutions in aromatic solvent or unsaturated liquid solutions,
- crystallization fullerenes solid solutions from saturated liquid solutions.

2. Experiment and results discussion

The (re)crystallization processes of fullerene extracts are based on the different solubilities of light fullerenes (C₆₀ and C₇₀) in o-xylene at different temperatures [12–14]. An actual description of the processes for fullerene extract (re)crystallization was the investigation of solubility diagrams in ternary systems of C₆₀–C₇₀ – o-xylene at 80 °C and –20 °C [15]. The dependence of individual fullerenes C₆₀ and C₇₀ solubilities in o-xylene on temperature is represented in Fig. 1 and Fig. 2, correspondingly [13].

The solubility of the individual fullerene C₆₀ in o-xylene at temperatures T~28–30 °C crosses through the maximum, and further warming decreases the solubility. Simultaneously, the solubility of the individual fullerene C₇₀ in o-xylene at the same experimental conditions monotonously increases along with temperature. The first experiments concerning the solubility of heavy fullerenes in o-xylene were made at 28 °C and 84 °C. It is well-known that the fullerene extract composition (when fullerene soot is provided by the method of carbon rods sublimation with the help of an electric arc in He-plasm) can vary widely, for example (in mass %): C₆₀ ~ 55–88, C₇₀ ~ 10–45, heavy fullerenes C_{n>70} > 1 [16]. The fullerene extract used in these studies had the following composition: (in mass %): C₆₀ ~ 73.3, C₇₀ ~ 24.9, C₇₆ ~ 0.90, C₇₈ ~ 0.26, C₈₄ ~ 0.64. The fullerene extract, representing a solid solution of fullerenes in each other, and o-xylene was magnetically stirred (at 28 °C, the time of saturation was 3 hours). Then, the temperature was

increased to 84 °C and mixing was continued for a longer period (for example 24 hours), during which the fullerene concentration in the solution was continuously monitored by express spectrophotometry. For more exact analysis of light fullerenes (C₆₀ and C₇₀) and heavy fullerenes content, HPLC analysis was used. Experiments were done at different combinations of quantitative characteristics of Liquid and Solid phases (L:S), where L — is volume of o-xylene in ml, S — is mass of fullerene extract in grams. In Table 1 the data are shown for the dynamics of the selective solution-extraction of light fullerenes from the initial fullerene extract at the temperatures T ~ 28 °C and T ~ 84 °C at L:S = 10 and L:S = 50 ml/g.

Table 1. Dynamics of the selective solution-extraction of light fullerenes from the initial fullerene extract at L:S = 10 and L:S = 50 ml/g

Time (min)	T °C	Extraction into liquid solution at L:S = 10 ml/g, %		Extraction into liquid solution at L:S = 50 ml/g, %	
		C ₆₀	C ₇₀	C ₆₀	C ₇₀
30	28	21.3	37.3	54.7	81.8
60	28	22.6	37.9	56.9	83.3
120	28	22.5	38.5	54.6	77.0
180	28	23.4	39.9	54.2	75.8
235	84	8.4	46.5	52.5	77.6
295	84	7.9	45.4	54.7	83.5
355	84	9.6	47.9	53.8	79.2

In the first case, the fullerene extract was treated with o-xylene at 28 °C and L:S = 10 ml/g, into liquid solution were extracted not more than 25 mass % of C₆₀ and 40 mass % of C₇₀, other light fullerenes remained in the solid state. During treatment of the heterogeneous system at 84 °C, (re)crystallization of fullerene solid solutions was realized, the solid solution was enriched by C₆₀ and liquid solution was enriched by C₇₀. In the second case, the fullerene extract was treated with o-xylene at 28 °C and L:S = 50 ml/g, one can get a more concentrated liquid solution of C₆₀ and C₇₀, but (re)crystallization, unfortunately, practically did not occur. According to literature data, the high temperature (re)crystallization of fullerenes in o-xylene is done, using the following conditions — at L:S = 30 g/g [5], L:S = (11±1) ml/g [8]. In Table 2, data are represented concerning the change of the fullerene (including heavy fullerenes) liquid solutions' compositions in the treatment of the fullerene extract with o-xylene at L:S = 10 ml/g.

According to the results of the experiment one can conclude the following: during (re)crystallization at 84 °C, the liquid solution is enriched by the fullerene C₇₀ (light) and C₇₆, C₇₈ (heavy), and simultaneously, the solid solution is enriched by the fullerene C₆₀ (light) and C₈₄ (heavy). On the basis of previous experimental data, the method for crude high-efficiency pre-chromatography separation of fullerenes was developed. As a result of these methods, the initial fullerene extract was separated into two fullerenes extracts basically and unequivocally enriched by light fullerenes C₆₀ and C₇₀, but also differently enriched by various heavy fullerenes. The main processes in these methods are: high temperature (re)crystallization (further high temperature process — HTP), low temperature (re)crystallization (further low temperature process — LTP). The high temperature process was developed in stages by mixing for 60–120 min at 70 to 90 °C, while the low temperature process utilized stirring for 10–30 hours at –25 to –15 °C. Separation

Table 2. Dynamics of the change of the composition of fullerene liquid solutions in the process of treatment of fullerene extract by o-xylene at L:S = 10 ml/g

Time (min)	T ° C	Concentration in liquid solution (mg/liter)					Mass fraction of fullerene in the relation to sum mass of all fullerenes in solution (mass %)				
		C ₆₀	C ₇₀	C ₇₆	C ₇₈	C ₈₄	C ₆₀	C ₇₀	C ₇₆	C ₇₈	C ₈₄
30	28	15628	9281	256	56	87	61.8	36.7	1.00	0.20	0.30
60	28	16546	9436	221	78	147	62.6	35.7	0.84	0.30	0.56
120	28	16457	9596	213	74	164	62.1	36.2	0.80	0.28	0.62
180	28	17179	9923	202	34	152	62.5	36.1	0.73	0.12	0.55
235	84	6118	11570	150	44	28	34.2	64.6	0.8	0.25	0.15
295	84	5763	11306	149	44	25	33.3	65.4	0.9	0.25	0.15
355	84	7025	11925	149	58	22	36.6	62.2	0.8	0.3	0.1

of liquid and solid fullerene solutions in HTP was effected by filtration at the temperature of HTP, however, for separation in LTP simple decantation was used. The multistage process of fullerene separation was accomplished by producing concentrates, enriched by C₆₀, and enriched by C₇₀ at each stage of the whole process. The movement of fullerene liquid solutions formed in LTP, countercurrent to the direction of the movement of solid solutions formed in HTP, was organized also. In the first stage of HTP, was pure solvent — o-xylene was used. In subsequent stages of HTP, the solid fullerene extract was mixed with the liquid fullerene solution from the previous stage of HTP. If such scheme of technological process is realized, one does not need any additional intermediate products, and all fullerenes are distributed between the two concentrates. Correction of the o-xylene volume used in the case of the change of the initial fullerene extract composition or in the case of technical losses was developed mainly in the last stage of HTP. Fig.3 shows the scheme of the n-stage of the fullerene separation process with 2-stage HTP, while in Fig. 4, the scheme of n-stage of the fullerene separation process with 3-stage HTP is depicted.

The following example highlights the data concerning the realization of the n-stage of fullerene separation with the production of the concentrate, enriched by the light fullerenes C₆₀ and C₇₀. For analysis of fullerene-containing phases we used chromatography — HPLC (Shimadzu LC-20 with spectrophotometric detection at 300 and 315 nm).

The composition of the initial extract was slightly different from the previous one: (in mass %): C₆₀ ~ 73.5, C₇₀ ~ 22.8, C₇₆ ~ 1.09, C₇₈ ~ 0.37, C₈₄ ~ 1.83 (some “oxides” of fullerene C₆₀ were also determined — C₆₀O ~ 1.07, C₆₀O₂ ~ 0.16. There was no information, concerning the “oxides” of the second light fullerene C₇₀O_n or “semi-oxides” of light fullerenes (C₆₀)₂O and (C₇₀)₂O, because the content of the last ones in initial fullerene extract was comparatively low (≤ 0.03 mass %). The first HTP stage was the mixing of 100 g of the initial fullerene extract in the returned from the second HTP stage previous (n-1)-stage solution at 85 ° C over 90 min. The volume of the returned solution was 1000 ml. After filtration, we got solid fullerene product enriched by C₆₀ and a liquid fullerene solution which was then subjected to LTP. LTP was performed for 20 hours at -20 ° C. After decantation, we obtained the C₇₀-enriched concentrate and a solution, which was then used in the second HTP stage. The second HTP stage was performed with mixing of solid fullerene product after the first HTP stage and the liquid fullerene solution after

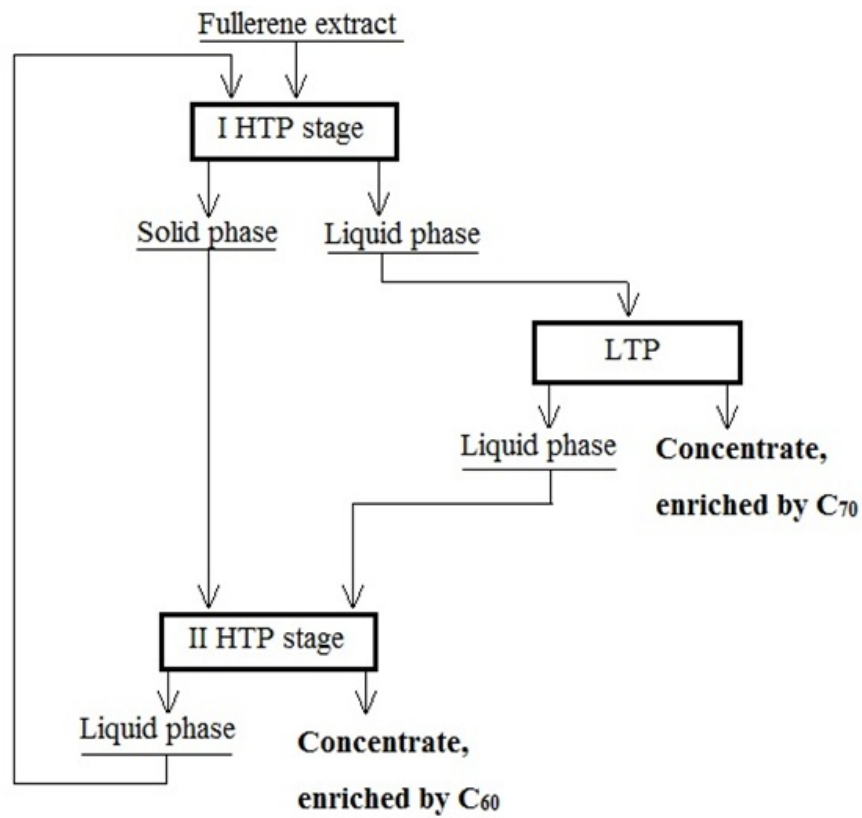


Fig. 3. Scheme of n-stage of the process of fullerene separation with 2-stage HTP

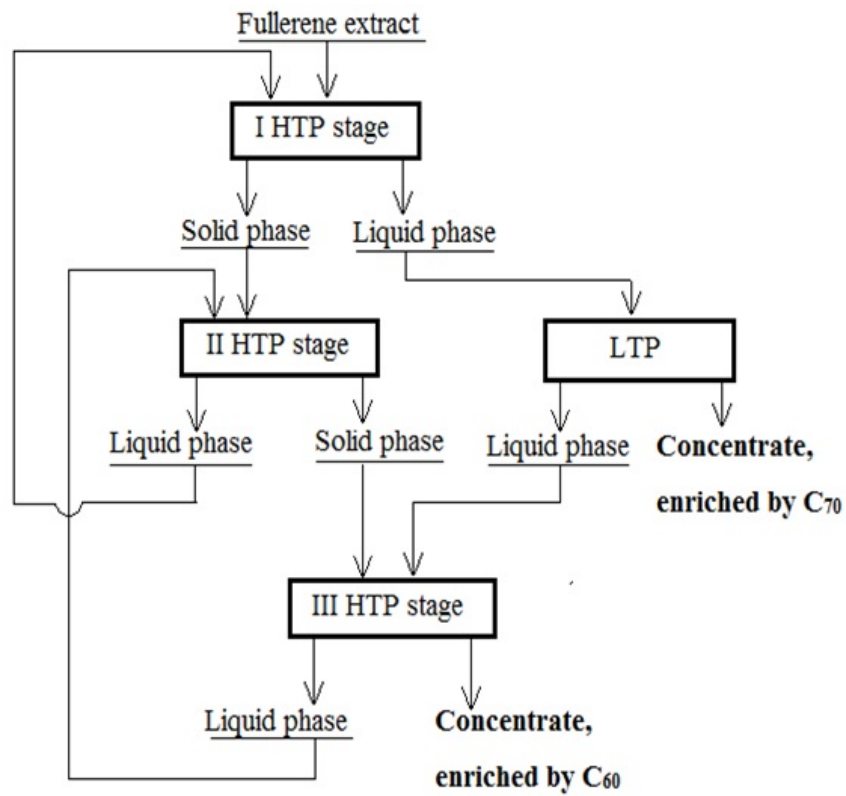


Fig. 4. Scheme of n-stage of the process of fullerene separation with 3-stage HTP

LTP again at 85 °C over 90 min. After filtration, we obtained the C₆₀-enriched concentrate and the solution which was given for the first HTP stage of the next (n+1)-stage. So, as a result of the n-stage separation process, we were afforded two concentrates: a C₇₀-enriched concentrate, consisting of 84.2 mass.% C₇₀, 5.6 mass.% C₆₀ and enriched by heavy fullerenes in comparison with the initial fullerene extract and a C₆₀-enriched concentrate, consisting of 9.4 mass.% C₇₀, 88.3 mass.% C₆₀, while the heavy fullerenes content in it was considerably lower than the previous concentrate. Characteristics of fullerene products in n-stage of process of fullerene separation are represented in Tables 3–5.

Table 3. Characteristics of fullerene solid products in n-stage of process of fullerene separation

Name of product	Fullerenes content in products (mass.%)						
	C ₆₀	C ₇₀	C ₇₆	C ₇₈	C ₈₄	C ₆₀ O	C ₆₀ O ₂
Initial fullerene extract	73.52	22.76	1.09	0.37	1.03	1.07	0.16
Solid fullerene product after the first HTP stage	79.4	17.4	0.8	0.3	1.0	1.0	0.1
Concentrate, enriched by C ₆₀	88.3	9.4	0.1	0.2	1.0	0.9	0.1
Concentrate, enriched by C ₇₀	5.6	84.2	5.4	1.3	1.3	1.8	0.4

Table 4. Characteristics of fullerene liquid solutions in n-stage of process of fullerene separation

Name of product	Individual fullerenes concentrations in the sum fullerene mass (mass.%)						
	C ₆₀	C ₇₀	C ₇₆	C ₇₈	C ₈₄	C ₆₀ O	C ₆₀ O ₂
Returned solution	36.1	56.7	3.4	0.9	0.8	1.9	0.2
Solution after the first HTP stage	17.4	74.0	4.4	1.0	1.0	1.8	0.4
Solution after LTP	58.2	38.8	0.6	0.2	0.1	1.9	0.2

In this process, as mentioned above, in HTP, the C₆₀-enriched concentrate is also enriched by C₈₄. In our separation process, 98.6 mass % C₆₀ was contained in that concentrate (from the sum content of C₆₀ in the initial extract), simultaneously, 65.9 mass % C₇₀ was contained in the C₇₀-enriched concentrate (from the sum content of C₇₀ in the initial extract). “Oxides” of C₆₀ were mainly isolated in the C₇₀-enriched concentrate, which is natural, since the specific electronic configuration of the last one, for example has both higher asymmetry and electric polarizability than C₆₀. The solutions after both HTP stages, after removing from the (re)crystallization system the C₆₀-enriched concentrate, naturally contained less C₆₀ than the initial fullerene extract and enriched by C₇₀ and heavy fullerenes. The solutions after the LTP, after removing from the (re)crystallization system the C₇₀-enriched concentrate, naturally contained less C₇₀ than initial fullerene extract and was enriched by C₆₀ but not by heavy fullerenes. The two-stage (re)crystallization process for producing the C₆₀-enriched concentrate, with the returning of counter-current liquid fullerene solutions, permitted us to get a concentrate, considerably more enriched by C₆₀ than was obtained for a one-stage (re)crystallization process. We could also considerably increase the mass of C₇₀ obtained in the C₇₀-enriched concentrate. One can easily understand that, using the (re)crystallization method of fullerene pre-chromatography crude

Table 5. Calculated characteristics of concentrates, got in the n-stage of fullerene separation

Characteristics	Concentrate, enriched by C ₆₀	Concentrate, enriched by C ₇₀
Content of C ₆₀ (mg)	72520	1000
Content of C ₇₀ (mg)	7760	15000
Content of C ₇₆ (mg)	120	970
Content of C ₇₈ (mg)	139	231
Content of C ₈₄ (mg)	796	234
Content of ₆₀ (mg)	750	320
Content of ₆₀₂ (mg)	90	70
Mass (mg)	82175	17825
Distribution of C ₆₀ (mass.%)	98.6	1.4
Distribution of ₇₀ (mass.%)	34.1	65.9
Distribution of ₇₆ (mass.%)	11.0	89.0
Distribution of ₇₈ (mass.%)	37.6	62.4
Distribution of ₈₄ (mass.%)	77.3	22.7

fullerene separation described above, we may produce fullerene concentrates with compositions, considerably varying from the above-described example. The factors, which can rule such (re)crystallization process are the following: composition of the initial fullerene extract, phases masses – L:S, temperature of HTP, temperature of LTP etc. Changing of other factors, such as time of HTP or LTP, regimes of mixing or saturation, to our opinion, make the process a-equilibrium, non-static and thus, not easily controlled.

3. Conclusion

We have elaborated an original, highly efficient method of pre-chromatography crude separation of light fullerenes (C₆₀ and C₇₀), based on the multistage processes of (re)crystallization – the solution of fullerenes solid solutions in liquid solvent (o-xylene) or in liquid o-xylene solutions and the crystallization of solid solutions from saturated liquid solutions. The process is developed in a poly-thermal regime in the temperature ranges from –20 °C to 85 °C. As a result, the initial fullerene extract (solid solution) may be efficiently divided into two different solid solutions – the first considerably enriched by fullerene C₆₀ and the second considerably enriched by fullerene C₇₀. Heavy fullerenes – C₇₆, C₇₈, C₈₄ . . . are distributed between these solid solutions.

Acknowledgement

The work was supported by Russian Found of Fundamental Researches – RFFI (Project No 09-03-00350–a).

References

- [1] Sidorov L. N., Yurovskaya M. A. , et al. *Fullerenes*. Ekzamen, Moscow, 688 pp. (2005).
- [2] Charykov N. A., Zuev V. V., Kuznetsova E. A. High-efficiency complex for fullerenes production. *Petersburg Electronics Journal*, **4**, P. 16–31 (2007).
- [3] Ermilov N. N., Charykov N. A., et al. Nanotechnology – from theory to practical application. *Journal of Innovations (rus.)*, **12**, P. 79–83 (2007).

- [4] Tour J. M., Scrivens W. A., Bedworth P. V. Purification of fullerenes. United States Patent 5662876, C01B 31/00 (1997).
- [5] Ng Ka Ming. Separation of fullerene C₆₀ and C₇₀ using crystallization. United States Patent 7875086, B01D 9/00 (2011).
- [6] Bolstren N. N., Ojchenko V. M., Olejnik S. V. Method of obtaining fullerene C₆₀. Patent RF 2327635, C01B 31/02 (2008).
- [7] Glushko Yu. S., Sedov V. P., Kolesnik S. G. Method of producing fullerene C₆₀. Patent RF 2456233, C01B 31/02 (2012).
- [8] Sedov V. P., Kolesnik S. G. Method of producing fullerene C₇₀. Patent RF 2455230, C01B 31/02 (2012).
- [9] Blokhin A. A., Keskinov V. A., Murashkin Yu. V., et al. Method for chromatographic separation of fullerenes. Patent RF 2302372, C01B 31/02 (2007).
- [10] Tsetsikova L. V., Keskinov V. A., Charykov N. A., et al. Extraction of Fullerene Mixture from Fullerene Soot with Organic Solvents. *Russian Journal of General Chemistry*, **5**, P. 920–926 (2011).
- [11] Semenov K. N. *Solubility of Light Fullerenes in Organic Solvents*. Ph.D. Dissertation (Chem.Sci), St. Petersburg, 173 pp. (2009).
- [12] Semenov K. N., Charykov N. A. *Solubility of Light Fullerenes and Derivatives*. LAP LAMBERT Academic Publishing GmbH & Co. KG, Saarbrücken, Germany, 238 pp. (2011).
- [13] Semenov K. N., Charykov N. A., Keskinov V. A., et al. Solubility of Light Fullerenes in Organic Solvents. *J. Chem. Eng. Data*, **55**, P. 13–36 (2010).
- [14] Arapov O. V., Aksel'rod B. M., Pronkin A. A., et al. Solubility in the fullerene C₆₀-fullerene C₇₀-o-C₆H₄(CH₃)₂ system. *Russian Journal of Applied Chemistry*, **76**(1), P. 33–36 (2003).
- [15] Ponomarev A. N., Aksel'rod B. M., Barchenko V. T., et al. Solution-solid phase equilibria in the fullerene C₆₀-fullerene C₇₀-C₆H₅CH₃ and fullerene C₆₀-fullerene C₇₀-o-C₆H₄(CH₃)₂ systems at 25 and 80 °C, respectively. *Russian Journal of Physical Chemistry*, **74**(12), P. 1942–1945 (2000).
- [16] Gruzinskaya E. A., Keskinov V. A., Keskinova M. V., et al. Fullerene soot Produced by Electric Arch. *Nanosystems: Physics, Chemistry, Mathematics*, **3**(6), P. 83–90 (2012).

STRUCTURE PECULIARITIES OF NANOCRYSTALLINE SOLID SOLUTIONS IN GdAlO_3 — GdFeO_3 SYSTEM

E. A. Tugova^{1,2}, V. V. Gusarov^{1,2}

¹Ioffe Physical Technical Institute of RAS, Saint Petersburg, Russia

²Saint Petersburg State Institute of Technology, Russia

katugova@inbox.ru; victor.v.gusarov@gmail.com

PACS 61.46.-w

Nanoparticles of solid solutions in GdAlO_3 — GdFeO_3 system have been synthesized. Plots of crystalline sizes for $\text{GdAl}_{1-x}\text{Fe}_x\text{O}_3$ series versus GdFeO_3 composition have been constructed. The sizes of solid solution nanoparticles were shown to decrease in comparison to the sizes of nanocrystalline individual compounds. The observed regularities allowed us to assume the formation of nanocrystalline $\text{GdAl}_{1-x}\text{Fe}_x\text{O}_3$ series with core-shell morphology.

Keywords: nanostructures, solid solutions, precipitation technique, non-autonomous phases, core-shell nanoparticles.

1. Introduction

Perovskite-type compounds possess unique electrical, magnetic, thermal properties [1–6]. Thus, the research of perovskite-like compounds and solid solutions based on it formation processes, as well as phase equilibria in systems, composing mentioned phases are of great interest [7–10]. Phase relations in pseudo-binary LnAlO_3 — LnFeO_3 section have been investigated in single works [11, 12] and basically were made for one LaAlO_3 — LaFeO_3 system. According to the presented data the solubility limits of LaAlO_3 and LaFeO_3 at 1200 °C were set to be $0 \leq x \leq 0.40$ for the $\text{LaFe}_{1-x}\text{Al}_x\text{O}_3$ series and $0 \leq y \leq 0.15$ for $\text{LaFe}_y\text{Al}_{1-y}\text{O}_3$ solid solutions [11]. Kuščer et al indicated the formation of continuous $\text{LaFe}_{1-x}\text{Al}_x\text{O}_3$ ($0 \leq x \leq 1$) series at 1300 °C [12]. Previously, samples were prepared by solid-phase chemical reactions using different starting components: hydroxides and oxides [11, 12].

It is of great interest to synthesize solid solutions based on nanoscaled perovskite-like oxides by “soft” chemistry methods [13–16]. The unusual effects observed during nanocrystalline solid solutions formation were fixed [17–19]. The mentioned effects were attributed to a number of factors, including the increase of component’s relative solubility in its nanosized state in comparison with macroparticles, the formation of nanoparticles with core-shell morphology and the decreasing of solid solutions nanoparticles sizes in comparison to those of nanocrystalline individual compounds.

These reasons demonstrate the importance of systematic investigations into the peculiarities of nanocrystalline solid solutions, and as a result, structural research with particular interest in the study of nanocrystallite formation in the GdAlO_3 — GdFeO_3 system was carried out.

2. Experimental

2.1. Synthesis procedure

$GdAl_{1-x}Fe_xO_3$ ($0 \leq x \leq 1$) series were prepared by precipitation from aqueous solutions of stoichiometric amounts of 1M $Gd(NO_3)_3 \cdot 5H_2O$, $Fe(NO_3)_3 \cdot 9H_2O$ and $Al(NO_3)_3 \cdot 9H_2O$. Aqueous 10 wt.% NH_4OH was used as the coagulating medium. To this NH_4OH solution aqueous solutions of gadolinium, iron and aluminum nitrates were added in a dropwise manner by adjusting the pH to 8–9. The co-precipitated mixtures were filtered immediately after preparation to remove traces of NO_3^- ions and were then dried at room temperature in air. The initial precipitates were subsequently pressed and calcined in air at 600–1300 °C for 3 h.

2.2. Characterization of prepared nanocrystals

The purity and crystallization of $GdAl_{1-x}Fe_xO_3$ samples were characterized by powder X-ray diffraction (XRD) using a Shimadzu XRD-7000 with monochromatic CuK_α radiation ($\lambda = 154.178$ pm). $\alpha-Al_2O_3$ was used as internal standard. Crystallite sizes of the obtained powders were calculated by the X-ray line broadening technique based on Scherer's formula.

3. Results and discussion

Fig.1 shows the X-ray powder diffraction (XRD) data of the initial mixture corresponding to stoichiometry of $GdAlO_3$, heat treated at 600 – 1300 °C for 3 h in air. The results of X-ray analysis of $GdAlO_3$ formation presented in Fig. 1 demonstrate the amorphous state of the initial mixture remains until 1000 °C. Crystallization of the $GdAlO_3$ phase is fixed at 1000 °C (Fig. 1). The latter is 300 °C higher than the temperature at which nanocrystalline $GdFeO_3$ is produced [20]. Thus, the investigation of the formation processes for $GdAl_{1-x}Fe_xO_3$ ($0 < x < 1$) solid solutions in $GdAlO_3 - GdFeO_3$ system was carried out at 1000–1300 °C. The ratio of components in $GdAlO_3 - GdFeO_3$ system was varied in 20 mol. % increments.

The mean size of coherent scattering regions of $GdAlO_3$ and $GdFeO_3$ individual perovskite-like compounds were approximately 60 nm.

The XRD patterns of initial mixtures corresponding to a stoichiometry of $GdAl_{1-x}Fe_xO_3$ ($0 < x < 1$) series which were heated at 1100 °C are presented in Fig. 2 as an illustration of the processing stages of target solid solutions research.

Fig. 3. shows the relationship between the mean size of coherent scattering regions and interstitial areas for peak with (111) index determined from X-ray data of the $GdAl_{1-x}Fe_xO_3$ series under 1000, 1100 and 1300 °C versus $GdFeO_3$ content.

The obtained data showed that the crystallite size of $GdAlO_3$ decreased at concentrations ranging from $0.2 < x < 0.5$ (Fig. 3), with the highest $GdFeO_3$ content giving the smallest values of 30–40 nm. These relationships are in agreement with data for interstitial areas (d/n) for the $GdAl_{1-x}Fe_xO_3$ series, for which the observed deviation of plotted d/n values from linearity were typical for solid solutions. These data can be connected with the formation of $GdAl_{1-x}Fe_xO_3$ nanoparticles with core-shell structure type which is in agreement with previous literature [18–19].

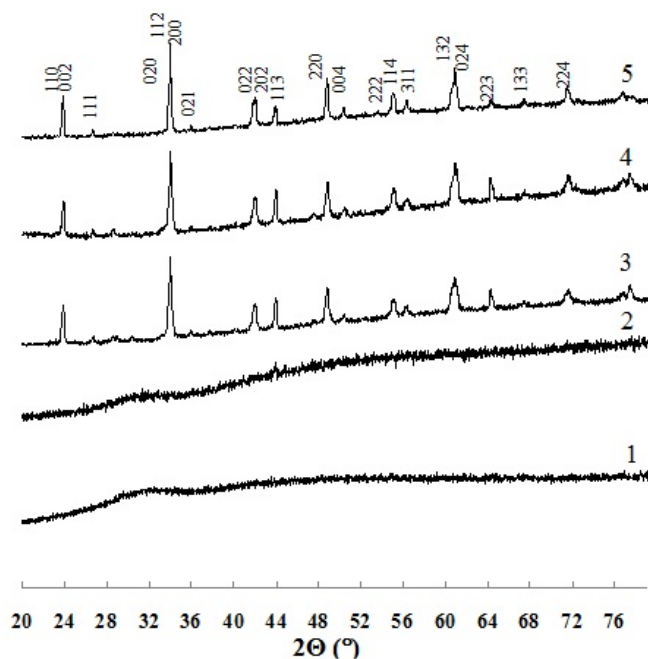


Fig. 1. X-Ray diffraction patterns of initial mixtures corresponding to stoichiometry of GdAlO_3 after sintering in air at °C: 1. 600; 2. 800; 3. 1000; 4. 1100; 5. 1300 °C for 3 h

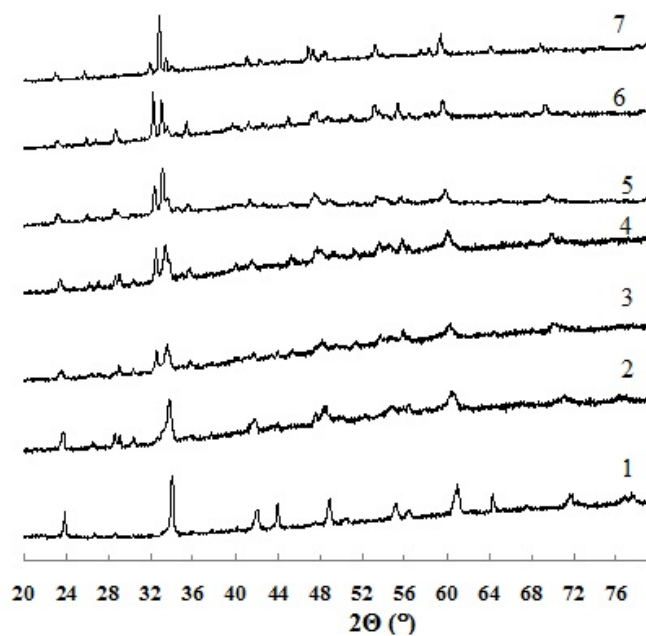


Fig. 2. X-Ray diffraction patterns, describing processes of $\text{GdAl}_{1-x}\text{Fe}_x\text{O}_3$ series formation for x : 1) 0; 2) 0.2; 3) 0.4; 4) 0.5; 5) 0.6; 6) 0.8; 7) 1 from initial mixtures heat treated at 1100 °C for 3 h

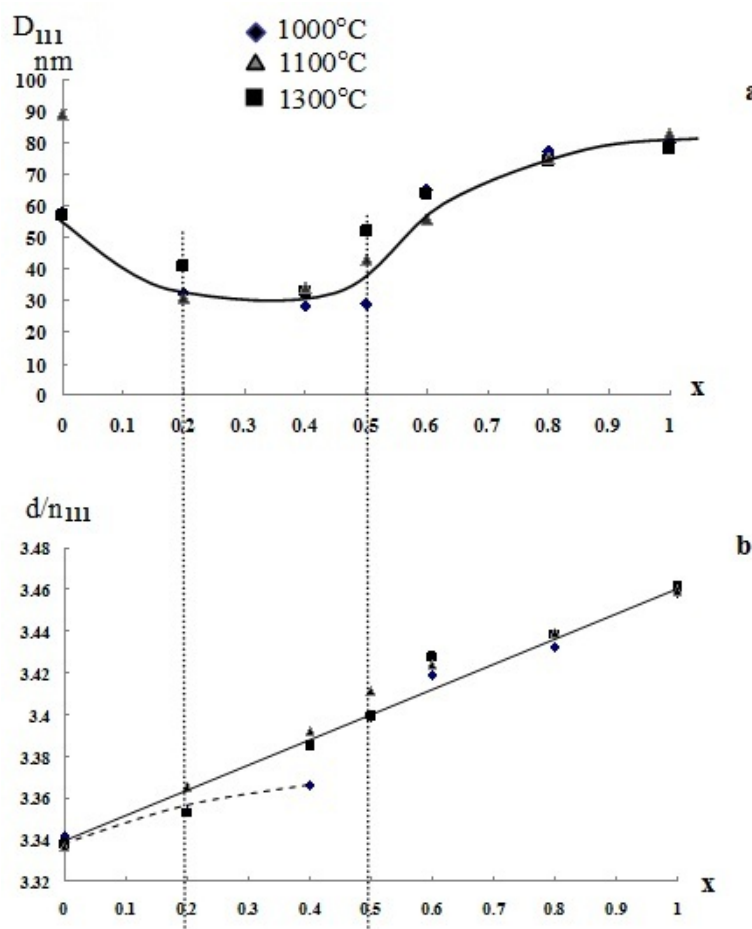


Fig. 3. a) The mean size of coherent scattering regions (D) and b) d/n for $GdAl_{1-x}Fe_xO_3$ series as a function of $GdFeO_3$ content (x)

4. Conclusion

These results showed that the formation of $GdAl_{1-x}Fe_xO_3$ continuous series in the $GdAlO_3-GdFeO_3$ system were observed at 1100-1300 °C. $GdAl_{1-x}Fe_xO_3$ nanoparticles ranging from 30–40 nm size were obviously attributed to the core-shell morphology.

Acknowledgments

This work was financially supported by the Russian Foundation for Basic Research, project No 13-03-00888.

References

- [1] Stølen S., Grønvold F., Brinks H. Heat capacity and thermodynamic properties of $LaFeO_3$ and $LaCoO_3$ from $T = 13$ K to $T=1000$ K, *J. Chem. Thermodynamics*, **30**, P. 365–377 (1998).
- [2] Zhang Yu., Yang J., Xu J., Gao Q., Hong Zh. Controllable synthesis of hexagonal and orthorhombic $YFeO_3$ and their visible-light photocatalytic activities. *Materials Letters*, **81**, P. 1–4 (2012).
- [3] Zong Ya., Fujita K., Akamatsu H., Murai Sh., Katsuhisa Tanaka K. Antiferromagnetism of perovskite $EuZrO_3$. *Journal of Solid State Chemistry*, **183**, P. 168–172 (2010).
- [4] Goto T., Kimura T., Lawes G., Ramirez A.P., Tokura Y. Ferroelectricity and giant magnetocapacitance in perovskite rare-earth manganites. *Physical review letters*, **92**, P. 257201 (2004).

- [5] Bondar' I. A., Shirvinskaya A. K., Popova V. F., Mochalov I. V., Ivanov, A. O., Thermal Stability of Orthoaluminates of Rare-Earth Elements of the Yttrium Subgroup. *Dokl. Akad. Nauk SSSR*, **246**(5), P. 1132–1136 (1979).
- [6] Petrosyan A. G., Popova V. F., Gusarov V. V., Shirinyan G. O., Pedrini C., Lecoq P. The $\text{Lu}_2\text{O}_3 - \text{Al}_2\text{O}_3$ system: relationships for equilibrium-phase and supercooled states. *J. Crystal Growth*, **293**, P. 74–77 (2006).
- [7] Tsipis E. V., Kharton V. V., Waerenborgh J. C., Rojas D. P., Naumovich E. N., Frade J. R. Redox behavior of acceptor-doped $\text{La}(\text{Al},\text{Fe})\text{O}_{3-\delta}$. *Journal of Alloys and Compounds*, **413**, P. 244–250 (2006).
- [8] Sagdahl L. T., Einarsrud M. A., Grande T. Sintering behaviour of $\text{La}_{1-x}\text{Sr}_x\text{FeO}_{3-\delta}$ mixed conductors. *J. Eur. Ceram. Soc.*, **26**, P. 3665–3673 (2006).
- [9] Ning L., Guoqing Ya., Guang Z., Huanyin G.. Effect of Dy doping on magnetism of $\text{La}_{0.7}\text{Sr}_{0.3}\text{CoO}_3$ system. *Rare Metals*, **31**(2), P. 135–139 (2012).
- [10] Savinskaya O. A., Nemudry A. P., Lyakhov N. Z. Synthesis and Properties of $\text{SrFe}_{1-x}\text{M}_x\text{O}_{3-z}$ (M=Mo, W) Perovskites. *Inorg. Mater*, **43**(12), P. 1350–1360 (2007).
- [11] Hrovat M., Holc J., Kuščer D., Bernik S. Preliminary data on subsolidus phase equilibria in the $\text{La}_2\text{O}_3-\text{Al}_2\text{O}_3-\text{Mn}_2\text{O}_3$ and $\text{La}_2\text{O}_3-\text{Al}_2\text{O}_3-\text{Fe}_2\text{O}_3$ systems. *J. Mater.Sci. Lett.* **14**(4). P. 265–267 (1995).
- [12] Kuščer D., Hanzžel D., Holc J., Marko Hrovat M., Kolar D. Defect Structure and Electrical Properties of $\text{La}_{1-y}\text{Sr}_y\text{Fe}_{1-x}\text{Al}_x\text{O}_{3-\delta}$. *J. Am. Ceram. Soc.*, **84**(5), P. 1148–1154 (2001).
- [13] Shivakumara C. Low temperature synthesis and characterization of rare earth orthoferrites LnFeO_3 (Ln=La, Pr and Nd) from molten NaOH flux. *Solid State Communications*, **139**, P. 165–169 (2006).
- [14] Popa M., Calderon Moreno J. M., Lanthanum ferrite ferromagnetic nanocrystallites by a polymeric precursor route. *Journal of Alloys and Compounds*, **509**, P. 4108–4116 (2011).
- [15] Cizauskaite S., Reichlova V., Nenartaviciene G., Beganskiene A., Pinkas J., Kareiva A. Sol-gel preparation and characterization of gadolinium aluminate. *Materials Chemistry and Physics*, **102**, P. 105–110 (2007).
- [16] Andrés-Vergés M., Morales M. del P., Veintemillas-Verdaguer S., Palomares F. Ja., Serna C.J., Core/shell magnetite/bismuth oxide nanocrystals with tunable size, colloidal and magnetic properties, *Chem. Mater.*, **24**, P. 319–324 (2012).
- [17] Melekhin V.G., Kolobkova E. V., Lipovskii A. A., Petrikov V. D., Almjasheva O. V. Formation of Nanostructures of the Core–Shell Type upon Diffusion Phase Decomposition of Fluorophosphate Glasses. *Glass Physics and Chemistry*, **33**(6), P. 569–575 (2007).
- [18] Tomkovich M. V., Andrievskaya E. R., Gusarov V. V. Formation under hydrothermal conditions and structural features of nanoparticles based on the system $\text{ZrO}_2-\text{Gd}_2\text{O}_3$. *Nanosystems: physics, chemistry, mathematics*, **2**(2), P. 6–14 (2011).
- [19] Al'myasheva O. V., Gusarov V. V. Nucleation in media in which nanoparticles of another phase are distributed. *Doklady Physical Chemistry*, **424**(2), P. 43–45 (2009).
- [20] Tugova E. A. GdFeO_3 nanoparticles formation in $\text{Gd}_2\text{O}_3-\text{Fe}_2\text{O}_3-\text{H}_2\text{O}$ system. Proceedings of “Scientific-practical conference dedicated to the 184th anniversary of St. Petersburg state institute of technology foundation”. St. Petersburg, 29-30th of November 2012, P. 200 (2012).

DIELECTRIC STUDIES OF NANOCRYSTALLINE MANGANESE TUNGSTATE

N. Aloysius Sabu¹, K. P. Priyanka¹, Smitha Thankachan², Anu Tresa Sunny³,
E. M. Mohammed², O. P. Jaseentha¹, Thomas Varghese^{1,*}

¹ Nanoscience Research Centre (NSRC), Department of Physics, Nirmala College, Muvattupuzha - 686 661, Kerala, India

² Department of Physics, Maharaja's College, Ernakulam - 682 011, Kerala, India

³ School of Chemical Sciences, MG University, Kottayam - 686 560, Kerala, India

*nanoncm@gmail.com

PACS 81.16.Be, 81.07.Bc, 73.63.Bd

The dielectric properties of monoclinic manganese tungstate have been studied as a function of frequency and temperature. It was found that the dielectric constant and dielectric loss for all temperatures had high values at low frequencies which decreased rapidly as frequency increased attaining a constant value at higher frequencies. The a.c. conductivity increased as frequency increased, conforming small polaron hopping. As temperature increased, the values of the a.c. conductivity are shifted to higher values. Higher values were also obtained when the particle size decreased. These properties make the nano-sized MnWO_4 as a promising material for fabricating humidity sensors.

Keywords: dielectric studies, manganese tungstate, nanoparticles, polaron hopping.

1. Introduction

Nanostructured tungstate materials have aroused much interest because of their luminescent behavior, structural properties and potential applications. Manganese tungstate (MnWO_4) is a promising material for fabricating humidity sensors due to its appropriate bulk electrical conductivity. Humidity sensors are important in many areas like meteorology, medicine, food production, agriculture, industrial and general household applications [1–3]. This compound is antiferromagnetic, with a magnetic moment of $5.44 \mu_B$ and a Neel temperature 14.4 K [4]. The various methods employed for the synthesis of MnWO_4 include the sol-gel method [2], chemical reaction in a molten salt solution, grinding in a vibrating mill, thermal treatment of a metathesis reaction product [5] and the solvothermal method [6]. In the present work, we report a successful room temperature synthesis of manganese tungstate nanoparticles, adopting careful control of the reaction kinetics of aqueous precipitation.

2. Experimental

Manganese chloride and sodium tungstate (99.9% purity) were purchased from Sigma Aldrich Chemicals and were used without further purification. Nanosized powders of manganese tungstate were prepared by reacting aqueous solutions of manganese chloride and sodium tungstate (0.001 M each) at room temperature keeping the pH = 7. The precipitate formed was centrifuged, filtered and washed with distilled water a number of times, and dried in an oven to obtain manganese tungstate as a fine powder. The precursor

was annealed in air at 450 °C, 600 °C and 750 °C for 3 hours. The structural characteristics of the synthesized manganese tungstate nanoparticles were then studied by X-ray powder diffraction (XRD) using Bruker D8 Advance X-ray diffractometer ($\lambda = 1.5406 \text{ \AA}$). The powder was consolidated in the form of cylindrical pellets of diameter 11 mm and thickness $d = 1.2 \text{ mm}$ at a pressure of $\sim 5 \text{ GPa}$ using a hydraulic press. Both faces of the pellets were coated with an air-drying silver paste. Dielectric measurements, as a function of frequency ranging from 100 Hz \sim 15 MHz were measured at selected temperatures from 300 K – 425 K using a LCR meter (Wayne Kerr H-6500 model) in conjunction with a portable furnace and temperature controller ($\pm 1 \text{ K}$) using the four probe method. The dielectric constant and a.c. conductivity (σ_{ac}) were calculated using Eq.(1) and (2) respectively.

$$\epsilon' = cd/\epsilon_0 a, \quad (1)$$

$$\sigma_{ac} = \epsilon' \epsilon_0 \omega \tan \delta, \quad (2)$$

where a is the face area, c the measured capacitance of the pellet, ϵ_0 the permittivity of vacuum, ω the angular frequency and $\tan \delta$, the loss tangent.

3. Results and discussion

Fig. 1 displays the powder X-ray diffraction pattern of the samples annealed at 450 °C, 600 °C and 750 °C for 3 hours. From XRD patterns, using the Scherrer equation, the size of the particles corresponding to different annealing temperatures were estimated to be 25 nm, 30 nm, and 40 nm for samples M1, M2 and M3 respectively. As the annealing temperature increased, XRD patterns showed much sharper peaks and were due to the larger particle sizes obtained at higher temperatures. The principal 'd' values taken from the JCPDS file No. 80-0135 for MnWO_4 are in close agreement with the observed 'd' values.

Fig. 2(A) shows the variation of dielectric constant with frequency for temperatures from 303 K to 423 K of sample M3. It can be seen that the real part of the dielectric constant for all temperatures had high values at low frequencies which decreased rapidly as frequency increased, attaining a constant value at higher frequencies. For 303 K, the value of ϵ' was 4.07 at 100 Hz, which decreased to 0.057 at 10MHz. At 363 K the values were 22.2 (100 Hz) and 0.16. The corresponding values for 423 K were 57.1 at 100 Hz and 0.186 at 10 MHz respectively. The inset figure 2(A) shows a similar variation for all the samples with different particle sizes, at 303 K, but the values were shifted upward when the grain size decreased. The value of ϵ' changed from 9057 at 100 Hz to 52.7 at 10 MHz for sample M1 while this quantity changed from 2357.6 (100 Hz) to 17.02 (10 MHz) for sample M2 and from 63.16 (100 Hz) to 0.19 (10 MHz) for sample M3 respectively.

In dielectric nanostructured materials, interfaces with large volume fractions contain a large number of defects, such as dangling bonds, vacancies, vacancy clusters, and microporosities, which can cause a change of positive and negative space charge distribution in interfaces. When subjected to an electric field, these space charges move. When they are trapped by defects, several dipole moments are formed. At low frequencies, these dipole moments are easy to follow by monitoring the variation of the electric field [7–8]. So, the dielectric loss, and hence, the dielectric constant showed large values at low frequencies. As the temperature increased, more and more dipoles were aligned, resulting in an increased dielectric constant for a given frequency [9].

At very high frequencies (MHz), the charge carriers would have moved before the field reversal occurred and thus, ϵ' decreased at higher frequencies. The nature of the

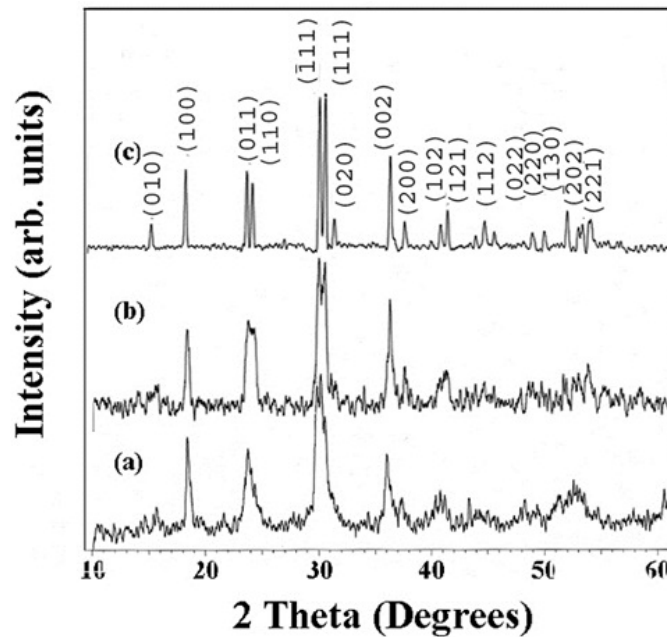


Fig. 1. Shows the XRD pattern of the samples annealed at (a) 450 °C, (b) 600 °C and (c) 750 °C

variation is similar for the other samples, but the values were increased when the grain size decreased. The amorphous nature of the surface, high surface energy, micromechanical stress, surface domain depolarization and domain wall effects were considered as reasons for this variation. Both space charge polarization and reversal of polarization direction contribute significantly to the ϵ' [10–11]. With increased particle volume, the interfacial volume decreased. Increasing the particle volume also increased the contribution to ϵ' by electronic relaxation polarization, which occurs mainly inside the particles. Decreasing the interfacial volume diminishes contribution to ϵ' by space charge polarization and rotation of the direction of polarization, which occur mainly in the interfacial region. As a result ϵ' decreased as particle size increased.

The variation of $\tan\delta$ with frequency of sample M3 is shown in Fig. 2(B). The variation of $\tan\delta$ is similar to that of ϵ' . For 303 K, $\tan\delta$ had a value of 4.72 at 100 Hz which decreased to 0.736 at 10 MHz. At 363 K the corresponding change was from 8.63 to 0.73. For 423 K, $\tan\delta$ had a value of 43.3 at 100 Hz which decreased to 3.38 at 10 MHz. The variation of $\tan\delta$ with frequency at 303 K for different grain sizes is shown in Fig. 2 (B). At 100 Hz the value was 71.4 for M1 which decreased to 2.20 (10 MHz). For M2 the values were 43.3 (100 Hz) and 3.38 (10 MHz), while for M3, the values were 4.72 (100 Hz) and 0.736 (10 MHz) respectively. In nanophase materials the heterogeneities present in the interface layers produce an absorption current, resulting in dielectric loss. This absorption current decreases with increases in the frequency of the applied field. The hopping probability per unit time increases with increased temperature. Correspondingly the loss tangent also increases with increase of temperatures [12–13]. From X-ray results it was found that the particle size and crystallinity increased as the sintering temperature was elevated. The volume percentage of interface boundaries, defects and imperfections were greatly reduced as the sintering temperature was increased. This explains the increase of tangent loss as the particle size was decreased. The loss in MnWO_4 can be explained by the electronic hopping model, which considers the frequency

dependence of the localized charge carriers hopping in a random array of centers. This model is applicable for materials in which the polarization responds sufficiently rapidly to the appearance of an electron on any one site so that the transaction may be said to occur effectively into the final state [14]. At higher frequencies, $\tan\delta$ becomes almost constant because the electron exchange interaction (hopping) between Mn^{+2} and Mn^{+3} cannot follow the alternatives of the applied a.c. electric field beyond a critical frequency.

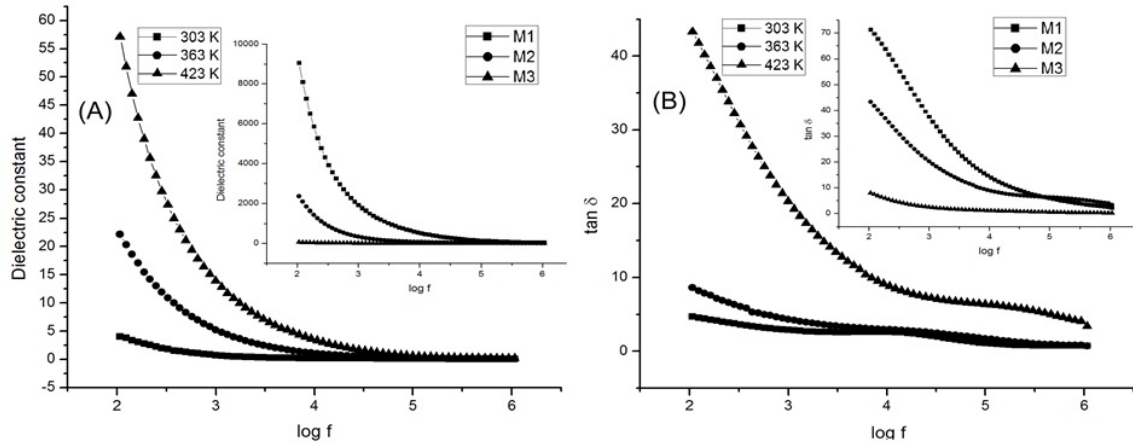


Fig. 2. (A) The variation of dielectric constant with frequency and (B) the variation of $\tan\delta$ with frequency for temperatures from 303 K to 423 K of sample M3

The variation of the a.c. electrical conductivity as a function of frequency for sample M3 is shown in Fig. 3. At lower frequencies σ_{ac} had a small value which increased at higher frequencies. The nature was similar for other temperatures but the values were shifted upwards at higher temperatures. For 303 K, σ_{ac} had a value of 0.0373×10^{-3} S/m at 100 Hz which increased to 0.434×10^{-3} S/m at 10 MHz. At 363 K, the corresponding variation was from 0.123×10^{-3} S/m (100 Hz) to 0.71×10^{-3} S/m (10 MHz), while at 423 K, the values were 1.62×10^{-3} S/m at 100 Hz and 3.78×10^{-3} S/m at 10 MHz. The variation of σ_{ac} with frequency at 303 K for different grain sizes is shown in Fig. 3. At 100 Hz the value was 3.83×10^{-3} S/m for M1, which increased to 6.88×10^{-3} S/m at 10 MHz. For M2, the values were 0.0826×10^{-3} S/m (100 Hz) and 1.15×10^{-3} S/m (10 MHz), while for M3, the figures were 0.0373×10^{-3} S/m (100 Hz) and 0.434×10^{-3} S/m (10 MHz) respectively.

It is clear from the figures that the conductivity increased as the frequency increased, conforming small polaron hopping. Small polaron formation takes place in those materials whose conduction band arise from incomplete 'd' or 'f' orbitals. In $MnWO_4$, both Mn^{+2} and W^{+6} have incomplete 'd' orbitals which are responsible for the formation of small polarons. Also, there is the possibility of conduction due to impurities at low temperatures. The thermoelectric power of $MnWO_4$ has been reported to increases with temperature [4]. At lower temperatures, the a.c. conductivity increases with warming. Dissanayeke et al., observed a similar variation, but at higher temperatures, σ_{ac} was independent of frequency [15]. In $MnWO_4$, the conduction was due to the exchange interaction (hopping of electrons) between the Mn^{+2} and Mn^{+3} . According to Elliot's barrier hopping model, the ac conductivity is given as Eq.(3),

$$\sigma_{ac} = n\pi^2 N N_p \varepsilon' \omega R_\omega^6 / 24, \quad (3)$$

where n is the number of polarons involved in hopping, NN_p , proportional to the square of concentration of states, ϵ' the dielectric constant and R_w the hopping distance [16]. When the grain size of the sample was reduced the hopping distance increased which increased the conductivity. The conduction in manganese tungstate is due to the hopping and ionic conduction of Mn^{+} ions. The high values of σ_{ac} for particles with small grain sizes are a direct confirmation of the theory.

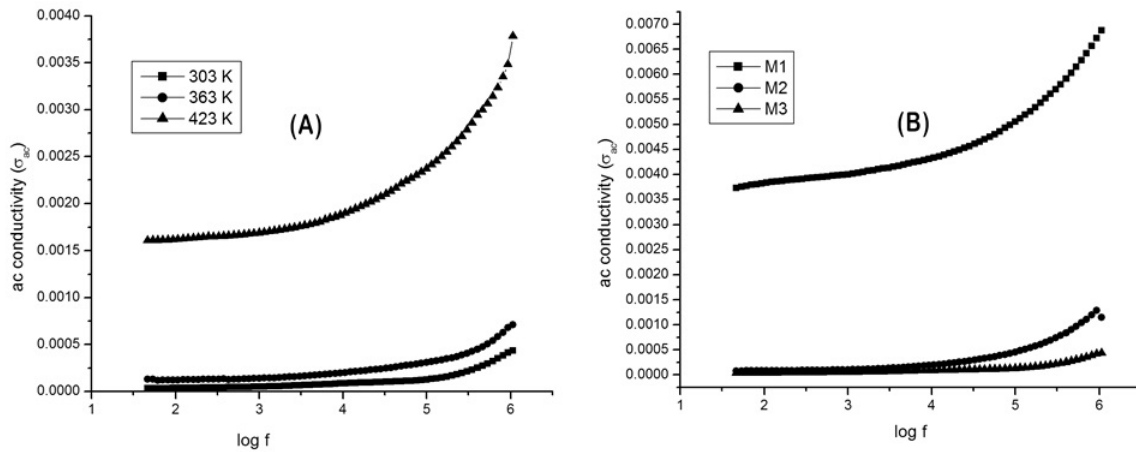


Fig. 3. The variation of a.c. electrical conductivity as a function of frequency

4. Conclusion

$MnWO_4$ nanoparticles with different average sizes were synthesized. The dielectric properties of $MnWO_4$ were determined as a function of frequency from 100 Hz to 10 MHz for temperatures ranging from 303 K to 423 K. At lower frequencies, ϵ' and $\tan\delta$ have higher values, while at higher frequencies, the values reach steady lower values. Similar variation was observed when the temperature was raised, but the values were shifted higher. Conductivity increased as frequency increased, conforming to small polaron hopping. The values were shifted upwards when the temperature was raised. The values of ϵ' , $\tan\delta$ and σ_{ac} showed considerable increase as the particle size was reduced.

Acknowledgements

The authors are grateful to KSCSTE, Thiruvananthapuram, Kerala and University Grants Commission (UGC), New Delhi for the financial support.

References

- [1] E. Traversa, Ceramic sensors for humidity detection: the state of the art and future developments. *Sens. Actuators B*, **23**, P. 135–156 (1995).
- [2] W. Qu, W. Wlodarski, J.U. Meyer, Comparative study on micromorphology and humidity sensitive properties of thin-film and thick film humidity sensors based on semiconducting $MnWO_4$. *Sens. Actuators B*, **64**, P. 76–82 (2000).
- [3] A.M.E. Suresh Raj, C. Mallika, O.M. Sreedharan, K.S. Nagaraja, MnO-manganese tungstate composite humidity sensors. *Mater. Lett.*, **53**, P. 316–320 (2002).
- [4] R. Bharati, R.A. Singh, B.M. Wanklyn, Electrical conduction in Manganese Tungstate. *J. Phys. Chem. Solids*, **43**, P. 641–644 (1982).
- [5] M.Jang, T.J.R. Weakley, K.M. Doxsee, Aqueous crystallization of Manganese (II) Group 6 Metal Oxides. *Chem. Mater.*, **13**, P. 519–525 (2001).

- [6] S.J. Chen, X.T. Chen, Z. Xue, J.H. Zhou, J. Li, Morphology control of MnWO_4 nanocrystals by a solvothermal route. *J. Mater. Chem.*, **13**, P. 1132–1135 (2003).
- [7] B. Parvatheeswara Rao, K.H. Rao, Electrical properties of nanocrystalline AlPO_4 . *J. Mater. Sci.*, **32**, P. 6049–6054 (1997).
- [8] C.M. Mo, L. Zhang, G. Wang, Characteristics of dielectric behavior in nanostructured materials Nanostruct. *Mater.*, **6**, P. 823–826 (1995).
- [9] T. Kar, R.N. Choudhary, S. Sharma, K.S. Singh, Structural and electrical properties of $\text{Ba}_2\text{Na}_3\text{RNb}_{10}\text{O}_{30}$ Ceramics. *Indian J. Phys.*, **73A**(4), P. 453–459 (1999).
- [10] B. Jiang, J.L. Peng, L.A. Busil, W.L. Zhong, Size effects on ferroelectricity of ultrafine particles of PbTiO_3 . *J. Appl. Phys.*, **87**(7), P. 3462–3467 (2000).
- [11] D. Ravinder, K. Vijayakumar, Dielectric behaviour of erbium substituted Mn–Zn ferrites. *Bull. Mater. Sci.*, **24**(5), P. 505–509 (2001).
- [12] S.N. Potty, M.A. Khader, Dielectric Properties of nanophase Ag_2HgI_4 and $\text{Ag}_2\text{HgI}_4\text{-Al}_2\text{O}_3$ nanocomposites. *Bull. Mater. Sci.*, **23**(5), P. 361–367 (2000).
- [13] J. Mathew, S. Kurien, S. Sebastian, K.C. George, Dielectric studies of nanocrystalline copper orthophosphate. *Ind. J. Phys.*, **78**(9), P. 947–950 (2004).
- [14] V. Murthy, K. Sobhanadri, Dielectric properties of some nickel-zinc ferrites at radio frequency. *Phys Status Solidi (a)*, **36**, P. K133 (1976).
- [15] M.A.K.L. Dissanayake, O.A. Ileperuma, P.A.G.D. Darmasena, AC conductivity of MnWO_4 . *J. Phys. Chem. Solids*, **50**, P. 359–361 (1989).
- [16] R. Shukla, Electrical properties of AgInTe_2 . *Ind. J. Pure Appl. Phys.*, **31**, P. 894–898 (1993).

STRUCTURAL PROPERTIES OF COBALT SUBSTITUTED BARIUM HEXAFERRITE NANOPARTICLES PREPARED BY A THERMAL TREATMENT METHOD

C. C. Chauhan¹, R. B. Jotania², K. R. Jotania³

¹Department of Physics, Institute of Technology, Nirma University, Ahmedabad 382 481, Gujarat, India

²Department of Physics, University School of Sciences, Gujarat University, Navrangpura Ahmedabad 380 009, Gujarat, India

³Department of Physics, Faculty of Science, The M. S. University of Baroda, Vadodara 390 002, Gujarat, India

chetumakwana@gmail.com, rbjotania@gmail.com, kanti.jotania@gmail.com

PACS 81.05.-t, 81.05.Zx, 81.07.b, 81.07.Wx, 81.40-z, 61.46.-W, 68.37.Hk

A series of M-type hexagonal ferrites with $\text{BaCo}_x\text{Fe}_{12-x}\text{O}_{19}$ ($x = 2.0, 3.0$) composition were synthesized using a simple heat treatment method. The aqueous solution, containing metal nitrates and polyvinyl pyrrolidone (PVP) as a capping agent was used to prepare M-type barium hexaferrite nanoparticles. The prepared hexaferrite particles were calcined at microwave frequency (2.45 GHz, power 900W, 5 min) as well as at 650 °C temperature. The structural properties of the samples were investigated using X-ray diffraction (XRD), Fourier transform infrared spectroscopy (FTIR) and scanning electron microscopy (SEM). XRD pattern shows the pure M-phase. The particle size of the powder prepared by this method ranged from 20 nm to 27 nm. The thermal properties of the sample were investigated by thermogravimetric Analysis (TGA), which confirmed the thermal stability of the barium hexaferrite sample prepared by the heat treatment method.

Keywords: capping agent, hexaferrite particles, thermal treatment.

1. Introduction

Hexaferrites are classified into six fundamental types: M, W, Y, X, Z and U on the basis of their chemical composition and crystal structure [1, 2]. The crystal structures of these different types of hexaferrites are very complex and can be considered as a superposition of T, R and S blocks along the hexagonal *c*-axis [3]. M-type barium hexaferrite is a very useful material as an absorber of electromagnetic radiation in the microwave region [4]. The molecular structure of M-type ferrite is made up of one R and one S block with an overlap of hexagonally and cubically packed layers. The crystal structure of $\text{BaFe}_{12}\text{O}_{19}$ is described as SRS^*R^* , where R is a three layer block ($\text{O}_4-\text{BaO}_3-\text{O}_4$) with composition $\text{BaFe}_6\text{O}_{11}^{2-}$ and S is a spinel like two layer block (O_4-O_4) with composition $\text{Fe}_6\text{O}_8^{2+}$. Here the asterisk (*) means the corresponding block has been turned 180 ° around the hexagonal *c*-axis. The O^{4-} and BaO^{3-} layers form a close packing. In this structure the smaller iron cations are distributed within five different kinds of sites (Three Octahedral — 12k, 2a, 4f₂, one tetrahedral — 4f and one pseudo tetrahedral trigonal bi pyramidal — 2b). The ordering of magnetic moments of Fe^{+3} ions and the strong super exchange interaction explain the excellent magnetic behaviour of these materials [5].

Barium hexaferrite is currently of technical interest because of its permanent magnetic property, high uniaxial magneto-crystalline anisotropy, saturation magnetization, excellent chemical stability and corrosion resistance [6, 7]. Recently, ceramic materials have been classified by their high resistivity and high permeability, resulting in their use in a number of applications, e.g. industry, technology, electronic devices, communication equipment, high density magnetic recording media, materials for permanent magnets and microwave devices [2, 8–12].

In the present work, barium hexaferrite nanoparticles were synthesized from an aqueous solution of metal nitrates, polyvinyl pyrrolidone and deionized water using a thermal treatment method. This method did not require the addition of other chemicals as surfactants, and had an advantage of simplicity, low cost, no byproducts and was environmentally benign. The structural and morphological characteristics of the prepared barium hexaferrite nanoparticles were studied to verify the particle size.

2. Sample Preparation

Barium hexaferrite particles were synthesized using metal nitrate precursors with polyvinyl pyrrolidone (PVP) as a capping agent and deionized water as the solvent. The aqueous solution of PVP was prepared by dissolving 3 g of PVP in 100 ml of deionized water. The mixture was heated at 70 °C for 2 hours then after 1.2 mmol iron nitrate and 0.1 mmol barium nitrate added in the solution (pH of solution was 1–2). The obtained solution was kept under constant magnetic stirring for 2 hours until a colourless transparent solution was obtained and then solution was heated at 80 °C for one hour to evaporate the water. The resulting orange solid dried powder was crushed for 15 min and heated at 650 °C for 3 hours in order to pyrolyze the organic compounds and crystallize the nanoparticles. The prepared barium hexaferrite particles were also calcined via microwave irradiation (2.45 GHz, 900 W, 5 min).

3. Experimental Techniques

Prepared barium hexaferrite samples were characterized using various experimental techniques to study structural properties and particle size. The structure and phase purity of $\text{BaCo}_x\text{Fe}_{12-x}\text{O}_{19}$ ($x = 2.0, 3.0$) samples were investigated on a Philips X-ray diffractometer (PW 1830) using $\text{CuK}\alpha$ radiation ($\lambda = 1.5405 \text{ \AA}$) with a scan rate of 0.02 degree/min. The room temperature infrared (IR) spectrum of $\text{BaCo}_2\text{Fe}_{10}\text{O}_{19}$ hexaferrite sample heated at 650 °C was recorded in the mid IR range (4000cm^{-1} to 400cm^{-1}) using a FTIR spectrophotometer (Bruker Tensor 27 Model). Scanning electron micrographs of prepared barium hexaferrite samples were obtained using a Make-Leo/Lica model Stereo scan 440 scanning electron microscope.

3.1. XRD Analysis

Fig. 1 shows the XRD patterns of $\text{BaCo}_x\text{Fe}_{12-x}\text{O}_{19}$ ($x = 2.0, 3.0$) hexaferrite samples calcined at 650 °C for 3 hours and heated with microwave irradiation. The XRD pattern of all samples showed pure M-phase. All samples exhibited quite similar XRD patterns. The average particle size of the M-type hexaferrite was calculated from the full width at the half maximum (FWHM) of the XRD patterns, using the well known Scherer formula:

$$d = 0.90 \frac{\lambda}{\beta \cos \theta}, \quad (1)$$

where d is the crystallite size (nm), β is the full width of the diffraction line at half of the maximum intensity measured in radians, λ is the X-ray wavelength of Cu $K\alpha = 0.154$ nm and θ is the Bragg angle.

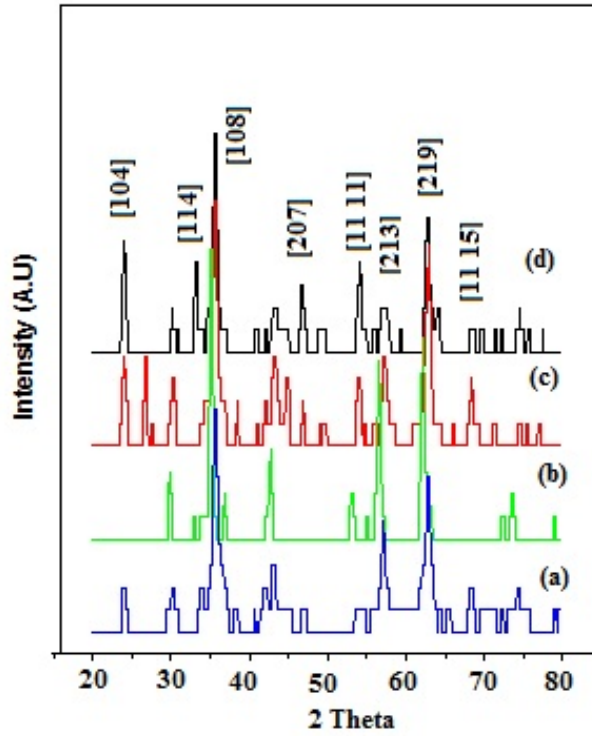


Fig. 1. X-ray diffraction pattern of (a) $\text{BaCo}_2\text{Fe}_{10}\text{O}_{19}$ calcinated at 650°C (b) $\text{BaCo}_2\text{Fe}_{10}\text{O}_{19}$ heated with microwave irradiation (c) $\text{BaCo}_3\text{Fe}_9\text{O}_{19}$ calcinated at 650°C and (d) $\text{BaCo}_3\text{Fe}_9\text{O}_{19}$ heated with microwave irradiation

Lattice constants a and c of hexagonal barium cobalt hexaferrites were calculated using Eq.(2):

$$\frac{1}{d} = \frac{4h^2 + k^2 + l^2}{3a^2} + \frac{l^2}{c^2}, \quad (2)$$

where h, k and l are Miller indices, d is inter planer distance. Lattice volume of all the samples can be obtained using Eq.(3):

$$V = \frac{\sqrt{3}}{2}a^2c \quad (3)$$

The cell volume was observed to increase with higher cobalt content (Table 1). The microwave heated samples showed small cell volume relative to conventionally-heated samples. It is seen from the table 1 that lattice parameters a and c were slightly decreased with increased cobalt content. The calculated values for lattice parameters a and c are in agreement with previous literature [13]. The cell volume changed little with varying cobalt content, as the ionic radius of both the ions are almost same ($\text{Co}^{+2} = 0.65 \text{ \AA}$ and $\text{Fe}^{+3} = 0.645 \text{ \AA}$).

Table 1. Structure Parameters a and c and cell volume V for hexaferrite samples

BaCo _x Fe _{12-x} O ₁₉ ($x = 2.0, 3.0$)	Heat treatment	a (nm)	c (nm)	c/a	Cell volume V (nm) ³
BaCo ₂ Fe ₁₀ O ₁₉	650 °C	0.550	2.3456	4.2647	1.291
BaCo ₂ Fe ₁₀ O ₁₉	Microwave	0.545	2.3780	4.3633	1.284
BaCo ₃ Fe ₉ O ₁₉	650 °C	0.548	2.3423	4.2742	1.36
BaCo ₃ Fe ₉ O ₁₉	Microwave	0.5445	2.3772	4.3658	1.294

Table 2. Crystalline Size from Debye Scherrer Formula

BaCo _x Fe _{12-x} O ₁₉ ($x = 2.0, 3.0$)	θ (degree)	Cos θ	β FWHM (rad)	Crystalline size d (nm)
BaCo ₂ Fe ₁₀ O ₁₉ (650 °C)	17.314	0.9546	0.0052	27.87
BaCo ₂ Fe ₁₀ O ₁₉ (microwave)	17.32	0.9546	0.0062	23.22
BaCo ₃ Fe ₉ O ₁₉ (650 °C)	17.171	0.9559	0.0061	23.89
BaCo ₃ Fe ₉ O ₁₉ (microwave)	17.22	0.9551	0.0068	20.89

3.2. FTIR Analysis

Figure 2 shows FTIR spectrum of BaCo₂Fe₁₀O₁₉ hexaferrite heated at 650 °C recorded in the mid IR range (4000 cm⁻¹ to 400 cm⁻¹). A few milligrams of BaCo₂Fe₁₀O₁₉ powder mixed with anhydrous KBr powder and made in the form of a pellet for measurement. The absorption bands at 2923.88 cm⁻¹ and 2151.35 cm⁻¹ were due to OH vibrations. The other bands are at 1445, 1427, 1415.5, and 858.26 cm⁻¹, corresponding to the stretching and bending vibrations of C=O, H-C-H, C-H and C-C respectively. The absorption bands between 544 and 468.57 cm⁻¹ assigned to the vibration of the bond between the oxygen atom and the metal ions (M-O), confirming the formation of hexaferrite [14]. The TGA curve of the dried precursor of BaCo₃Fe₉O₁₉ was recorded using a SII Differential Thermal analyzer Model No. SSC 5100 from 50 °C to 700 °C with a rate of 10 °C/min.

3.3. SEM Analysis

Fig. 3 (a-d) shows the SEM images of barium cobalt hexaferrite samples heated at 650 °C and microwave irradiation. The morphology and grain size are found to be porous, non-uniform and agglomerated in all samples, these agglomerations may be due to small particle size and the magnetic nature of the hexaferrite particles.

3.4. Thermogravimetric Analysis (TGA)

Figure 4 shows TGA curve of BaCo₃Fe₉O₁₉ precursor. TG curve shows three steps of weight loss. The first weight loss between 50 °C to 150 °C (~5 wt%) is due to the desorption of absorbed water molecules. In the second step, a sharp weight loss is observed between temperature of 150 °C to 200 °C (~57 wt%). In the third step, the weight loss is very less (~1.2 wt%) in the temperature range between 200 and 350 °C. These weight losses may be due to combustion of organic substances [14, 15]. There is no weight loss

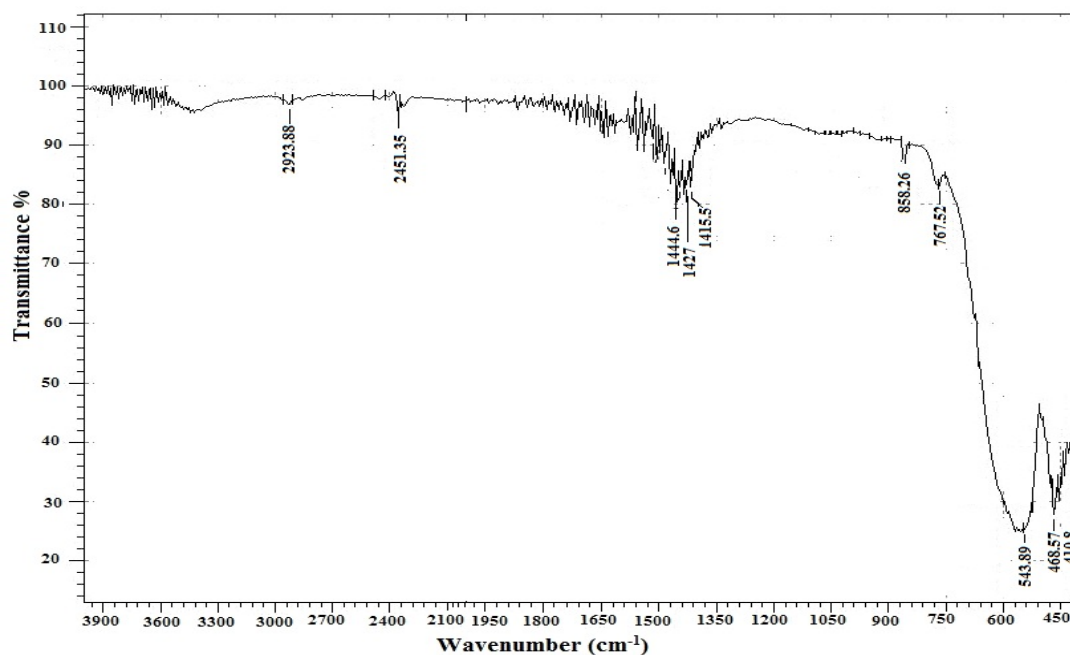


Fig. 2. FTIR spectra of $\text{BaCo}_2\text{Fe}_{10}\text{O}_{19}$ hexaferrite heated at 650°C

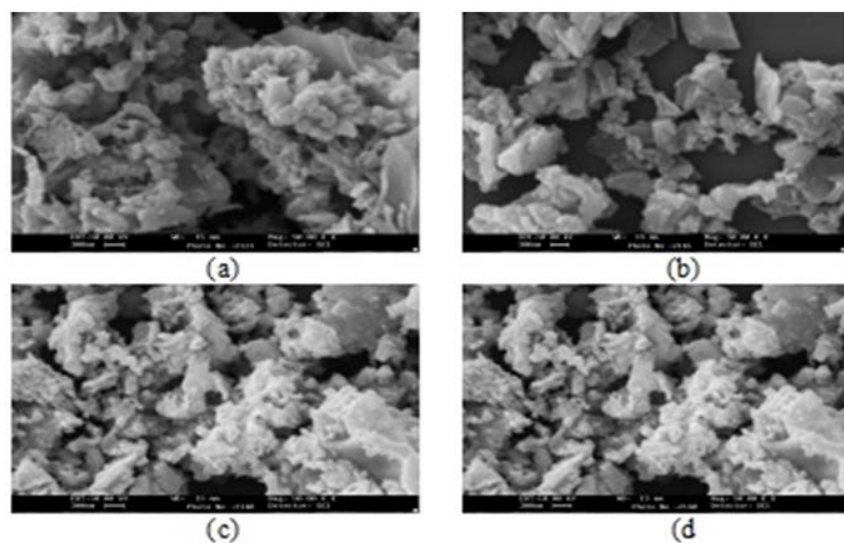


Fig. 3. SEM images of $\text{BaCo}_2\text{Fe}_{10}\text{O}_{19}$ (a) calcinated at 650°C (b) heated at microwave frequency, $\text{BaCo}_3\text{Fe}_9\text{O}_{19}$ (c) calcinated at 650°C and (d) heated at microwave frequency

above 305°C , which confirms the high thermal stability of the sample synthesized by a thermal treatment method.

4. Conclusion

M-type hexagonal ferrites $\text{BaCo}_x\text{Fe}_{12-x}\text{O}_{19}$ ($x = 2.0, 3.0$) were synthesized using a simple thermal treatment method. The samples were heated using a muffle furnace and a microwave oven. The observations from the XRD, SEM and TGA studies are summarized as follows:

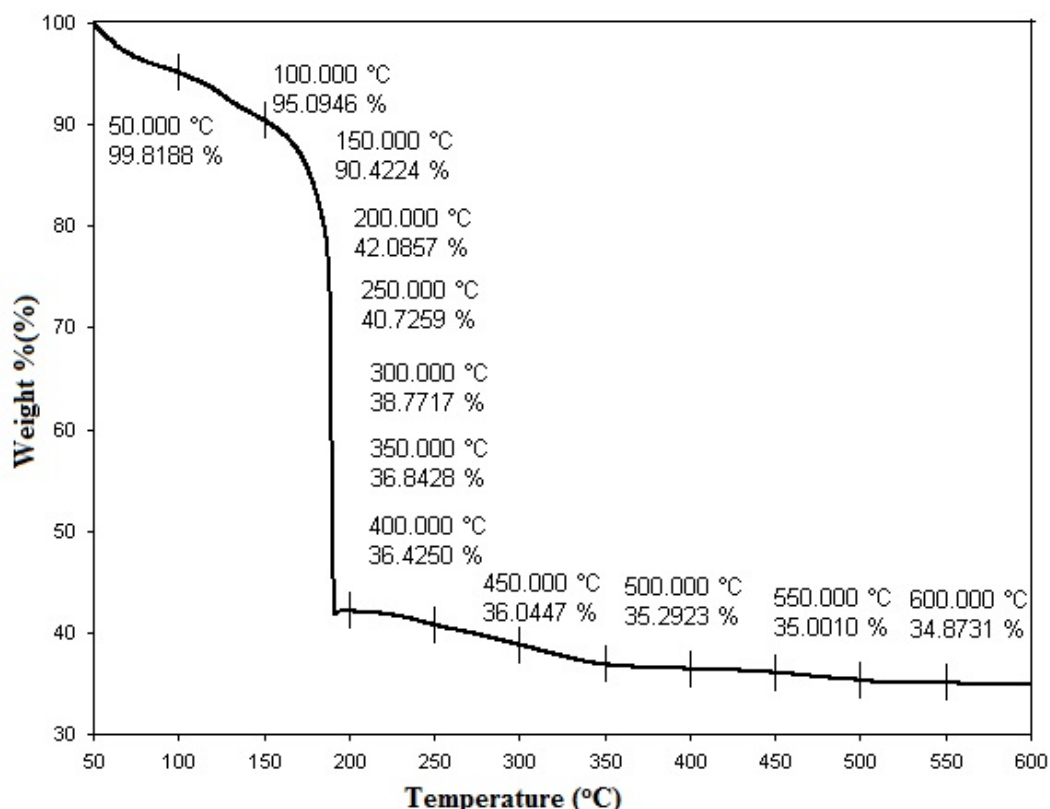


Fig. 4. TGA curve of $\text{BaCo}_3\text{Fe}_9\text{O}_{19}$ precursor

- I. XRD results confirm the formation of mono phase.
- II. SEM images confirm formation of agglomerated grains.
- III. Thermal stability of prepared barium-cobalt hexaferrite sample is high.

Acknowledgment

This work was carried out under DRS-SAP programme of UGC, Physics Department, Gujarat University, Navrangpura, Ahmedabad, India.

References

- [1] Salunkhe M.Y., Kulkarni, D.K. Structural, magnetic and microstructural study of $\text{Sr}_2\text{Ni}_2\text{Fe}_{12}\text{O}_{22}$. *J. Magn. Magn. Mater.*, **279**, P. 64–68 (2004).
- [2] Smit J., Wijn H.P.J., in: Ferrites, Philip's Tech. Library, New York (1959).
- [3] Zhang Haijun, Yao Xi, Zhang Liangying, The Preparation and microwave properties of $\text{BaZn}_{2-x}\text{Co}_2\text{Fe}_{16}\text{O}_{27}$ ferrite obtained by a sol-gel process, *Ceram. Int.*, **28**(1), p. 171–175 (2002).
- [4] Eugene P., et al., *Chem. Sustain. Dev.* **10**, P. 161 (2002).
- [5] Carp O., Barjega R., Segal E., Brezeanu M., *Thermo-chem. Acta*, P. 57–62 (1998).
- [6] Pullar R. C., Bhattacharya A. K., Crystallisation of hexagonal M-ferrite from a stoichiometric sol-gel precursor without formation of $\alpha - \text{Fe}_2\text{O}_4$ intermediate phase, *Mater. Lett.* **537**, P. 537–542 (2002).
- [7] Dho J., Lee E. K., Park J. Y., Hur N. H., Effects of the grain boundary on the coercivity of barium ferrite $\text{BaFe}_{12}\text{O}_{19}$, *J. Magn. Magn. Mater.*, **285**, P. 164–168 (2005).
- [8] Vishwanathan B., Murthy V. R. K., *Ferrite Materials; Science and Technology*. Narosa publishing house, New Delhi, U. P. (1990).
- [9] Snelling E. C., *Soft Ferrites/Properties and Application*, second ed. Butter Worths, London (1988).

- [10] Morisako A., Matsumoto M., Naoe M., The effect of oxygen gas pressure on Ba-ferrite sputtered films for perpendicular magnetic recording media, *IEEE Trans. Magn.*, **24**(6), P. 3024–3026 (1988).
- [11] Hylton T. L., Parker M. A., Ullah M., Coffey K. R., Umphress R., Haward J. K., Ba ferrite thin film media for high density longitudinal recording media, *J. Appl. Phys.*, **75**(10), P. 5960–5965 (1994).
- [12] Niesen T. P., M., de Guire, Deposition of ceramic thin films at low temperatures from aqueous solutions, *J. Electroceram.*, **6**, P. 169–207 (2001).
- [13] He H. Y., preheating effects on the particle size and anisotropy of M-type BaAl₂Fe₁₀O₁₉ powders prepared via sol gel method, *Advances in Natural and Applied Sciences*, **3**(1), P. 211–215 (2009).
- [14] Temuujin J. J., Aoyama M., Senna M., Masuko T., Ando C., Kishi, H. *J. Solid State Chem.*, **177**, P. 221 (2004).

PREPARATION AND ANTIMICROBIAL OBSERVATIONS OF ZINC DOPED NANOHYDROXYAPATITE

C. Deepa¹, A. Nishara Begum^{2*} and S. Aravindan³

¹Department of Physics, Vellalar College for Women (Autonomous), Erode-12

²Department of Physics, Chikkaiah Naicker College, Erode-4, Phone: +919443544946

³Department of Physics, Government Arts College (Autonomous), Salem-7

*anishara@yahoo.com

PACS 87.85.jc; 87.83.+a; 82.33.Ln; 61.46.Df; 68.37.Hk

Hydroxyapatite [$\text{Ca}_{10}(\text{PO}_4)_6(\text{OH})_2$, HAp] is the major constituents of bones and hard tissues in mammals. In the last few years, HAp nanoparticles have been used as an ideal tool for the transformation of human hard tissues due to their high biocompatibility and easy biodegradability. Currently, metals are widely used in orthopedics to increase the bioactivity of hydroxyapatite. Among these metals, zinc is an essential trace element present in human bones and teeth. It plays important roles in increasing osteoblast adhesion and alkaline phosphatase activity of bone cells. In the present study, different amounts of pure and ZnO (0% – 43%) doped nano Hydroxyapatite powders were synthesized by the sol-gel method. The properties of pure and Zn doped nHAp powders were characterized using X-ray diffraction (XRD), Scanning electron microscopy (SEM), and Energy dispersive X-ray analysis (EDAX). The results of X-ray diffraction studies revealed the progressive increase in the average crystallite size from 49 to 100 nm with increasing ZnO concentration found to be 49–100 nm. The in vitro antimicrobial activities of the synthesized pure and Zn-doped nHAp powders were investigated against gram-negative bacterial strains using the disc diffusion method. The antimicrobial activities of pure and doped nHAp samples were observed irrespective of the ZnO content.

Keywords: Nano hydroxyapatite, Zinc oxide, Antimicrobial.

1. Introduction

Recently, the development of hydroxyapatite [$\text{Ca}_{10}(\text{PO}_4)_6(\text{OH})_2$, HAp] with various additives has been one of the primary aims in the field of biomaterials, mainly to obtain superior quality materials suitable for use in artificial bone substitution. It is well known that, hydroxyapatite has a chemical similarity to the inorganic portion of human bone. The emerging trend of bone tissue engineering with hydroxyapatite has attracted intense interest due to its biofunctional properties, such as bioactivity and biocompatibility. Hap's properties such as morphology, stoichiometry, crystallinity and crystal size distribution (CSD) have great influence in the production of materials for biomedical applications. Hence, it is essential to optimize how these HAp properties are affected by different additives. Obviously, the incorporation of foreign elements can drastically alter the properties of HAp. It has already been demonstrated that introducing CO_3^{2-} and SiO_4^{4-} ions into the crystal lattice of HAp is effective at improving its degradation rate [1]. Since, the degradation rate of HAp plays a vital role in determining its biological performance, the inclusion of additives and their quantities attracts more significance.

Biological apatite is basically an impure form of Hap, but the non-stoichiometric HAp which incorporates a variety of trace ions such as Ca^{2+} , Mg^{2+} , Sr^{2+} , Ba^{2+} , Pb^{2+} , Zn^{2+} , Cu^{2+} , Na^+ , K^+ , Fe^{3+} , etc. is also useful to prepare the HAp with an atomic ratio (trace ion/P) of 1.5 – 1.67 [1], which is an essential requirement for it to become a biological apatite. The biological performance of HAp has been found to be improved with the incorporation of trace metal ions

such as zinc, silver and manganese, which exhibit their vibrant role in improving the biological ability of HAp during the additions [2]. Among the metal ions, zinc is one that is abundantly present as a trace element in bone minerals [3], in addition, zinc promotes the bone density and prevents bone loss [4].

The synthesis of nano biomaterials with a specific range of particle sizes, morphologies and chemical compositions has always been a challenge for researchers. In recent years, interest in the development of zinc oxide (ZnO) nano particles has been greatly increased, mainly because of their altered physical, chemical and biological properties. The development of nano HAp is more significant because of its specific affinity towards many adhesive proteins and its influence on bone cell differentiation and mineralization process. In orthopedics, post-surgical infections on implant materials is a major issue. The role of zinc like coatings on implant material is well documented to minimize bacterial adhesion. It is hoped that the incorporation of ZnO nanoparticles with a biomineral such as HAp can provide useful outcomes towards the development of anti-microbial requirements. In general, the anti-microbial activity of the zinc ion is involved in three major processes, e.g. protein deactivation, microbial membrane interaction and thereby structural change and permeability.

Recently, nano-sized particles have gained importance in biomedical fields, since the reduced size and surface activated particles are able to exhibit entirely new behaviors during dissolution and precipitation. Earlier reports [5] reveal the successful incorporation of metal ions with HAp, but they failed to demonstrate antimicrobial effects. The aim of this research is to synthesize zinc oxide doped nano-HAp powders and to examine their crystallinity, *in vitro* and plot antimicrobial activity against zinc oxide content.

2. Materials and Methods

Pure nano-HAp powders were prepared employing the sol-gel method with 0.55 M of calcium hydroxide $\text{Ca}(\text{OH})_2$ (95% SIGMA ALDRICH) and 0.33 M of di ammonium hydrogen phosphate $(\text{NH}_4)_2\text{HPO}_4$ (99% SIGMA ALDRICH) respectively, used as sources for calcium and phosphorous. $\text{Ca}(\text{OH})_2$ and $(\text{NH}_4)_2\text{HPO}_4$ were dissolved in 500 ml de-ionized water separately to obtain a stoichiometric molar ratio of 1.67. The pH of each aqueous solution was maintained at ~ 11 by the addition of ammonium hydroxide solution NH_4OH (99%, SIGMA ALDRICH) [6]. A gelatinous white precipitate was produced by the dropwise addition of $(\text{NH}_4)_2\text{HPO}_4$ solution to the vigorously stirred $\text{Ca}(\text{OH})_2$ solution at 333 K for an hour. Then, the precipitate was aged for 24 h at room temperature followed by washing three times with de-ionized water and dried in hot air oven at 423 K for 10 h. The dried powder was then milled using a mortar and pestle and finally calcined in an alumina crucible using a muffle furnace at 673 K for 5 h.

Nano-HAp samples with varying amounts of zinc oxide were synthesized using mixed aqueous solutions of prepared pure nano-HAp powder and zinc oxide. The dopants were used in the amount of 0, 10, 25, 50 and 75 wt. % (hereafter named as (a) Z_0H , (b) Z_{10}H , (c) Z_{25}H , (d) Z_{50}H and (e) Z_{75}H). The mixed solutions were stirred for an hour. The obtained suspensions were filtered and dried in a hot air oven at 373 K for 5 h. The resultant pure and ZnO doped nano-HAp powders were characterized by XRD and SEM-EDAX.

2.1. X-ray Diffraction (XRD)

X-ray diffraction (XRD) studies were used to observe the structural properties of prepared pure and zinc oxide-doped nano-HAp powders. The analyses were carried out using a PAN analytical X'PERT-PRO diffractometer with high intensity of $\text{CuK}\alpha$ (wavelength $\lambda = 1.54060 \text{ \AA}$) radiation. The diffraction spectra were recorded in the angle 2θ ranging from

10° to 90°. The average crystallite size of pure and ZnO doped HAp nano powders were calculated using the Debye-Scherrer's formula [7]

$$D = 0.9\lambda/\beta \cos \theta, \quad (1)$$

where D is the crystallite size in nanometers, λ is the wavelength of CuK α radiation (1.5406 Å), β is full width of the peak at half of the maximum (FWHM) and θ is the diffraction angle of the corresponding reflection. The unit cell volume (V) and lattice parameters a and c of pure and ZnO incorporated HAp nano powders are calculated using the equations (2 & 3).

$$V = 2.589a^2c, \quad (2)$$

$$1/d_{hkl}^2 = 4/3 [h^2 + hk + k^2] / a^2 + l^2/c^2, \quad (3)$$

where d is the crystallite size, h , k and l are miller indices of the plane, a and c are lattice constants.

2.2. Fourier Transform Infrared Spectroscopy (FTIR)

Fourier transform Infrared (FTIR) spectroscopy (PERKIN ELMAR; SPECTRUM RX1) was used to identify the elemental composition of pure and ZnO doped HAp nano powders. The FTIR spectra were obtained over the region from 400–4000 cm⁻¹ in pellet form for 1 mg powder samples mixed with 200 mg spectroscopic grade KBr.

2.3. Morphology and Elemental Analysis (SEM/EDAX)

The Scanning Electron Microscopy (SEM) was performed using a JEOL JSM 6390, SEI model to determine microstructure and particle size on the surface of nano-HAp powders. The elemental analyses on the surface of pure and doped nano-HAp powders were performed by Energy dispersive X-ray analysis.

2.4. Antimicrobial Activity

The antibacterial activity of the prepared nano-HAp samples was tested against the bacterial strain *Klebsiella pneumonia* (ATCC 13883) by the modified disc-diffusion method [8]. The bacterial species were cultured for 24 h at 310 K and thereafter, the growth inhibition zones around the disc were measured.

3. Results and Discussion

3.1. XRD Characterization

Figure 1 shows the XRD patterns of the pure and ZnO incorporated HAp samples. The observed diffraction peaks of all prepared samples ensured the emergence of calcium rich phosphate apatite phases by matching well with the peaks in the standard JCPDS data file (09-0432). The intensity of the diffraction peak of plane (211) of HAp increased with the ZnO content, mainly because of the preferential orientation of ZnO in the apatite crystal. The peak intensity of the ZnO-incorporated HAp peak, increased with increasing ZnO content. Therefore, the added zinc content was also involved in the formation of HAp. The measured crystallite size, lattice parameter values and unit cell volumes are shown in Table 1. These data confirm the emergence of apatite mineral on the nanometer scale. The measured average crystallite size and unit cell volume of the HAp increased with increasing ZnO content. Particularly, the cell parameter a gradually increased with ZnO while another parameter c fluctuated with the incorporation of ZnO above 25 wt%. According to Fuzeng Ren et al. [7], the lattice parameters

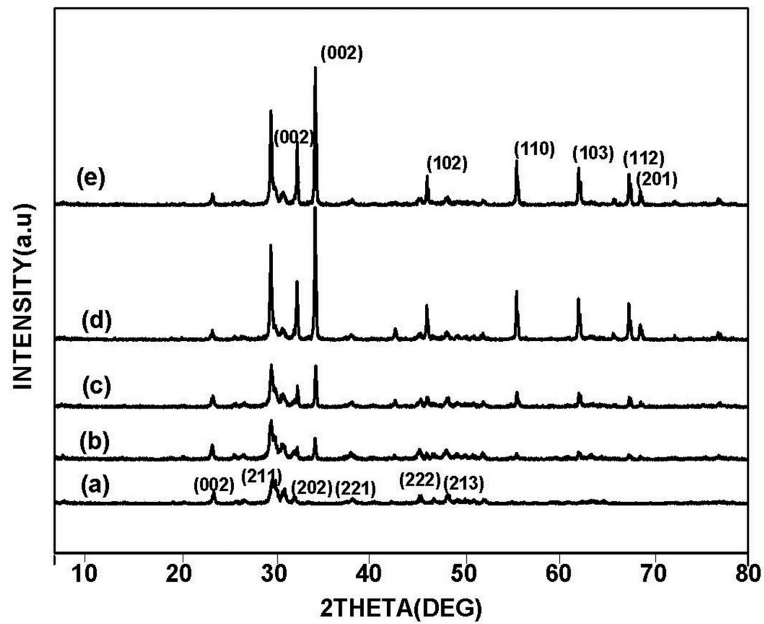


FIG. 1. XRD pattern of pure and Zn added HAP Samples
(a – Z₀H, b – Z₁₀H, c – Z₂₅H, d – Z₅₀H, e – Z₇₅H)

TABLE 1. Structural parameters of the zinc free and added HAP crystalline samples

Sample code	Average Crystallite Size D (nm)	Cell parameters		Unit cell volume V (Å) ³
		a (Å)	c (Å)	
Z ₀ H	49	9.4226	6.833	525
Z ₁₀ H	77	9.4225	6.8666	527
Z ₂₅ H	82	9.4395	6.8536	528
Z ₅₀ H	86	9.4561	6.8692	531
Z ₇₅ H	99	9.4901	6.864	535

a and c of crystalline HAP increased with the incorporation of ZnO. In addition, the substitution of H₂O in the lattice for OH sites in ZnO-doped HAP resulted in the increase of lattice parameter values [9].

3.2. Fourier Transforms Infrared Spectroscopy (FTIR) Analysis

The FTIR spectra of pure and ZnO-doped HAP nano powders synthesized by the sol-gel method are shown in Fig. 2. The FT-IR bands observed at 962 and 472 cm⁻¹ were assigned to symmetric stretching modes ν_1 and ν_2 of phosphate group. Peaks observed at 568 and 603 cm⁻¹ were assigned to ν_4 O-P-O bending bands corresponding to nano HAP. The ν_3 P-O asymmetric stretching mode was observed from 1041–1091 cm⁻¹. The bands observed at 3569 and 634 cm⁻¹ were due to the stretching vibration of hydroxyl groups. The peak observed at 1430 cm⁻¹ is a residue of atmospheric carbon dioxide present during the synthetic process. The bands at 3430 and 1637 cm⁻¹ in HAP were attributed to the presence of lattice water. Bands observed at 1430 and 1637 cm⁻¹ decreased with increasing ZnO content. According to FT-IR results, there is no obvious peak present for any other impurity [10].

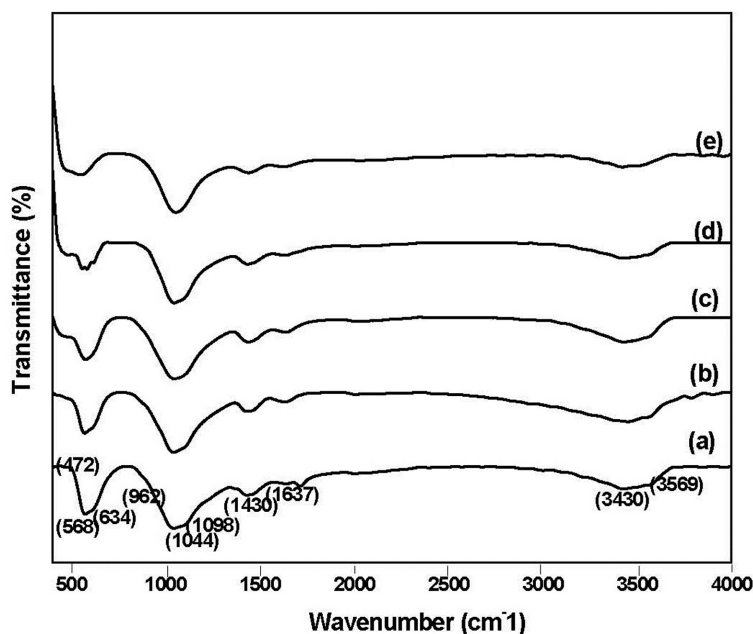


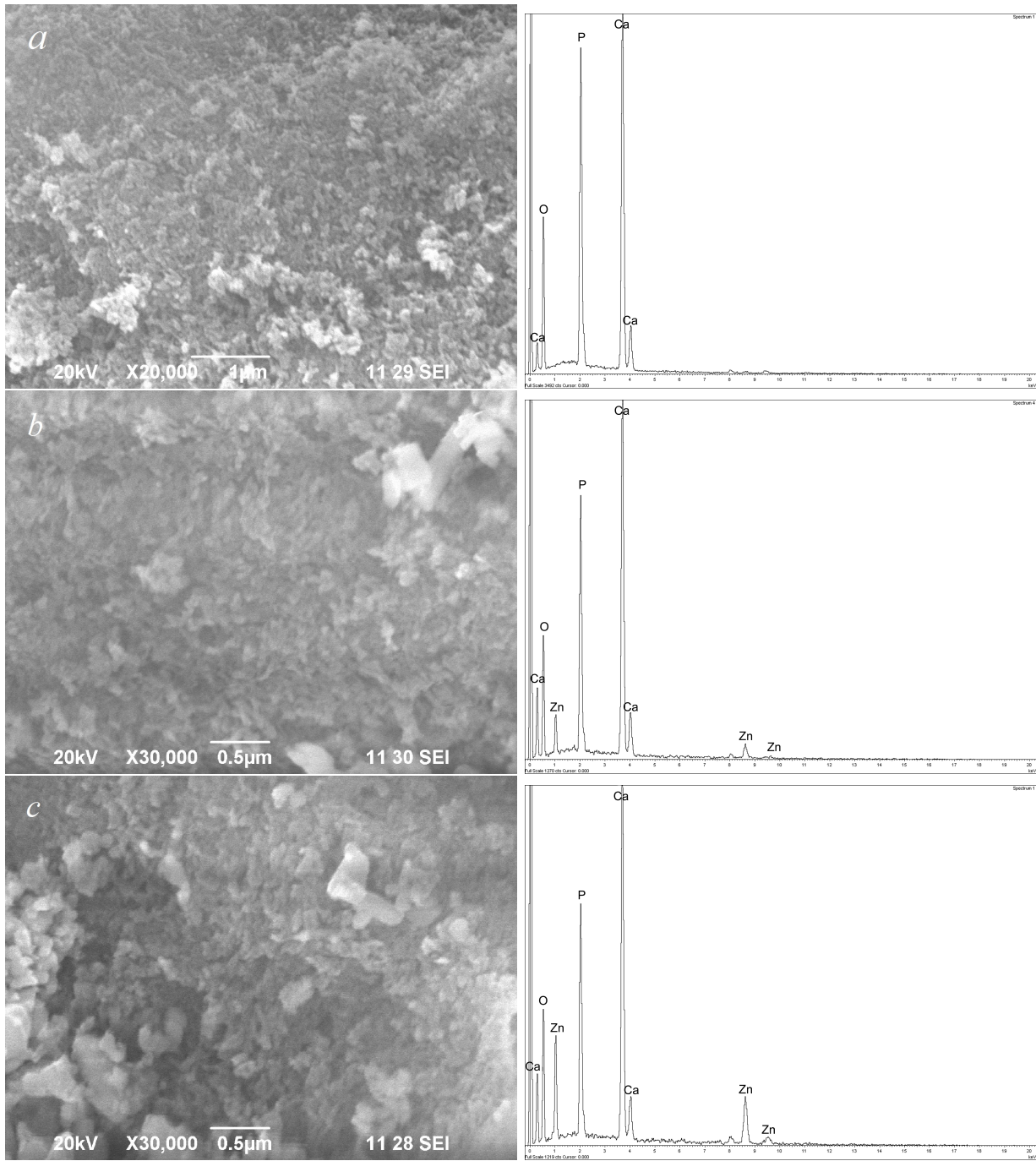
FIG. 2. FTIR spectra of pure and ZnO doped HAp nano powders (a – Z_0H , b – $Z_{10}H$, c – $Z_{25}H$, d – $Z_{50}H$, e – $Z_{75}H$)

3.3. SEM-EDAX Analysis

The morphologies and elemental analyses of pure and ZnO-doped nano-HAp samples were examined employing scanning electron microscopy (SEM) and energy dispersive X-ray (EDAX) analysis as shown in Fig. 3. The SEM micrographs revealed the emergence of rod-like crystalline species in ZnO-doped samples. The micrograph confirmed that particle sizes ranged from 49–67 nm with the incorporation of ZnO [10]. The result of elemental analysis (EDAX) of pure and ZnO-doped nano HAp confirmed the presence of Ca, P, O and Zn. The observed elemental concentration confirmed the Ca-P rich apatite crystalline phase. As expected, the elemental concentration of Zn was found to increase with increased ZnO content in HAp. The resultant Ca/P ratio of pure HAp was observed as 1.45, while in ZnO-incorporated samples, it increased up to the addition of 25 wt. % and decreases with further additions of ZnO to 75 wt. %.

3.4. Antimicrobial Activity

In vitro antibacterial activity of the synthesized pure and ZnO-incorporated nanoHAp samples were examined against Gram-negative *Klebsiella Pneumoniae* bacteria. Irrespective of the ZnO content, all the prepared HAp samples exhibited antimicrobial activity. The resultant data are shown in Table 2. These data revealed the influence ZnO had in decreasing the antimicrobial activity of the HAp as shown in Fig. 4. At 200 $\mu\text{g}/\text{ml}$, the sample Z_0H recorded the highest level of antimicrobial activity against *Klebsiella pneumoniae* by exhibiting the highest inhibition zone diameter. The zone diameter decreased with increased ZnO content, as shown in Fig. 5. It is obvious that the antibacterial property of apatite samples was dependent on the molecular structure of compound, the types of bacterial strains and the solvent used [11]. The incorporation of ZnO resulted in the formation of nano HAp with a modified structure and reduced antimicrobial activity.



See the figure's caption on the next page

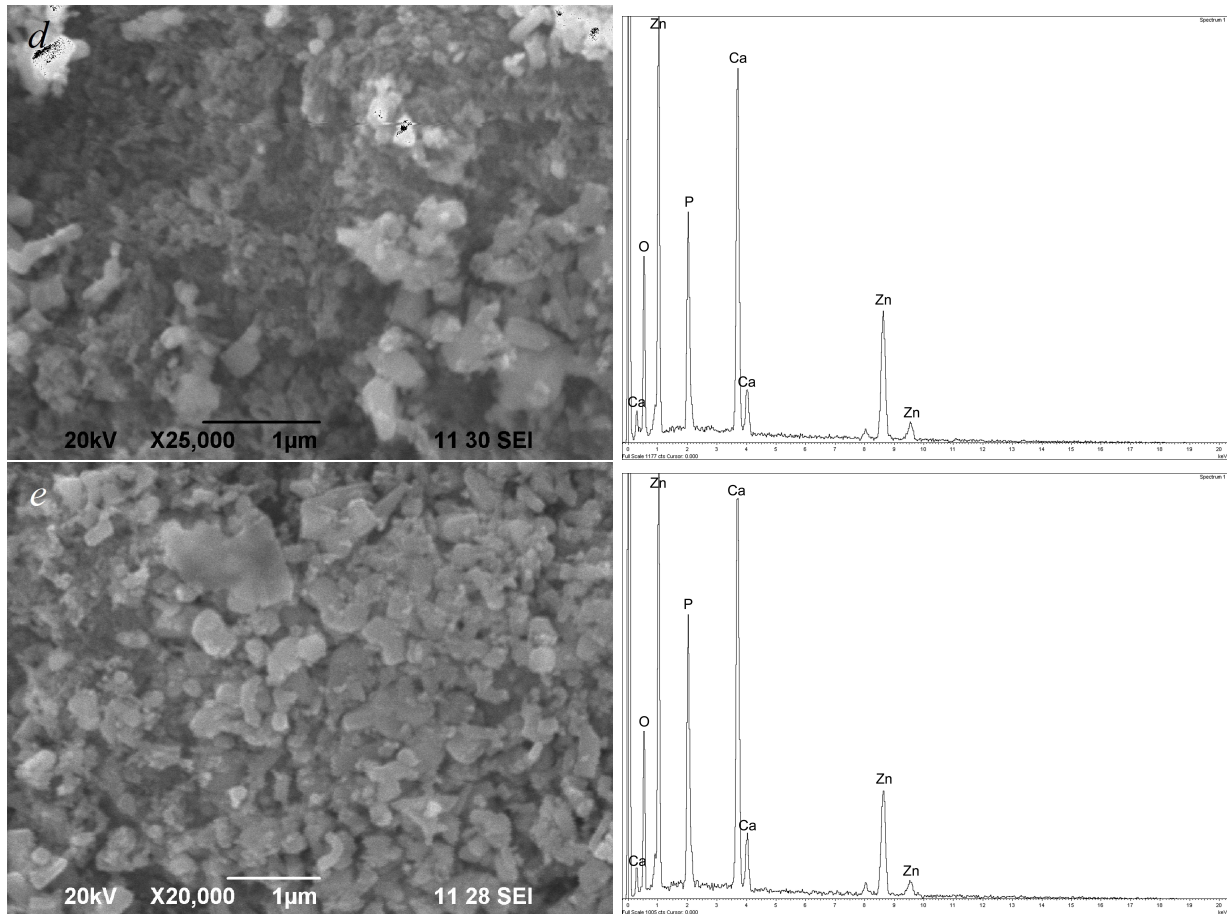


FIG. 3. SEM and EDAX images of Zinc free and added HAP samples (a – Z_0H , b – $Z_{10}H$, c – $Z_{25}H$, d – $Z_{50}H$, e – $Z_{75}H$)

TABLE 2. Antibacterial activity of pure and ZnO added nano HAP

Organism	Sample name (representation of Zone of inhibition (diameter in mm))				
	Z_0H	$Z_{10}H$	$Z_{25}H$	$Z_{50}H$	$Z_{75}H$
<i>Klebsiella pneumonia</i>	200 $\mu\text{g/ml}$	200 $\mu\text{g/ml}$	200 $\mu\text{g/ml}$	200 $\mu\text{g/ml}$	200 $\mu\text{g/ml}$
	15	14	12	12	11

4. Conclusions

Pure and ZnO-incorporated nano HAP samples were prepared employing the sol-gel method. The obtained XRD results confirmed the crystallite size of the samples in nanoscale. The influence of ZnO was used to increase the average crystallite size and unit cell volume of the Ca-P apatite crystal. The ZnO incorporations modified the morphology of HAP in rod like structure. Elemental analyses confirmed the emergence of calcium rich apatite crystalline phases. The *in vitro* antimicrobial activity of HAP was shown to be decreased by the addition of zinc oxide.

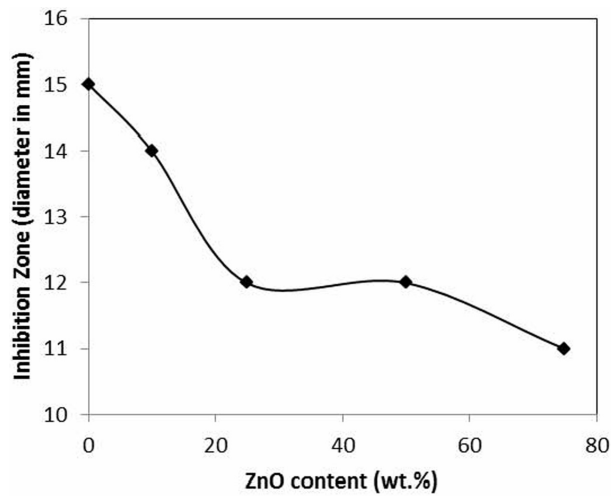
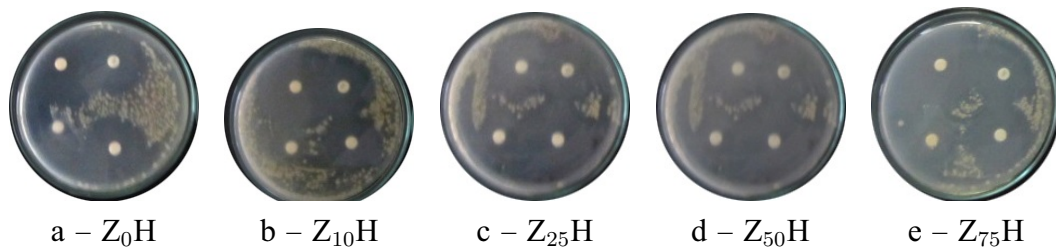


FIG. 4. Antimicrobial activity of HAp against ZnO additions

FIG. 5. Antibacterial activity of Pure and ZnO-HAp against *Klebsilla pneumonia*

References

- [1] D.G. Guo, Y. Wang, K. Han, W. Xu. Characterization, physico-chemical properties and biocompatibility of La-incorporated apatites. *Acta Biomaterialia*, **5**, P. 3512–3523 (2009).
- [2] G. Mestres, C. Le Van, M.-P. Ginebra. Silicon-Stabilized α -tricalcium phosphate and its use in a calcium phosphate cement: Characterization and cell response. *Acta Biomaterialia*, **8**, P. 1169–1179 (2012).
- [3] A. Ito, M. Otsuka, et al. Zinc-containing tricalcium phosphate and related materials for promoting bone formation. *Curr Appl phys*, **5**, P. 402-6 (2005).
- [4] R.Z. Legeros. Calcium phosphate-based materials containing Zinc, Magnesium, Fluoride and carbonate. US Patent 7, 419,680. September 2 (2008).
- [5] T.N. Kim, Q.L. Feng, et al. Antimicrobial effects of metal ions (Ag^+ , Cu^{2+} , Zn^{2+}) in hydroxyapatite. *J. Mater. Sci. Mater. Med.*, **9**, P. 129–134 (1998).
- [6] T.K. Anee, M. Ashok, M. Palinichamy, S. Narayana Kalkura. A novel technique to synthesize hydroxyapatite at low temperature. *Materials Chemistry and Physics*, **80**, P. 725–730 (2003).
- [7] F. Ren, R. Xin, X. Ge, Y. Leng. Characterization and structural analysis of zinc-substituted hydroxyapatites. *Acta Biomaterialia*, **5**, P. 3141–3149 (2009).
- [8] A.W. Baur, W.M.M. Kirby, J.C. Scherris, M. Turck. Antibiotic susceptibility testing by a standardized single disk method. *Amer. J. Cl. Pathol*, **45**, P. 493–496 (1966).
- [9] F. Miyaji, Y. Kono, Y. Suyama. Formation and structure of zinc-substituted calcium hydroxyapatite. *Mater. Res. Bull.*, **40**, P. 209–220 (2005).
- [10] M.H. Santos, Luiz Guilherme, Dias Heneine. Synthesis and Characterization of calcium phosphate/collagen biocomposites doped with Zn^{2+} . *Material Science and Engineering C*, **28**, P. 563–571 (2008).
- [11] A. Tripathi, S. Saravanan, S. Pattnaik. Bio composite scaffolds containing chitosan/nano-hydroxyapatite/nano-copper-zinc for bone tissue engineering. *International Journal of Biological Macromolecules*, **50**, P. 294–299 (2012).

DIELECTRIC WAVEGUIDE OPTIMIZATION FOR THE ENHANCEMENT OF TE-POLARIZATION TRANSMISSION OF PLASMONICS-BASED MSM-PD

Ayman Karar¹, Chee Leong Tan², Kamal Alameh^{1,4}, Yong Tak Lee^{2,3,4}

¹Electron Science Research Institute, Edith Cowan University, AU.

²School of Photonics Science, Gwangju Institute of Science and Technology (GIST),
Gwangju, Republic of Korea

³Department of Information and Communications, GIST, Republic of Korea.

⁴Department of Nanobio Materials and Electronics, World Class University (WCU),
GIST, Republic of Korea

a.karar@ecu.edu.au, ccheelong@gist.ac.kr, k.alameh@ecu.edu.au, ytleee@gist.ac.kr

PACS 42.25.Bs, 42.25.Ja, 73.50.Pz

In this paper, we use the finite difference time-domain (FDTD) method to optimize the TE-polarized light transmission of a metal-semiconductor-metal photodetector (MSM-PD) employing a dielectric waveguide on top of metal nano-gratings. Simulation results demonstrate that the funneling transmission of the TE-polarized light through the nanoslit of the MSM-PD structure is highly dependent on the structure geometries, such as the waveguide and nano-grating heights. We also demonstrate that adding a dielectric waveguide layer on top of the nano-metal gratings supports both the TM- and TE polarizations, and enhances the light transmission for TE-polarization around 3-times in comparison with conventional plasmonics MSM-PD structures.

Keywords: FDTD simulation, MSM-PD, waveguide, plasmonics, nano-gratings, surface plasmon.

1. Introduction

Metal-semiconductor-metal photodetectors (MSM-PDs) have several attractive features, such as high speed, ease of fabrication and monolithic integration with VLSI circuitry, which make them an excellent candidate for application in high-speed optical interconnects, high-speed sampling, and ultra-high speed optical fibre communications [1, 2]. For very high-speed applications, the MSM-PD is a better option than a p-i-n PD, since the real capacitance of the MSM-PD's interdigitated electrode geometry is much lower than that of a p-i-n PD of comparable size [3].

Typically, the speed of the MSM-PD is largely limited by the transit time of the photo-generated carriers. Scaling down the distance between the interdigital contacts and overall dimensions of the MSM-PD has been the most common way to increase the photodetector speed [4, 5]. By decreasing the spacing between the electrode fingers down to the optical diffraction limit, the response time could be reduced to tens of picoseconds [6]. However, the surface reflectivity and the shadowing effect of the metal fingers prevent conventional MSM-PDs from achieving external quantum efficiency greater than 50% for equal electrode width and spacing. This is due to the blocking of light by the detector's interdigitated finger structure.

Since Ebbesen et al. [7] reported extraordinary optical transmission (EOT) of periodic metal aperture arrays through surface plasmons, many efforts have been devoted

to exploring the EOT through metallic gratings [8, 9]. Later, it was demonstrated experimentally that the transmission of light through a sub-wavelength slit structure can be enhanced if the metal is patterned as nano-gratings, which enable the incident light to couple into surface plasmon polaritons (SPPs) propagating at the interface between metal and the air, thus focusing the light into the sub-wavelength slit [10, 11].

Recently, several MSM-PD structures, driven by TM-polarized light and based on nano-patterned metal fingers, have been reported to demonstrate substantial transmission enhancement through the excitation and guidance of SPPs into the photodetector slits [12, 13]. For example, the MSM-PD comprising Ag/GaAs nano-gratings reported by Collin et al. [14] exhibited a cut off frequency greater than 300 GHz and a quantum efficiency exceeding 50%. Lee et al. have reported a plasmonic metal photonic crystal (MPC) integrated on a quantum dot infrared photodetector demonstrating more than 2-times enhancement in detectivity [15].

Since there is no cut-off wavelength for the fundamental TM-polarized slit mode, it is possible to achieve extraordinary transmission with almost any sub-wavelength slit width. However, since the SPPs are TM-polarized mode, only the TM-polarization component of the incident light can be resonantly enhanced via transmission through the subwavelength slits. In this case, sub-wavelength slits act as polarization selector, which means that the penetration of the TE-polarized mode is suppressed. Furthermore, the TE-polarized mode intrinsically has a cut-off wavelength, making such MSM-PD structures polarization sensitive, and hence, less attractive for applications requiring polarization insensitive operation.

In this paper, we use the FDTD analysis to optimize a novel MSM-PD structure employing a dielectric thin layer waveguide deposited onto nano-patterned metal fingers. Our simulation results demonstrate 3-times enhancement in TE-polarized light transmission in comparison with conventional MSM-PDs.

2. Design of MSM-PD with enhanced TE-polarization transmission

Recently, a MSM-PD structure based on the deposition of a dielectric layer on top of metal fingers has been proposed by Nikitin et al. using the coupled mode method [16]. This was subsequently developed by Guillaumée et al., who experimentally demonstrated transmission enhancement for TE-polarized light through a subwavelength slit [17]. However, such a structure is sensitive to two parameters, namely, the height of the dielectric layer as well as the periodicity of the nano-patterned metal gratings, which were not fully optimised. In this paper, we investigate and optimize the key parameters of the dielectric-based MSM-PD structure, shown in Figure 1(a), to maximise the transmission of both the TE- and TM- polarized modes. The dielectric waveguide based MSM-PD structure consists of a subwavelength aperture of width X_w sandwiched between linear metal nano-gratings of heights h_g , and a period (Λ). The entire structure is grown on top of a semiconductor substrate. The metal contact is covered with a thin dielectric film with height h_{WG} . The presence of a thin dielectric layer on top of patterned metal gratings allows a TE-polarized incident light to couple to the dielectric waveguide modes and be guided towards the slit. At the same time, the extraordinary transmission of the TM-polarised light is maintained.

A 2D Finite Difference Time Domain (FDTD) software developed by Optiwave Inc was used to simulate the structure shown in Figure 1(a). A mesh step size of 10 nm was used in the simulation, with a time step satisfying the condition $\delta t < 0.1\delta_x/c$, where δ_x is the mesh size and c is the speed of light. This high-resolution sampling yielded solutions that converged at reasonable computation times. The excitation field was modeled as a

Gaussian-modulated continuous plane wave in the x-direction. The anisotropic perfectly matched layer (APML) boundary conditions were applied in both the x- and z- directions to accurately simulate the light reflected off both sides, as well as the light reflected off the top and bottom surface of the MSM-PD structure. In all the simulations, the light wave was normally incident on the top surface of the metal nano-gratings site. The gold (Au) dielectric permittivity was defined by the Lorentz-Drude model [3] and the refractive index for the dielectric layer was chosen to be 2.3, mainly to demonstrate the concept of TE-polarized light transmission enhancement.

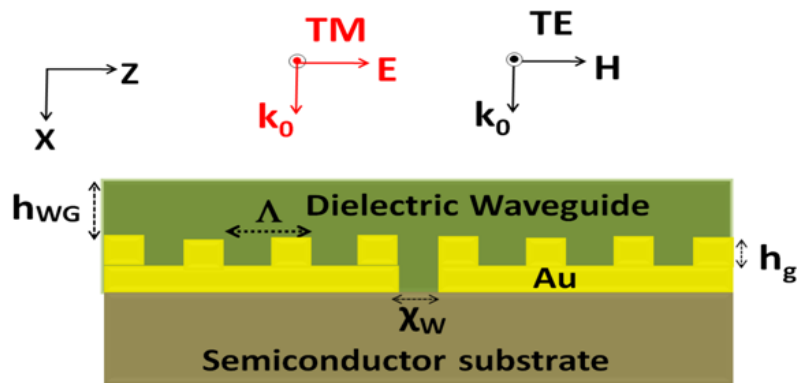
The TE and TM transmission spectra for two MSM-PD structures (without a dielectric waveguide), one with and the other without metal nano-gratings, are shown in Figure 1(b). An essential difference between the spectra for the TM- and TE- polarizations is already noticeable for a single slit without metal nano-gratings. While the TM-polarized mode spectra show interlaced maxima associated with the Fabry-Perot slit waveguide resonance, the TE-polarized mode resonance maxima display a rapid fall-off, due to the slit mode cut-off seen at longer wavelengths. No significant difference was noted in the TE-polarized mode transmission spectra for the structure with and without metal nano-gratings. However, the TM mode was resonantly enhanced by using the nano-gratings. Figure 1(c) shows the measured I-V characteristics for a nano-grating-patterned GaAs MSM-PD illuminated with 6.42 mW of laser power, for two input polarization states that correspond to the maximum, i.e. TM mode (dashed-dot), and minimum, i.e. TE mode (dashed), possible measured photocurrents, respectively. These results indirectly reveal the polarization dependent loss of the plasmonics-based MSM-PD device.

3. Results and discussion

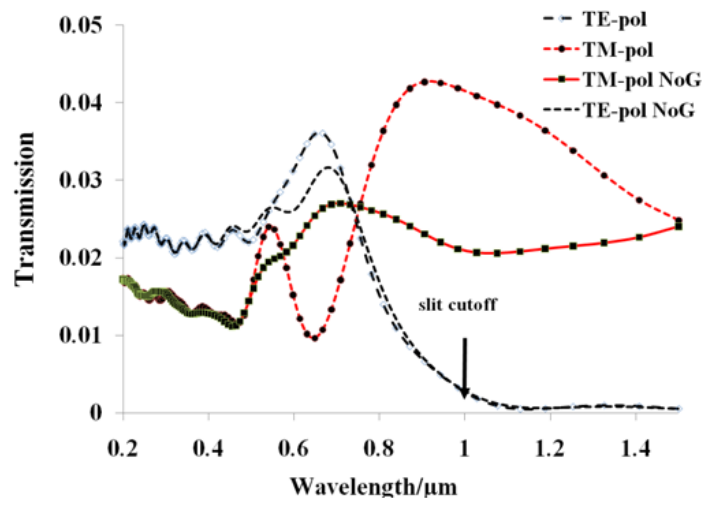
Several parameters of the dielectric-waveguide-based MSM-PD structure were optimized. These parameters are the nano-grating height, h_g , nano-grating period, Λ , waveguide height, h_{WG} , duty cycle of the nano-gratings. Each parameter was varied over a certain range of values, while all other parameters were kept constant. Initially, we used the structure shown in Figure 1(a) with metal nano-gratings to optimize the waveguide height h_{WG} . The dielectric waveguide height was varied, while keeping the subwavelength aperture width X_w and h_g constant at 430 nm and 200 nm, respectively. Moreover, the duty cycle, grating period and pitch number were kept at 0.5, 830 nm and 7, respectively.

Figure 2(a) illustrates the TE-polarized transmission spectra with no dielectric waveguide, 150 nm, 200 nm and 250 nm waveguide height. It is apparent from Figure 2(a) that the dielectric waveguide not only affects the amount of the light flux transmitted through the slit, but also the peak resonance wavelength. This indicates that the dielectric layer allows the incident light to resonantly couple to the metal nano-gratings. As seen from Figure 2(a), the resonance peak was highly dependent on the waveguide height and was red-shifted with increasing the waveguide height. Keeping the dielectric waveguide height at 200 nm and the other parameters constant, the simulated TE-polarized transmission spectra, shown in Figure 2(b), was evaluated for metal nano-grating height from 50 nm to 200 nm. As seen in Figure 2(b) while the metal nano-grating height affected the TE-polarized light transmission flux, it had no impact on the resonance wavelength. It was also noted that the transmission peak increases with decreasing the metal nano-grating height.

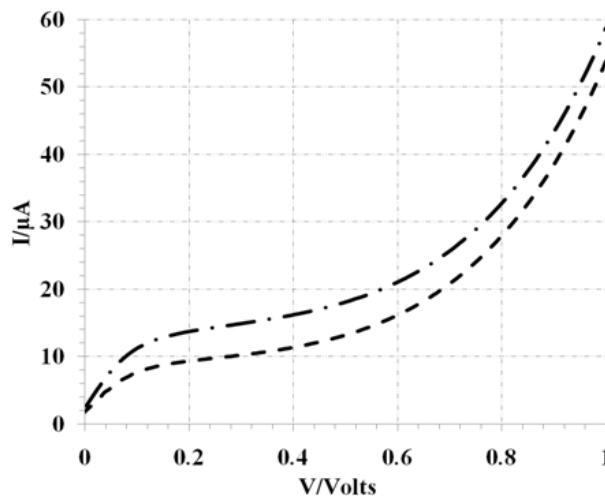
Figures 3(a and b) show the simulated TE-polarization transmission spectra for different metal nano-grating periods, and duty cycles, for a slit width of 430 nm, a nano-grating height of 50 nm and a dielectric waveguide height of 200 nm. The duty cycle



(a)

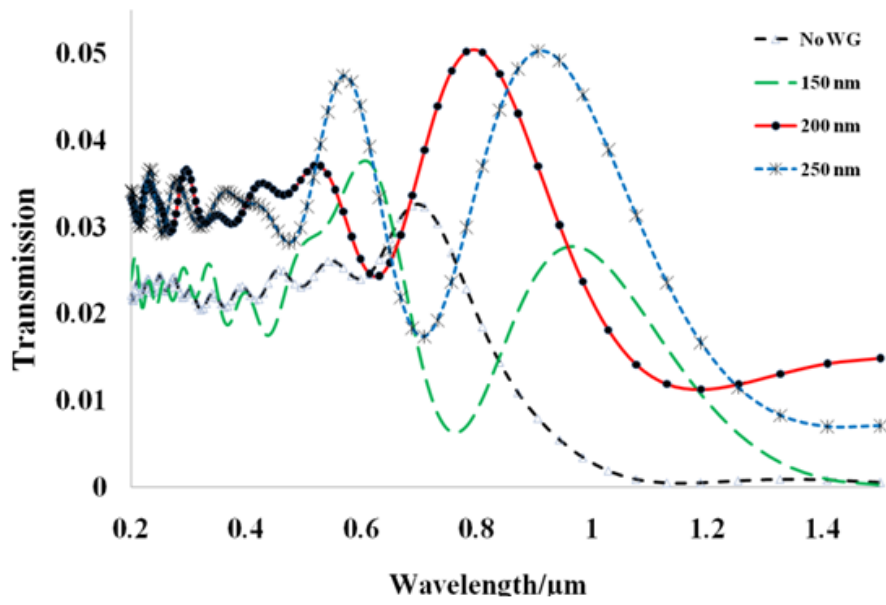


(b)

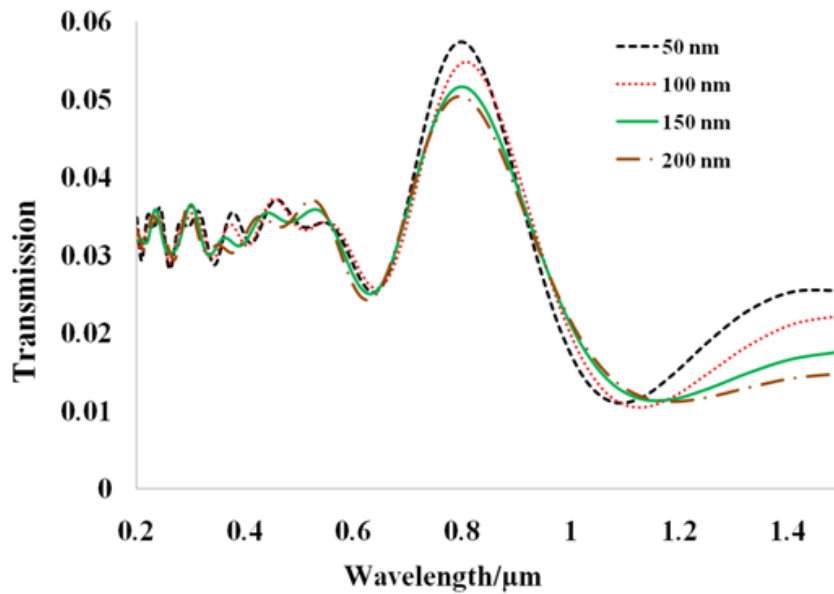


(c)

Fig. 1. **a)** 2-dimensional schematic of the dielectric-based MSM-PD structure, **b)** transmission spectra of two structures without dielectric waveguides, for fingers with and without metal nano-gratings, **c)** I-V characteristics of the MSM-PD with nano-gratings for TE- and TM-polarized input laser beams of power 6.42 mW

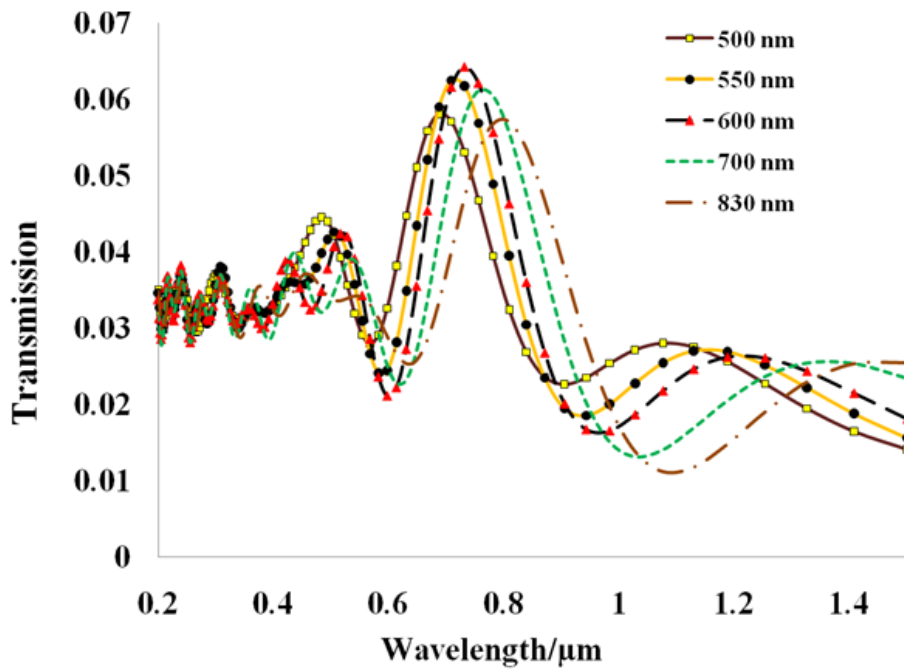


(a)

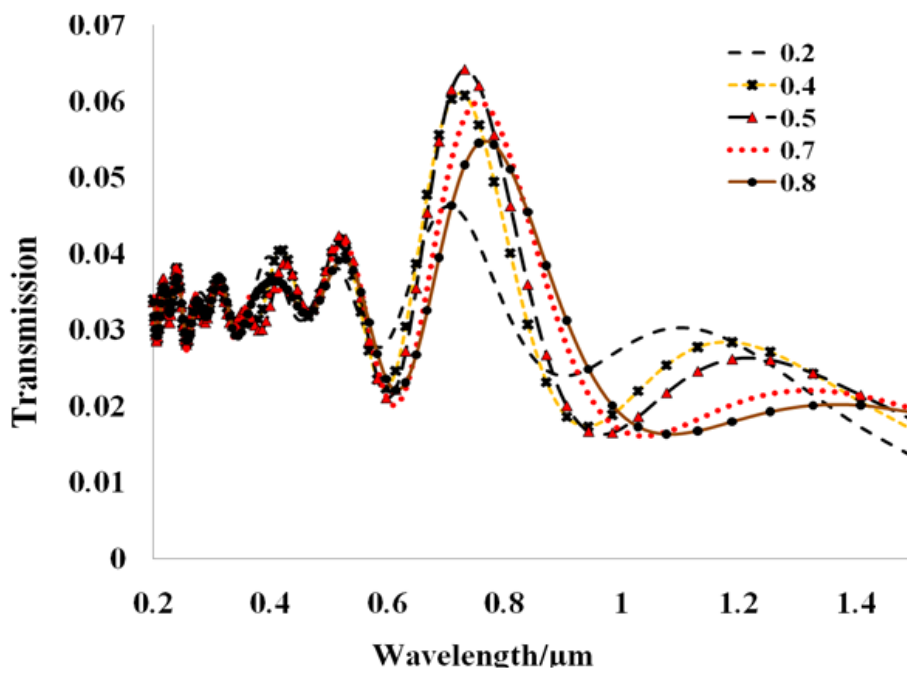


(b)

Fig. 2. Simulated TE-polarization transmission spectra for different **a)** dielectric waveguide height and, **b)** nano-grating height. The slit width was 430 nm



(a)



(b)

Fig. 3. Simulated TE-polarisation transmission spectra for different **a)** periodicity and, **b)** duty cycle with 430 nm slit width, 50 nm nano-grating height and 200 nm dielectric waveguide height

is defined as the ratio of the nano-grating line width to the period, Λ . It is seen from Figure 3(a) that the resonance peak of the TE-polarized light transmission was red-shifted when the periodicity increased. The maximum attainable transmission peak occurred at 730 nm for a nano-grating period of 600 nm. Figure 3(b) shows that the nano-grating duty cycle had a significant impact on both the transmission peak and the resonance wavelength, and that the resonance wavelength was red-shifted when the duty cycle increased, while the maximum transmission occurred when the duty cycle was 50%.

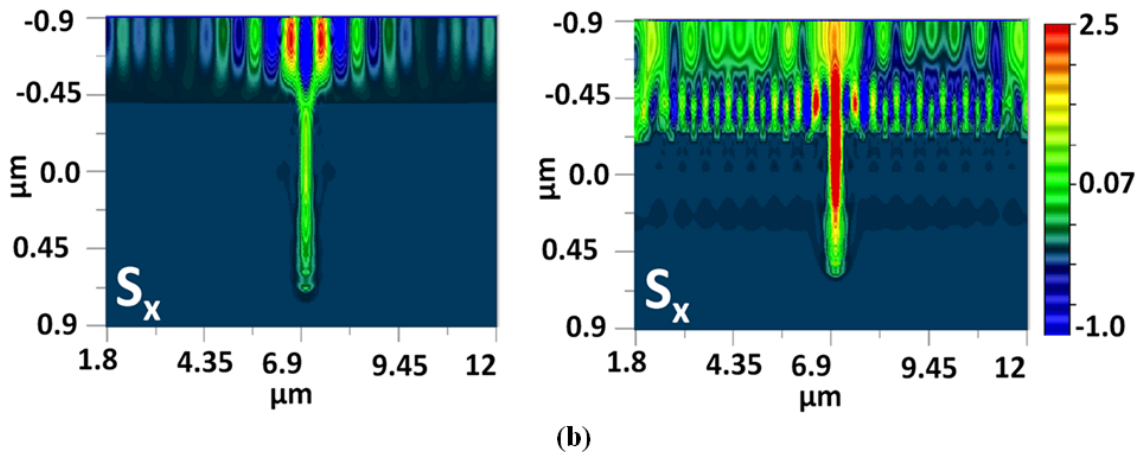
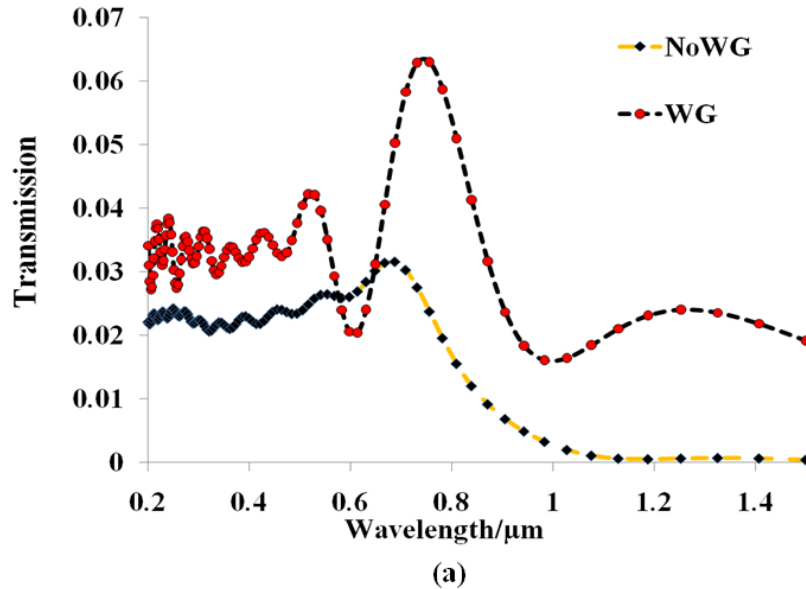


Fig. 4. **a)** Simulated TE-polarization transmission spectra and, **b)** simulated power distribution without (left) and with (right) dielectric waveguide

The TE-polarized light transmission spectra are shown in Figure 4(a), for two optimized MSM-PDs with and without a dielectric waveguide (WG). From these spectra it is obvious that the dielectric waveguide on top of the metal nano-gratings significantly enhanced the TE-polarized light transmission, compared with the conventional MSM-PD device without a dielectric waveguide (NoWG). The resonance wavelength (corresponding to the highest transmission) was 755nm for $\Lambda = 600$ nm and the transmission enhancement was almost 3-times that of a conventional MSM-PD device without a dielectric waveguide.

Moreover, as seen in Figure 4(a), the cut-off wavelength was increased when the slit was filled with the dielectric. The simulated S_x poynting vectors, i.e. energy flowing along the x direction, are shown in Figures 4(b), for the MSM-PD without (left) and with (right) a dielectric waveguide. It is worthwhile noting that for an MSM-PD without a dielectric waveguide, the power transmitted into the active area of the semiconductor is insignificant, compared with the power transmitted for an MSM-PD with a dielectric waveguide.

4. Conclusions

The finite difference time-domain (FDTD) method has been used to optimize the TE-polarized light transmission of a metal-semiconductor-metal photodetector (MSM-PD) employing a dielectric waveguide and metal nano-gratings. Simulation results have confirmed the dependence of the TE-polarized light through the MSM-PD nanoslit of the structure on the metal nano-grating height and dielectric waveguide height. Three-fold enhancement of TE-polarized light transmission has been demonstrated through MDM-PD parameter optimization.

Acknowledgements

We acknowledge the support of Edith Cowan University and the World-Class University Program funded by the Ministry of Education, Science, and Technology through the National Research Foundation of Korea (R31-10026).

References

- [1] Soole, J. and Schumacher, H., InGaAs Metal-Semiconductor-Metal Photodetectors for Long Wavelength Optical Communications. *IEEE J. Q. Elec.*, **27**(3), P. 737–752 (1991).
- [2] Liu, M.Y. and Chou, S.Y., Internal emission metal-semiconductor-metal photodetectors on Si and GaAs for 1.3 μm detection. *Appl. Phys. Lett.*, **66**, P. 2673–2675 (1995).
- [3] Rogers, D. L., Integrated Optical Receivers using MSM Detectors. *J. Lightwave. Technol.*, **9**(Dec.), (1991).
- [4] Averine, S., Chan, Y. C., and Lam, Y. L., Geometry optimization of interdigitated Schottky-barrier metal–semiconductor–metal photodiode structures. *Solid-State Electron.*, **45**(Mar.), P. 441–446 (2001).
- [5] Burm, J., Litvin, K. I., Schaff, W. J., and Eastman, L. F., Optimization of high-speed metal-semiconductor-metal photodetectors. *IEEE Photon. Technol. Lett.*, **6**, P. 722–724 (1994).
- [6] Chou, S. Y., Liu, Y., and Fischer, P. B., Fabrication of sub-50 nm finger spacing and width high-speed metal-semiconductor-metal photodetectors using high-resolution electron beam lithography and molecular beam epitaxy. *J. Vac. Sci. Technol*, **9**(Nov.), P. 2920–2924 (1991).
- [7] Ebbesen, T. W., Lezec, H. J., Ghaemi, H. F., Thio, T., and Wolff, P. A., Extraordinary optical transmission through sub-wavelength hole arrays. *Nature*, **391**(Feb. 12), P. 667–669 (1998).
- [8] Martín-Moreno, L., García-Vidal, F. J., Lezec, H. J., Degiron, A., and Ebbesen, T. W., Theory of Highly Directional Emission from a Single Subwavelength Aperture Surrounded by Surface Corrugations. *Phys. Rev. Lett.*, **90**(25 Apr.), P. 167401 (2003).
- [9] Sondergaard, T., Bozhevolnyi, S. I., Novikov, S. M., Beermann, J., Devaux, E., and Ebbesen, T. W., Extraordinary optical transmission enhanced by nanofocusing. *Nano Lett.*, **10**(Aug. 11), P. 3123–8 (2010).
- [10] Shackelford, J. A., Grote, R., Currie, M., Spanier, J. E., and Nabet, B., Integrated plasmonic lens photodetector. *Appl. Phys. Lett.*, **94**(Feb. 23), P. 083501, P. 1–3 (2009).
- [11] Dunbar, L. A., Guillaume, M., Len-Prez, F. D., Santschi, C., Grenet, E., Eckert, R., Lopez-Tejiera, F., Garca-Vidal, F. J., Martín-Moreno, L., and Stanley, R. P., Enhanced transmission from a single subwavelength slit aperture surrounded by grooves on a standard detector. *Appl. Phys. Lett.*, **95**(9 Jul.), P. 011113 (2009).
- [12] Karar, A., Das, N., Tan, C.L., Alameh, K., Lee, Y.T., and Karouta, F., High-responsivity plasmonics-based GaAs metal-semiconductor-metal photodetectors. *Appl. Phys. Lett.*, **99**, P. 33112–33112 (2011).

- [13] Ren. F.F., Ang. K.W., Ye. J, Yu., M, Lo. G.Q., and Kwong. D.L., Split Bull's Eye Shaped Aluminum Antenna for Plasmon-Enhanced Nanometer Scale Germanium Photodetector. *Nano Lett.*, **11**, P. 1289-93 (2011).
- [14] Collin. S., Fabrice. P., Teissier. R., and Pelouard. J.-L., Efficient light absorption in metal-semiconductor-metal nanostructures. *Appl. Phys. Lett.*, **85**(Jul.), P. 194-196 (2004).
- [15] Lee. S. C., Krishna. S., and Brueck. S. R. J., Light direction-dependent plasmonic enhancement in quantum dot infrared photodetectors. *Appl. Phys. Lett.*, **97**(Jul. 12), P. 021112 (2010).
- [16] Nikitin. A.Yu., Garcia-Vidal. F.J., and Martin-Moreno. L., Enhanced optical transmission, beaming and focusing through a subwavelength slit under excitation of dielectric waveguide modes. *J. Opt. A: Pure Appl. Opt.*, **11** (2009).
- [17] Guillaume. M., Nikitin. A. Yu., Klein. M.J.K., Dunbar. L.A., Spassov. V., Eckert. R., Martn-Moreno. L., Garca-Vidal. F.J. and Stanley. R.P., Observation of enhanced transmission for s-polarized light through a subwavelength slit. *Opt. Express*, **18**(9), P. 9722-9727 (2010).

SILVER-NANOPARTICLE-BASED ETCH MASK CONTROL FOR SUBWAVELENGTH STRUCTURE DEVELOPMENT

Nazme Moushumi¹, Kamal Alameh^{1,2}, V. Rajendran³, Yong Tak Lee²

¹Electron Science Research Institute, Edith Cowan University, 270 Joondalup Dr, Joondalup, WA 6027, Australia

²Department of Nanobio Materials and Electronics, Gwangju Institute of Science and Technology, World-Class University (WCU), Gwangju Institute of Science & Technology (GIST), Gwangju 500–712, South Korea

³Centre for Nano Science and Technology, K S R College of Technology, K S R Kalvi Nagar, Tiruchengode - 637 215, Namakkal (Dt.), Tamil Nadu, India
nmoushum@our.ecu.edu.au, veerajendran@gmail.com

In this paper, we investigate the impact of silver thin film thickness and annealing temperatures for the fabrication of silver nano-particles of controlled size and spacing distributions. We also use these measured distributions to predict the performance of subwavelength grating structures developed using dry and isotropic etching of semiconductor substrates. Silver (Ag) thin films of different thicknesses were deposited on Si and GaAs semiconductor substrates and annealed at different temperatures. Experimental results demonstrate that by annealing the Ag thin films with different temperature profiles it is feasible to develop Ag nanoparticles of an average diameter ranging from 50 nm to 400 nm on silicon substrates and 100 nm to 500 nm on GaAs substrates.

In addition, different subwavelength structures developed by etching the Ag nanoparticle deposited Si and GaAs substrates are simulated using a Finite-Difference Time Domain (FDTD) software package. Simulation results show that substantial reduction in light reflection can be achieved by optimizing the heights of the subwavelength structures through the control of the etching process time.

Keywords: Subwavelength gratings (SWG), nanoparticles, nano-structures, solar cells, reflection loss, Finite Difference Time Domain (FDTD) simulation.

1. Introduction

Multilayered thin film coatings have been used extensively in a wide range of applications to realize antireflection (AR) properties that suppress reflection losses. However, the issues of thermal mismatch between the various layer materials of AR coatings makes their AR property unstable, thus limiting their bandwidth and practicality. On the other hand, subwavelength grating (SWG) structures have gained enormous interest recently, mainly in the field of photovoltaics due to several interesting advantages. For example, integrating a SWG onto the top surface of a solar cell device provides an almost a lossless reflecting surface that enhances the solar cell's efficiency [1]. A SWG often takes a one- and/or two-dimensional periodic form. If the pitch (or period) of a single grating structure is less than the wavelength of the incident light, it behaves like an homogeneous medium with an effective refractive index [1]. Thus, SWG structures give gradual changes in the refractive index assuring an excellent antireflective medium along with a light trapping phenomena in comparison to the planar thin films [2–4]. A nanorod structure acts as a single layer AR coating, while triangular (conical) and parabolic shaped grating structures are more advantageous since they behave like a multilayer broadband AR coating [2].

In this paper, we describe annealing approaches for controlling the size and spacing of silver nanoparticles that act as etch masks for the development of low-reflectivity sub-wavelength structures. Silver nanoparticles formed onto Si or GaAs substrates by thermal annealing enable conical shaped SWG structures to be realized through dry etching. Results show several silver (Ag) thin films of thicknesses 10nm, 8nm and 5nm deposited on GaAs and Si substrates and annealed at different temperatures, leading to the development of randomly distributed silver nanoparticles on the surface of each sample. The diameters and spacing of the Ag nanoparticles are controlled by varying the annealing temperature and film thickness, leading etch masks tailored for different profiles, which can be used in conjunction with etching processes for the realization of SWG structures of various characteristics. FDTD simulation of the SWG structures confirms that much lower anti reflection can be attained in comparison with non-patterned semiconductor substrates.

2. Theoretical Background and Experimental results

The use of SWG structures was inspired by a natural model, moth's eyes. The surface of a moth's eye is covered with a nano-structured film that absorbs most of the incident light with minimal reflection. The nano-structured film, which consists of a hexagonal bump pattern, is 200 nm high and acts as an AR coating because the bumps are smaller than the wavelength of visible light. The refractive index between the air and the surface changes gradually, in which case the reflection of the light is also decreased. This model is being applied in solar cells to increase the cell conversion efficiency by allowing large amount of electromagnetic waves to reach the embedded charge carrier zone [4].

However, in order to develop practical SWG structures, several issues must be overcome, including (i) optimising the SWG pattern to maximise the AR property for each application, (ii) the ability to fabricate uniform patterns with appropriate shapes, such as conical, triangular or parabolic and (iii) develop such patterns over large areas cost-effectively.

Two main methods have been reported for the fabrication of SWGs, namely, the lenslike shape transfer process and the Ag nanoparticle process. The lenslike shape transfer method employs laser interference lithography (LIL) in conjunction with thermal reflow, which lead to pattern transfer. This approach requires long photolithography processes and is practical for small-area devices. On the other hand, dry etch processes based on thermally dewetted Ag nanoparticles have been used for the development of large-area SWGs. While this approach is cost effective, it yields SWGs with random shape and spacing, as well as non-optimized antireflection properties. However, if the distribution of the shape and spacing can be controlled, the attained AR properties can still be much better than non-patterned semiconductor surfaces.

2.1. Antireflective coating and SWG structure

The etching of Si or GaAs substrates on which Ag nanoparticles are embedded, results in the formation of SWGs which act as antireflective coatings that enhance the transmission through the substrates. As mentioned earlier, minimum reflection can be obtained through multilayer thin-film coatings [1], however, in addition to their complex fabrication process [1–3], such optical coatings have practical drawbacks, such as adhesion and material mismatching, making the thin-film mechanically unstable and susceptible to thermal fluctuations.

For the rectangular-shaped grating structure shown in Fig. 1, the refractive index changes very sharply from air ($n = 1$) to the grating zone or structure (approximately 2.5 at TM mode) [1]. The reflection loss can be calculated easily using Fresnel's equation:

$$R = \left(\frac{n_2 - n_1}{n_2 + n_1} \right)^2 \quad (1)$$

where n_1 is the refractive index of first medium and n_2 is the refractive index of second medium. The total reflection of a SWG structure can be calculated using the following equation:

$$R_{total} = R_1 + R_2 \quad (2)$$

Where R_1 is the reflection at the interface of air and grating structure and R_2 is the reflection at the interface of the grating structure and substrate.

If the SWG structure has a shorter period than the wavelength of the incident light, then it acts as an homogeneous medium with an effective refractive index [3]. According to Fig. 1, the refractive index of a rectangular-shaped SWG structure changes suddenly at the air-SWG interface, however, for the conical shaped SWG structure, the effective refractive index changes gradually, resulting in lower reflection [3]. For a parabolic-shaped SWG structure, the reflection can be as low as 5% over the entire solar spectrum [1].

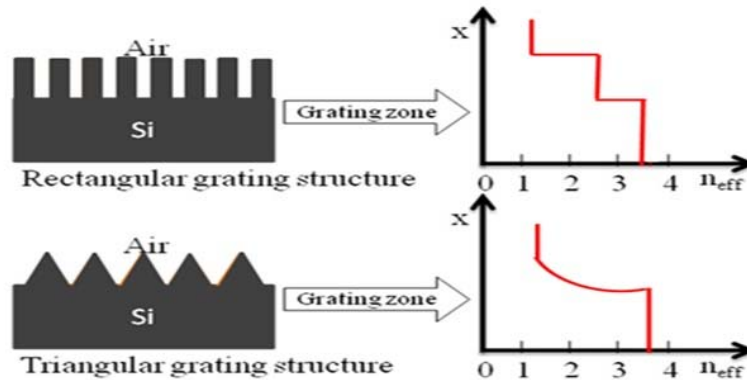


Fig. 1. Grating geometry and plot of subwavelength grating (SWG) height versus refractive index (n) in silicon (Si)

2.2. SWG fabrication steps

There are several conventional methods for the fabrication of conical SWG structures, such as photolithography, colloidal formation, nanoimprint and nanoparticles. Unfortunately, perfect conical shapes cannot be obtained by any of these methods. The formation of uniformly distributed nanoparticles and the use of dry etching in conjunction with additional isotropic etching processes can produce SWG with almost conical shapes. Fig. 2 illustrates the fabrication steps for creating the SWG structure, which were reported by Song et al. [2].

At first, the nanoparticles can be formed using the annealing process, then CF_4 or O_2 gas is passed through them using the dry plasma etching process. To shape the formed nanorods in a perfect conical shape, an additional isotropic etching process can be used as reported in [2, 4]. In this paper, the fabricated Ag nano-particles were proposed to be used as a mask to realize the conical shapes in a two-dimensional grid-like distribution to realize the SWG structure.

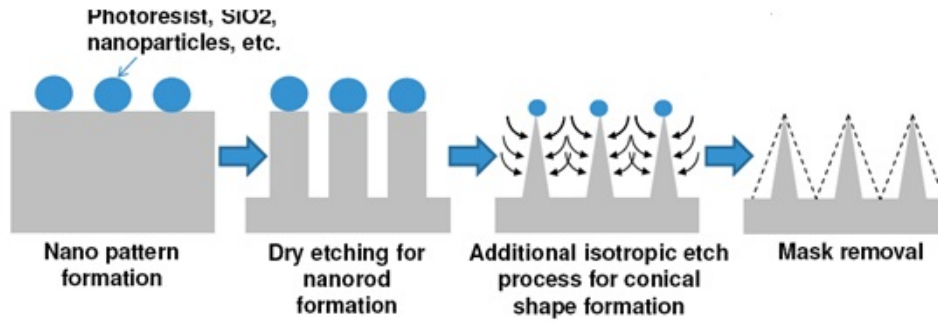


Fig. 2. Steps for the formation of SWG structure

2.3. Experimental results

Silver (Ag) nanoparticles on GaAs and silicon were fabricated through initial sputtering and subsequent annealing. Annealing was performed in an oven placed in an aerobic environment. After setting the temperature, time and ramp, the oven was allowed to reach the desired temperature and then cool down to ambient temperature.

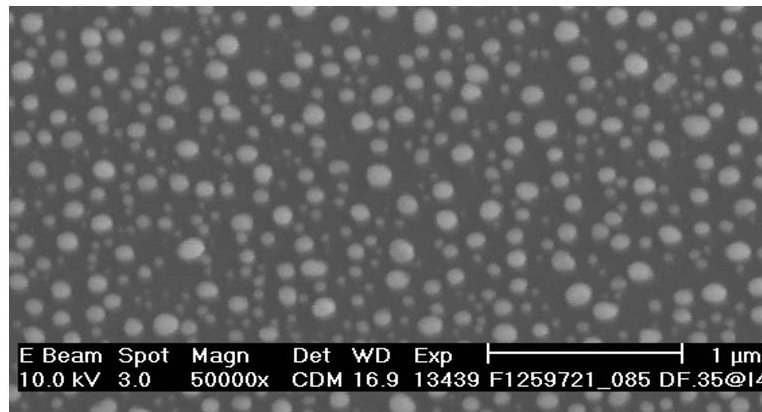


Fig. 3. Scanning Electron Microscope (SEM) image of Ag nanoparticles on GaAs developed using a 10 nm Ag film annealed for 30 min at 523 K

Ag thin films of thicknesses 10 nm, 8 nm, 5 nm were deposited onto GaAs and Si substrates and annealed at different temperatures, namely 523 K, 573 K, 623 K, 673 K and 723 K. Characterization of the annealed samples was carried out using the SEM method and ImageJ software.

Figure 3 shows the SEM image of Ag nanoparticles on GaAs substrates. The average diameter and average distance between nearest nanoparticles were measured by ImageJ software package. With the recorded data, we simulated the reflection of an SWG structure having a triangular pattern of base size and spacing equal to the average nanoparticle diameter and spacing respectively, using Opti-FDTD software package (developed by Optiwave Inc.) [5]. This software package numerically solves the Maxwell's equations within a certain medium, the light propagation, scattering, reflection and polarization. Simulation results showing the electric field distribution for the conical shaped SWG structure are shown in Fig. 4. The incident light hits directly on top of the SWG grating structure (or nano-structure). A major portion of incident electromagnetic wave is

absorbed by the grating zone due to the gradual change of refractive index, while the rest is reflected or transmitted.

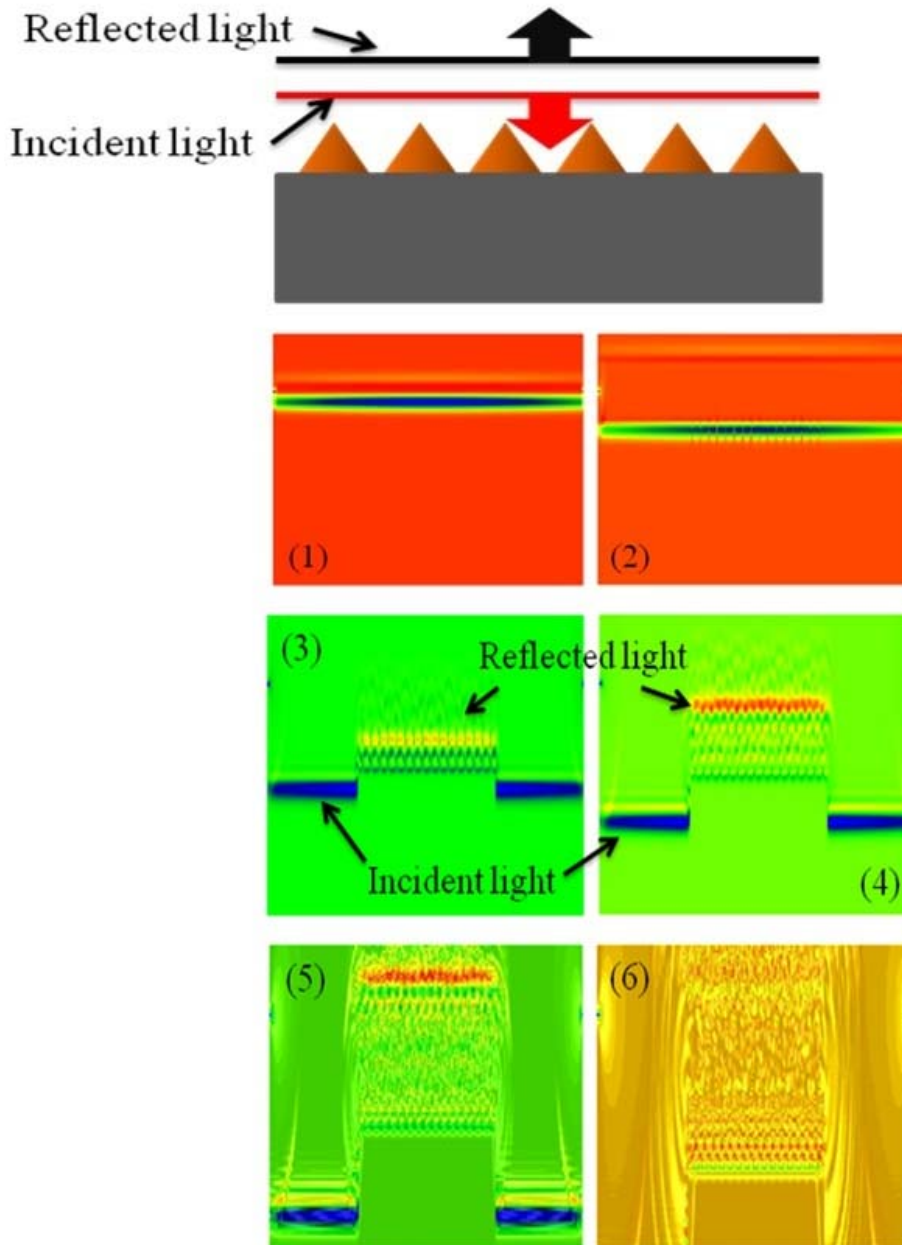


Fig. 4. Schematic diagram of conical shaped subwavelength grating (SWG) structure and the steps for simulating the propagation of the electromagnetic waves across the simulated structure

Fig. 5 shows the average spacing between the silver nanoparticles versus the annealing temperature for a 10 nm thick Ag thin film deposited onto Silicon and GaAs substrates. It is obvious that for the silicon substrate, the average spacing of 200 nm is maintained over the temperature range of 520-575 K, whereas for a GaAs films the spacing increases with increasing temperature (this is, however, useful for some applications required some degrees of spacing control).

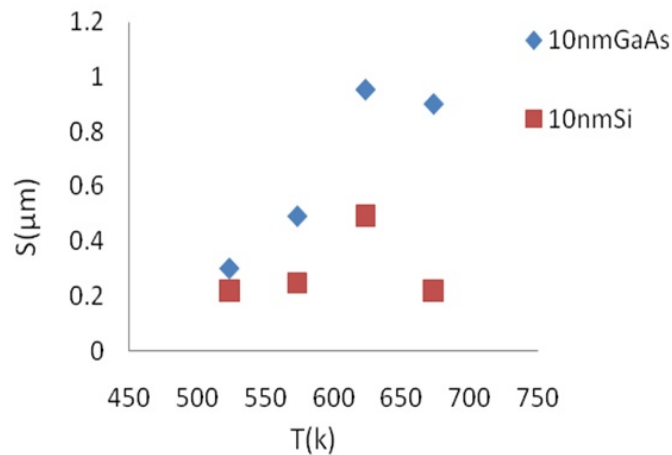


Fig. 5. Average spacing $S(\mu\text{m})$ between the Ag nanoparticles versus annealing temperature for a 10 nm Ag thin film deposited onto Si and GaAs substrates

Fig. 6 shows the reflection spectra for Ag films of different thicknesses deposited onto Si and GaAs substrates, and annealed at different temperatures. It is seen from Fig. 6 that a 10 nm thick Ag film on Si annealed at 523 K yielded a maximum reflection as low as 12%, while the 8 nm thick Ag film, annealed at 573 K, resulted in maximum reflection of 13%. The 5 nm thick Ag film which was annealed at 623 K produced maximum reflection below 7% over a wide range of wavelengths. Conversely, the Ag film on GaAs annealed at 523 K showed reflection below 10% over a wide range of wavelengths. The 8 nm Ag film on GaAs annealed at 673 K exhibited lower reflection in comparison with other annealing temperatures, and the reflection of the 5 nm Ag film on GaAs annealed at 723 K was as low as 15%.

3. Conclusions

Ag thin films with different thicknesses have been deposited on semiconductor substrates and annealed at different temperatures to fabricate Ag nano-particles that can be used to cost-effectively develop SWGs that perform as AR coatings for semiconductor devices. We have found that the desired diameter and spacing between nanoparticles can be achieved by controlling the annealing temperature and Ag film thickness that can be ultimately used to fabricate SWG structures having patterns of arbitrary sizes and spacing, which control the reflective properties.

Acknowledgement

This research is supported by the Faculty of Computing, Health and Science, Edith Cowan University, and the World-Class University Program funded by the Ministry of Education, Science, and Technology through the National Research Foundation of Korea (R31-10026).

References

- [1] Song, Y.M. and Lee, Y.T. Simulation of antireflective subwavelength grating structure for optical device applications. In: Proceedings of the 9th International Conference on Numerical Simulations of Optoelectronic Devices 2009 (NUSOD 09), P. 103–104 (2009).

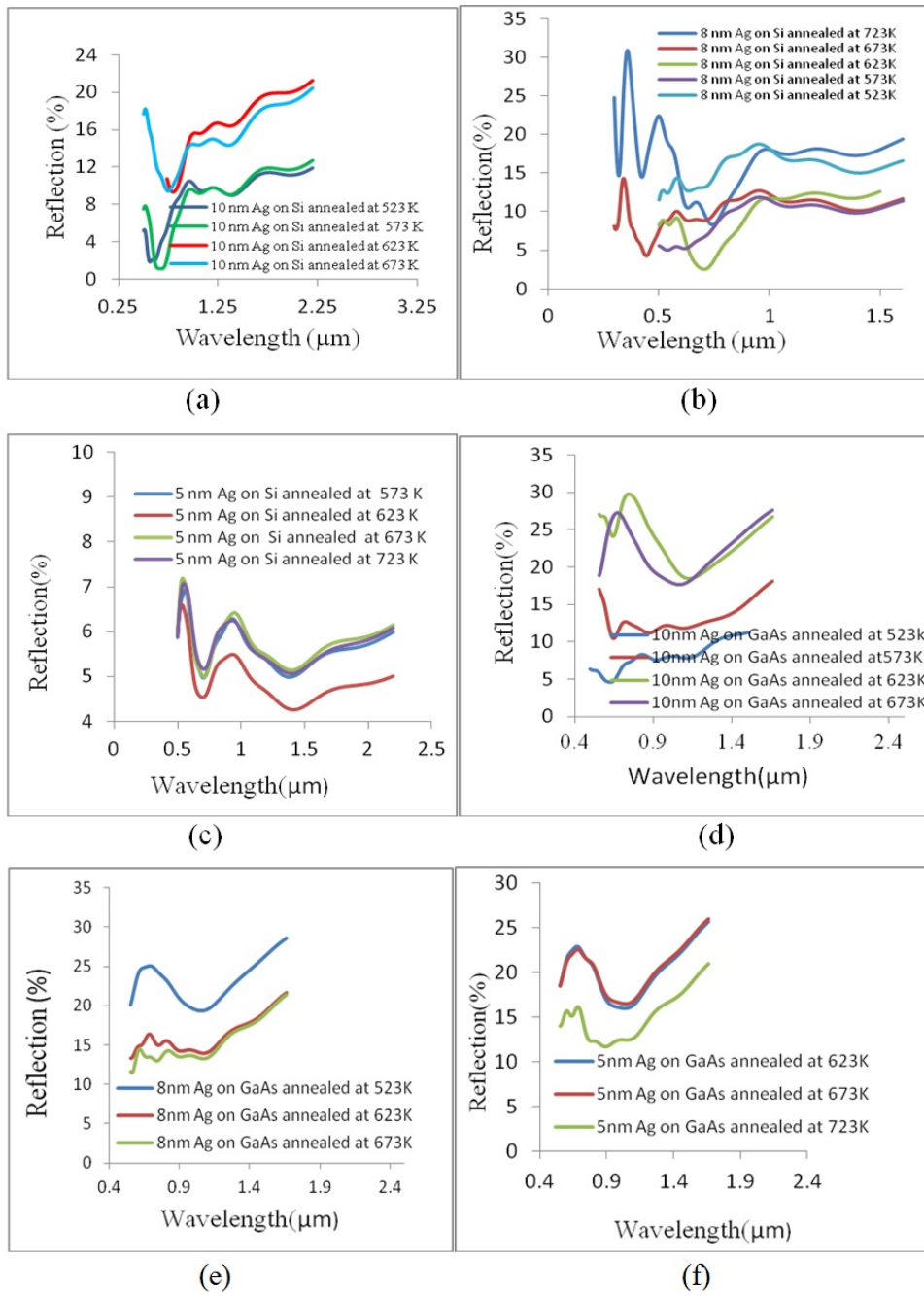


Fig. 6. Reflection spectra for various SWG structures developed using 10 nm, 8 nm and 5 nm thick Ag films on Si and GaAs substrates, annealed at different temperatures

- [2] Song. Y. M., Jang. S. J., Yu. J. S., and Lee. Y. T., Bioinspired parabola subwavelength structures for improved broadband antireflection. *Small*, **6**, P. 984–987 (2010).
- [3] Schmid. J.H., Cheben. P., Janz. S., Lapointe. J., E.Post, Delage. A., Densmore. A., Lamontagne. B., Waldron. P., Xu. D.-X., Subwavelength grating structures in planar waveguide facets for modified reflectivity. In: Proceedings of the Photonics North 2007 conference, Ottawa, Ontario, Canada, Proc. SPIE, **6796**, P. 67963E (2007).
- [4] Lee. Y. T., High-efficiency GaInP/LCM-GaInP/GaAs triple-junction solar cells with antireflective sub-wavelength structures. Gwangju Institute of Science and Technology (GIST), Republic of Korea, 2009.
- [5] Finite Difference Time Domain Photonics Simulation Software, OptiFDTD Technical background and Tutorials. Version 8.

EFFECT OF Li⁺ CO-DOPING ON THE LUMINESCENCE PROPERTIES OF ZnO:Tb³⁺ NANOPHOSPHORS

Partha P. Pal¹, J. Manam

¹Department of Applied Physics, Indian School of Mines, Dhanbad-826004, India
phys.ppal@gmail.com, jairam_manam@yahoo.co.in

PACS 78.67.Qa, 78.55.Et

Li⁺ co-doped ZnO:Tb³⁺ nanocrystals were synthesized via the chemical co-precipitation method in order to study the effect of Li⁺ co-doping. The samples were characterized by means of SEM, XRD, FTIR, Reflectance, PL and TL studies. SEM images showed that the samples were composed of nanorods with diameters of 50 to 90 nm and lengths of approximately 600 nm to 1.3 μm. XRD analysis revealed pure phase of ZnO with hexagonal wurtzite structure. XRD study also showed no change in the peak pattern for Li⁺ co-doping; a slight shift of the (101) peaks towards lower angle can be seen. Sample crystal sizes were found to be in the 10–25 nm range. Photoluminescence intensity was enhanced due to a minute amount of Li⁺ co-doping in the sample. The X-induced thermoluminescence gave a glow peak at 320 °C for the Li⁺ co-doped sample, which was shifted to a lower temperature and had twice the intensity of the ZnO:Tb³⁺ sample.

Keywords: terbium, rare-earth, lithium, photoluminescence, thermoluminescence, zinc oxide.

1. Introduction

Rare earth doped ZnO has been the subject of interest over the last few years. Recently, nanocrystalline ZnO has been synthesized in various shapes, like nanorods, nanospheres, nanoflowers etc. while being doped with rare-earth (RE) ions to obtain enhanced luminescence properties. These qualities make the aforementioned structures useful in various optoelectronic devices like vacuum fluorescent display (VFD), field emission display (FED) and electroluminescent display (ELD) etc [1–5]. The intra-shell transition between the 4f shells of the RE ions make their luminescence properties very attractive. Doping RE ions into the ZnO matrix is very difficult because, firstly, the ionic radii of RE ions (e.g. Tb³⁺ ~0.92Å) are much larger than that of Zn²⁺ ions (~0.74Å) and secondly substitution creates a charge imbalance, as RE³⁺ ions (Charge: +3) substitutes the Zn²⁺ sites (Charge: +2) in the ZnO host matrix. The charge compensation from the local defect sites results in lattice deformation, which is not desired. It would be much more convenient to provide a charge compensating material for the formation of a stable compound. The alkali metals like Na, K, Li etc. are the most suitable candidates in this regard.

In the case of high temperature treatment, the luminescence efficiency of rare-earth materials is often found to decrease due to self-quenching. That is why room temperature synthetic methods, like precipitation method, sol-gel method, etc. are considered very convenient methods for rare-earth doping. Terbium (Tb) is a very interesting rare-earth element known for its bright green emissions due to Tb³⁺ related peaks at 490 nm (⁵D₄ → ⁷F₆) and 544 nm (⁵D₄ → ⁷F₅) and thus, very suitable for doping in ZnO; because that oxide is itself a green emitting phosphor and generally gives broad green (532 nm) and blue-green (450 nm, 472 nm) emissions. Earlier studies showed that a small amount

of Li^+ doping enhanced the luminescence efficiency [6] due to charge compensations and the creation of defects and traps. It is expected that with a minute amount of Li^+ co-doping, the green photoluminescence (PL) and thermoluminescence (TL) emissions will be enhanced.

In this work, undoped ZnO, ZnO:Tb^{3+} and Li^+ co-doped ZnO:Tb^{3+} , were synthesized successfully by the co-precipitation method. The optical properties of these samples were systematically studied by UV-Vis Diffuse reflectance (DR), thermoluminescence (TL) and photoluminescence (PL) separately, whereas the structural properties were carried out by X-ray diffraction (XRD), scanning electron microscopy (SEM) and Fourier transform infrared spectroscopy (FTIR). The effects of Li^+ co-doping on its different properties were followed, observed, described and explained.

2. Experimental

Undoped, Tb^{3+} doped and Li^+ co-doped ZnO were prepared by the co-precipitation method. The undoped ZnO sample was prepared by mixing equal volumes of 0.05 M ethanolic ZnCl_2 solution with 0.20 M ethanolic NaOH at room temperature. Firstly, suitable amounts of ZnCl_2 and NaOH were separately dissolved in ethanol to prepare 0.05 M ZnCl_2 and 0.20 M NaOH solutions at room temperature. Then, the two solutions were mixed and magnetically stirred for 6 hours at room temperature. During this process, NaOH reacts with ZnCl_2 to form ZnO. The mixed sample was then filtered with a 125 mm Whatman-42 filter paper. After complete filtration, the residue on the paper was collected and dried. The filtrand was then washed in ethanol and dried at 80°C to provide a favorable temperature for nanorod formation. For co-doping Li^+ and Tb^{3+} ions, the requisite amounts of LiCl and TbCl_3 [Sigma-Aldrich, 99.9%] were added before mixing the 0.05 M ZnCl_2 and 0.20 M NaOH solutions. After drying and collecting, the samples were annealed at 200°C for two hours.

The powder sample was characterized over a wide range of Bragg angles 2θ ($10^\circ \leq 2\theta \leq 80^\circ$) with a Bruker D8 Focus XRD instrument with a Cu target ($K_\alpha=1.5406 \text{ \AA}$) at a scanning rate of 2° per min. The FTIR spectrum (KBr pellet) was taken from 400 to 4000 cm^{-1} on a 'FTIR Spectrum RX I', (Perkin Elmer, Switzerland) spectrometer. The SEM image was taken with Hitachi S 3400-N Scanning Electron microscope. The differential scanning calorimetry (DSC) analysis was carried out using a Perkin Elmer DSC7 Differential Scanning Calorimeter. PL emission and excitation studies were carried out by a commercially available personal computer-based Hitachi FL 2500 Fluorescence spectrophotometer with a 150W xenon lamp over the wavelength range 350 to 700 nm. Thermoluminescence studies were carried out by using a personal computer-based Thermoluminescence Analyzer System (TL 1007) supplied by Nucleonix Systems private ltd. India.

3. Results and Discussion

3.1. SEM Studies

Fig.1 (a) and (b) shows the particle morphologies of ZnO:Tb^{3+} and 1wt% Li^+ co-doped ZnO:Tb^{3+} nanophosphors. As can be seen, the particles are composed of nanorods and nanoparticles. In the case of ZnO:Tb^{3+} sample, the diameters and length of the nanorods were found to range from 70 to 90 nm and 800 nm to $1.3 \mu\text{m}$ respectively, whereas from the image of the Li^+ co-doped ZnO:Tb^{3+} , it is clear that there is loss of sample crystallinity due to the oxygen vacancy brought about by Li^+ ion incorporation

[7, 8]. Here, the diameters and lengths of most nanorods were found to range from 50 to 70 nm and 600 nm to 800 nm respectively, which were less than that of the ZnO:Tb³⁺ sample. Due to the Li⁺ ion, the growth of nanocrystals was found to be suppressed here and nanorods were partially formed, although some of the nanorods in this case were also found to be more than 1 μm in length. The formation of these morphologies can be attributed to the supersaturation of ZnO nuclei [9]. Nanorod growth begins when both Zn²⁺ and OH⁻ ions reach supersaturated levels. The PH value in the solution plays a vital role in this regard.

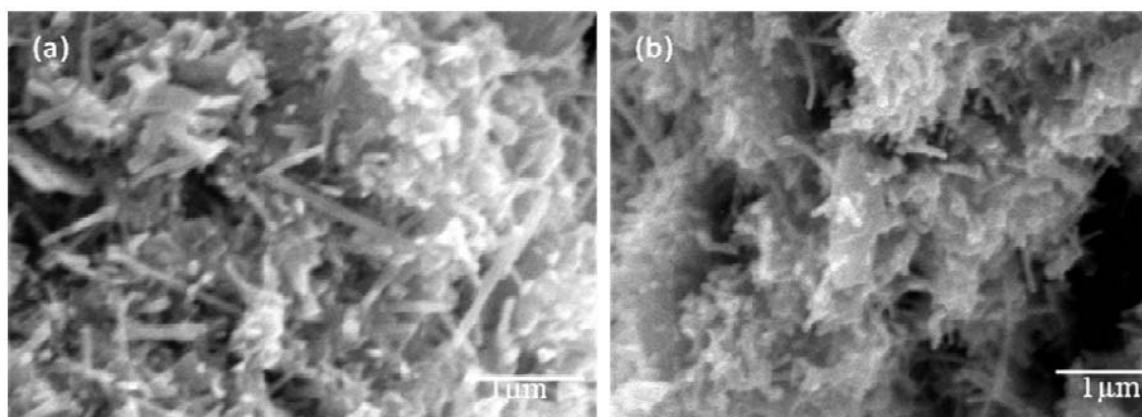


Fig. 1. SEM image for the (a) ZnO:Tb³⁺ and (b) 1wt% Li co-doped ZnO:Tb³⁺ nanorods

3.2. XRD Studies

The room temperature XRD patterns of the undoped, ZnO:Tb³⁺ and Li⁺ co-doped ZnO:Tb³⁺ powder samples are shown in Figure 2. The XRD study was done over a wide range of Bragg angles (20° – 80°). The XRD pattern of all the samples showed ZnO hexagonal wurtzite structure. The peaks were well matched with the JCPDS data card No. 79-0206. The data with particle sizes are shown in Table 1. The grain size of ZnO:Tb³⁺ calculated by the Debye-Scherrer formula was found to be in the 10–25 nm range. The XRD study showed no change in the XRD peak pattern, confirming that Li⁺ ions were well incorporated in the crystal lattice. In all likelihood, the slight shift of the (101) peak towards lower angle seen for the Li⁺ co-doped sample may indicate an increase in the lattice parameters due to Li⁺ doping. This increase in lattice parameters is due to lattice distortion as Li⁺ ions occupy the lattice sites [10]. The crystal sizes in the sample were calculated by the Debye-Scherrer formula:

$$D = 0.9\lambda/\beta\cos\theta$$

where β is the full-width at half-maximum (FWHM), and λ is the wavelength of the X-Ray used. The wavelength of the X-Ray used here is $K_{\alpha}=1.5406\text{\AA}$ (Cu target). The crystal sizes were calculated to be in the of 15 to 20 nm range for Li⁺ co-doped ZnO:Tb³⁺ and 20 to 30 nm for ZnO:Tb³⁺.

3.3. FTIR Studies

The 'FTIR' spectra of the undoped ZnO, Tb³⁺ doped ZnO and Li⁺ co-doped ZnO:Tb³⁺ were also studied systematically and the results are shown in Fig. 3. The FTIR spectra of the undoped ZnO sample consisted of four large absorption bands. The

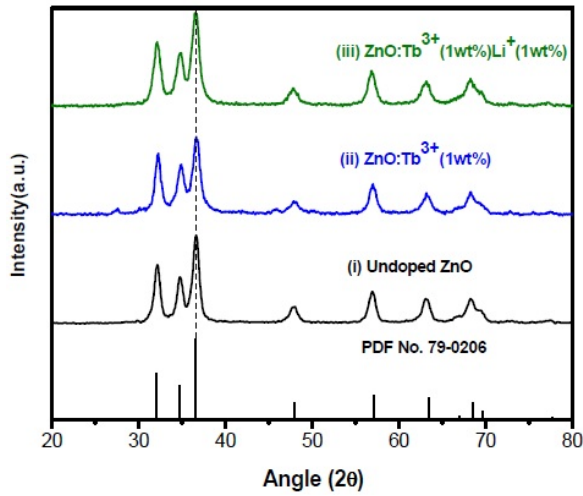


Fig. 2. Room temperature XRD pattern (i) undoped ZnO, (ii) ZnO:Tb³⁺ (1wt%), (iii) Li⁺ (1wt%) co-doped ZnO:Tb³⁺ (1.0 wt%) along with the standard XRD peaks for ZnO (JCPDS No. 79-0206)

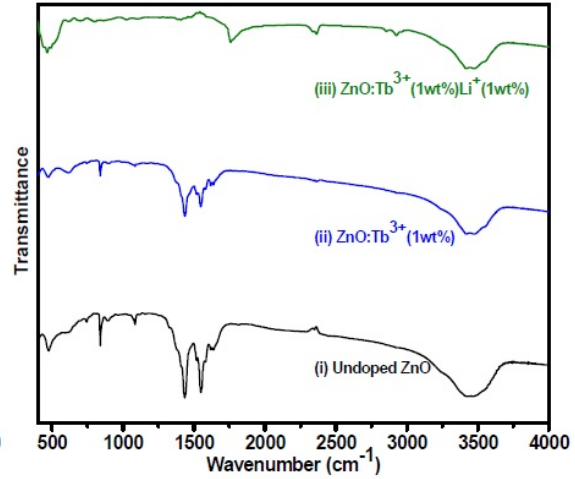


Fig. 3. FTIR spectra of the (i) as synthesized ZnO, (ii) annealed ZnO and (iii) annealed ZnO:Tb³⁺ (1wt%) nanorods

Table 1. Comparison of the experimental and reference values [PDF no. –79–0206] of XRD peak Positions and d-spacings of Li⁺ co-doped ZnO:Tb³⁺ sample. The crystal sizes are indicated corresponding to each peak

Peak position (2θ exp.)	Peak position (2θ ref.)	d spacing exp. [Å]	d spacing ref. [Å]	Particle Size (nm)	h	k	l	Relative Intensity (%)
32.214	31.768	2.7765	2.8145	18.14	1	0	0	52.4
34.890	34.422	2.5694	2.6032	17.87	0	0	2	49.4
36.584	36.253	2.4543	2.4759	20.72	1	0	1	80.7
47.859	47.540	1.8991	1.9111	16.58	1	0	2	17.9
56.926	56.594	1.6162	1.6249	18.96	1	1	0	25.8
63.114	62.858	1.4818	1.4772	16.12	1	0	3	28.2
66.233	66.374	1.4099	1.4072	19.53	2	0	0	8.3
68.305	67.947	1.3802	1.3784	18.65	1	1	2	42.6
69.931	69.875	1.3607	1.3585	16.31	2	0	1	20.2

large band at 475 cm⁻¹ was attributed to the Zn-O stretching in the ZnO lattice. Two others bands locating at 1545 and 1431 cm⁻¹ were attributed to asymmetric and symmetric C=O stretching vibration modes. The presence of C=O may be due to the atmospheric CO₂. The wide absorption band at 3438 cm⁻¹ corresponds to the stretching mode of OH group [11]. These bands were present in both the Tb³⁺-doped and Li⁺ co-doped ZnO:Tb³⁺ samples. There was no change in the Zn-O and -OH peak positions due to the Li⁺, but the peak for Zn-O stretching was found to be more prominent for the Li⁺ co-doped sample and there was a shift for C=O peak. An increase in peak sharpness was also noted, indicating a better crystal quality for the Li⁺ doping. The corresponding peak positions are shown in Table 2. Also the FTIR study showed that the samples were free from any other organic impurities and suitable for the PL and TL studies.

Table 2. Assignment of FTIR bands of Undoped, 1wt% Tb³⁺ and 1wt% Li co-doped Tb³⁺ doped ZnO nanocrystals

Samples	ZnO Stretching mode (cm ⁻¹)	OH stretching mode (cm ⁻¹)	C=O stretching modes (cm ⁻¹)	CO ₂ Mode (cm ⁻¹)
Undoped ZnO	474	3440	1439, 1542	2351 2351
ZnO:Tb ³⁺ (1wt%)	470	3420	1437 1503	2369
Li ⁺ (1wt%) co-doped ZnO:Tb ³⁺ (1wt%)	440	3422	1391 1517	2378

3.4. DSC analysis

The Differential Scanning Calorimetric analysis of the Tb³⁺ doped ZnO sample is shown in fig. 4. Though the DSC curve did not show much variation after the initial rise at 30 °C, it showed a fall up to 200 °C. This may be due to the weight loss of the samples for the removal of water. The exothermic rise at 330 °C may be due to the crystallization of wurtzite ZnO structure [12]. The endothermic broad peaks of the curve near 355 °C may be due to the auto combustion reaction or possibly the removal of other organic compounds which were attached during sample preparation but not removed during washing. The peak after 500 °C showed no significant weight loss, indicating that the sample was crystalline in nature.

3.5. UV-Vis Diffuse Reflectance Studies

Fig. 5 represents the diffuse reflectance (DR) spectra of the undoped ZnO:Tb³⁺ and 1wt% Li⁺ co-doped ZnO:Tb³⁺ samples. In all cases, two absorption edges were observed; near 350 nm and 235 nm. The absorption edge of the Li⁺ co-doped sample was found to have red shifted. Earlier, a significant change in the crystallinity and particle size was observed, and now, a clear red-shift of the absorption edge was seen due to the introduction of Li⁺ ions into ZnO:Tb³⁺. This occurred because, when Zn²⁺ sites were occupied by Li⁺ ion, there was an increase of oxygen vacancies, which changed the energy band structure resulting in a narrowing of the band gap and subsequently shifting of the absorption edge to a higher wavelength [13]. Meanwhile, the reflectance of ZnO:Tb³⁺ sample has a blue-shift followed by bandgap widening due to the increase of Fermi level because of doping with rare-earth ions. The reflectance intensity, in the case of the Li⁺ co-doped sample,

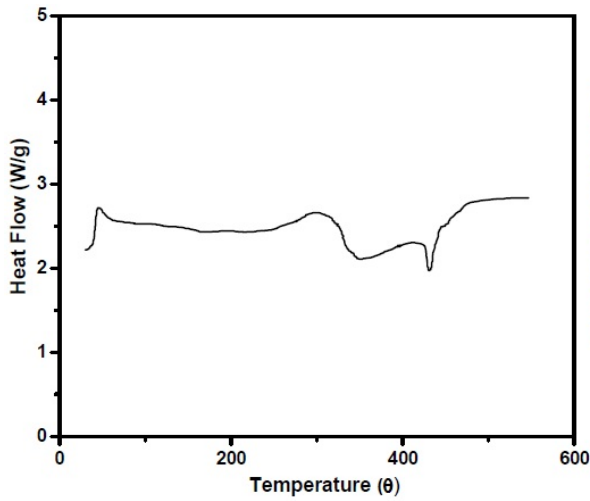


Fig. 4. DSC curves for Tb^{3+} doped ZnO nanocrystals

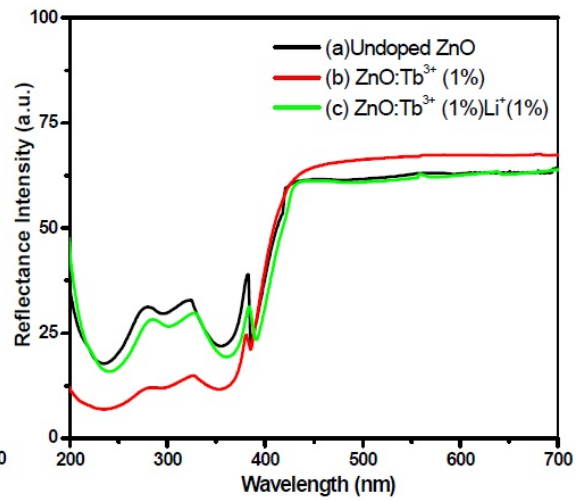


Fig. 5. Room temperature diffuse reflectance of the (a) Undoped (b) 1wt% Tb^{3+} and (c) 1wt% Li co-doped Tb^{3+} doped ZnO nanocrystals

was found decreased, which is an effect of crystallinity loss due to the oxygen vacancy. Conversely, the reflectance intensity was found to increase in the $ZnO:Tb^{3+}$ sample, which may result from the Fermi level increase due to the presence of rare-earth ions [14].

The bandgaps of undoped ZnO, Tb^{3+} doped ZnO and Li^+ co-doped $ZnO:Tb^{3+}$ samples were calculated from the reflectance study (Fig. 6) using the Kubelka-Munk function, which is a function equivalent to the absorption coefficient and is denoted by:

$$F(R_{\alpha}) = (1 - R_{\alpha})^2 / 2R_{\alpha}$$

where R_{α} is the reflectance intensity. More accurately, R_{α} is the reflectance of an infinitely thick sample with respect to a reference at each wavelength [15]. The square of the function multiplied by $h\nu$ i.e. $[F(R_{\alpha})h\nu]^2$ were plotted against photon energy $h\nu$. The intercept of the slope of the graph at x-axis gave the required bandgap. The plotted graphs are shown fig. 5. The bandgap energies calculated here had values of 3.22 ± 0.01 eV, 3.23 ± 0.01 eV, 3.21 ± 0.01 eV for undoped ZnO, Tb^{3+} doped ZnO and Li^+ co-doped $ZnO:Tb^{3+}$ respectively. The bandgap values decreased due to Li^+ co-doping, whereas the value increased for the rare-earth doped sample, which is a consequence of the reasons described above.

The bandgap values for doped compounds were much lower than that of bulk pure ZnO (3.37 eV). This was due to the presence of a single crystal in the sample [16].

3.6. Photoluminescence Studies

The room temperature photoluminescence spectra of the Li^+ co-doped $ZnO:Tb^{3+}$ and $ZnO:Tb^{3+}$ sample are shown in Figure 7. Fig 7 (I) shows the PL emission spectra of the Li^+ co-doped $ZnO:Tb^{3+}$, $ZnO:Tb^{3+}$ and the undoped ZnO sample. The photoluminescence intensity increased due to the inclusion of Li^+ . While all samples gave a broad blue peak near 435 nm due to the host lattice, the Tb^{3+} -doped sample showed a blue-green emission peak near 534 nm, which was due to the transition ${}^5D_4 \rightarrow {}^7F_5$ in Tb^{3+} ions [17]. The peak for this transition was found to be more prominent and intense

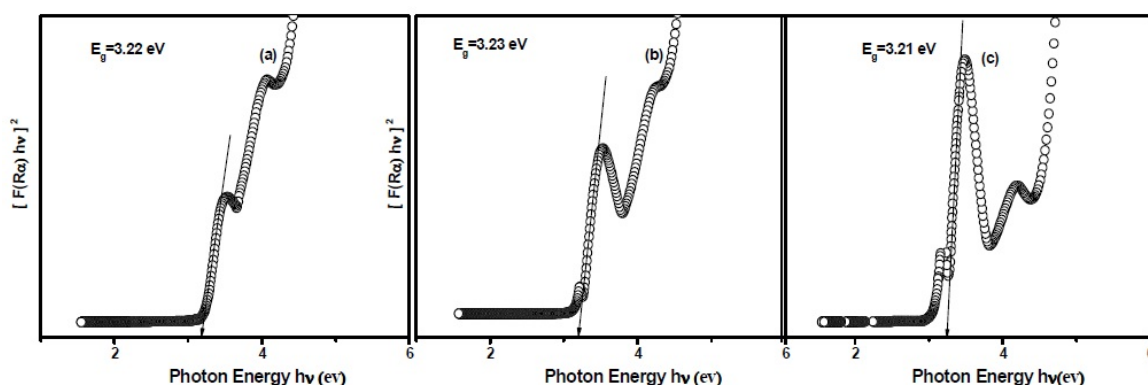


Fig. 6. Plot for $[F(R\alpha)h\nu]^2$ as a function of the incident photon energy ($h\nu$) for the (a) Undoped (b) 1wt% Tb^{3+} and (c) 1wt% Li co-doped Tb^{3+} doped ZnO nanocrystals

in the Li^+ co-doped sample at 554 nm. The corresponding excitation spectra are shown in Fig. 7 (I), providing confirmation of the above study. The charge compensation by the Li^+ ions provided chemical stability, and the improved crystal quality had a great influence on the enhancement of PL peak intensities in the Li^+ co-doped sample. One must keep in mind that excess Li^+ brings excess oxygen vacancies, which leads to more luminescence quenching. So, Li^+ should always be present in lower concentration than the rare-earth ion, which is sufficient for charge compensation and thus producing high luminescence.

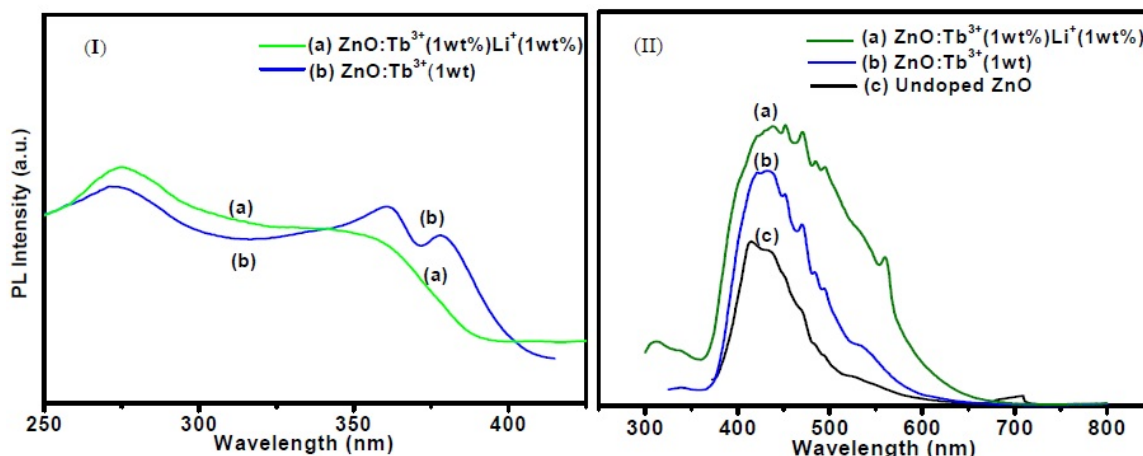


Fig. 7. Room temperature (I) excitation spectra of the (a) Li^+ codoped $\text{ZnO}:\text{Tb}^{3+}$ and (b) Tb^{3+} doped ZnO at $E_x=540$ nm and (II) emission spectra of the (a) Li^+ co-doped $\text{ZnO}:\text{Tb}^{3+}$ (b) Tb^{3+} doped ZnO and (c) undoped ZnO sample at $E_m=275$ nm

3.7. Thermoluminescence Studies

The thermoluminescence study of the co-doped, RE doped and undoped samples were carried out at temperatures ranging from 27–400 °C. Fig. 8 shows the TL glow curves of the undoped, Tb^{3+} doped and Li^+ co-doped $\text{ZnO}:\text{Tb}^{3+}$ samples. The Li^+ co-doped sample showed an intense peak at 320 °C, while the Tb^{3+} -doped sample gave a shifted peak at 355 °C. The undoped sample showed peak at 185 °C. The TL intensity of

the Li^+ co-doped sample was found to be almost twice that of the ZnO:Tb^{3+} sample. This showed that the inclusion of Li^+ ion in the lattice increased the TL intensity by about two orders of magnitude more than that of the ordinary Tb^{3+} doped sample. Co-doping the ZnO:Tb^{3+} with Li^+ not only shifted the TL peak to lower temperatures, but also appeared to enhance the intensity of that peak [18]. This enhancement of the TL peak arising from Li^+ doping can be attributed to the formation of traps. In the case of TL, the traps are responsible for the glow curves. Due to the high energy X-ray irradiation, traps are formed in the lattice and charge carriers, released by the dopant ions, remain in those traps. Then, on thermal stimulation, these trapped charge carriers are released, which then recombine with their counterpart i.e. electrons recombine with the holes to produce energy for luminescence. In case of first order kinetics, there is negligible re-trapping and recombination is in dominant, however in the case of second order kinetics, re-trapping dominates. The glow peaks were found to be of anti symmetric nature in first order kinetics, viz. the glow peaks for both Li^+ co-doped ZnO and ZnO:Tb^{3+} were found to be antisymmetric in nature. Whereas, the second order glow peaks are more symmetric in nature viz. the glow peak of undoped ZnO observed here.

3.8. Role of Li^+ in defect formation

The paper discusses the effect of the charge compensating Li^+ ion on the luminescence properties of rare-earth (Tb^{3+}) activated ZnO . For luminescence phenomena, defect formation plays a key role. Previous studies have shown that a small amount of Li^+ doping resulted in increased luminescence intensity when the concentration of Li^+ ion was much less compared to the corresponding rare-earth ions. This may be due to the increase of lattice energy caused by the addition of Li^+ ions [19]. To minimize this lattice energy, Tb^{3+} ions were distributed uniformly in the lattice due to which the PL intensity was enhanced [20, 21]. In the case of high Li^+ ion concentration, many lattice defects may be induced, which is also not suitable for photoluminescence; thus decreasing the PL intensities of the phosphors. For luminescence to occur, electron-hole pair recombination is necessary, and in this case, the Li^+ ion has a role in the transfer of the electron between the following: the surface level and the Tb^{3+} ion; the hole transfer between the valence band and the Tb^{3+} ion; the electron transfer between the conduction band and the surface level; and the transition probabilities between the 4f levels [22]. The broad green PL emission from ZnO may also be affected by both Li^+ and Tb^{3+} incorporation. Under reducing conditions, Li^+ insertion leads to a series of shallow donor levels. Also, the Li^+ ions invite oxygen vacancies, thus increasing lattice distortion. The Li^+ ions leads to series of energy levels near the conduction band. The recombination of the intrinsic shallow donors in the conduction band causes the green emission in ZnO , however, for Li^+ co-doped ZnO:Tb^{3+} the green emission was due to the recombination of the shallow donors created by the impurities like the interstitial Li^+ . Earlier studies showed that due to the rare-earth activator (Tb^{3+}) and the charge compensator (Li^+), the lifetime of the green emission was increased, which indicates that the electrons remained trapped inside the shallow donor levels. These electrons were then released with the radiation to recombine with the holes which were trapped earlier by the defects, e.g. oxygen vacancies. This phenomenon is similar to the thermoluminescence discussed above.

4. Conclusions

ZnO:Tb^{3+} nanoparticles were co-doped with Li^+ by the precipitation method using ethanol as solvent and the effect this co-doping had on the luminescence properties were

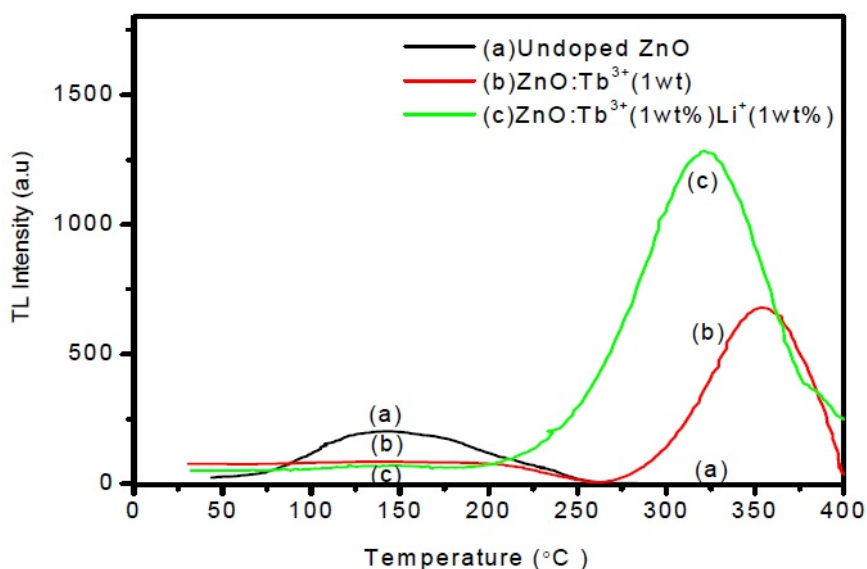


Fig. 8. X-irradiated TSL glow curve for Li^+ co-doped ZnO, ZnO:Tb^{3+} and undoped ZnO irradiated for 5 mins

discussed. SEM image showed the formation of nanorods and the FTIR study showed that the samples were suitable for PL and TL studies. XRD study revealed no impure phase due to Li^+ doping; it was found that Li^+ ion can influence the lattice parameters. Both the PL and TL peak intensities were improved due to charge compensation by the Li^+ ions. The TL glow peak was found to be shifted to a lower temperature than that of the rare-earth doped sample without Li^+ co-doping, which showed that the sample can be readily used in display devices and thermal sensors. In brief, a minute amount of Li^+ co-doping on rare-earth doped ZnO nanorods was very effective at improving its luminescence properties.

Acknowledgements

One of the authors, Pal gratefully acknowledges the ISM research fellowship by Govt. of India. The authors are thankful to Dr. S.K. Sharma, Prof. A. Sarkar, Dr. N.M. Mishra for PL, FTIR and DSC studies.

References

- [1] Nakanishi Y., Miyake A., Kominami H., Aoki T., Hatanaka Y., Shimaok G. Preparation of ZnO thin films for high-resolution field emission display by electron beam evaporation. *Appl. Surf. Sci.* **142**, P. 233–236 (1999).
- [2] Huang M.H., Mao S., Feick H., Room temperature ultraviolet nanowire nanolasers. *Science*, **292**, P. 1897–1899 (2001).
- [3] Zhang J., Feng H., Hao W., Wang T. Luminescence of nanosized ZnO/polyaniline films prepared by self-assembly. *Ceramics International*, **33**, P. 785–788 (2007).
- [4] Hellemans A., Laser Light From a Handful of Dust. *Science*, **284**, P. 24–25 (1999).
- [5] Yi L., Hou Y., Zhao H. Photo- and electro-luminescence properties of ZnO: Zn thin film. *Displays*, **21**, P. 147–149 (2000).
- [6] Prokić M. Development of highly sensitive $\text{CaSO}_4 : \text{Dy/Tm}$ and $\text{MgB}_4\text{O}_7 : \text{Dy/Tm}$ sintered thermoluminescent dosimeters. *Nucl. Inst. Meth.*, **175**(1), P. 83–86 (1980).
- [7] Y. Wu, Y. Wang, D. He, M. Fu, Z. Chen and Y. Li. Spherical $\text{Zn}_2\text{SiO}_4:\text{Eu}^{3+}@\text{SiO}_2$ phosphor particles in core-shell structure: Synthesis and characterization. *J. Lumin.*, **130**, P. 1768 (2010).

- [8] H. Liu, Y. Hao, H. Wang, J. Zhao, P. Huang and B. Xu. *J. Lumin.*, **131**, P. 2422 (2011).
- [9] Sreekantan S., Gee L.R., Lockman Z. Room temperature anodic deposition and shape control of one-dimensional nanostructured zinc oxide. *J. Alloys and Comp.*, **476**, P. 513 (2009).
- [10] Sun L., Qian C., Liao C., Wang X., Yan C. Luminescent properties of Li⁺ doped nanosized Y₂O₃:Eu. *Solid State Commun.*, **119**, P. 393 (2001).
- [11] Maensiri S., Laokul P., Promarak V. Synthesis and optical properties of nanocrystalline ZnO powders by a simple method using zinc acetate dihydrate and poly(vinyl pyrrolidone). *J. Cryst. Growth*, **289**, P. 102 (2006).
- [12] Majumder S.B., Jain M., Dobal P.S., Katiyar R.S., Investigations on solution derived aluminium doped zinc oxide thin films. *Materials Science and Engineering B*, **103**, P. 16–25 (2003).
- [13] Maa Q., Zhou Y., Zhang A., Lu M., Zhou G., Li C. Synthesis and optical properties of novel red phosphors YNbTiO₆:Eu³⁺ with highly enhanced brightness by Li⁺ doping. *Solid State Sci.* **11**, P. 1124–1130 (2009).
- [14] Burstein E., Anomalous Optical absorption limit in in Sb, *Phys. Rev.* **93**, P. 632 (1954).
- [15] Tiekun Jia, Weimin Wang, Fei Long, Zhengyi Fu, Hao Wang, Qingjie Zhang, Fabrication, characterization and photocatalytic activity of La-doped ZnO nanowires. *J. Alloy. Compd.*, **484**, P. 410 (2009).
- [16] Srikant V., Clarke D.R., On the optical band gap of zinc oxide. *J. Appl. Phys.*, **83**, P. 5447 (1998).
- [17] Zhang J., Feng H., Hao W., Wang T. Luminescent properties of ZnO sol and film doped with Tb³⁺ ion. *Mat. Sci. Eng. A*, **425**, P. 346–348 (2006).
- [18] Rojas S.S., Yukimitu K., De Camargo A.S.S., Nunes L.A.O., Hernandez A.C. *J. Non-Cryst. Solids*, **352**, P. 3608 (2006).
- [19] Xu Huibing, Zhuang Weidong, Wen Xiaofan, Liu Ronghui, Hu Yunsheng, Xia Tian, Effect of Li⁺ ions doping on structure and luminescence of (Y,Gd)BO₃:Tb³⁺. *J. Rare Earths*, **28**, P. 701 (2010).
- [20] Liu Bingjie, Gu Mu, Liu Xiaolin, Zhang Rui, Xiao Lihong. Effects of Li⁺ and Zn²⁺ Co-doping luminescent properties of Gd₂O₃:Eu³⁺ nanoparticles. *J. Rare Earths*, **25**(2), P. 164 (2007).
- [21] Yu Zhijian, Huang Xiaowei, Zhuang Weidong, Cui Xiangzhong, He Huaqiang, Li Hongwei. Coprecipitation preparation and luminescent behavior of (Y,Gd)BO₃:Eu phosphor. *J. Rare Earths*, **22**, P. 829 (2004).
- [22] Bachir S., Azuma K., Kossanyi J., Valat P., J. C. Ronfard-Haret. Photoluminescence of polycrystalline zinc oxide co-activated with trivalent rare earth ions and lithium. Insertion of rare-earth ions into zinc oxide. *J. Lumin.*, **75**, P. 35–49 (1997).

THE EFFECTS OF DEFECTS ON ELECTRON TRANSPORT IN METALLIC SINGLE WALL CARBON NANOTUBES

S. Sivasathya and D. John Thiruvadigal*

Department of Physics and Nanotechnology, Centre for Material Sciences and Nanodevices,
SRM University, Kattankulathur – 603203, Tamilnadu, India,
*Mobile number: +91-9840665078, Fax: +91-44-27453903

*john.d@ktr.srmuniv.ac.in

PACS 73.63Fg, 85.35Kt, 71.15Mb

We report the transport behavior of an open-end metallic single wall carbon nanotube (SWCNT) with and without local structural defects using the non-equilibrium Green's functions approach together with the density functional theory (DFT). The transmission spectra and the projected density of states for the devices such as SWCNT (3, 3), (4, 4), (5, 5) and (6, 6) with and without defects were compared. In all cases, we found that the Stone-Wales defect had an almost negligible impact on the electrical performance compared to the monovacancy defect of the single wall carbon nanotubes at the Fermilevel. The Current-Voltage (I-V) characteristics of the devices were studied using the generalized Landauer - Buttiker formalism under low bias conditions. From our results, we concluded that our systems were suitable for use in various CNT based nano-electronic devices.

Keywords: Density functional theory, Single wall carbon nanotubes, Transport properties, I-V characteristics.

1. Introduction

In recent years, carbon nanotube (CNT) based electronics has received much attention because of its tremendous potential in applications such as active components, switches, memory devices, display devices and sensors. Single walled carbon nanotubes (SWCNT) exhibit metallic or semiconducting behaviour, depending on its diameter and chirality [1,2]. Single wall armchair carbon nanotubes are one dimensional conductors with only two open conduction channels. Hence, the conduction of electrons ultimately becomes localized owing to defects in the tube which is inevitable with increasing length due to the interactions between the tube and its environment. These transport properties have been studied extensively. Early theoretical and experimental work on SWCNT predicted that a special achiral subset of these structures known as armchair nanotubes should be metallic. That coherent electron transport can be maintained through the nanotubes was confirmed experimentally by Tans, et al. [3]. Recently, the ab-initio method [4] based on Non-equilibrium Green's Function(NEGF), in combination with Density Functional Theory(DFT), has allowed the determination of electronic transport properties of systems with hundreds of atoms in the presence of a finite voltage, which is more accurate. In this paper, we report a study on the effects of defects such as monovacancy and Stone-Wales on the electron transmission in metallic SWCNTs. The I-V characterizations were analyzed, and a negative Differential Resistance (NDR) effect was observed, which is a very useful property in nano devices such as switches, logic cells and memory storage.

2. Computational Formalism

To analyse the quantum transport through the ab-initio method, one must deal with open systems within the DFT formalism, as the system is either isolated or periodic and can be considered as two semi-infinite electrodes coupled via a contact region. Hence, the SWCNTs were divided into three regions, namely, the left electrode, right electrode and the scattering region in between the electrodes. The scattering region consisted of five unit cells and the length of the electrode was 0.492nm. For convergence, a tolerance of 1×10^{-5} of the total energy was used. Electron transport was performed on devices of metallic single wall nanotubes by a fully self-consistent NEGF combined with first-principles DFT, which is implemented in the Atomistic Tool kit (ATK) [5] package (Version 11.8.2). The generalized gradient approximation (GGA) with Perdew Zunger (PZ) pseudo potentials was used in the calculation. A double- ζ polarization (DZP) basis set was employed to describe the localized atomic orbitals and the multigrid poisson-solver must be set with the same boundary conditions. The K-point sampling is $1 \times 1 \times 100$.

In our calculations, the transmission function was calculated by

$$T(E, V) = \text{Tr} [\Gamma_L(E, V)G(E, V)\Gamma_R(E, V)G^+(E, V)], \quad (1)$$

where $\Gamma_{L/R}$ stands for the coupling matrix between the left/right electrode and scattering region, G and G^+ are the retarded and advanced Green's function.

The I-V characteristics were calculated by using Landauer-Buttiker [6] formula, which relates the conductance to the transmission probability $T(E, V)$

$$I(V) = G_0 \int_{\mu_L}^{\mu_R} dE T(E, V) \{f(E - \mu_L) - f(E - \mu_R)\}, \quad (2)$$

where $G_0 = 2e^2/h$ is a quantum unit of conductance, μ_L and μ_R are the chemical potential of left and right electrodes respectively, $f(E - \mu_{L/R})$ is the Fermi-Dirac distribution function. The resistance was derived from the current-voltage relationship.

3. Results and Discussion

The electron transmission coefficients of metallic SWCNTs with and without defects are shown in Fig. 1. In all the cases, the electron transmission coefficient of the defect-free was equal to 2 around the Fermi level (0 eV), indicating that there are two transmission channels, π -bonding and π^* -antibonding state. But a sudden drop at 0 eV occurs in the (4, 4) nanotubes because of weak coupling. The transmission coefficient for Stone-Wales defect does not reduce at the Fermi level for all the nanotubes. Hence, the electrical conductance of all metallic nanotubes at the Fermi level is not affected. In the case of monovacancy, the transmission coefficient was significantly reduced due to the formation of dangling bonds where σ -bond states are perpendicular to the π -valence bond states. As a result of this, weak coupling occurs between them [7, 8].

Under bias condition, the transmission peaks were shifted from Higher Occupied Molecular orbitals (HOMO) to the Lower Unoccupied Molecular Orbitals (LUMO). Above 1 Volts, there is a formation of symmetric gap in the transmission channels for all the nanotubes, however, this appears at 0.2 Volts for the (4, 4) nanotube. Hence, the transmission channels are suppressed in that position.

Based on the calculated electron coefficient, the current-voltage (I-V) relationship of the systems can be determined as shown in Fig. 2. Ohmic behavior occurs at low bias voltages

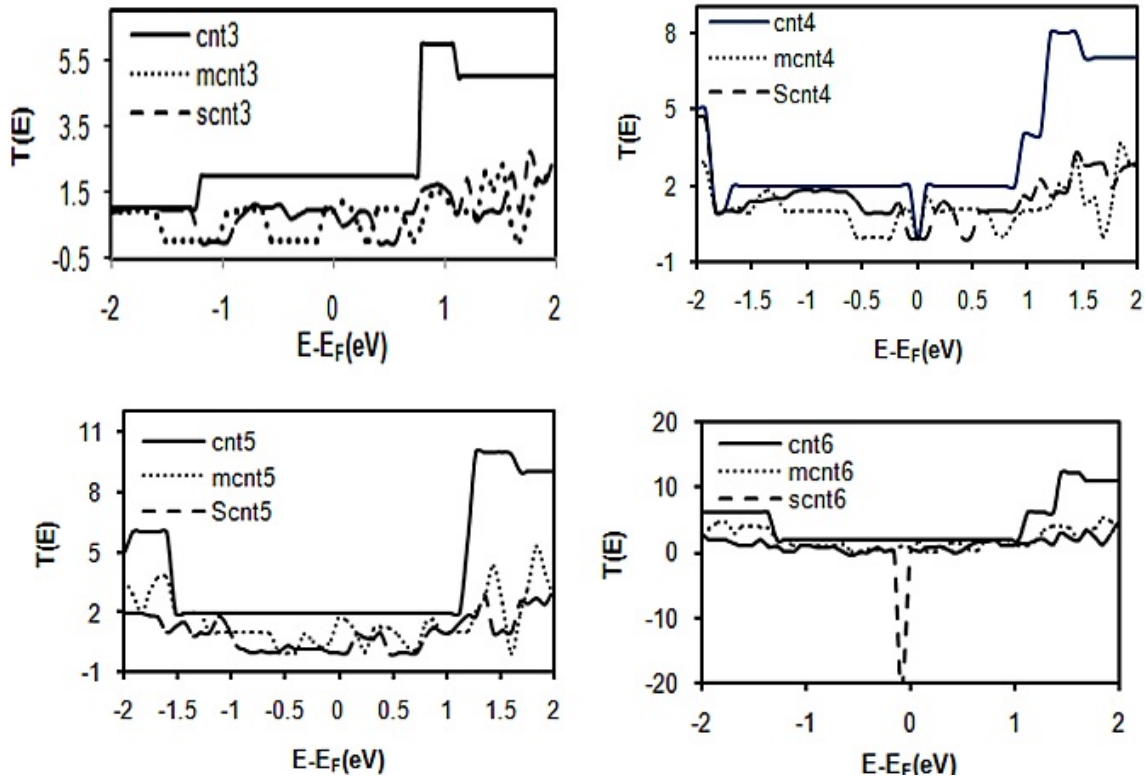


FIG. 1. Transmission spectra of metallic single wall nanotubes at zero voltage (a) (3, 3); (b) (4, 4); (c) (5, 5); (d) (6, 6)

(0-1 Volts). However, above 1-2 Volts, the current decreases as the bias voltage increases and the nanotubes exhibit a non-Ohmic behavior known as Negative Differential Resistance (NDR) [9,10] in all the cases. The NDR occurs at 0.2 V for the (4, 4) nanotube. Hence, the I-V characteristics of the systems will depend on the leads and the radius of the nanotubes (i.e.) nature of the nanotubes. The monovacancy shows low current than the Stone-Wales defect in all the cases except (6, 6) nanotubes due to the monovacancy defect near the open ends of the nanotube. In other cases, the monovacancy and Stone-Wales defects are in the curvature. These are comparable with diode characteristics, indicating diode-like applications of nanotubes.

4. Conclusion

We have investigated the electron transport properties of metallic SWCNTs with or without defects using NEGF formalism combined with first-principles DFT. From our results, we concluded that all the metallic nanotubes had similar characteristics under low bias conditions and Stone-Wales defect had negligible effect on the electrical conductance of the SWCNTs at the Fermi level while monovacancy defect significantly reduced the electrical conductance by severely blocking one of the transmission channels. These conclusions demonstrate the effective application of our systems in various CNT-based nano-electronic devices such as memory devices, switches and sensors.

Acknowledgment

The authors are thankful to the financial support from DST-FIST (Government of India) under Ref. No. SR / FST / PSI - 010 / 2010.

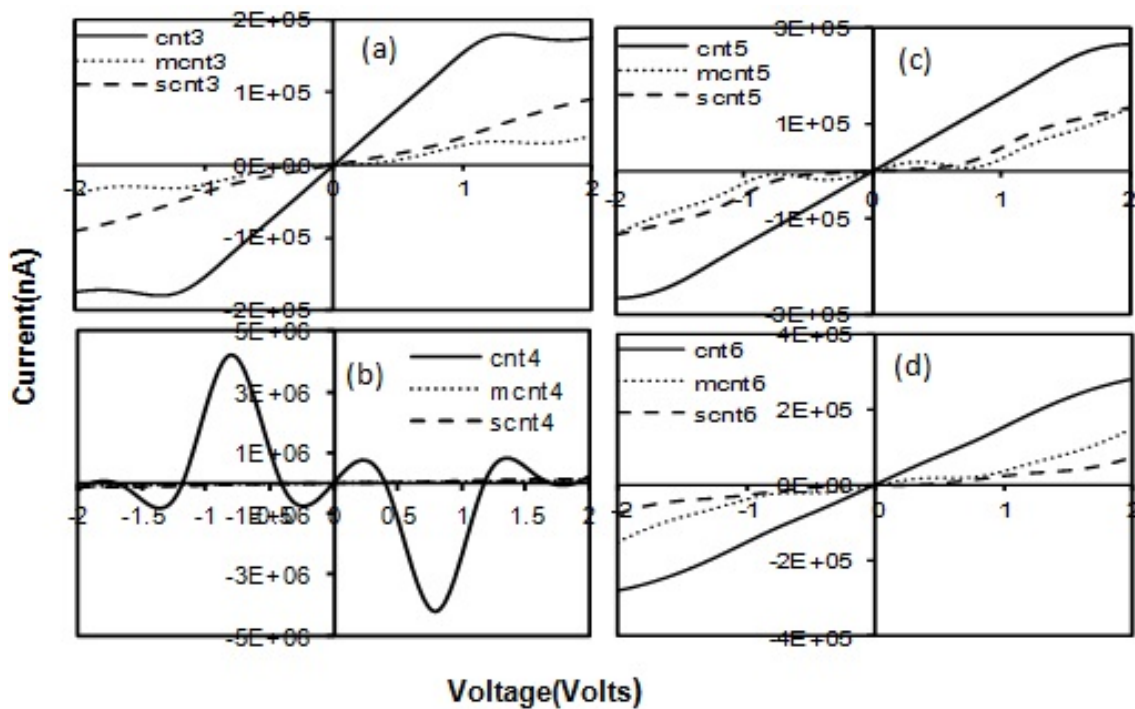


FIG. 2. The I-V characteristics of metallic nanotubes (a) (3, 3); (b) (4, 4); (c) (5, 5); (d) (6, 6)

References

- [1] S.Iijima. Helical microtubules of graphitic carbon. *Nature*, **354**, P. 56–58 (1991).
- [2] R.Saito, G.Dresselhaus, M.S.Dresselhaus. *Physical properties of carbon nanotubes*. Imperial College press, London (1998).
- [3] S.J.Tans, et al. Individual Single wall carbon nanotubes as quantum wires. *Nature*, **386**, P. 474–477 (1997).
- [4] Kikuji Hirose, et al. *First-principles calculations in real-space formalism*. Imperial College Press, London (2005).
- [5] ATOMISTITIX TOOL KIT 11.8.2 version, Quantumwise A/S, www.quantumwise.com.
- [6] M.Buttiker, et al. Generalised many-channel conductance formula with application to small rings. *Phys. Rev. B*, **31**, P. 6207 (1985).
- [7] Y.V.Shtogun, L.M.Woods. *Properties of Carbon Nanotubes under External Factors*, Carbon Nanotubes, Jose Mauricio Marulanda (Ed.), USA (2010).
- [8] B.C.Pan, et al. Formation energies of topological defects in carbon nanotubes. *Phys. Rev. B*, **62**, P. 12652–12655 (2000).
- [9] J.B.Neaton, et al. Electron transport and optical properties of carbon nanostructures from first principles. *Computer physics communications*, **169**, P. 1–8 (2005).
- [10] Yingying Zhang, et al. Negative differential resistance behavior of silicon monatomic chain encapsulated in carbon nanotubes. *Computational material science*, **62**, P. 87–92 (2012).

ELECTROFABRICATION OF NANOSTRUCTURED MULTILAYER COATINGS FOR BETTER CORROSION PROTECTION

R. R. Vaishaka, A. C. Hegde*

Electrochemistry Research Laboratory, Department of Chemistry
National Institute of Technology Karnataka, Surathkal, Srinivasnagar-575025, India

*hegdeac@rediffmail.com

PACS 81.65.Kn

In an effort to improve the corrosion resistance of monolayer Zn-Ni alloy coatings, nanostructure multilayer coating (NMC) has been developed using a pulsed current. Successive layers of alloys with alternately changing compositions were deposited on mild steel (MS) by making the cathode current cycle between two values during deposition. Multilayer coatings with different configurations in terms of composition and number of layers were developed and their corrosion behaviors were studied by electrochemical methods. The effect of cyclic cathode current densities (CCCD's), and the number of layers have been studied, and coating configurations have been optimized for highest corrosion resistances. Multilayer coatings and their degradation during corrosion were confirmed by Scanning Electron Microscopy (SEM) analysis. The improved corrosion resistance of NMC in relation to monolayer alloy coatings, deposited from same bath has been analyzed and results were discussed in terms of increased number of interfaces due to layering.

Keywords: Zn-Ni alloy, Multilayer alloy, Corrosion study, SEM and XRD.

1. Introduction

A new type of coating system called the composition modulated multilayer alloy (CMMA), or alternatively, nanostructure multilayer coating (NMC) is gaining interest due to its improved functional properties, such as mechanical strength, micro hardness, giant magnetoresistance and corrosion resistance [1]. The NMC basically consists of alternating layers of metals/alloys in micro/nanometric scale deposited electrolytically by making the cathode cycle between two current densities (c.d.) at regular time intervals. The multilayered coatings exhibit enhanced properties (e.g. hardness, mechanical strength, wear and corrosion resistance) compared to the respective, simple monolithic coatings [2]. Deposition techniques such as evaporation, molecular beam epitaxy and sputtering are some of the common methods still in use for the development of multilayer coatings, although their higher costs and practical difficulties make the electrolytic deposition process more favorable. Though Zn-Ni alloy coatings offer better corrosion protection than pure Zn, the electrofabrication of multilayer coatings is more viable and is of distinct commercial interest.

The development of NMC consisting of Zn and Ni alloy as alternate layers was found to show the best corrosion protection. Kalantary et. al have demonstrated that the presence of high Ni content in Zn-Ni alloy is responsible for enhanced corrosion protection [3]. The first multilayer deposition was reported by Blum as early as 1921 [4], and later by Brenner [5]. Many attempts have been made to understand the reasons for improved corrosion performance of multilayer coatings [6, 7]. Kirilova et al. [8, 9] have reported the deposition of CMMA coatings of Zn-Co using a single bath technique (SBT). Tench and White fabricated Cu/Ni metal multilayers and studied their mechanical properties [10]. It was proposed that the presence of Ni

TABLE 1. The composition and deposition conditions of optimized bath

Bath ingredients	Composition (g/L)	Operating parameters
ZnCl ₂ · 7H ₂ O	27.2	Anode: Nickel
NiCl ₂ · 6H ₂ O	94.9	Cathode: Mild Steel
Boric acid, BA	27.7	pH: 4
NH ₄ Cl	100	Temperature: 303 K
Gelatin	5.0	
Glycerol	2.5	

in the deposited layers was responsible for the improved corrosion protection that was observed. Recently, Thangaraj et. al optimized a chloride bath for the galvanostatic production of CMMA Zn-Ni coatings, and showed that they are ~ 45 times more corrosion-resistant than monolayer (bulk) Zn-Fe alloy coatings, even if deposited from same bath [11]. Though many reports are available with regard to the development of NMC of Zn-Ni alloy using different additives, no work has been reported for gelatin and glycerol, as additives. Hence the present work looks at optimization of deposition conditions for the development of NMC of Zn-Ni alloy which afford the best protection of mild steel (MS). The bath composition and operating parameters have been optimized by the Hull cell method. The process and products of electrolysis were analyzed using different instrumental methods, such as scanning electron microscopy (SEM) and X-Ray diffraction (XRD), and results are discussed. All electroplatings were carried out on pre-cleaned MS panels of 7.5 cm² active surface area at 303 K and pH = 4.0. A sensitive DC power source (N6705, Agilent Technologies) was used for pulsing the current during deposition. The modulation of composition in alternate layers was effected by periodic pulsing of the current. The power patterns used for monolayer and multilayer coatings are shown in Fig. 1. The corrosion behaviors of the coatings were evaluated using 5% NaCl (a representative corrosion medium). All coatings were carried out for 10 min ($\sim 20 \mu\text{m}$ thickness) for comparison purpose.

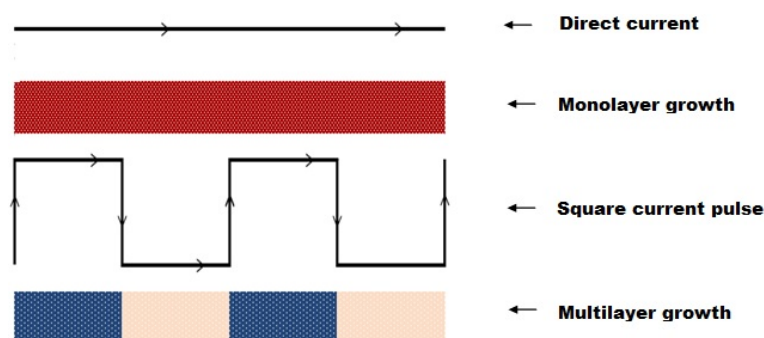


FIG. 1. Power pattern used for the deposition of monolayer (Direct current) and multilayer (square current pulse) coatings

2. Experimental

The optimal composition and operating parameters for the deposition of monolayer bright, uniform and homogeneous Zn-Ni alloy on MS were determined by the Hull cell method, and are given in Table 1.

The depositions were characterized by different analytical techniques, such as spectrophotometry, XRD, SEM and electrochemical methods. A standard three electrode system

was used for the corrosion study, at scan rate of 1 mV/s. The EIS measurements were made in frequency range of 100 kHz to 10 mHz in 10 mV perturbing voltage. The NMC's with alternate layers of alloys with different compositions are represented as: $(\text{Zn-Ni})_{1/2/n}$ (where 1 and 2 indicate the first and second cathode current density (CCCD's) and 'n' represents the number of layers formed during total plating time, i.e. (10 min).

3. Result and Discussion

3.1. Electrodeposition of Zn-Ni Alloy Coating

Zn-Ni multilayer alloy coatings were electrofabricated on polished MS with 7.5 cm² exposed area. Monolayer coatings were developed at different c.d.'s, 1.0 to 4.0 A/dm² and their corrosion rates (CR) were calculated by Tafel extrapolation method, corresponding data are given in Table 2. It may be noted that at 3.0 A/dm², the Zn-Ni alloy coating was found to be most corrosion resistant, and was selected as optimal configuration, represented by $(\text{Zn-Ni})_{3.0/\text{mono}}$. Under all conditions of the c.d. studied, the wt. % Ni in the deposit was found to be less than ca. 8.0%, which is much less than that in the bath (64.5 %). Hence, it may be inferred that the proposed bath followed an anomalous type of codeposition, characteristic of Zn-Fe group metal alloys [5].

TABLE 2. Corrosion data for Zn-Ni Monolayer Coatings

c.d. (A/dm ²)	Wt. % of Ni	Vickers hardness (V ₁₀₀)	$-E_0$ (V vs. SCE)	i_{corr} (μ A/cm ²)	CR $\times 10^{-2}$ (mm/y)
1.0	2.62	146	1.019	17.62	23.42
2.0	4.05	144	1.086	13.87	18.44
3.0	7.95	202	1.105	10.88	14.46
4.0	8.07	184	1.162	12.53	16.66

3.2. Optimization of Cyclic Cathode Current Densities (CCCD's)

The objective of the present work to improve the corrosion resistance of monolayer Zn-Ni alloy coating by multilayer technique is guided by three principles [12–14]:

- i) The successive change in current density (c.d.) allows the growth of alloys having successive changes in its chemical composition.
- ii) The corrosion resistance property of multilayer coatings or any functional property in general reaches its maximum value when the thickness of the individual layers reaches to optimum nanoscale.
- iii) The layering of alloys having different noble metal content leads to the formation of distinct interfaces.

Hence multilayer coatings having 10 layers (arbitrarily chosen) have been accomplished at different CCCD's, namely at 1.0/3.0 and 2.0/4.0 A/dm² using same binary alloy bath, given in Table 1. The coatings at different sets of CCCD's were developed to try different possible modulations in composition of individual layers, and their corrosion behaviors were studied, and corrosion data are reported in Table 3.

It was observed that the $(\text{Zn-Ni})_{1.0/3.0/10}$ and $(\text{Zn-Ni})_{2.0/4.0/10}$ showed the lowest corrosion rates when compared to $(\text{Zn-Ni})_{3.0/\text{mono}}$. However, for coatings at 2.0 and 4.0 A/dm², the differences between CCCD's were found to be more corrosion resistant. These CCCD's were employed for optimizing the number of layers for better corrosion protection.

TABLE 3. Corrosion rates of NMC Zn-Ni alloy coatings with 10 layers to set CCCD's

CCCD's (A/dm ²)	$-E_0$ (V vs. SCE)	i_{corr} (μ A/cm ²)	CR $\times 10^{-2}$ (mm/y)
(Zn-Ni) _{1.0/3.0/10}	1.085	8.416	11.18
(Zn-Ni) _{2.0/4.0/10}	1.108	6.606	8.78
(Zn-Ni) _{3.0/mono}	1.105	10.88	14.46

3.3. Optimization of Number of Layers in NMC's

The incredible claims of electroplating can be exploited for development of nanostructure multilayer coatings (NMC) for better corrosion protection. Hence, by choosing the above CCCD's, multilayer coatings with higher degrees of layering, i.e. with 10, 30, 60, 120, 300 and 600 layers, have been electrofabricated by proper setting up of the power source. The corrosion behavior of NMC's having different number of layers have been studied, and corresponding polarization behaviors are as shown in Fig. 2 (only representative). The corrosion data are reported in Table 4. It may be noted that the CRs decreased drastically with increase in number of layers in both sets of CCCD's.

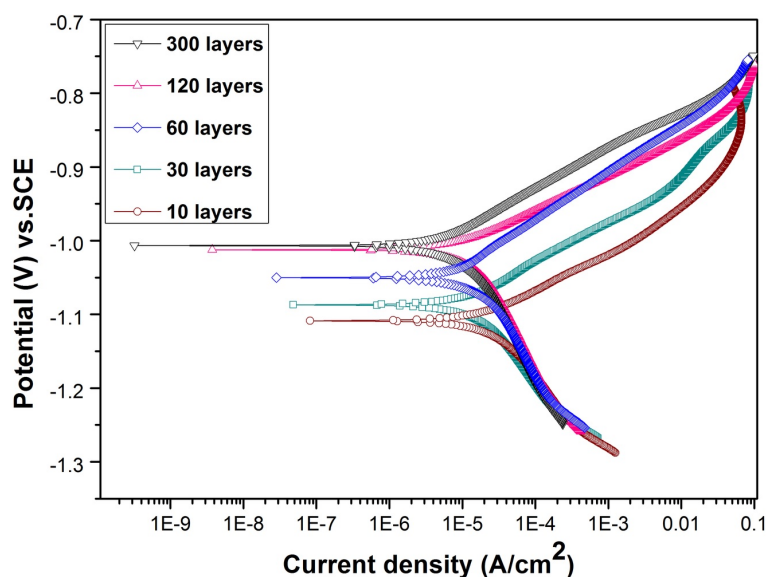


FIG. 2. Potentiodynamic polarization behaviors of NMC (Zn-Ni) coatings having different number of layers, deposited from optimized bath at 303 K

It indicates that the improvement in corrosion behavior of NMC's is not the unique property of individual layer; instead, the combined effect of composition modulation and number of layers. Further, the CR of multilayer Zn-Ni coating decreased only up to 300 layers and then started increasing, i.e. 600 layers as shown in Table 4. This decrease of CR at higher degrees of layering was due to less relaxation time for the deposition of metal ions on the cathode. In other words, at a very high degree of layering, multilayer coatings tend to become monolayer, showing higher CR's. Thus it may be stated that the amplitude of the composition modulation diminished.

TABLE 4. Effect of layering on corrosion behavior of NMC (Zn-Ni)_{1.0/3.0} and (Zn-Ni)_{2.0/4.0} coating in comparison with monolayer (Zn-Ni)_{3.0/mono} deposited from same bath at 303 K

Coating configuration	Number of layers	E_0 vs. SCE (volts)	i_{corr} (μ A/cm ²)	CR $\times 10^{-2}$ (mm/y)
(Zn-Ni) _{1.0/3.0}	10	1.085	8.416	11.18
	30	1.037	7.125	9.47
	60	1.056	4.531	6.02
	120	1.067	2.357	3.13
	300	1.041	1.319	1.75
	600	1.050	3.577	4.75
(Zn-Ni) _{2.0/4.0}	10	1.108	6.606	8.78
	30	1.085	4.989	6.63
	60	1.050	2.125	2.82
	120	1.007	1.056	1.40
	300	1.006	0.295	0.39
	600	1.036	1.975	2.61
(Zn-Ni) _{3.0/mono}	—	1.105	10.88	14.46

3.4. Comparison of Monolayer and Multilayer Coatings

The corrosion behaviors of monolayer and multilayer Zn-Ni alloy coatings, electrofabricated from the same bath for the same time (under optimal conditions) are shown in terms of DC and AC polarizations Fig. 3. Corrosion data revealed that NMC (Zn-Ni)_{2.0/4.0/300} is about 37 (CR = 0.39×10^{-2} mm/y) times more corrosion resistant than (Zn-Ni)_{3.0/mono} (CR = 14.46×10^{-2} mm/y) coatings.

3.5. Scanning Electron Microscopy Study

The scanning electron microscopy (SEM) image of (Zn-Ni)_{2.0/4.0/10} coating is shown in Fig. 4. Figs. 4a and 4b show the surface morphology of the coating before and after the bend test (electroplated coatings on thin foil of MS were bent by 135 repeatedly), respectively. The fractured coating under SEM displays the layers, as seen in Fig. 4b (shown by arrow mark). The high corrosion resistance of multilayer coatings can be envisaged due to the formation of pores, crevices occurring in one layer is blocked or neutralized by the successively deposited coating layers, and thus the corrosion agent's path is delayed or blocked. The improved corrosion resistance afforded by multilayer coatings can be also explained in terms of formation of alternate layers of alloys with low and high wt. % of Ni as shown in Table 2.

3.6. Powder X-Ray Diffraction (XRD) Study

Figure 5 shows the XRD patterns of Zn-Ni alloy deposited at different c.d. from the same bath. A necessary requirement for better physicochemical properties of the multilayer coatings is compositional modulation, i.e. phase structure should vary with cyclic cathode current density (CCCD). In the present study, the deposits obtained at 1.0, 2.0, 3.0 and 4.0 A/dm² were found to exhibit a marked difference in phase structure as shown in Fig. 5. It has been reported that the phases obtained by the coatings with 0 to 13% nickel do not correspond to that reported on the thermodynamic phase diagram [15]. However, it may be noted that deposition at the optimal c.d., having about 7.95% Ni showed the highest corrosion resistance, due to Zn(101),

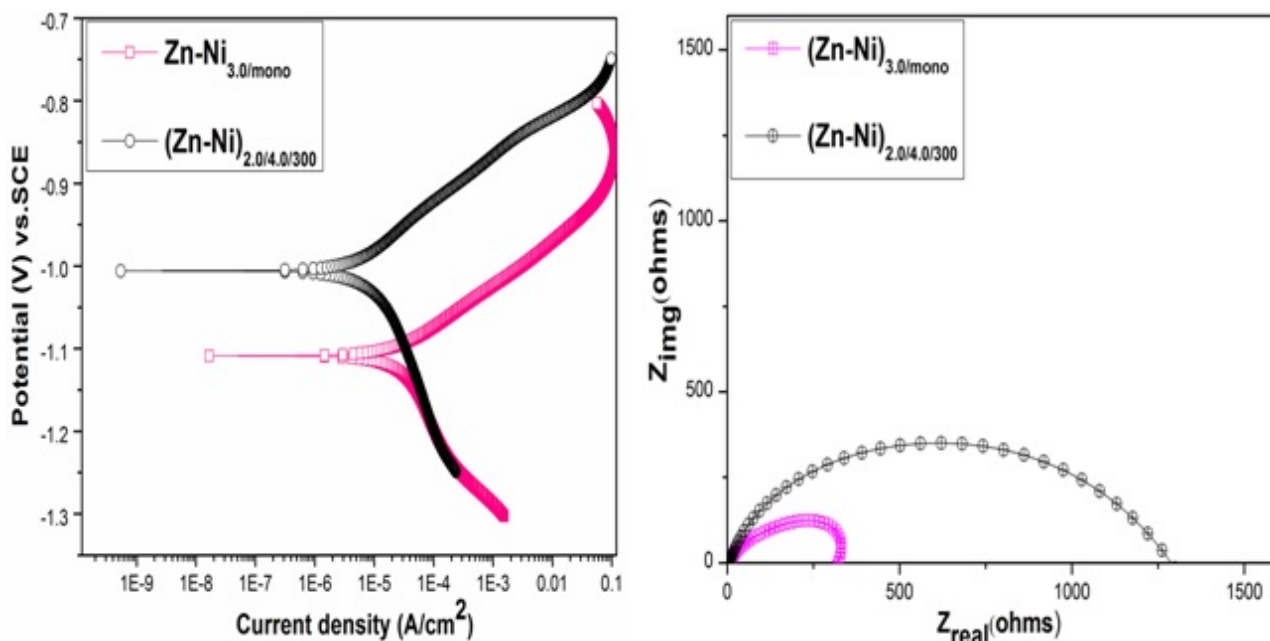


FIG. 3. Comparison of corrosion behaviors of monolayer and multilayer coatings of (Zn-Ni) alloy: a) Potentiodynamic polarization behaviors and b) Nyquist response under same frequency limit

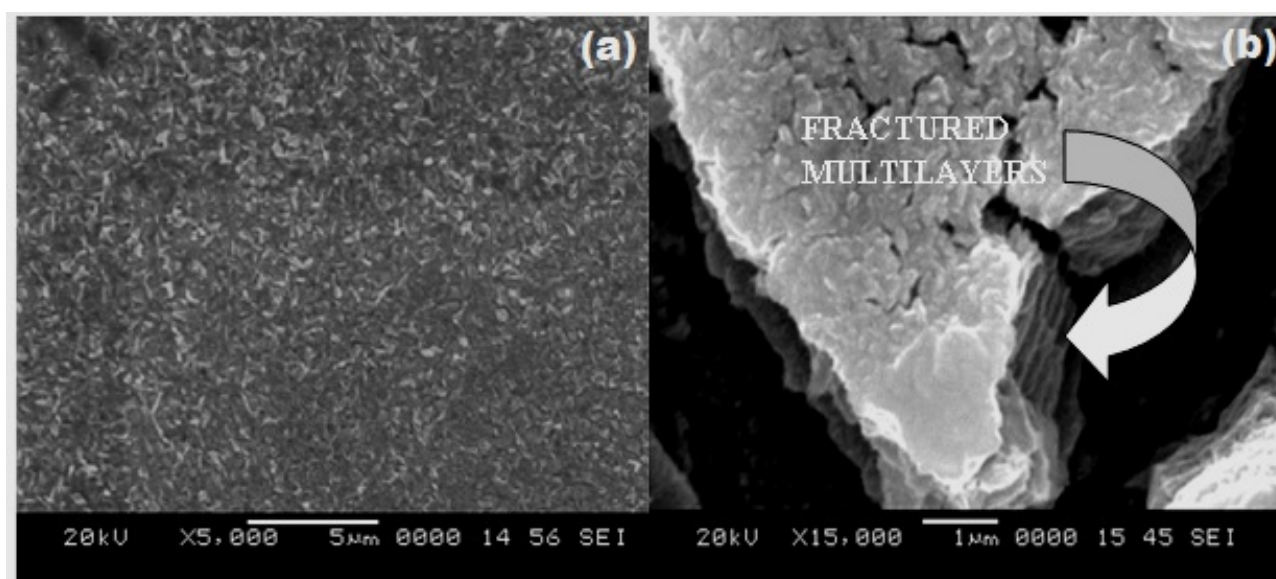


FIG. 4. SEM images of NMC $(\text{Zn-Ni})_{2.0/4.0/10}$ coatings electrofabricated from optimized bath: (a) surface structure and (b) cross-sectional view after bend test

γ -phase ($\text{Ni}_5\text{Zn}_{21}$), Zn(103) phases and a small amount of $\text{Ni}_3\text{Zn}_{22}$ (335). This particular ratio of phases was found to be responsible for the uniformity and brightness of the coating at the optimal c.d. (3.0 A/dm^2). In the case of coatings at 1.0 and 2.0 A/dm^2 , the reflection corresponding to γ -phase and Zn(101) phases are highly suppressed. The above experimental observation reveals how the cathode current density (CCD) can be used as tool for compositional modulation of individual layers, and how their duration can be used for controlling the thickness

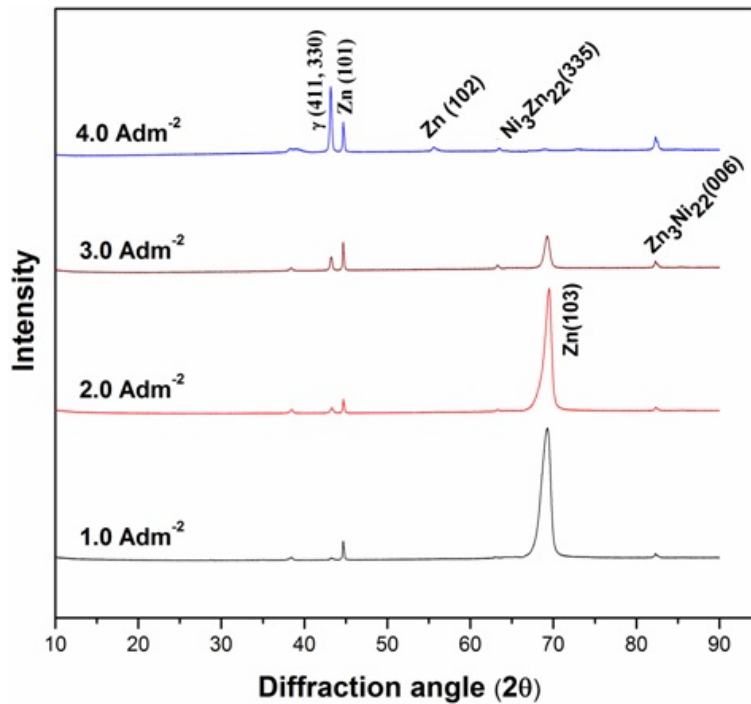


FIG. 5. XRD patterns of Zn-Ni alloy coatings at different c.d.s.

of layers. Hence, layered coatings having distinct compositions were responsible for modulation in composition, as evidenced by XRD study.

4. Conclusions

- The proposed Zn-Ni bath followed an anomalous type of deposition, i.e. the wt. % Zn in deposit is more than that in the bath at all deposition c. d.'s.
- At different c.d., Zn-Ni alloy coatings of different phase structures have formed, which enabled the compositional modulation in layered coating, as evidenced by XRD and SEM analysis.
- The amplitude of the compositional modulation diminished rapidly when layer thickness falls below certain limit, i.e., less than 1000 Å. Hence, NMC's fail to offer the improved properties at higher number of layers.
- Improved corrosion behavior at a different set of CCCD's revealed that improvement is not specific to individual layers, instead it is a combined effect of compositional modulation and number of layers.
- The extended protection of NMC's is due to fact that the failure during the single layer deposition process is masked or neutralized by the successively electrofabricated layers. Hence, the path for the corrosive agents is extended or blocked.
- Under optimal conditions, multilayered Zn-Ni alloy coatings were about 37 times more corrosion resistant than corresponding monolayer alloy electrofabricated from the same bath at the same time.

Acknowledgment

Mr. Vaishaka R. Rao acknowledges National Institute of Technology Karnataka (NITK), Surathkal for supporting this research in the form of Institute Fellowship.

References

- [1] J.Fei, G.D.Wilcox. Electrodeposition of zinc-nickel compositionally modulated multilayer coatings and their corrosion behaviours. *Surf. Coat. Technol*, **200**, P. 3533–3539 (2006).
- [2] A.Maciej, G.Nawrat, W.Simka, J.Piotrowski. Formation of compositionally modulated Zn-Ni alloy coatings on steel. *Mater. Chem. Phys*, **132**, P. 1095–1102 (2012).
- [3] M.R.Kalantary, G.D.Wilcox, D.R.Gabe. The production of compositionally modulated alloys by simulated high speed Electrodeposition from a single bath solution. *Electrochim. Acta*, **40**, P. 1609–1616 (1995).
- [4] W.Blum. The structure and properties of alternately deposited metals. *Trans Am Electrochem Soc*, **40**, P. 307–320 (1921).
- [5] A.Brenner. *Electrodeposition of Alloy*. Academic Press, New York (1963).
- [6] M.Rahsepar, M.E.Bahrololoom. Corrosion study of Ni/Zn compositionally modulated multilayer coatings using electrochemical impedance spectroscopy. *Corros. Sci*, **51**, P. 2537–2543 (2009).
- [7] F.Jing-yin, L.Guo-zheng, X.Wen-li, W.Wei-kang. Compositionally Modulated Multilayer Coatings. *J. Iron. Steel Res. Int*, **13** (4), P. 61–67 (2006).
- [8] I.Kirilova, I.Ivanov. Corrosion behaviour of Zn-Co compositionally modulated multilayers electrodeposited from single and dual baths. *J. Appl. Electrochem*, **29**, P. 1133–1137 (1999).
- [9] I.Kirilova, I.Ivanov, St.Rashkov. Anodic behaviour of composition modulated Zn-Co multilayers electrodeposited from single and dual baths. *J. Appl. Electrochem*, **28**, P. 1359–1363 (1998).
- [10] D.Tench, J.White. Tensile Properties of Nanostructured Ni-Cu Multilayered Materials Prepared by Electrodeposition. *J. Electrochem. Soc*, **138**, P. 3757–3758 (1991).
- [11] V.Thangaraj, K.Ravishankar, A.C.Hegde. Surface modification by compositionally modulated multilayered Zn-Fe alloy coatings. *Chin. J. Chem*, **26**, P. 1–10 (2008).
- [12] V.Thangaraj, N.Eliaz, A.C.Hegde. Corrosion behavior of composition modulated multilayer Zn-Co electrodeposits produced using a single-bath technique. *J. Appl. Electrochem*, **39**, P. 339–345 (2009).
- [13] S.Yogesha, A.C.Hegde. Optimization of deposition conditions for development of high corrosion resistant Zn-Fe multilayer coatings. *J. Mater. Process. Technol*, **211**, P. 1409–1415 (2011).
- [14] P.Ganesan, S.P.Kumaraguru, B.N.Popov. Development of compositionally modulated multilayer Zn-Ni deposits as replacement for cadmium. *Surf. Coat. Technol*, **201**, P. 7896–7904 (2007).
- [15] C.Bories, J.P.Bonino, A.Rousset. Structure and thermal stability of zinc-nickel electrodeposits. *J. Appl. Electrochem*, **29**, P. 1045–1051 (1999).

NOISE CANCELLATION IN UNSHIELDED MAGNETOCARDIOGRAPHY BASED ON LEAST-MEAN-SQUARED ALGORITHM AND GENETIC ALGORITHM

Valentina Tiporlini, Hoang N. Nguyen and Kamal Alameh

Electron Science Research Institute, Edith Cowan University, Joondalup, Western Australia
v.tiporlini@ecu.edu.au, h.nguyen@ecu.edu.au, k.alameh@ecu.edu.au

PACS 87.85.-d

This paper discusses adaptive noise cancellation in magnetocardiographic systems within unshielded environment using two algorithms, namely, the Least-Mean-Squared (LMS) algorithm and the Genetic Algorithm (GA). Simulation results show that the GA algorithm outperforms the LMS algorithm in extracting a weak heart signal from a much-stronger magnetic noise, with a signal-to-noise ratio (SNR) of -35.8 dB. The GA algorithm displays an improvement in SNR of 37.4 dB and completely suppresses the noise sources at 60Hz and at low frequencies; while the LMS algorithm exhibits an improvement in SNR of 33 dB and noisier spectrum at low frequencies. The GA algorithm is shown to be able to recover a heart signal with the QRS and T features being easily extracted. On the other hand, the LMS algorithm can also recover the input signal, however, with a lower SNR improvement and noisy QRS complex and T wave.

Keywords: Magnetocardiography, adaptive noise cancellation, Least-Mean-Squared algorithm, genetic algorithms.

1. Introduction

The human heart is made of conductive tissues that produce both an electric and a magnetic field, depending on cardiac activity. Measuring the electric and/or magnetic fields enables various heart parameters as well as diseases to be diagnosed, such as heart beat rate and arrhythmia. Electrocardiography (ECG) enables the detection of heart-generated electric fields through electrodes placed on the surface of the human body. However, magnetocardiography (MCG) has been shown to be more accurate than electrocardiography for the (i) diagnosis of atrial and ventricular hypertrophy, (ii) non-invasive location of the heart's conduction pathways, (iii) the identification of spatial current dispersion patterns, and (iv) the detection of circular vortex currents which give no ECG signal [1]. Cardiac magnetic fields surround the human body and are typically very low in magnitude (about 100 pT for adults [2] and between 5 to 10 pT for a fetus [3]), necessitating the use of a high-sensitivity magnetometer to measure them. Furthermore, the environmental electromagnetic noise is typically much higher (in the order of 1 nT) than the heart-generated magnetic field, resulting in an extremely low signal-to-noise ratio, if patients are examined outside a magnetic shielded room.

Magnetic noise suppression in magnetically unshielded environments has been demonstrated. For example, the performance of a multichannel system based on SQUID magnetometry in an unshielded environment has been shown to be comparable with magnetic field measurements performed inside a shielded room [4]. This demonstration, in conjunction with recent advances in adaptive signal processing, has triggered the use of adaptive magnetic noise suppression techniques for magnetically-unshielded magnetocardiography. The most common algorithm used for adaptive noise cancellation is the Least-Mean-Squared (LMS) algorithm that has been

very effective in removing low noise levels, especially in Electrocardiography [5,6]. However, the LMS algorithm has limitations, namely, (i) it requires the calculation of the punctual derivative of the squared error; (ii) it suffers high convergence time, especially if the noise power to be removed is much higher than the signal power; and (iii) it is susceptible to the risk of falling into local minima. Recently heuristic algorithms, such as genetic algorithms, are finding large application in adaptive noise cancellation applications. With respect to the LMS algorithm, the GA provides additional benefits, including (i) ability to perform parallel search for population points rather than for a single point, thus avoiding the fall into local minima; (ii) no prior information on the gradient of the signal is needed; (iii) the use of probabilistic rules instead of deterministic ones, thus ensuring the convergence to an optimum solution.

In this paper, we adopt the concept of adaptive noise cancellation shown in Fig. 1, and use two potential adaptive signal processing algorithms, namely the Least-Mean-Squared (LMS) algorithm and the Genetic Algorithm (GA), and compare their capabilities in minimizing the mean-squared of the error signal $e(k)$ and improving the SNR performance.

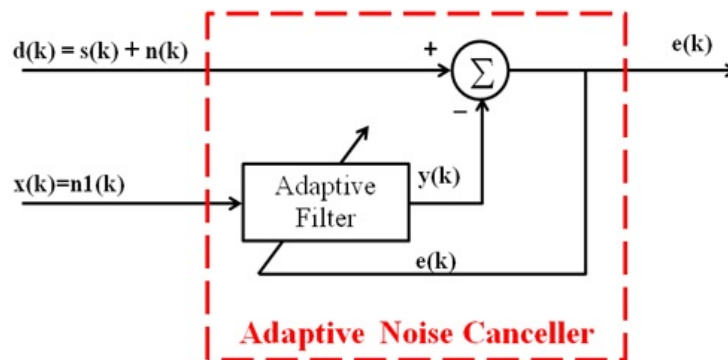


FIG. 1. Typical block diagram of an adaptive noise canceller

2. Adaptive Noise Canceller

Adaptive noise suppression techniques are typically based on adaptive filtering. To suppress the noise, a reference input signal is required, which is typically derived from one or more magnetic sensors placed at positions where the noise level is higher than the signal amplitude. Fig. 1 shows a block diagram of an adaptive noise canceller. The primary input to the canceller, denoted $d(k)$, is the sum of the signal of interest $s(k)$ and the noise $n(k)$, which is typically uncorrelated with $s(k)$. The reference input signal of the system, $x(k) = n1(k)$, is a noise signal that is correlated in some unknown way with $n(k)$, but uncorrelated with the signal of interest $s(k)$. As shown in Fig. 1, $n1(k)$ is adaptively filtered to produce a replica of the noise $n(k)$ that can be subtracted from the primary input to eventually produce an output signal $e(k)$ equals to $s(k)$.

The objective of the noise canceller is to minimize the mean-squared error between the primary input signal, $d(k)$, and the output of the filter, $y(k)$.

Referring to Fig. 1, the output signal is given by [7]:

$$e(k) = d(k) - y(k) = s(k) + n(k) - y(k). \quad (1)$$

Therefore, the mean-squared of $e(k)$ is given by:

$$E \{e^2(k)\} = E \{s^2(k)\} + E \{(n(k) - y(k))^2\} + 2E \{s(k) (n(k) - y(k))\}. \quad (2)$$



FIG. 2. Genetic Algorithm (GA) flowchart

Since $s(k)$ is uncorrelated with $n(k)$ and $y(k)$, the last term in (2) is zero, yielding:

$$E \{e^2(k)\} = E \{s^2(k)\} + E \{(n(k) - y(k))^2\}. \quad (3)$$

It is noticed from (3) that the mean-squared error is minimum when $n(k) = y(k)$, and hence, when the output signal $e(k)$ is equal to the desired signal $s(k)$.

The LMS algorithm aims to minimize the mean-squared error by calculating the gradient of the squared-error with respect to the coefficients of the filter. Assuming that the adaptive filter is a FIR filter of order M , the updating procedure is applied on coefficients b_i according the following rule [8]:

$$b_i^{(k+1)} = b_i^{(k)} + 2\mu e(k)x(k-i), \quad (4)$$

where $i = 0, 1, \dots, M-1$, k is the iteration index and μ is the step size that indicates the adaption rate of the algorithm and is usually included in the range $(0, 1]$.

Genetic Algorithms (GA) are part of the Evolutionary Algorithms, which are stochastic, population-based techniques inspired by the natural evolution process [9]. Using GA, the optimal solution is found through the minimization of a defined function, called the fitness function. For the problem of magnetic noise cancellation, the objective of the optimization process is to minimize the MSE, defined in (5):

$$E \{e^2(k)\} = \frac{\sum_{k=1}^L e^2(k)}{L}. \quad (5)$$

Figure 2 shows a typical flowchart of the Genetic Algorithm. The initialization process produces a random initial population. For each individual belonging to the population, the fitness function is evaluated to find the fitness value of that individual. If the value of the fitness function for the best point in the current population is less or equal to a pre-defined threshold value, it is therefore considered as the optimum value and the iteration will be terminated. A few predefined end conditions are evaluated to avoid an infinite loop in case the optimum value cannot be found. If none of the predefined end conditions is verified, the algorithm proceeds with the reproduction, i.e., the creation of new generation. The individuals that have best fitness

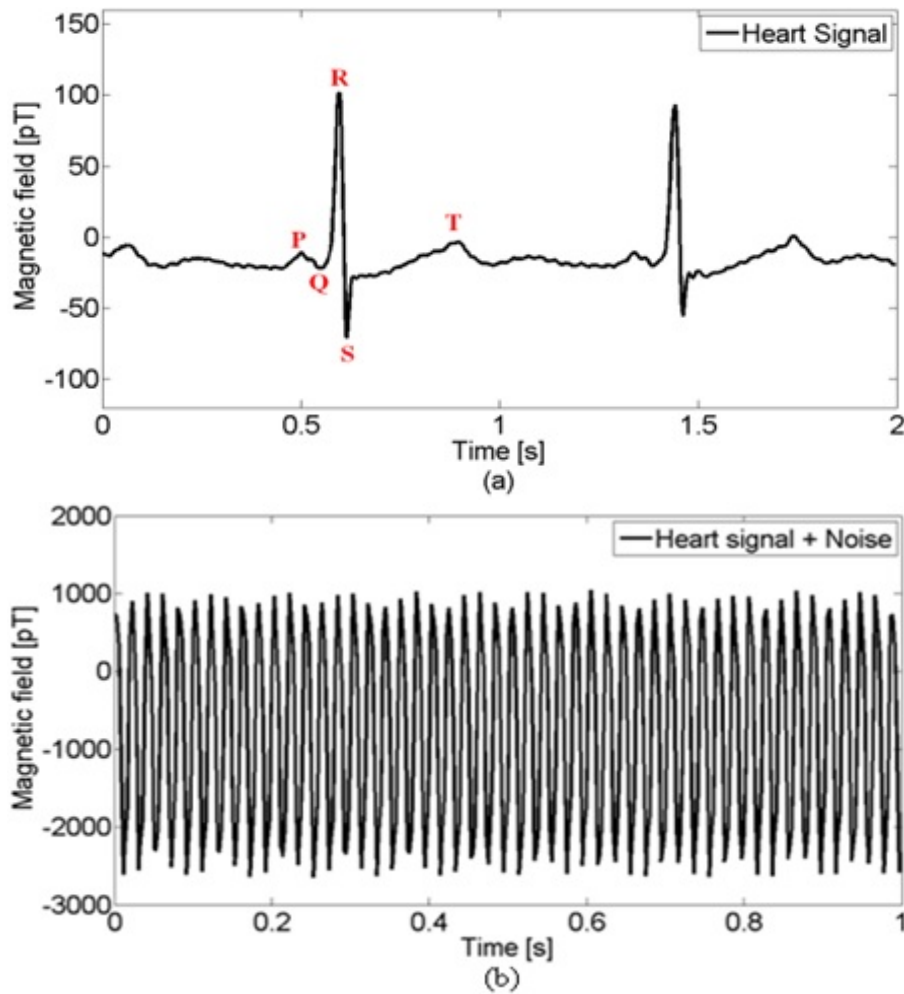


FIG. 3. a) Measured heart signal showing the typical P wave, QRS complex and T wave, which correspond to atrial depolarization, ventricular depolarization and ventricular repolarization, respectively; b) Input signal of the noise canceller obtained by adding the heart signal to the environmental magnetic noise measured inside the laboratory

values are chosen as parents to produce children either by mutation (making random changes to a single parent) or crossover (combining the vector entries of pair of parents).

Each individual can be seen as an array of chromosomes. As for natural evolution, during the reproduction the chromosomes of parents are mixed together to form the children, according to the following rule [10]:

$$C = \alpha P_1 + (1 - \alpha)P_2, \quad (6)$$

where C is a child, $P_{1,2}$ are the two parents and α is a randomly generated number in the range $(0, 1)$.

The current population is then replaced with the new generation and the iteration continues.

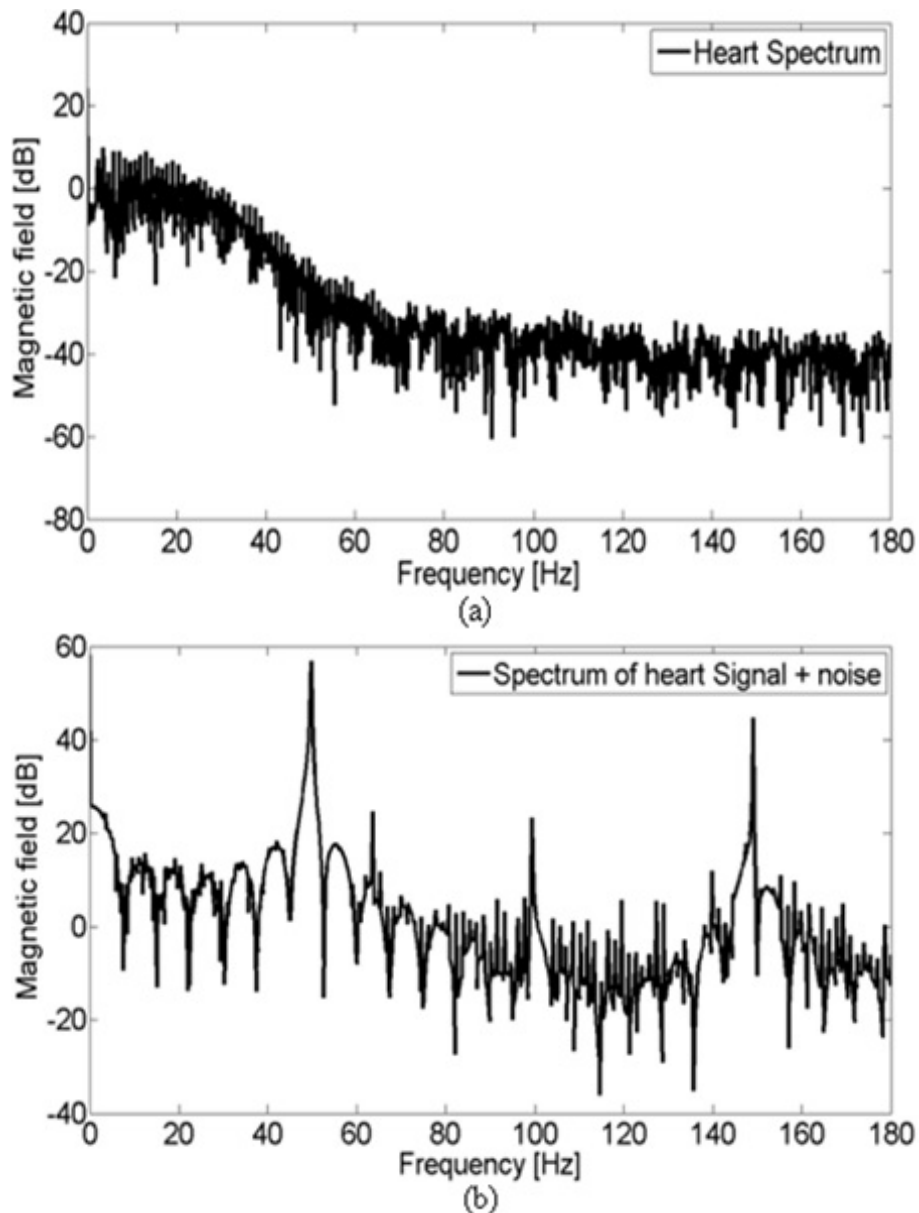


FIG. 4. a) Spectrum of the heart signal; b) Spectrum of the input signal of the noise canceller, exhibiting a strong peak at 50 Hz and weaker peaks at 60 Hz, 100 Hz and 150 Hz

3. Simulations Results and Discussion

A measured cardiac signal taken from the MIT-BIH Arrhythmia Database (220.dat file) [11, 12] is used to verify the ability of both LMS and GA algorithms to extract heart signals from noisy measured cardiac signals. This signal was captured by electrodes placed on the surface of a patient chest. The magnetic field and the electric field generated by human heart have similar waveforms [13]; therefore, it is accurate to assume that the measured MCG signal has similar shape as the measured ECG signal but with amplitude of 100 pT, which corresponds to the typical amplitude of a heart-generated magnetic signal.

Figure 3(a) shows the heart signal with the typical cardiac features, namely, P wave, QRS complex and T wave, which correspond to atrial depolarization, ventricular depolarization

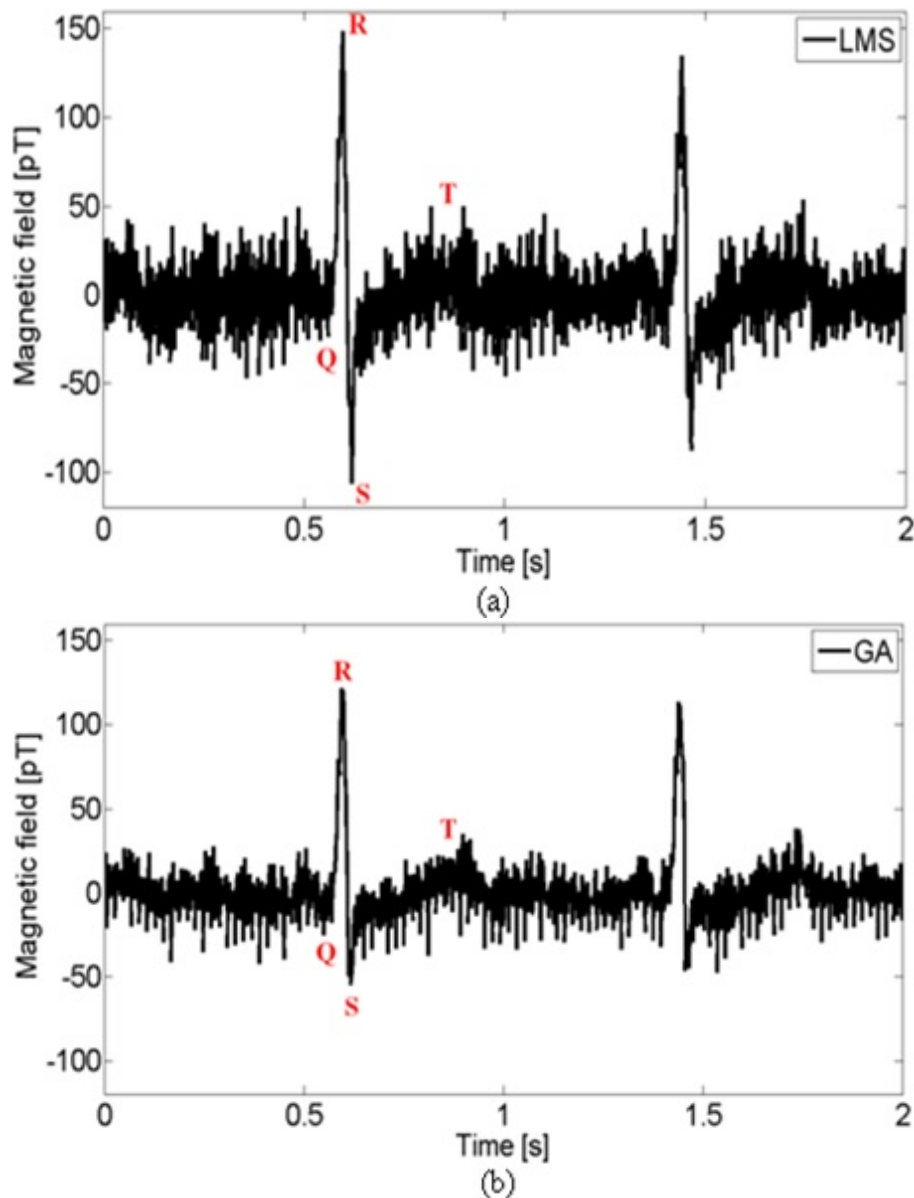


FIG. 5. a) Heart signal recovered by LMS algorithm, calculated SNR improvement factor was 33 dB; b) Heart signal recovered by GA algorithm, calculated SNR improvement factor was 37.4 dB

and ventricular repolarization, respectively. The environmental magnetic noise was measured in our laboratory. The measured environmental noise was due to two main sources, namely, the dc magnetic field of the earth and the magnetic noise caused by alternating signals generated by surrounding equipment in the laboratory. It is also noted that the magnetic noise is more than 10 times higher than the heart signal shown in Fig. 3(a). The signal-to-noise ratio (SNR) was -35.8 dB, calculated by integrating the measured signal and noise powers over several signal periods. The environmental magnetic noise was added to the heart signal to produce the input signal of the noise canceller. This signal is shown in Fig. 3(b). The environmental magnetic noise was also linearly filtered to produce a correlated noise which was used as the reference signal input to the noise canceller, as illustrated in Fig. 1.

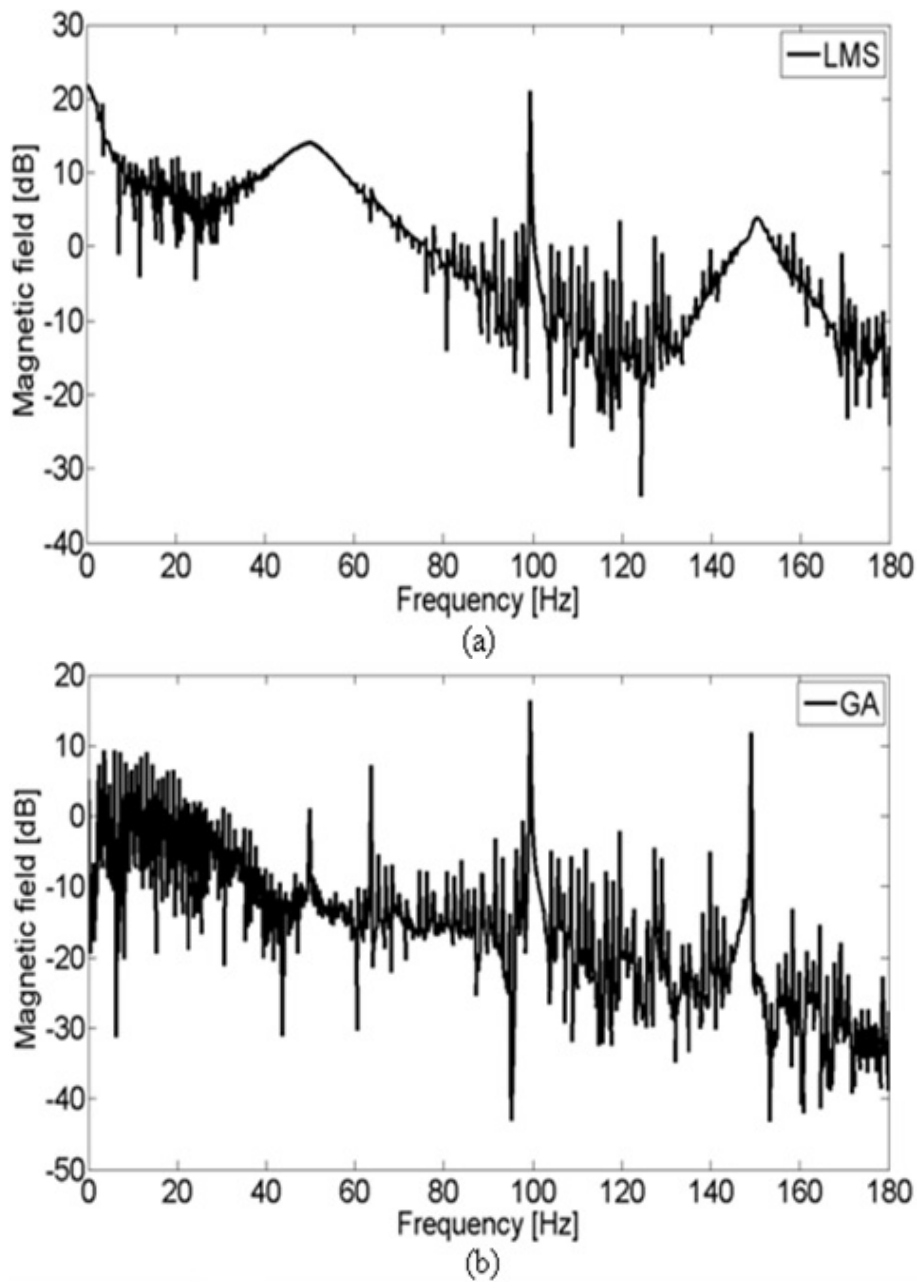


FIG. 6. a) Spectrum of the heart signal recovered by the LMS algorithm; b) Spectrum of the heart signal recovered by the GA algorithm

Figure 4(a) shows the cardiac spectrum that is mainly spread over low frequencies, while Fig. 4(b) shows the spectrum of the input signal of the noise canceller. It is noticed that the heart spectrum was completely encircled by the noise; particularly strong noise peaks were exhibited at dc and 50 Hz whereas the other dominant peaks at the 60 Hz, 100 Hz and 150 Hz had lower levels.

The LMS algorithm produced a SNR improvement of around 33 dB while for the GA algorithm the improvement in SNR was 37.4 dB. Fig. 5(a) and (b) show the heart magnetic signal recovered using the LMS and GA algorithms, respectively. It is obvious that for both recovered signals the QRS and T features are noticeable, whereas the heart magnetic signal

recovered by the LMS algorithm is noisier, making the QRS complex and the T wave hardly detectable.

Figure 6(a) and (b) show the spectra of the heart magnetic signals recovered by the LMS and GA algorithms, respectively. As seen from the results, the Genetic Algorithm outperforms the LMS algorithm at low frequencies, strongly reducing the noise. It is also important to notice that both algorithms are unable to completely cancel the noise at high frequencies; however, this is not crucial as most of the signal information lies in the low-frequencies range.

4. Conclusion

The use of LMS and GA algorithms has been investigated for adaptive noise suppression and the recovering of heart signals in magnetically-unshielded environment. Measured heart signals and magnetic noise have been used to compare the performances of both LMS and GA algorithms in terms of SNR improvement and heart peaks reconstruction. Simulation results have shown that the GA algorithm attains better SNR improvement than the LMS algorithm. A measured heart signal has been recovered by the GA algorithm with a SNR improvement of 37.4 dB and the QRS complex and T wave have successfully been detected. The LMS algorithm has also recovered the input signal, however, with a lower SNR improvement of around 33 dB and noisy QRS complex and T wave. The noise cancellation results shown in this paper are useful for signal processing applications where the signal to noise ratio is much less than unity.

References

- [1] F.E.Smith, et al. Comparison of magnetocardiography and electrocardiography: a study of automatic measurement of dispersion of ventricular repolarization. *The European Society of Cardiology*, **8**, P. 887–893 (2006).
- [2] G.Bison, R.Wynards, A.Weis. Dynamical mapping of the human cardiomagnetic field with a room-temperature, laser-optical sensor. *Optics Express*, **11**, P. 904–909 (2003).
- [3] J.Q.Campbell, et al. Fetal Magnetocardiographic Source Separation: Independent Component Analysis Techniques and Signal-Space Projection. *International Journal of Bioelectromagnetism*, **7**, P. 329–333 (2005).
- [4] R.Fenici, D.Brisinda, A.M.Meloni, P.Fenici. First 36-Channel System for Clinical Magnetocardiography in Unshielded Hospital laboratory for Cardiac Electrophysiology. *International Journal of Bioelectromagnetism*, **5**, P. 80–83 (2003).
- [5] N.V.Thakor, Y.-S.Zhu. Applications of Adaptive Filtering to ECG Analysis: Noise Cancellation and Arrhythmia Detection. *IEEE Transactions on Biomedical Engineering*, **38**, P. 785–794 (1991).
- [6] M.Z.U.Rahman, R.A.Shaik, R.K.Reddy. Noise Cancellation in ECG Signals using Computationally Simplified Adaptive Filtering Techniques: Application to Biotelemetry. *Signal Processing: An International Journal*, **3**, P. 120–131 (2009).
- [7] B.Widrow, et al. Adaptive Noise Cancelling: Principles and Applications. *Proceedings of the IEEE*, **63**, P. 1692–1716 (1975).
- [8] P.S.R.Diniz. *Adaptive Filtering Algorithms and Practical Implementation*, Springer (2008).
- [9] D.E.Goldberg. *Genetic Algorithms in Search, Optimization, and Machine Learning*, Addison-Wesley publishing company, inc. (1989).
- [10] A.Chipperfield, P.Fleming, H.Pohlheim, C.Fonseca. *Genetic Algorithm Toolbox For Use with Matlab. User's Guide*, version 1.2 (2005).
- [11] M.GB and M.RG. The impact of the MIT-BIH Arrhythmia Database. *IEEE Engineering in Medicine and Biology*, **20**, P. 45–50 (2001).
- [12] MIT-BIH Arrhythmia Database. Available: <http://physionet.org/physiobank/database/mitdb/>.
- [13] J.Malmivuo, R.Plonsey. *Bioelectromagnetism. Principles and Applications of Bioelectric and Biomagnetic Fields*. New York Oxford: Oxford University Press (1995).

COMPOSITES OF SINGLE WALLED CARBON NANOTUBES AND LIQUID CRYSTALS AS SWITCHABLE CONDUCTORS

M. Vijay Kumar¹, S. Krishna Prasad¹

¹ Centre for Soft Matter Research, Jalahalli, Bangalore 560 013, India
vijayphy@csmr.res.in, skpras@gmail.com

PACS 61.30.-v, 64.70.mj, 52.25.Mq, 77.84.Nh, 81.07.De

Realizing large anisotropic electrical conductivity in systems wherein the magnitude of the anisotropy can be switched and controlled by employing an external field such as magnetic, electrical or optical fields is of significant interest. The large electrical conductivities possible with carbon nanotubes (CNT) have been combined with the field-switchable orientation of liquid crystals (LC), although the stabilization of such composites is a difficult proposition. Recently we have performed measurements over reasonable lengths of time where the LC-CNT composites are stable without any serious segregation. Here, we describe the results of electrical conductivity, which establish that the LC-CNT composites have a bright future in applications using switchable electrical insulator-conductor devices, for example Mott insulator-conductor systems. The added advantage, as a result of LC use, is the phenomenal ease with which large scale devices can be fabricated. The present work also discusses possible methods for increasing the loading factor, which currently is quite low.

Keywords: carbon nanotube, liquid crystals.

1. Introduction

The research and development of nano materials in science and technology have received significant interest over the past decade [1–4]. From different dimensions, carbon nanotubes (CNT) and liquid crystals have established their own niches, owing to many interesting properties, and a few similarities. Composites of the two materials are expected to yield extraordinary properties, especially with the combination of switchability arising from liquid crystallinity, and the large mechanical and electrical anisotropy of CNTs. The anisotropy of the electric conductivity, being large along the tube axis and small perpendicular to it, has led to proposals of nano-tubes being used in the fabrication of electronic devices [5–8]. Carbon nanotubes occur in two general morphologies, single-wall (SWNT) and multi-wall nanotubes (MWNT), and are normally produced by the techniques of arc-discharge, chemical vapor deposition, or laser ablation [9–11]. For many applications, a uniform alignment of CNTs is essential, and in general, the ability to provide nanotubes in a predetermined direction is of great importance. Additionally, it is desirable to be able to manipulate this direction, for example, by the application of external fields, such as electric, magnetic, or mechanical. Liquid crystals (LC) are anisotropic fluids, located between the isotropic liquid and three-dimensional positionally ordered solid states [12]. Due to molecular self-assembly, LCs exhibit orientational order of e.g., rod-shaped molecules, resulting in anisotropic physical properties while maintaining flow properties in their least ordered structure – the nematic phase. The average direction of the long molecular axes called the director n , can easily be controlled by suitable surface treatment or external fields. The phenomenon of reorientation when achieved with an electric field,

known as the Freedericksz transition [13], is exploited in all common LCD applications from cheap wrist watches to highly sophisticated laptop displays. Attempts have been made [14–20] to employ liquid crystals for imposing alignment on dispersed carbon nanotubes, and to use the Freedericksz transition to manipulate the alignment direction through elastic interactions with the liquid crystal director field. This approach makes it possible to dynamically and collectively change the orientation of nanotube assemblies, and thus, their direction of mechanical and especially electrical anisotropy.

2. Experimental

For the experiments, two liquid crystal compounds were chosen, one of which (labelled SPLC) is strongly polar, having a nematic (N) to isotropic (I) transition temperature (T_{NI}) at 35 °C. The other liquid crystal (WPLC) is weakly polar and has a much higher T_{NI} at 123.8 °C. Both compounds have a positive dielectric anisotropy $\Delta\epsilon$ ($= \epsilon_{\parallel} - \epsilon_{\perp}$, where ϵ_{\parallel} and ϵ_{\perp} indicate the dielectric permittivity parallel and perpendicular to the nematic director). The CNT which were used were procured from Heji and had an average length of 500 nm and diameter of 2 nm. Several LC-CNT composites comprising low ($<0.1\text{wt}\%$) CNT concentrations were prepared. However, we present here the results obtained for a representative mixture with 0.05wt% concentration. A novel method for preparing the mixture, similar to that previously described [19] was employed. The procedure used resulted in the prepared composites appearing slightly darker in color than pure LCs materials with no CNT sedimentation, a problem seen generally with LC-CNT mixtures. The samples were placed in prefabricated Indium Tin Oxide coated glass cells with an electrode dimension of 0.5 cm \times 1 cm and a cell gap of 25 μm through capillary action in the nematic phase. The cell was then observed under a polarizing optical microscope in the crossed polarizer configuration to ascertain the uniform dispersion of CNT. For dielectric and conductivity measurements, the cell was kept inside a homemade heater and placed between the poles of an electromagnet with a maximum field of 1.6 T. The orientation of the cell normal being parallel or perpendicular to the magnetic field direction yields $(\sigma_{\parallel}, \epsilon_{\parallel})$ or $(\sigma_{\perp}, \epsilon_{\perp})$. The measurements were carried out using an impedance analyzer (HP 4294A) at five different frequencies spanning 100 Hz – 1 MHz.

3. Results and Discussion

Figures 1 (a) and (b) depict the temperature dependence of conductivity in \parallel and \perp directions for SPLC as well as WPLC along with their CNT-composites obtained, at a frequency of 1 kHz. The composites with both LC materials exhibited significant enhancement of the conductivity upon the addition of CNT. The magnitude of the enhancement is about 2 orders of magnitude for SPLC, whereas it is a further one order higher with the WPLC compound. The anisotropy in conductivity was retained in the composites. Furthermore, for the SPLC composite there was a 2.5-fold increase in the ratio $\sigma_a = \sigma_{\parallel}/\sigma_{\perp}$ with respect to that of the pure material. The WPLC case had the opposite behavior, with the ratio σ_a being roughly halved for the composite [For purposes of better comparison, the data in the isotropic phase obtained with the two orientations have been matched]. In fact, σ_a values less than 1 are known to be associated with the appearance of smectic ordering or 1-dimensional periodicity parallel to the director. Since it is clear from microscopic observation that the system remains in the nematic phase, this feature suggests that the additional ordering is only short range. Detailed measurements for mixtures with different concentrations as well studies such as XRD are being planned to understand the difference in the behavior between SPLC and WPLC composites.

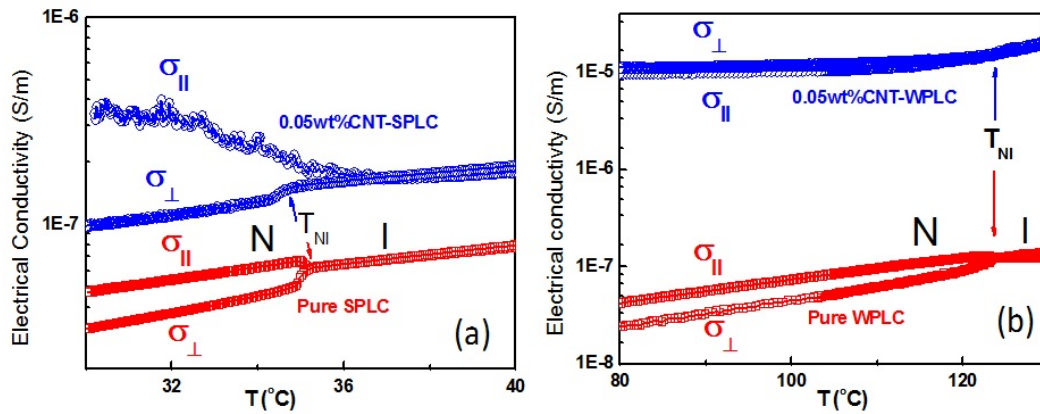


Fig. 1. Electrical conductivity at 1 kHz as a function of temperature \parallel and \perp to the nematic director for pure and composites of (a) SPLC and (b) WPLC materials

Figures 2(a) and (b) present the thermal behavior of ϵ_{\parallel} and ϵ_{\perp} for both pure compounds and their composites. In these cases the addition of CNT resulted in a significant increase in both ϵ_{\parallel} and ϵ_{\perp} as well in the permittivity of the I phase. However, the magnitudes of increases were definitely dependent on the polar nature of the host material: for SPLC the increase for the isotropic permittivity was $\sim 25\%$, but for WPLC, the value was tripled. A possible reason for the amplified change in WPLC value could be connected with the low frequency dielectric relaxation that the pure WPLC exhibits. Further study of director relaxation dynamics is expected to shed more light on this feature.

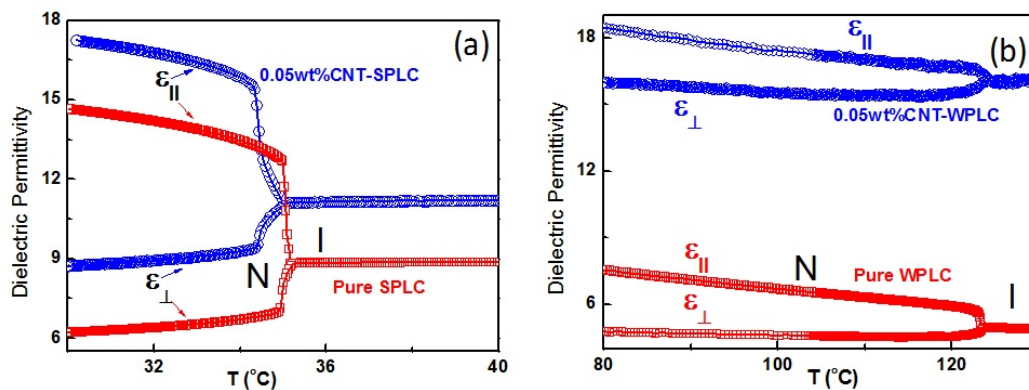


Fig. 2. Thermal variation of the dielectric permittivity at 1 kHz along (\parallel) and perpendicular (\perp) to the director for pure and composites of (a) SPLC and (b) WPLC

Another interesting aspect observed is the temperature dependent permittivity behavior in the I phase of the strongly polar material. The pure material exhibits a concave shaped anomaly (CSA) that has been argued to be associated with the antiparallel arrangement of the molecules even in the I phase, but in the vicinity of T_{NI} . It is observed that the temperatures at which the anomaly has a maximum and the highest ϵ value obtained are larger for the SPLC composite than for the pure SPLC compound. We propose that this is a direct indication of the enhancement of the nematic-like short range order in the

I phase resulting from the presence of CNT particles. Since CSA is not seen for even the pure WPLC, it is not possible to compare the effects between the two types of composites.

Preliminary studies indicate that the composites of both types can be switched using an electric field, causing a reorientation of the nematic molecules. The notable changes in conductivity between the parallel and perpendicular directions for the SPLC composite makes it attractive for possible use in electrically-controlled conductivity altering devices. Development of systems in which the conductivity change is substantially higher than seen here would make the LC-CNT composites quite attractive.

4. Conclusions

We have reported anisotropic electrical conductivity and dielectric permittivity studies on two liquid crystals and their low concentration composites with SWCNT. The two liquid crystals are chosen such that one of them is strongly polar having its dipole moment parallel to the long axis of the molecule whereas the other one is weakly polar with its dipole in the transverse direction. Both conductivity and permittivity retained their anisotropic nature, even in the composites. More importantly, the conductivity exhibited a large increase, as much as 3 orders of magnitude, for the composite with the weakly polar material. The qualitative permittivity behavior was also quite different upon the inclusion of CNT. Along with the mentioned switchable electrical character, which imparts a field-modifiable conductivity value, these materials are quite promising for inclusion in future electronic devices.

Acknowledgments

The financial support by SERB, DST under the project No. SR/S2/CMP-0029/2011 is gratefully acknowledged.

References

- [1] Harris P. J. F. *Carbon Nanotubes and Related Structures*, Cambridge University Press. Cambridge (1999).
- [2] Saito R, Dresselhaus G and Dresselhaus M. S. *Physical Properties of Carbon Nanotubes*. Imperial College Press, London (2001).
- [3] Rao C. N. R., Tatishkumar B. C., Govindaraj A., and M. Nath, *Chem Phys Chem*, **2**(2), P. 78–105 (2001).
- [4] Nalwa H. S., Ed., *Encyclopedia of Nanoscience and Nanotechnology*, 15-volume set (11-25 vols). American Scientific Publishers (2011).
- [5] Baughman R. H., Zakhidov A. A., and de Heer W. A., *Science*, **297**(5582), P. 787-792 (2002).
- [6] Tans S. J., Verschueren A. R. M., and Dekker C. *Nature Londond*, **393**, P. 49-51 (1998).
- [7] Avouris P., Hertel T., Martel R., Schmidt T., Shea H. R., and Walkup R. E., *Appl. Surf. Sci*, **141**, P. 201-209 (1999).
- [8] Thelander C. and Samuelson L., *Nanotechnology*, **13**, P. 108–113 (2002).
- [9] Iijima S., *Nature Londond*, **354**, P. 56–58 (1991).
- [10] Endo M., Takeuchi K., Igarashi S., Kobori K., Shiraiishi M., and Kroto H. W., *J. Phys. Chem. Solids*, **54**, P. 1841–1848 (1993).
- [11] Thess A., Lee R., Nikdaev P., Dai H., Petit P., Robert J., Xu C., Lee Y. H., Kim S. G., Rinzler A. G., Colbert D. T., Scuseria G. E., Tomanek D., Fischer J. E., and Smalley R. E., *Science*, **273**, P. 483 (1996).
- [12] See for e.g., Chandrasekhar S., *Liquid Crystals*, 2nd Edition. Cambridge University Press (1992).
- [13] Freedericksz V. and Tsvetkov V., *Phys. Z.*, **6**, P. 490 (1934).
- [14] Dierking I., Scalia G., and Morales P., and LeClere D., *Adv. Mater.*, **16**, P. 865–869 (2004).
- [15] Lagerwall J. P. F., Scalia G., Haluska M., Dettlaff U., Roth S., and Giesselmann F., *Adv. Mater.*, **19**, P. 359–364 (2007).

- [16] Basu R. and Iannacchione G., *Appl. Phys. Lett.*, **93**, P. 183105 (2008).
- [17] Lee W., Wang C. Y., and Shin Y. C. , *Appl. Phys. Lett.*, **85**, P. 513 (2004).
- [18] Shah H. J., Pan H., and Hsieh C., *Jpn. J. Appl. Phys.*, Part 1, **45**, P. 6392–6394 (2006).
- [19] Jayalakshmi V. and Krishna Prasad S., *Appl. Phys. Lett.*, **94**, P. 202106 (2009).
- [20] Muklesur Rahman and Wei Lee *J. Phys. D: Appl. Phys.*, **42**, P. 063001 (2009).

EFFECT OF SINTERING TEMPERATURE ON THE STRUCTURAL AND MAGNETIC PROPERTIES OF COBALT FERRITE NANOPARTICLES

Sheena Xavier, Smitha Thankachan, Binu P. Jacob, E. M. Mohammed
Research Department of Physics, Maharaja's College, Ernakulam, Kerala, India
emmohammed.2005@yahoo.com, sheena.xavier1@gmail.com

PACS 81.07.Bc, 61.46.Df, 75.50.Tt

Cobalt ferrite nanoparticles have been synthesized by the sol-gel method. The prepared sample was sintered at four different temperatures (300 °C, 400 °C, 500 °C and 700 °C) for four hours. The structural characterizations of all the prepared samples were done using XRD, TEM and FTIR. Crystallite size was found to increase with sintering temperature and this can be attributed to the grain growth of the particles. The particle size of each sample was determined using TEM. The FTIR spectra show two strong absorption bands in the range of 1000–400 cm^{-1} , characteristic of spinel ferrites. The room temperature magnetic measurements showed a strong influence of sintering temperature on saturation magnetization and coercivity.

Keywords: sol gel, ferrites, sintering temperature, magnetic properties.

1. Introduction

Nanosized spinel ferrite particles have attracted much attention in recent years because of their potential applications in high density magnetic recording, magnetic fluids, spintronics, data storage and gas sensors [1, 2]. Among the ferrite nanoparticles, cobalt ferrite has been widely studied due to its excellent chemical stability, mechanical hardness, reasonable saturation magnetization and high magneto-crystalline anisotropy [3]. These properties make it a promising candidate for many applications, such as magnetic data storage, magnetic drug targeting, biosensors and magnetic refrigeration [4].

Nano ferrites are simultaneously good magnetic and dielectric materials. These properties of the nano ferrites are affected by the preparation conditions, chemical composition, sintering temperature and the method of preparation [5]. Several chemical and physical methods such as spray pyrolysis, sol-gel, co-precipitation, combustion technique, high energy milling etc. have been used for the fabrication of stoichiometric and chemically pure nano ferrite materials [6]. Among the available chemical methods, the sol-gel technique is an excellent method to synthesize nanoparticles with maximum purity [7]. This method has the advantage of good stoichiometric control and the production of ultrafine particles with a narrow size distribution.

Mathew George et al [2] studied the effect of finite size on the structural and magnetic properties of nickel ferrite nanoparticles. They reported a decrease in saturation magnetization with decreased grain size. Chinnasamy et al [9] reported the synthesis of cobalt ferrite nanoparticles by co-precipitation method. They observed that the magnetic properties of cobalt ferrite nanoparticles are strongly dependent on their size. In spite of the development of a variety of synthesis routes, the production of cobalt ferrite nanoparticles with desirable size and magnetic properties is still a challenge. This would justify any effort to produce size tuned cobalt ferrite nanoparticles with size ranging from the superparamagnetic threshold of 10 nm to the critical single domain size of 70 nm [10, 11]. In

the present paper, the structural and magnetic properties of nanocrystalline cobalt ferrite in relation to sintering temperature were investigated.

2. Experimental

2.1. Synthesis

Nano particles of cobalt ferrite were synthesized by the sol-gel combustion method. A stoichiometric ratio of cobalt nitrate and ferric nitrate (AR grade MERCK) were dissolved in ethylene glycol using a magnetic stirrer. The solution was then heated at 60 °C for 3 hours until a wet gel of the metal nitrates was obtained. The gel was then dried at 120 °C. This resulted in the self ignition of the gel producing a highly voluminous and fluffy product. The combustion can be considered as a thermally induced redox reaction of the gel wherein ethylene glycol acts as the reducing agent and the nitrate ion acts as an oxidant. The nitrate ion provides an oxidizing environment for the decomposition of the organic component. The obtained powder was ground well and divided into four portions. They were sintered for four hours in a muffle furnace at four different temperatures 300, 400, 500 and 700 °C.

2.2. Characterization

The cobalt ferrite samples were characterized by an X-ray powder diffractometer (XRD, Bruker AXS D8 Advance) using Cu-K α radiation ($\lambda = 1.5406\text{\AA}$) at 40 kV and 35 mA. Lattice parameter was calculated assuming cubic symmetry. The crystal structure, crystallite size and X-ray density were determined. The particle size was determined by subjecting the sample to Transmission Electron Microscopy (Philips, CM200). Wavelength Dispersive X-ray Fluorescence (WD-XRF) Spectrometer (Bruker S4-Pioneer) was used for elemental analysis. The Fourier transform infrared (FTIR) absorption spectra of the samples were recorded using FTIR spectrometer (Thermo Nicolet, Avatar 370) in the wave number range 4000–400 cm^{-1} with Potassium bromide (KBr) as binder. The Magnetic characterization was carried out using a vibrating sample magnetometer (VSM; Lakeshore 7410) at room temperature up to a maximum field of 20kOe.

3. Results and Discussion

3.1. Structural Analysis

The XRD patterns of CoFe_2O_4 nanoparticles sintered at 300, 400, 500 and 700 °C are depicted in Fig. 1 and are typical of spinel structure.

Comparing the XRD pattern with the standard data (JCPDS PDF card No. 22-1086), the formation of cobalt ferrite nanoparticles was confirmed. The sample sintered at 700 °C showed an extra peak, indicating the formation of hematite phase at this temperature. The diffraction peaks are broad because of the nanometer size of the crystallite. The crystallite size 'D' of the samples has been estimated from the broadening of XRD peaks using the Scherrer equation [7].

$$D = \frac{K\lambda}{\beta \cos \theta} \quad (1)$$

The lattice parameter 'a' is calculated for prominent peak (311) using Bragg's equation.

$$a = d_{hkl} \sqrt{h^2 + k^2 + l^2} \quad (2)$$

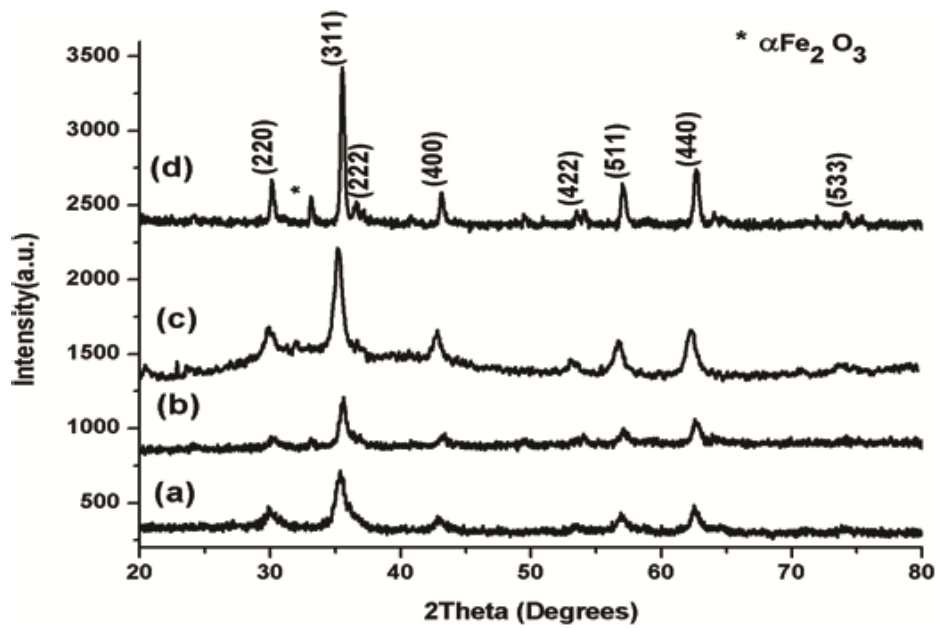


Fig. 1. XRD patterns of CoFe_2O_4 sintered at (a) 300 °C, (b) 400 °C, (c) 500 °C, (d) 700 °C

The actual X-ray density, ρ_x was calculated using the formula

$$\rho_x = \frac{8M}{Na^3} \quad (3)$$

where, 'M' is the molecular weight, 'N' is Avogadro's number and 'a' is the lattice parameter. Calculated values of lattice parameter, crystallite size and X-ray density of all the samples are listed in Table 1.

Table 1. Lattice parameter, crystallite size, X-ray density and vibrational frequency band positions of CoFe_2O_4

Sintering temperature (°C)	Lattice parameter (nm)	Crystallite size D (nm)	X-ray density (g/cc)	ν_1 (cm^{-1})	ν_2 (cm^{-1})
300	0.841	12.82	5.243	575	397
400	0.836	18.47	5.330	581	399
500	0.842	19.72	5.217	575	399
700	0.838	52.49	5.306	580	405

The crystallite size was observed to increase with higher sintering temperatures. It has been reported that the sintering process generally decreases lattice defects and strain, but this technique can cause the coalescence of smaller grains, resulting in an increased average grain size for the nanoparticles [12]. Calculated values of lattice parameter of cobalt ferrite samples were in close agreement with standard data [13].

3.2. WD-XRF Analysis

The stoichiometry of the powder samples were checked by WD-XRF analysis. The composition of the elements present in the sample sintered at 400 °C is shown in Table 2.

From the table it is obvious that the samples show the expected stoichiometry. No trace of any impurity was found. This indicated the purity of the samples.

Table 2. Elemental analysis of CoFe_2O_4

Elements present	Expected (wt. %)	WD - XRF (wt. %)
Co	25.11	25.25
Fe	47.61	47.30
O	27.26	27.30

3.3. TEM Analysis

Fig. 2 shows the TEM image of CoFe_2O_4 sample sintered at 400°C . In the figure most of the nanoparticles appear with an almost spherical shape and are agglomerated. The average particle size determined from TEM analysis was 28 nm, which was found to be in reasonable agreement with the figure obtained from XRD analysis.

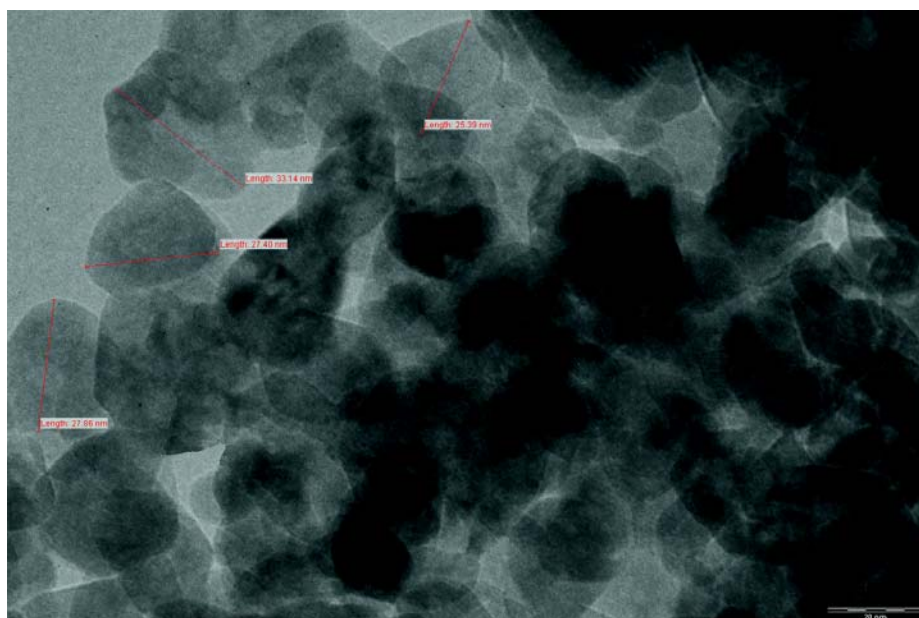


Fig. 2. TEM image of CoFe_2O_4 sintered at 400°C

3.4. FTIR Analysis

Ferrite possesses the structure of mineral spinel MgAl_2O_4 . It crystallizes in the cubic form with the space group $\text{Fd}\bar{3}\text{m}$. Ferrite can be considered as a continuously bonded crystal with atoms bonded to all nearest neighbours by equivalent forces [14]. In the wave number range $1000\text{--}300\text{ cm}^{-1}$, the infrared bands of solids are usually assigned to vibration of ions in the crystal lattice. FTIR spectra of the investigated samples are shown in Fig. 3.

Two main broad metal-oxygen bands are seen in the IR spectra of all spinels, and ferrites in particular. The highest one (ν_1) generally observed in the range $600\text{--}550\text{ cm}^{-1}$, corresponds to intrinsic stretching vibrations of the metal at the tetrahedral site, whereas the lowest band (ν_2), usually observed in the range $450\text{--}385\text{ cm}^{-1}$, is assigned octahedral-metal stretching [15]. The spectra showed prominent bands near 3400 and 1600 cm^{-1} ,

which were attributed to the stretching modes and H-O-H bending vibrations of the free or absorbed water. The vibrational frequencies of IR bands are listed in table 1, which are in agreement with the reported values.

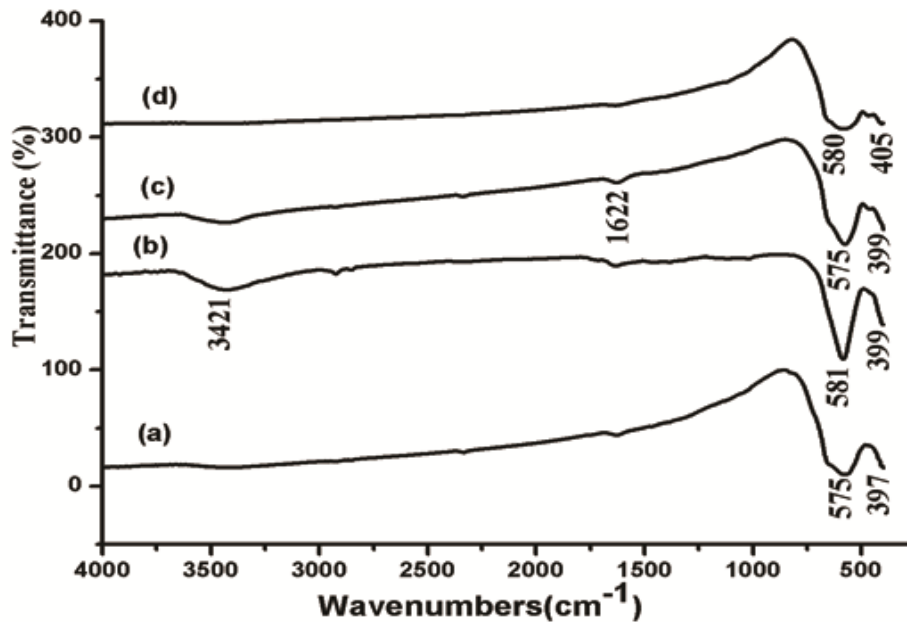


Fig. 3. FTIR spectra of CoFe_2O_4 sintered at (a) 300 °C (b) 400 °C (c) 500 °C (d) 700 °C

4. Magnetic Properties

Hysteresis loops were measured to determine magnetic parameters such as the saturation magnetization M_s , coercivity H_c and remnant ratio R for all the samples. Fig. 4 shows the typical magnetic hysteresis loops of CoFe_2O_4 sintered at 300, 400, 500 and 700 °C.

The saturation magnetization values of the cobalt ferrite samples were found to be lower than the corresponding bulk value of 80.8 emu/g [1]. The low value of saturation magnetization compared with that of the bulk can be understood on the basis of the core-shell model, which explains that the finite size effects of the nanoparticles lead to canting or non-collinearity of spins on their surface, thereby reducing magnetization [16, 17]. The saturation magnetization increased linearly with the sintering temperature. The coercivity varied from 1379.2 to 1893.4 Oe. The coercivity values for cobalt ferrite samples synthesized by the sol gel method were higher than the figures obtained for the same compound produced by other synthesis methods [18, 19]. The changes in the magnetic properties of cobalt ferrite can be attributed to the modification of the particle sizes, which is dependent upon the sintering temperature. With an increase in the sintering temperature, the crystallite size of the cobalt ferrite nanoparticles changed from 12.82 (300 °C) to 52.49 nm (700 °C).

The decrease in saturation magnetization along with particle size can be attributed to the following: in the ferrimagnetic ferrite structure, the magnetization of tetrahedral sublattice is antiparallel to that of the octahedral sublattice, however, ultrafine ferrites have non-collinear magnetic structure on the surface layer. The reduction in particle size causes an increase in the proportion of non-collinear magnetic structure, in which the magnetic

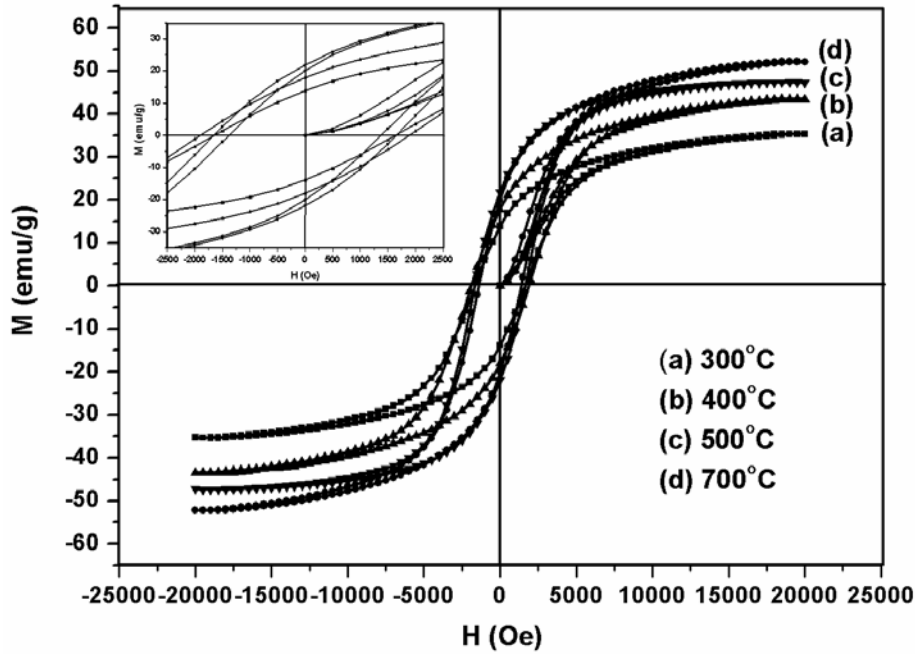


Fig. 4. Room temperature magnetic hysteresis of CoFe_2O_4

moments are not aligned with the direction of external magnetic field. This increase in the proportion of non-collinear structure decreases the saturation magnetization.

Table 3. Magnetic parameters of CoFe_2O_4 nanoparticles

Sintering temperature ($^{\circ}\text{C}$)	M_S (emu/g)	M_R (emu/g)	H_C (Oe)	R
300	35.38	13.85	1640.3	0.3915
400	43.50	17.95	1893.4	0.4126
500	47.37	21.84	1652.9	0.4611
700	52.24	20.07	1379.2	0.3842

The coercivity first increased as the sintering temperature increased, reaching a maximum value of 1893 Oe at 400°C , and then decreased for any further increase in temperature. It is reported that coercivity is affected by the factors such as magneto-crystallinity, micro strain, size distribution, anisotropy and the magnetic domain size [20–22]. In the multidomain regime, the coercivity is inversely proportional to the size of the nanoparticles [20]. The low value of coercivity at 300°C may be due to the presence of superparamagnetic particles, particularly for values close to 10 nm. The saturation magnetization is related to coercivity through the Brown's relation;

$$H_C = \frac{2 K_1}{\mu_0 M_s}, \quad (4)$$

where K_1 is the anisotropy constant and μ_0 is the permeability of free space. According to this relation, coercivity is inversely proportional to the saturation magnetization. The results of our experiments also lead to the above relation except for the sample sintered at 300°C . As indicated earlier this deviation could be attributed to the presence of superparamagnetic particles. The variation of coercivity and saturation magnetization with

sintering temperature is shown in figure 5. The remnant ratio $R=M_r/M_s$ is an indication of the ease with which the direction of magnetization reorients to the nearest easy axis magnetization direction after the magnetic field is removed. The values of the remnant ratio of the prepared samples are in the range 0.38–0.46. The low value of R is an indication of the isotropic nature of the material [23].

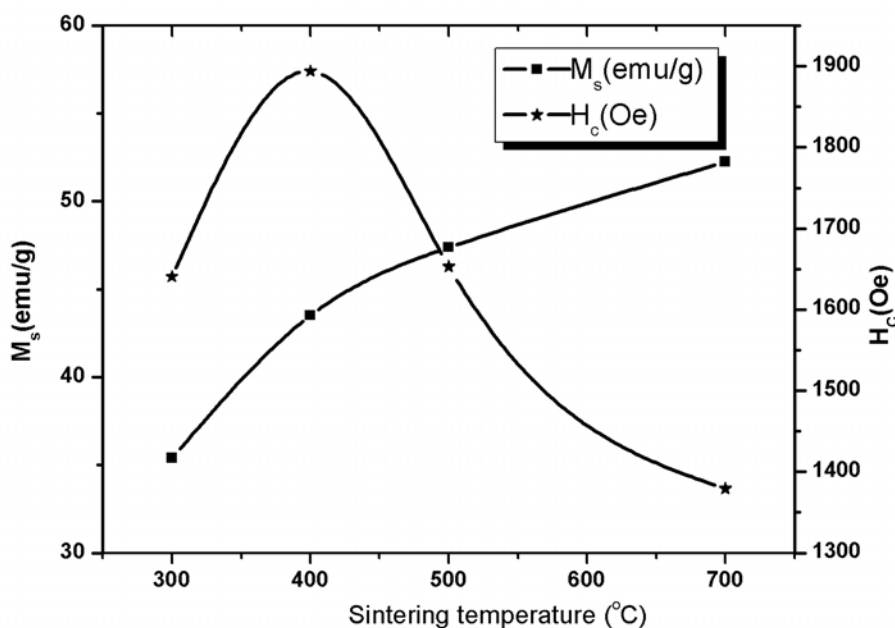


Fig. 5. Variation of saturation magnetization and coercivity as a function of sintering temperature

5. Conclusions

Nanocrystalline cobalt ferrite has been successfully synthesized by the sol-gel method. XRD results confirmed the formation of cubic spinel structure in all the samples. The crystallite size of the samples increased with the higher sintering temperatures. The crystallite size varied from 13 to 52 nm and was in reasonable agreement with the results obtained from TEM. The FTIR analysis corroborated the spinel structure of the samples. The expected stoichiometry of the samples was confirmed by the XRF elemental analysis. The saturation magnetization increased gradually with increasing sintering temperatures, while coercivity initially increased, attaining a maximum value and then decreased. These results have been explained based on the particle size and surface effects of the ultrafine materials and were in agreement with the Brown's relation.

Acknowledgements

SX acknowledges the University Grants Commission of India for providing teacher fellowship. EMM thanks DST and UGC for the financial support. Authors thank SAIF, CUSAT Kochi, SAIF, IIT Madras and SAIF IIT Mumbai for providing XRD, FTIR, VSM and TEM measurement facilities.

References

- [1] Veena Gopalan E., Joy P.A., I.A Al-Omari, Sakthi Kumar D., Yasuhiko Yoshida, Anantharaman M.R., On the Structural, Magnetic and Electrical Properties of Sol-gel derived Nanosized Cobalt Ferrite. *J. Alloys compd*, **485**, P. 711–717 (2009).
- [2] Mathew George, Asha Mary John, Swapna S. Nair, p.A.Joy, M.R. Anantharaman, Finite size effects on the structural and magnetic properties of sol gel synthesized NiFe₂O₄ powders. *Journal of Magnetism and Magnetic Materials*, **302**, P. 190–195 (2006).
- [3] Yue Zhang, Zhi Yang, Di Yin, Yong Liu, ChunLong Fei Composition and magnetic properties of cobalt ferrite nanoparticles prepared by the co-precipitation method. *J.Magn.Magn.Mater*, **322**, P. 3470–3475 (2010).
- [4] Zhenfa Zi, Yuping Sun, Xuebin Zhu, Wenhai Song, Synthesis and magnetic properties of CoFe₂O₄ ferrite nanoparticles. *J.Magn.Magn.Mater*, **321**, P. 1251–1255 (2009).
- [5] Veena Gopalan E., I.A Al-Omari, Sakthi Kumar D., Yasuhiko Yoshida, Joy P.A. et.al. Inverse magnetocaloric effect in sol-gel derived nanosized cobalt ferrite. *Appl. Phys. A: Materials Science & Processing*, **99**(2), P. 497–503 (2010).
- [6] Gul I.H., Masqood A., Structural, magnetic and electrical properties of cobalt ferrites prepared by the sol-gel route. *J. Alloys compd*, **465**, P. 227–231 (2008).
- [7] Pawan Kumar, Sharma S.K., Knobel M., Singh M., Effect of L^{a3+} doping on electric, dielectric and magnetic properties of cobalt ferrite processed by co-precipitation technique. *J. Alloys compd*, **508**, P. 115–118 (2010).
- [8] Binu P. Jacob, Smitha Thankachan, Sheena Xavier, E M Mohammed, Effect of Gd³⁺ doping on the Structural and Magnetic Properties of nanocrystalline Ni-Cd mixed ferrite. *Physica Scripta*, **84**, P. 045702–045708 (2011).
- [9] C. N. Chinnasamy, M. Senoue, B. Jeyadevan, Oscar perales-Perez, K.Shinoda and K.Tohipi, Synthesis of size controlled cobalt ferrite particles with high coercivity and squareness ratio. *Journal of colloids and Interface Science* **263**, P. 80–83 (2003).
- [10] Dunlop D.J. Hysteretic properties of synthetic and natural monodomain grains. *Philos.Mag.* **19**, P. 329–338 (1969).
- [11] Berkowitz A.E., Schuele W.J., Magnetic properties of some ferrite Micropowders. *J.Appl. Phys* **30**, P. 1345 (1959).
- [12] Raming T.P., Winnubust A.J.A., Van Kats C.M., Philipse P., The synthesis and Magnetic Properties of nanosized Hematite particles. *J. Colloid Interface Sci.* **249**, P. 346 (2002).
- [13] Smit J., Wijn H.P.J., *Ferrites*. Philips Technical Library, Netherlands (1959).
- [14] Maldron R.D. *Phys. Rev.* **99**, P. 1727–35 (1955).
- [15] Ahmed M.A., Ateia E., Salah L.M., El-Gamal. Structural and electrical studies on La³⁺ substituted Ni-Zn ferrites. *Mater. Chem. Phys.* **92**, P. 310–321 (2005).
- [16] Priyadarshini P., Pradeep A., Rao. P.S, Chandrasekharan G., Structural, spectroscopic and magnetic study of nanocrystalline Ni-Zn ferrite. *Mater. Chem. Phys.*, **116**, P. 207–13 (2009).
- [17] Kodama R H Magnetic Nanoparticles. *J. Magn. Magn. Mater.*, **200**, P. 359–72 (1999).
- [18] Lijun Zhao, Hua Yang, Xueping Zhao, Lianxiang Yu, Yuming Cui, Shouhua Feng Magnetic Properties of CoFe₂O₄ ferrite doped with rare earth ion. *Mater. Lett.*, **60**, P. 1-6 (2006).
- [19] Panda R. N., Shih J. C., Chin T. S., Magnetic properties of nanocrystalline Gd- or Pr- substituted CoFe₂O₄ synthesized by the citrate precursor technique. *J.Magn.Magn.Mater.*, **257**, P. 79-86 (2003).
- [20] Suvankar Chakraverty, Malay Bandyopadhyay, Coercivity of magnetic nanoparticles: a stochastic model. *J.Phys.: Condens. Matter*, **19**, P. 216201-16 (2007).
- [21] M.K. Khan., Z.J Zhang., Synthesis and magnetic properties of spinel ferrite nanoparticles doped with lanthanide ions. *Appl. Phy. Lett.*, **78**, P. 3651 (2001).
- [22] Jiang Jing, Li Liangchao, Xu Feng, Structural Analysis and Magnetic properties of Gd-Doped Li-Ni Ferrites Prepared using rheological Phase Reaction Method. *J. Rare Earths*, **25**, P. 79 (2007).
- [23] Toksha B.G., Sagar E. Shirsath, S.M. Patange, K.M.Jadhav, Strutural investigations and magnetic properties of cobalt ferrite nanoparticles prepared by sol-gel auto combustion method, *Solid State Commun.* **147**, P. 479–483 (2008).



NANOSYSTEMS:

PHYSICS, CHEMISTRY, MATHEMATICS

INFORMATION FOR AUTHORS

The journal publishes research articles and reviews, and also short scientific papers (letters) which are unpublished and have not been accepted for publication in other magazines. Articles should be submitted in English. All articles are reviewed, then if necessary come back to the author to completion.

The journal is indexed in Chemical Abstract Service of the American Chemical Society and in Russian Scientific Citation Index.

Author should submit the following materials:

1. Article file in English, containing article title, the initials and the surname of the authors, Institute (University), postal address, the electronic address, the summary, keywords, MSC or PACS index, article text, the list of references.
2. Files with illustrations, files with tables.
3. The covering letter in English containing the article information (article name, MSC or PACS index, keywords, the summary, the literature) and about all authors (the surname, names, the full name of places of work, the mailing address with the postal code, contact phone number with a city code, the electronic address).
4. The expert judgement on possibility of publication of the article in open press (for authors from Russia).

Authors can submit a paper and the corresponding files to the following addresses: nanojournal.ifmo@gmail.com, popov1955@gmail.com.

Text requirements

Articles should be prepared with using of text editors MS Word or LaTeX (preferable). It is necessary to submit a pdf copy. In the name of files the English alphabet is used. The recommended size of short communications (letters) is 4-6 pages, research articles – 6-15 pages, reviews – 30 pages.

Recommendations for text in MS Word:

Formulas should be written using Math Type. Figures and tables with captions should be inserted in the text. Additionally, authors present separate files for all figures and Word files of tables.

Recommendations for text in LaTeX:

Please, use standard LaTeX without macros and additional style files. The list of references should be included in the main LaTeX file. Single LaTeX file of the paper with the corresponding pdf file should be submitted.

References in the article text are given in square brackets. The list of references should be prepared in accordance with the following samples:

- [1] N. Surname. *Book Title*. Nauka Publishing House, Saint Petersburg, 281 pp. (2000).
- [2] N. Surname, N. Surname. Paper title. *Journal Name*, **1**(5), P. 17-23 (2000).
- [3] N. Surname, N. Surname. Lecture title. In: Abstracts/Proceedings of the Conference, Place and Date, P. 17-23 (2000).
- [4] N. Surname, N. Surname. Paper title (2010). URL: <http://books.ifmo.ru/ntv>.
- [5] N. Surname, N. Surname. Patent Name. Patent No. 11111, Bul. No. 33, 5 pp. (2010).
- [6] N. Surname, N. Surname. Thesis Title. Thesis for full doctor degree in math. and physics, Saint Petersburg, 105 pp. (2000).

Requirements to illustrations

Illustrations should be submitted as separate black-and-white files. Formats of files – jpeg, eps, tiff.



NANOSYSTEMS:

PHYSICS, CHEMISTRY, MATHEMATICS

Журнал зарегистрирован

Федеральной службой по надзору в сфере связи, информационных технологий и массовых коммуникаций

(свидетельство ПИ № ФС 77 - 49048 от 22.03.2012 г.)

ISSN 2220-8054

Учредитель: федеральное государственное бюджетное образовательное учреждение высшего профессионального образования «Санкт-Петербургский национальный исследовательский университет информационных технологий, механики и оптики»

Издатель: федеральное государственное бюджетное образовательное учреждение высшего профессионального образования «Санкт-Петербургский национальный исследовательский университет информационных технологий, механики и оптики»

Отпечатано в типографии «Фалкон Принт»

Адрес: 197101, г. Санкт-Петербург, ул. Большая Пушкарская, 54

Подписка на журнал НФХМ

На 2013 год подписка осуществляется через ОАО Агентство «Роспечать»

Подписной индекс 57385 в каталоге «Издания органов научно-технической информации»